# GEOMECHANICAL CHARACTERIZATION AND RESERVOIR SIMULATION OF A $CO_2$ SEQUESTRATION PROJECT IN A MATURE OIL FIELD, TEAPOT DOME, WY

A DISSERTATION
SUBMITTED TO THE DEPARTMENT OF GEOPHYSICS
AND THE COMMITTEE ON GRADUATE STUDIES
OF STANFORD UNIVERSITY
IN PARTIAL FULFILLMENT OF THE REQUIREMENTS
FOR THE DEGRREE OF
DOCTOR OF PHILOSOPHY

Laura Chiaramonte

December 2008

I certify that I have read this dissertation and that in my opinion it is fully adequate, in scope and quality, as a dissertation for the degree of Doctor of Philosophy.

_____

(Mark D. Zoback) Principal Adviser

I certify that I have read this dissertation and that in my opinion it is fully adequate, in scope and quality, as a dissertation for the degree of Doctor of Philosophy.

_____

(S. Julio Friedmann)

I certify that I have read this dissertation and that in my opinion it is fully adequate, in scope and quality, as a dissertation for the degree of Doctor of Philosophy.

_____

(Jerry M. Harris)

Approved for the University Committee on Graduate Studies.

# ABSTRACT

There is increasing evidence that reinforces the view that climate and greenhouse gas cycles are intimately related. Carbon dioxide ($CO_2$) is the main anthropogenic gas contributing to the greenhouse effect and global warming. The main anthropogenic source of $CO_2$ comes from the burning of fossil fuels which currently dominates commercially supplied energy worldwide. Since it is generally accepted that concentration in the atmosphere of greenhouse gases, in particular $CO_2$, must be restricted, a technique capable of reducing the $CO_2$ emissions to the atmosphere while still allowing the use of fossil fuels is a key advance in the short to medium term solution to this problem. One such solution that has been proposed is Carbon Capture and Sequestration (CCS) has been.

However, for CCS to be a viable carbon management solution, one of the main issues to be addressed is the risk of $CO_2$ leakage. In light of this, a key step in the evaluation of any potential site being considered for geologic carbon sequestration is the ability to predict whether the increased pressures associated with $CO_2$ sequestration are likely to affect seal capacity.

In this dissertation, I present my contribution towards the understanding and prediction of the risk of $CO_2$ leakage through natural pathways (i.e. faults and

fractures). The main portion of this dissertation deals with geomechanical aspects of $CO_2$ Sequestration in Teapot Dome, WY, a mature oil field. The last study investigates the use of induce microseismicity to enhance permeability and injectivity in tight reservoirs and to monitor carbon sequestration projects.

In the first three projects, the Tensleep Formation, a Pennsylvanian age eolian fractured sandstone, is evaluated as the target horizon for a pilot $CO_2$ EOR-carbon storage experiment, in a three-way closure trap against a bounding fault, termed the S1 fault. In the first study, a geomechanical model of the Tensleep Fm. has been developed to evaluate the potential for $CO_2$ injection inducing slip on the S1 fault and thus threatening seal integrity. The geomechanical analysis demonstrated that $CO_2$ sequestration will not induce slip on the reservoir-bounding fault, nor is fracking the cap rock a concern. However, various sets of pre-existing minor faults in the reservoir are critically stressed (i.e., active) in the current stress field. Hence, raising pore pressure during sequestration will activate slip on these minor faults. The presence of these minor faults enhances formation permeability and injectivity of $CO_2$. However, the potential for slip on these features could potentially compromise the top seal capacity of the Tensleep if these minor faults extend up into the cap rock.

In the second study, a 3D reservoir model and fluid flow simulation of the Tensleep Fm., under these geomechanical constraints, was developed to model the migration of the injected $CO_2$ as well as to obtain limits on the rates and volumes of $CO_2$ that can be injected without compromising seal integrity. The results of the numerical simulations corroborate the analytical results of the geomechanical analysis that seal integrity will not be compromised by the pilot injection. The simulations also showed that the EOR pilot project could recover from 8% to 30% incremental oil, by sequestering 2175 tonnes (42 MMcf) in 6 weeks or 4350 tonnes (168 MMcf) in 12 weeks respectively. However mobility of $CO_2$ through the highly permeably fracture network could present a problem and a well control strategy needs to be implemented to co-optimize EOR and sequestration.

In the third study, we test an Amplitude Versus Angle and Azimuth (AVAZ) analysis to identify the presence of fractures using wide-azimuth 3D seismic data. The objective of the project was to obtain a 3D characterization of the fracture network on both the reservoir and the caprock that will allow for a more accurate assessment of the impact of these features in reservoir permeability and in the risk of $CO_2$ leakage. The AVAZ results were calibrated with fracture intensity and orientations obtained from FMI logs recorded in the area as well as stress orientation and the macro fault network of the anticline. During the analysis of these results, we did not find enough evidence to indicate whether the observed anisotropy is influenced by stress, structural or sedimentary features. Furthermore, it is possible that the method does not work with this data set, because particularities of this setting do not follow the assumptions of the method.

In the final project of this dissertation, we focus on deep saline formations, which have great potential for geologic sequestration of $CO_2$. Such formations are widespread, and in theory, easily accessed from point sources of $CO_2$, such as power plants, factories, etc. Unfortunately, many deep saline aquifers of the mid-continental U.S. appear to have very low porosity and permeability, which results in limited injectivity and storage capacities.

In this study, we investigate the use of induced microseismicity to enhance permeability and injectivity of a tight formation as well as to monitor a carbon sequestration project. During the injection-induced microseismicity stimulation, more than 10,000 metric tons of supercritical $CO_2$ were injected into the Bass Island Dolomite (BILD) during a period of 40 days. A total of 803 events were recorded in more of three sensors in each of the two monitoring arrays. However, no definite seismic activity could be related to the injection in the BILD. A preliminary possible hypothesis relates this microseismicity to a $CO_2$ injection from a deeper and preexisting EOR project in this area, which could be migrating upwards along the monitoring wells.

# ACKNOWLEDGMENTS

The list of people I would like to thank for their help and support during my PhD study is quite long. But especially, I would like to thank my advisor Mark Zoback who has been a wonderful mentor, that not only taught me about geomechanics but also serve as a great role model both as a scientist and as a person. He has an enthusiasm for geophysics and for life in general that is very motivating. He also makes sure to create a supportive, friendly, challenging, and collaborative work environment. He pays particular attention in encouraging work-life balance for his students. *Thank you Mark!*

I would also like to thank my committee members, Julio Friedmann, Jerry Harris, and Lynn Orr for their support, help, and patience. Their insight and suggestions have greatly improved my work and my knowledge over these past few years. Additionally I would like to thank the help and guidance of the members of my original Qualifying Exam committee Gary Mavko and Steve Graham. Steve also kindly chair my defense and has been and invaluable source of knowledge, support, and friendship during all my years at Stanford.

I would like to thank the people that, at different stages these past years, have helped me with my research. Paul Hagin, thanks for your support, insight and helpful discussions. Also many thanks to Tapan Mukerji, Tony Kovscek, Khalid Aziz, Kyle Spikes, Andres Mantilla, Fernando Garcia Parodi, Alejo Lopez, and Joe Morris.

I would like to acknowledge the Global Climate and Energy Project for their funding as well as to the Fulbright Scholarship, which sponsored me to get to Stanford in the first place.

I want to acknowledge my collaborators on the several projects I have worked. I greatly enjoyed working with them and also benefit enormously from their contributions. I especially would like to thank Julio Friedmann and Vicki Stamp. Julio has been an excellent guide to the world of carbon sequestration and his suggestions greatly improved this dissertation. Vicki has been a wonderful collaborator, always available for my endless questions, and always with the sweetest disposition. I also want to thank the valuable help of RMOTC staff which was always very helpful for my requests of data: Tom Anderson, Brian Black (sorry for the many requests!), and Mark Milliken. Similarly, I would like to thank Neeraj Gupta and Jackie Gerst of the Battelle Memorial Institute. And finally, I enjoyed working and learning from Marco Bohnhoff and David Gray from CGGVeritas.

I would like to thank all the past and present members of the Stress and Crustal Mechanics research group: Marco Bohnhoff, Naomi Boness, Lourdes Colmenares, Alvin Chan, Indrajit Das, Amy Day-Lewis, Paul Hagin, Robert Heller, Owen Hurd, Madhur Johri, Amie Lucier, Ellen Mallman, Pijush Paul, Hannah Ross, Norm Sleep, Hiroke Sone, George Thompson, John Vermylen, Charley Weiland, Sonata Wu. And many, many thanks to Susan Phillips Moskowitz for taking such a good care of all of us.

One of the greatest things about studying at Stanford is the richness of the people here. I greatly benefitted from studying, working, and sharing time with other students, but even more important, I found many great friends! And the same applies to the life outside Stanford, by playing soccer with friends, sharing many *asados*, and playing even more soccer… ok, I did other things besides playing soccer, but definitely I spent many of my most memorable moments in the fields (Roble, Sand Hill Road, …). It kept me sane in stressful moments and I even met my *Búlgaro* there!!! I would like to thank all the friends with whom we shared many

unforgettable moments: Fabrizio, Kyle, Ezequiel, Tricia, Nico, Jeff, María Leticia, Karla, Paula, Valeria, Mariel, Jordan, Kevin. Thank you all!

I would also like to thank two people that had have the most influence in my career since the beginning and help me get here: my undergraduate advisor from Universidad de Buenos Aires, Victor A. Ramos and Rene Manceda. Thank you!

I also wouldn't be here if it weren't for the love, support and encouragement from my family: my dad José Carlos, my mom Susana, my sister Marina, my brother Gustavo, and their kids: Mariano, Federico, Julieta, Clarita, and Luciana, who make me laugh and love.

Finally, I want to thank my husband Tzanko for his love, support, patience, the shared fun, and amazing life he makes me live!

# TABLE OF CONTENTS

# LIST OF TABLES

# LIST OF FIGURES

# CHAPTER 1

# INTRODUCTION

## 1.1 OVERVIEW AND MOTIVATION

There is increasing evidence that reinforces the view that climate and greenhouse gas cycles are intimately related. $CO_2$ is the main anthropogenic gas contributing to the greenhouse effect and global warming, and there is no evidence at any time in the past 650,000 years of levels of carbon dioxide as high as the current atmospheric concentrations (Brook, 2005). $CO_2$ levels are a third higher than in pre-industrial times, and are projected to increase at 0.4% per year.

The main anthropogenic source of $CO_2$ is the burning of fossil fuels which currently dominate commercially supplied energy worldwide. Since it is generally accepted that concentration in the atmosphere of greenhouse gases, in particular $CO_2$, must be restricted, several solutions have been proposed to try to stabilize carbon dioxide concentrations that include carbon capture and storage (CCS). Nevertheless, for CCS to be a viable carbon management solution, one of the main issues to be addressed is the risk of $CO_2$ leakage.

This thesis is composed of four interrelated investigations that focus on the geomechanical aspects of carbon storage with emphasis on the assessment of the leakage risks. Three of these studies analyze a $CO_2$-EOR and Sequestration project planned for the fractured Tensleep Formation at Teapot Dome Oil Field, WY. While the fourth one investigates the use of induced microseismicity as a tool to enhance permeability and monitor sequestration projects in a deep saline formation in the Michigan Basin.

The first study consist of the geomechanical characterization at Teapot Dome; its goal is to understand the effect that $CO_2$ injection will have in fault stability and seal integrity to ultimately predict the potential risk of $CO_2$ leakage through natural pathways. The second study develops of a stochastic reservoir model of the Tensleep Fm. and a fluid flow simulation to model the migration of the injected $CO_2$ as well as to obtain limits on the rates and volumes of $CO_2$ that can be injected without compromising seal integrity. The third project describes an Amplitude Versus Angle and Azimuth (AVAZ) analysis performed at Teapot Dome to identify the presence of fractures using wide-azimuth 3D seismic data. The objective of the this analysis is to expand the 1D scattered fracture characterization performed from four wells in the anticline to a 3D characterization of the fracture network on both the reservoir and the caprock that will allow for a more accurate assessment of the impact of these fractures in reservoir permeability and in the risk of $CO_2$ leakage.

From a technical perspective, depleted or mature oil and gas reservoirs hold great promise as sequestration sites because they have hold hydrocarbons for geological periods of time, implying the presence of effective trap and seal mechanisms. However, it has long been recognized (e.g., Raleigh et al. 1976) that fluid injection causes changes in the pore pressure and stress field that could potentially alter the initial seal of the reservoir by either hydraulically fracturing the cap rock or triggering slip on pre-existing faults by reducing the effective normal stress on the fault plane (see review by Grasso, 1992).

In light of this, a key step in the evaluation of any potential site being considered for geologic carbon sequestration is the ability to predict whether the increased pressures associated with $CO_2$ sequestration are likely to affect seal capacity. To that end, the last study consists in the analysis of an injection-induced microseismicity experiment in the Bass Island Dolomite (BILD) in the Michigan Basin. One of the biggest challenges for $CO_2$ sequestration in deep saline formations is the very low porosity and permeabilities often shown that translates into limited injectivity and storage capacities. Injection-induced microseismicity has been frequently used in the oil industry to enhance permeability. Microseismic stimulation is initiated by increasing the fluid pressure in the target formation, thus reducing the effective normal stress on optimally-oriented faults and fractures triggering slip and creating high-permeability paths within the reservoir. The induced failure is mainly triggered by a diffusive process of pore pressure perturbation and often occurs as a sequence of many small events. The volume of rock stimulated can be imaged by locating these microearthquakes induced by the injection (Albright and Pearson, 1982) therefore constituting an excellent monitoring technique.

## 1.2 THESIS OUTLINE

This thesis is composed of six chapters. Chapter 1 is the present Introduction. Chapters 2, 3, 4 and 5 are related with the Teapot Dome investigations and Chapter 6 describes the microseismicity experiment in the Michigan Basin.

In Chapter 2, **Teapot Dome Oil Field – National Geological Carbon Storage Test Center**, I present an overview of the Teapot Dome geology and history and the characteristics of the Carbon Storage Test Center. The planned $CO_2$-EOR and sequestration pilot is described as wells as the source for the injected $CO_2$.

In Chapter 3, **Seal Integrity and Feasibility of $CO_2$ Sequestration in the Teapot Dome EOR Pilot: Geomechanical Site Characterization**, I present the geomechanical characterization performed at Teapot Dome to establish the potential risk of leakage

due to $CO_2$ injection. The first part of the chapter focuses on the S1 fault area and the Tensleep Fm., characterizing fault stability and seal integrity to establish the feasibility of the $CO_2$-EOR and Sequestration pilot. This manuscript was published in the June 2008 issue of Environmental Geology (v.54, no. 8). The rest of the chapter completes the analysis with a fracture characterization on the Tenlseep and the caprock and the evaluation of the effect of these features on reservoir permeability along with their potential risk of reactivation and becoming pathways for $CO_2$ leakage. Finally, the S2 fault area at the depth of the 2$^{nd}$ Wall Creek member is evaluated as the target of a controlled $CO_2$ leakage experiment.

In Chapter 4, **3D Stochastic Reservoir Model and Reservoir Simulation of the Tensleep Fm.**, I combine the previous geomechanical analysis, geostatistical reservoir modeling and fluid flow simulations to model the migration of the injected $CO_2$ as well as to obtain limits on the rates and volumes of $CO_2$ that can be injected without compromising seal integrity. The $CO_2$-EOR pilot was modeled and the storage capacity of the Tensleep in this particular trap was assessed. Finally, a sensitivity analysis was conducted to estimate the response of the pilot performance to several parameters such as fracture permeability, porosity and spacing, relative permeability curves, matrix porosity and permeability, and grid size.

In Chapter 5, **Fracture Detection Using Amplitude Versus Angle and Azimuth at Teapot Dome Oil Field, WY**, I describe an analysis performed at Teapot Dome to identify the presence of fractures using wide-azimuth 3D seismic data. This project is the result of collaboration with David Gray from CCGVeritas, Canada. David Gray was in charge of the AVAZ processing, and I provided the geomechanical and fracture characterization obtained in Chapter 3, as well as the interpretation of the results. From the AVAZ analysis, anisotropy direction and magnitudes were obtained. I analyzed and calibrated them with stress, fractures, fault, and sedimentary data from wells and seismic interpretation to try to determine if the origin of the anisotropy could be related to the stress state, the structural framework or to a sedimentary control. The results from the AVAZ analysis are extremely variable, and at this point,

there is no conclusive evidence to discriminate which of these factors is primarily affecting the observed anisotropy. Furthermore, it is possible that the method does not work with this data set, because particularities of this setting do not follow the assumptions of the method.

In Chapter 6, **Using Microseismic Stimulation to Enhance Permeability in Tight Formations**, I present a preliminary geomechanical characterization and fluid flow simulation performed as a base for an Induced Microseismicity Experiment in the Bass Island Dolomite (BILD) in the Michigan Basin. The original objectives of this experiment were to enhance permeability and injectivity in a tight deep saline formation, a target for a $CO_2$ sequestration pilot. A further objective was to test microseismicity as a monitoring technique in the carbon sequestration context. During the experiment a total of ~10,000 metric tons of supercritical $CO_2$ were injected into the BILD over a period of 40 days. The passive seismic monitoring started 16 days prior to the start of injection and ended after 47 days of operation. The last part of the chapter describes the microseismicity data processing and analysis led by Dr. Marco Bohnhoff, currently a visiting professor at Stanford. I participated in this process helping to analyze waveforms, picking wave onsets and performing a frequency and filtering analysis. The results form this work will be published, where I will be the second author after Bohnhoff.

# CHAPTER 2

# TEAPOT DOME OIL FIELD – NATIONAL GEOLOGICAL CARBON STORAGE TEST CENTER

## 2.1 ABSTRACT

Mature oil and gas reservoirs are attractive targets for geological sequestration of $CO_2$ because of their potential storage capacities and the possible cost offsets from enhanced oil recovery (EOR).

The Teapot Dome Field Experimental Facility presents an exciting opportunity to conduct $CO_2$ sequestration experiments since it is fully owned by the US government, and this Federal ownership grants a stable platform for long-term

scientific investigations in a steady business context, absent the commercial drivers of a privately owned oil field. Furthermore, the extensive data set of Teapot Dome as well as any experimental result is public domain. This framework allows joint research of all kinds (Friedmann et al., 2004b).

A $CO_2$-EOR and Sequestration Pilot is projected to start at Teapot Dome, early in 2009, targeting the Pennsylvanian Tensleep Formation. The objective is to test the EOR and sequestration potential of the Tensleep in the area denominated Section 10.

In this chapter we will describe the proposed pojects related to $CO_2$ sequestration that we investigated throughout this dissertation. We will also present the geology and the characteristics of Tapot Dome, as well as the available data set.

## 2.2 INTRODUCTION

### 2.2.1 GREENHOUSE EFFECT, CLIMATE CHANGE, AND $CO_2$ EMISSIONS

Human activity in the last 200 years has caused considerable changes in the levels of several atmospheric greenhouse gases, including carbon dioxide ($CO_2$). These changes are particularly noticeable since the industrial revolution. Although direct measurements began in the latter half of the 20th century, atmospheric concentration of these gases from earlier times are known from coring samples of polar ice (Petit et al., 1999, Siegenthaler et al., 2005). This data highlights the fact that at no time in the past 650,000 years were carbon dioxide or methane ($CH_4$) levels significantly higher than values just before the Industrial Revolution (Brook, 2005). Similarly, it also points out the evident co-variation of $CO_2$ and $CH_4$ with climate cycles (Brook, 2005, Falkowski et al., 2000). This relationship reinforces the view that climate and greenhouse gas cycles are intimately related. Although the exact effect of how greenhouse gases will change the climate is still uncertain, a rise in the global average temperature, or global warning, is expected.

The primary greenhouse gas produced by human activity is $CO_2$ with a current atmospheric concentration of 383.9 ppm (Blasing, 2008), approximately a third more since pre-industrial times. It continues to increase at 0.4% per year (IEA Greenhouse Gas R&D Programme, 2005).

The main anthropogenic source of $CO_2$ comes from the burning of fossil fuels such as oil, coal and natural gas, around 23.5 - 31.3 Gt $CO_2$ (6 - 8 GtC) per year (Parson & Keith, 1998, & IEA Greenhouse Gas R&D Programme, 2001). In addition, changes in tropical land use, such as deforestation by forest burning, contribute about a quarter of the effect of fossil fuels. For these reasons, it is now generally accepted that concentration in the atmosphere of greenhouse gases, in particular $CO_2$, must be restricted. Several scenarios have been proposed in the so called "pathway to stabilization" to steady $CO_2$ concentrations from 450 to 750 ppm (Beecy and Kuuskraa, 2001).

Several techniques have been proposed in this pathway, such as to reduce consumption of energy services, increase energy efficiency, switch to lower carbon-content fuels, enhance $CO_2$ sinks (forests, soils and oceans), use energy sources with very low $CO_2$ emission (renewable energy or nuclear energy) and capture and storage of $CO_2$ (IEA Greenhouse Gas R&D Programme, 2001). The use of each of these techniques will depend on several factors, including emission-reduction target costs, available energy resources, environmental impact and social factors. However none of them is sufficient by itself (Beecy and Kuuskraa, 2001), and all of them will take time to be ready to implement.

Among those alternatives, underground $CO_2$ sequestration is an attractive option to pursue because it can be applied in the short-term, with available technology developed mainly in the oil and gas industry. This approach becomes even more attractive when we consider that currently around 85% of the world's commercial energy needs are supplied by fossil fuel. Therefore, a technique capable of reducing the $CO_2$ emissions, while still using fossil-fuel based energy, could be of crucial help

to avoid the significant disturbance that a rapid change of non-fossil energy sources could cause (IEA Greenhouse Gas R&D Programme, 2001).

Pacala and Socolow (2004) defined the concepts of stabilization triangle and stabilization wedges (Figure 2.1). The stabilization triangle represents the desired amount of $CO_2$ emission reduction in 50 years. It is the difference between the projection of the current carbon emission path and a flat path at the current carbon emission rate. This triangle is divided in wedges, where each wedge coresponds to a strategy to reduce carbon emissions that grow in 50 years from zero to 1.0 GtC/yr. A requisit for all strategies is that they have to be already commercialized.

Carbon capture and storage (CCS) has been proposed as one of these strategies. There are currently three sequestration projects worldwide, each of which inject ~1 million tons of $CO_2$ per year. In order for this technology to became a solution to the $CO_2$ problem, at least 3500 such projects must be in place by 2055 (Carbon Mitigation Initiative, 2008).

To have an idea of the urgency of the problem, when this concept was developed in 2004, seven wedges were defined. Currently, already eight wedges form the stabilization triangle.

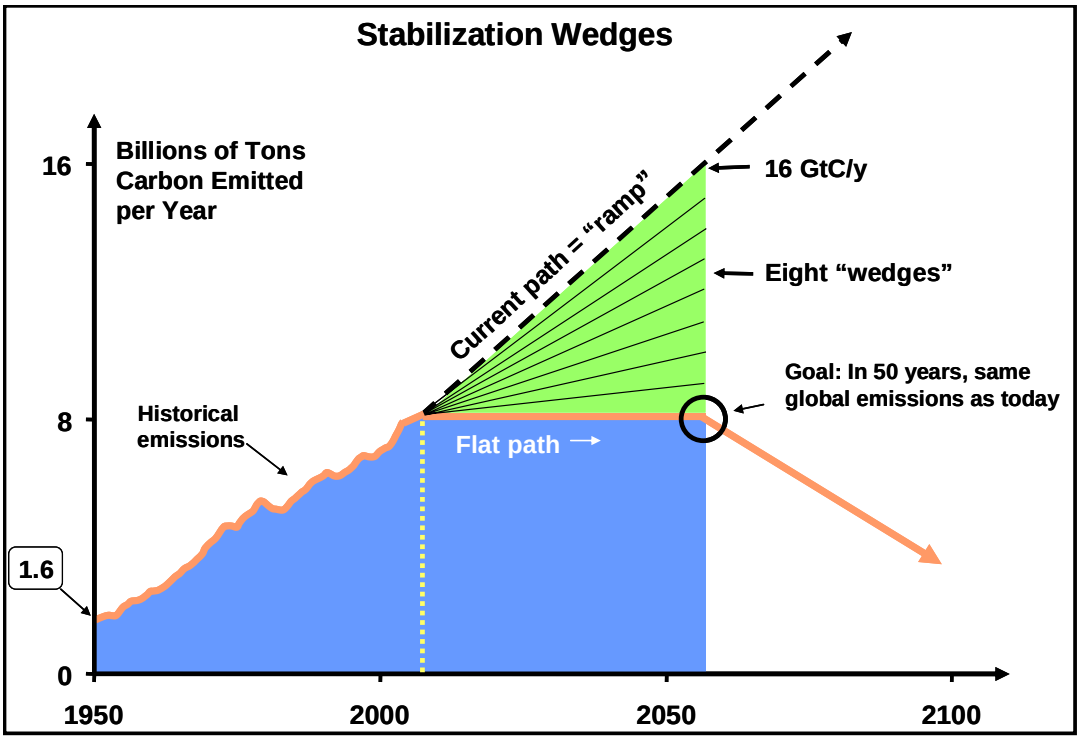


**Figure 2.1**: Stabilization wedges (Carbon Mitigation Initiative, 2008). See text for explanation.

### 2.2.2 Previous $CO_2$ Sequestration around the world

Due to increasing focus on the necessity to slow the $CO_2$ atmospheric concentrations, a number of government funded research programs have been established in Canada, Norway and Japan in addition to major industrial projects in Australia and Algeria. Some of these projects include assesing $CO_2$ sequestration in mature Oil and Gas fields, such as the following: the Weyburn project in Canada, which was initiated in 2000 and has already injected 1.90 billion $m^3$ of $CO_2$ in a carbonate reservoir (White et al, 2004); the Sleipner project in the North Sea, where the $CO_2$ extracted from gas production is injected in an aquifer above the production unit; and the In Salah Gas project in Algeria, where 1 million metric tons of $CO_2$ per year is separated from natural gas and re-injected into carboniferous sandstone reservoirs (R&D Project Database). In addition, several $CO_2$ sequestration pilots and

demos are currently in place (30 Mt $CO_2$ per year) as well as $CO_2$ enhanced oil recovery (EOR) applications.

The majority of the EOR projects are located in Texas, USA, where this technology started in the early 1970s. Presently, most of the $CO_2$ used in such applications comes from natural reservoirs in the western US, but a portion of it comes from anthropogenic sources such as natural gas processing plants (Gale, 2004 & IPCC, 2005).

### 2.2.3 $CO_2$ SEQUESTRATION UNDERGROUND – STORAGE OPTIONS

Several factors suggest that geologic storage of $CO_2$ underground is a viable alternative that can be implemented with techniques similar to those used in the oil and gas industry. Natural analogues, such as oil and gas, as well as $CO_2$, fields demonstrate that fluids have been stored and preserved underground for millions of years. Successful industrial analogues include natural gas storage projects, liquid waste disposal projects and $CO_2$ sequestration or $CO_2$-EOR projects such as Sleipner and Weyburn, where positive outcomes are anticipated through monitoring projects.

According to the IPCC report (September 2005) geological storage of $CO_2$ can make a substantial impact on carbon dioxide emission reduction. The main proposed options to store $CO_2$ underground are saline reservoirs, unminable coal beds, and mature oil and gas reservoirs.

My research focuses mainly on mature oil and gas fields (O&G), where the upper estimate of storage capacity could account for approximate 45% of global emissions for the year 2050 (IEA Greenhouse Gas R&D Programme, 2001). Parson & Keith (1998) estimated the global capacity of depleted Oil and Gas fields in between ~740 – 1850 Gt $CO_2$ (~200 to 500 GtC). However, this estimate should be considered theoretical, because geographical relationships between large emission sources and storage reservoirs have to be evaluated (Gale, 2004). Geological $CO_2$ sequestration is considered a short-term solution, and in order to have a real impact, the

sequestration rates have to be approximately one third of projected global oil production rates, which is highly ambitious. However, if these rates can be met while the impact of potential leakags is minimized, then the practice of sequestration can be publicly acceptable.

### 2.2.4 $CO_2$ SEQUESTRATION IN MATURE OIL & GAS FIELDS

In addition to their potential capacities, mature O&G reservoirs are an attractive target for sequestration because of potential cost offsets from enhanced oil recovery (EOR) using $CO_2$, which is current practice in the oil industry. However, mainly due to economic and regulatory characteristics, these applications are typically designed to obtain maximum oil production with minimum $CO_2$ injection (GEO-SEQ Best Practice Manual 2004). For the opposite scenario to exist, in which a maximum quantity of $CO_2$ were to remain in the reservoir while still increasing production, some type of financial incentive (tax credits or emission trading) must be present for the operator. Until then, this ideal scenario is considerably different from conventional EOR projects.

O&G reservoirs also present some advantages compared to saline aquifers and unminable coal beds due to the exploration and development activities that they have undergone. These fields have the entire production infrastructure in place, fewer regulatory barriers could be encountered, and they present an extensive knowledge base accumulated since the early exploratory stages of the field. Large volumes of fluids were stored for geologic periods of time, which implies that adequate seal capacities, porosity and permeabilities existed at one time.

### 2.2.5 RISK OF LEAKAGE DURING $CO_2$ SEQUESTRATION

One of the main problems of $CO_2$ sequestration underground is the risk of global and local $CO_2$ leakage. The term global leakage refers to the scenario where $CO_2$

make its way out to the atmosphere canceling the sequestration effect, and local leakage refers to the impact that the $CO_2$ will cause to people and ecosystems in the surroundings of the injection sites, i.e. contamination of drinking water and ground concentrations of $CO_2$ (> 10% concentration is toxic) (Socolow, 2005). Therefore, a full understanding of leakage and the ability to predict it is one of the key steps towards the implementation of this technique through the design of effective risk management strategies.

It has been established that the most dangerous leakage path in a depleted oil and gas field is the numerous abandoned wells, however, the study of this process is beyond the scope in this research. Here I focus on another important leakage condouits which are the so called natural pathways, i.e. faults and fractures. I evaluate the effect of $CO_2$ injection on fault stability and seal integrity with the objective of making predictions of the potential leakage risk through such pathways.

## 2.3 TEAPOT DOME

Teapot Dome is an elongated asymmetric, basement-cored anticline with a north-northeast axis located in the southwestern edge of the Powder River Basin (Figure 2.2). It is part of the Salt Creek structural trend, with Salt Creek anticline to the north and Sage Spring Creek and Cole Creek oil fields to the south (Beinkafner, 1986, Cooper & Goodwin, 1988 and Cooper et al, 2001).

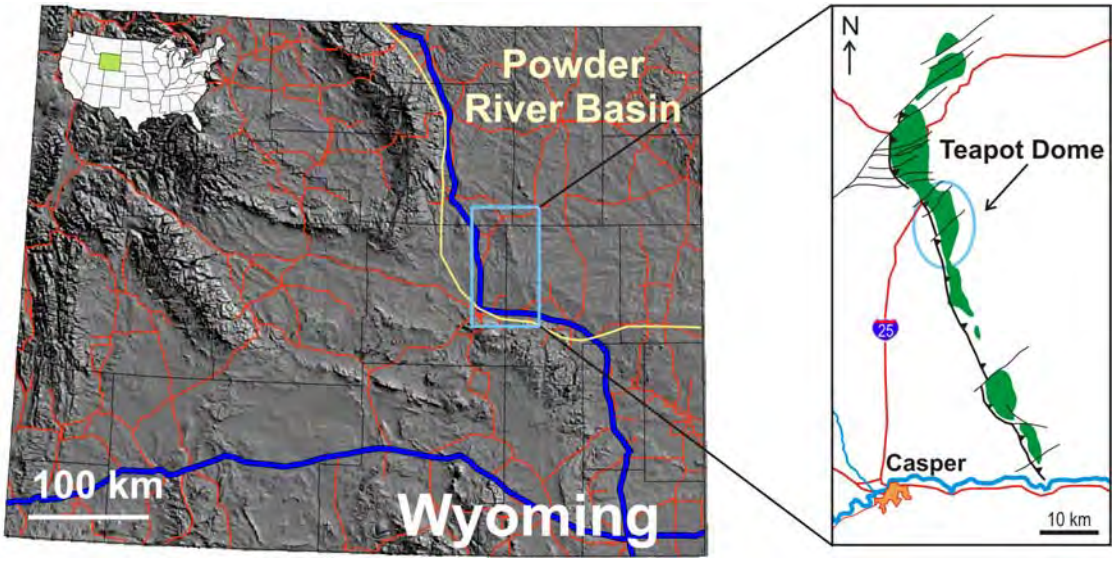


**Figure 2.2**: Location of Teapot Dome. Satellite image of Wyoming (left), Salt Creek structural trend, topographic relief in green (right) (courtesy of RMOTC).

### 2.3.1 History of Teapot Dome

The name of Teapot Dome is well know due to the big corruption scandal of the early 1920s, involving the secret leasing of federal oil reserves during Harding's administration.

After president Warren G. Harding transferred supervision of the naval oil reserve lands from the navy to the Department of the Interior in 1921, Albert B. Fall (secretary of the interior) secretly granted to Harry F. Sinclair of the Mammoth Oil Company exclusive rights to the Teapot Dome reserves. In return for the leases, Fall received large cash gifts and no-interest "loans". The affair became known and Congress directed President Harding to cancel the leases. The Supreme Court declared the leases fraudulent and ruled illegal Harding's transfer of authority to Fall. The investigation led to criminal prosecutions and Fall was indicted for conspiracy and for accepting bribes. The oil fields were restored to the U.S. government through a Supreme Court decision in 1927 (Encyclopedia Britannica, 2008). The field was shut down for production for more than 50 years.

Teapot Dome was reopened in 1976 and in 1977 became a US Department of Energy (US DOE) facility. DOE directed RMOTC to collaborate with the petroleum industry to improve domestic oil and gas production through the field testing of new technology, and in October 2003, established Teapot Dome as a national geological carbon storage test center (Friedmann et al., 2004a).

Regarding the production history, Teapot Dome started its production in 1908 from the "Dutch" well (200 BOPD) at the First Wall Creek sandstone In 1909 a few more wells were drilled to develop the Shannon sandstone. Before the reopening of the field and the development and exploration program at Teapot Dome in 1976, a total of 233 wells had been drilled in all the producing formations. In 1996, additional 1007 development wells and 90 exploratory wells were drilled. 27 of the development wells were drilled targeting the Tensleep Fm., and two of them experienced the highest initial production rates of any wells in Wyoming at that time (Gaviria, 2005).

### 2.3.2 REGIONAL GEOLOGY

Wyoming includes a large part of the Central Rocky Mountains and a smaller part of the Southern Rocky Mountains, most of Wyoming basin province and a part of the northern Great Plains. This situation positions Wyoming in a Phanerozoic tectonic transition zone, extending from the flat rocks of the continental interior to the folded and trusted strata of the Rocky Mountains (Snoke, 1993).

During early and middle Paleozoic times, central Wyoming was on the northwestern flank of the Transcontinental Arch, a major basement high southwest-northeast trending, that influenced the depositional history of the Rocky Mountain shelf. A considerable gap in the geologic record exists after mid-Proterozoic until this time. Therefore, early to mid Paleozoic shelf-facies strata lay directly on top of Precambrian basement. These deposits reflect a progressive west-to-east marine transgression and are usually separated by disconformities due to relative changes in

the sea level. Late Paleozoic and early Mesozoic deposits also includes several paleoenvironments such as paralic, eolian, and fluvial settings (Snoke, 1993, Hennings et al, 2008).

In particular, a transgression period resulted in the deposition of the Amsden Formation, which underlies the Tensleep and Phosphoria/Goose Egg Formations (Hennings et al., 2008), the focus of the present work.

By mid-Cretaceous until early Eocene occurred the thin-skinned, fold-and-thrust belt of the Sevier orogeny, one of the three overlapping events that have deformed the west central US Cretaceous times. At the end of the Maastrichtian and during Paleocene times, the Laramide orogeny produced a NE-trending compression (Dickinson and Snyder, 1978, Bird, 1989) east of the thin-skinned thrusting of the Sevier orogeny.

The Laramide orogeny formed basement-cored uplifts separated by deep, actively subsiding basins (Dickinson et al., 1988, Bird, 1989, Stone, 1993 and Hennings et al., 2008). Teapot Dome is a typical example of a Laramide anticline, that given its NW-SE orientation it probably formed perpendicular to the Laramide direction of compression (NE-SW).

### 2.3.3 TEAPOT DOME ANTICLINE

Teapot Dome is a double–plunging asymmetrical anticline where the west flank beds dip steeper (20 – 50°) than the east flank ones (<20°). It is bound on the west by a main thrust fault, consisting probably of a series of high angle reverse faults (Figure 2.3) of approximate 35° to 40° east-northeast, offsetting the Precambrian igneous and metamorphic basement mapped in outcrop in adjacent ranges (McCutcheon, 2003, Friedmann and Stamp, 2006).

The anticline is compartmentalized in several blocks by major oblique strike-slip to normal faults (Figure 2.4 and 2.5) that have been assigned arbitrary names S1, S2, S3, and S4 (McCutcheon, 2003). These faults are well defined in both the seismic data

and in the outcrops. They offset the basement and are oriented along a NE-SW trend, parallel to both the vergence direction of the main fold and basement foliation in neighboring outcrops. Their orientation and complexity varies locally, but generally have steep dips (Figure 2.4). At the surface, these faults have apparent lateral offsets, and sub-horizontal or oblique-slip striations have been observed, thus they have usually been interpreted as tear or accommodation faults (Cooper et al., 2003, Friedmann et al., 2004 and Friedmann and Stamp, 2006). Friedmann and Stamp (2006) noted that their timing appears to be coeval with Laramide shortening but thickness changes across the faults in Paleozoic and Mesozoic strata suggest that there were some earlier fault slip and growth strata events.

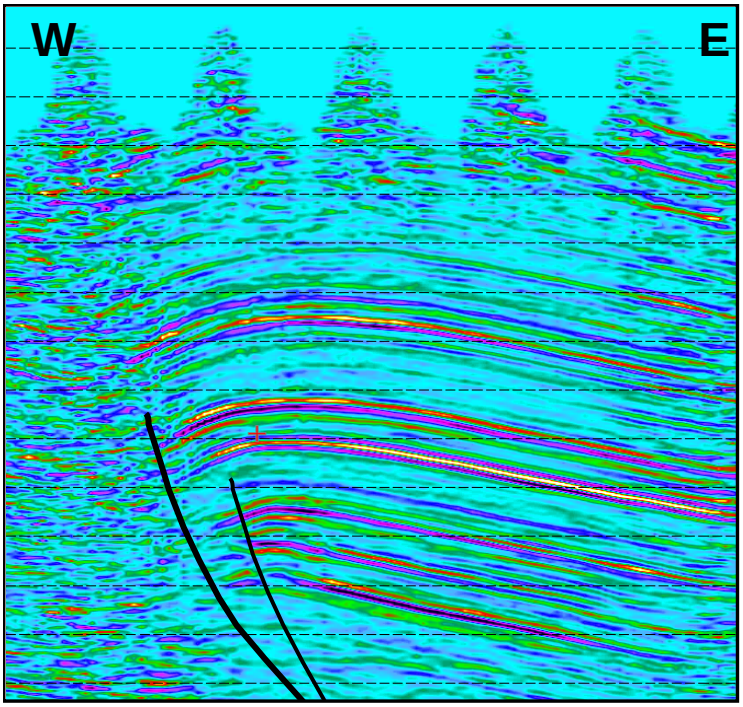


**Figure 2.3**: E-W cross section, with major reverse faults. Modified from McCutcheon, 2003 (location in Figure 2.4).

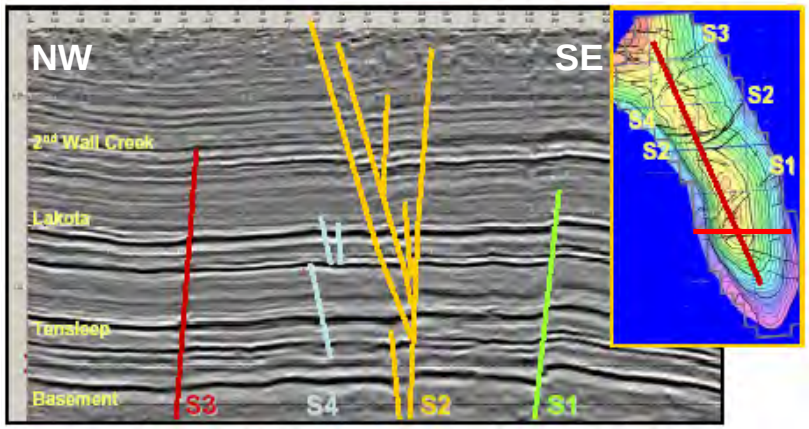


**Figure 2.4**: NW-SE cross section through Teapot Dome (left). Depth-structure map on the 2nd Wall Creek Sandstone with locations of seismic lines (right), modified from Friedmann et al., 2004b.

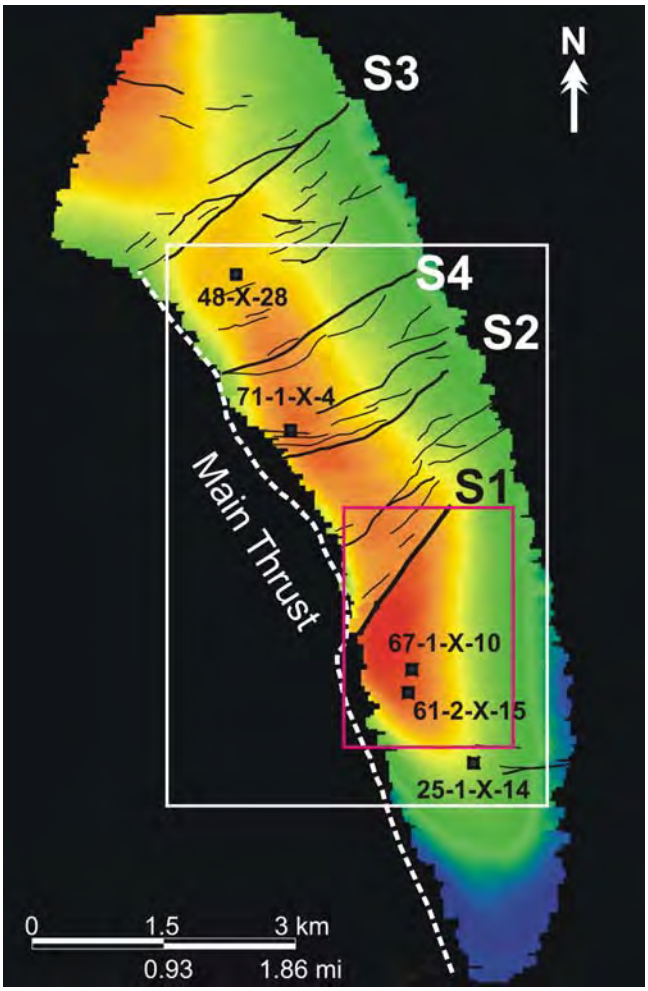


**Figure 2.5**: Time structure map of the Tensleep Fm. showing the oblique strike-slip to normal fault sets and location of Figure 2.6 (magenta box) and Figure 2.7 (white box).

### 2.3.4 SEQUESTRATION AND LEAKAGE PROJECTS

In the present work, we focus on two projects proposed at Teapot Dome to study carbon sequestration issues. In the first case, the objective is to evaluate the feasibility of a $CO_2$-EOR and Sequestration project in the S1 fault area. Whereas in the second one the focus is to find an optimal location for a potential control of $CO_2$ leakage experiment, initially proposed at the S2 fault zone. These projects are described in Section 2.4.

#### *2.3.4.1 S1 FAULT AREA - SECTION 10*

The target for the proposed $CO_2$-EOR and Sequestration Pilot is the Tensleep Fm. trapped against the S1 fault (green line in Figure 2.4 and Figure 2.5). In this area, the Tensleep Fm. presents a 3-way closure trap against the reservoir-bounding fault to the north and it has its structural crest at ~1670 m (5500 ft). To the south, the closure dips away from the structural crest, covering an area of ~1.2 $km^2$ (Figure 2.6) (Friedmann and Stamp, 2006).

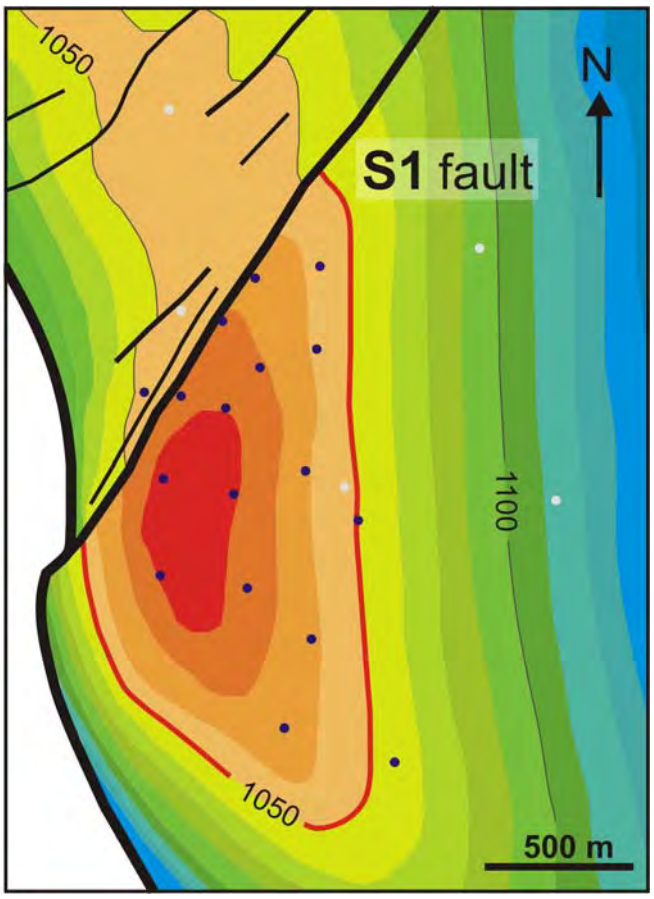


**Figure 2.6**: Time structure map of the Tensleep Fm. trapped against the S1 Fault. The blue and white dots are the wells in the area and the red line represents the oil-water contact (modified from McCutcheon, 2003). See location in Figure 2.5.

#### *2.3.4.2 S2 FAULT AREA*

The S2 fault area (orange lines in Figure 2.4) is structurally more complex than S1 area in Section 10. At the depth of the Tensleep Fm. there is not a distinct main fault, but rather a set of faults with a different azimuths ranging from approximately 36° Az (similar to the S1 fault) to 95° A; but the general trend is closer to the E-W direction.

Figure 2.7 shows a time structure map of the 2nd Wall Creek member of the Frontier Fm., and the S2 fault area. As it can be seen in the figure, the S2 fault network presents a great complexity in geometry and azimuths, which was the first reason to pre-select this area as a candidate for the mentioned controlled leakage

experiment. Secondly, S2 fault zone outcrops support alkali springs and contains hydrocarbon samples within fault veins and gouge, suggesting at some point the occurrence of leakage through this network (Friedmann, et al, 2004).

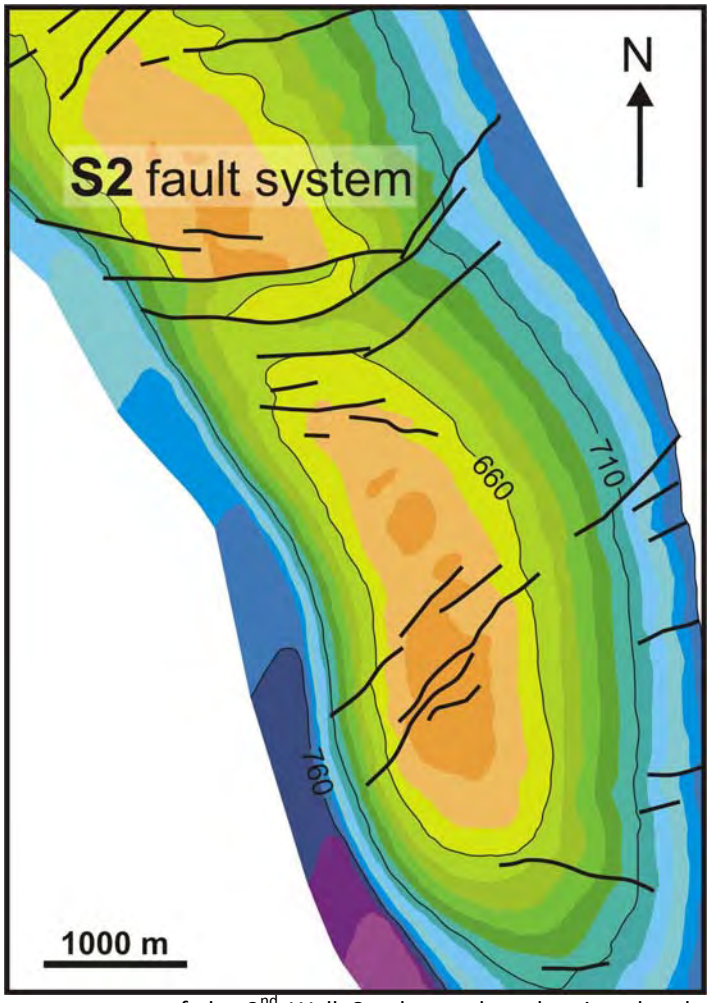


**Figure 2.7**: Time structure map of the 2nd Wall Creek member showing the the S2 fault network (modified from McCutcheon, 2003). See location in Figure 2.5.

### 2.3.5 STRATIGRAPHY

The stratigraphy of Teapot Dome consists of Devonian to Upper Cretaceous strata of diverse origin from coastal sandstone dunes, marine and lacustrian carbonates and shallow-shelf siliciclastics, overlying a granitic basement (Figure 2.8). Nine units are oil-bearing and six water-bearing. The relative fluctuations of base level, mentioned

above, resulted in the intercalation of porous and permeable units with impermeable rocks that serve as seals (Table 2.1), where many of these are excellent targets for $CO_2$-enhanced oil recovery (Nummedal et al., 2003, Friedmann and Stamp, 2006).

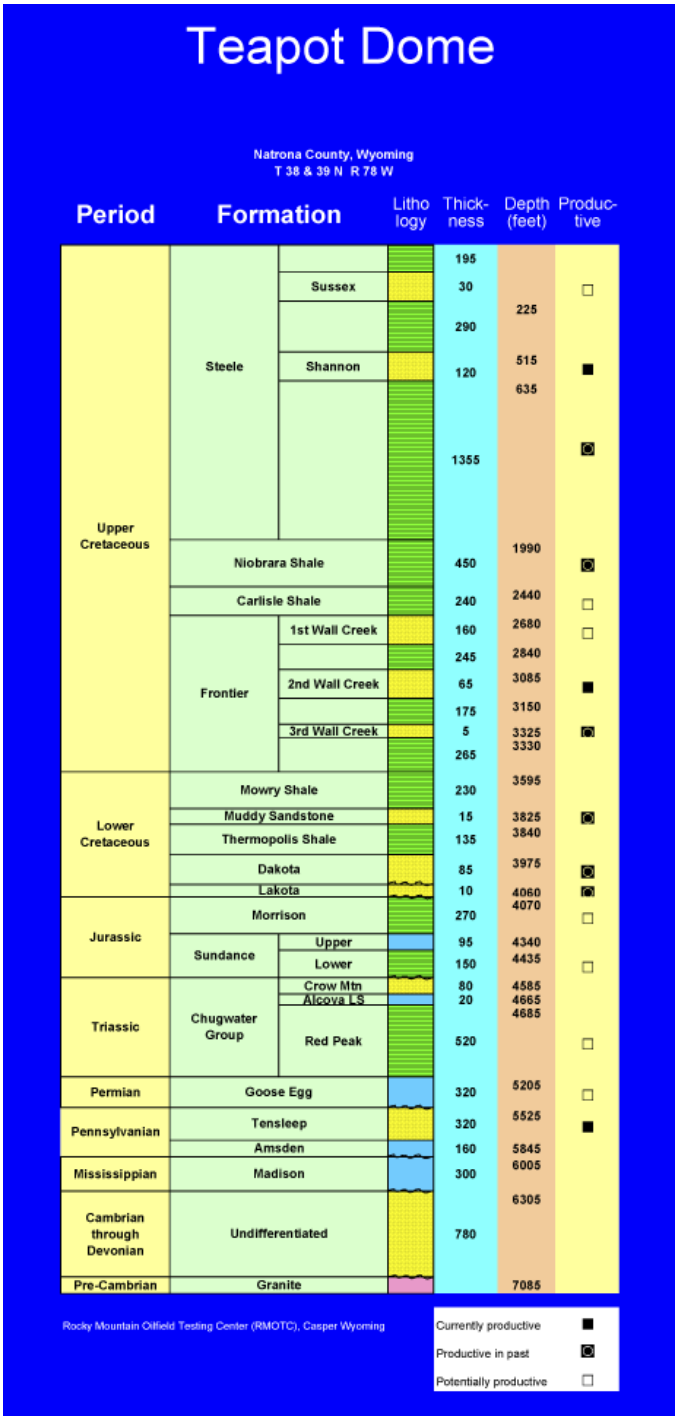


**Figure 2.8**: Stratigraphic column of Teapot Dome (Courtsy of RMOTC).

| Unit | Age | Lithology; Depositional Environment | Depth/Thickness (in ft [m]) | Seal | Pore fluid |
|---|---|---|---|---|---|
| Shannon Sandstone | Upper Cretaceous | Sandstone; fluvial-tidal | 515 (157)/120 (37) | Carlisle shale | Oil |
| First Wall Creek Sandstone | Upper Cretaceous | Sandstone; deltaic | 2650 (808)/160 (49) | Frontier shale | Brine |
| Second Wall Creek | Upper Cretaceous | Sandstone; fluvial-deltaic | 3086 (941)/65 (20) | Frontier shale | Oil |
| Third Wall Creek | Upper Cretaceous | Sandstone; deltaic | 3325 (1013)/5 (1.5) | Frontier shale | Oil |
| Muddy Sandstone | Lower Cretaceous | Sandstone; shoreface | 3840 (1170)/15 (4.6) | Mowry Shale | Oil |
| Dakota Sandstone | Lower Cretaceous | Sandstone; fluvial | 3975 (1212)/85 (26) | Thermopolis Shale | Oil |
| Lakota Sandstone | Lower Cretaceous | Conglomeratic sandstone; fluvial | 4060 (1237)/10 (3) | Thermopolis Shale | Oil |
| Sundance Sandstone | Jurassic | Sandstone; shoreface | 4340 (1323)/95 (29) | Morrison Formation shales | Brine |
| Crow Mountain | Triassic | Sandstone; fluvial | 4585 (1378)/80 (24) | Lower Sundance shales | Brine |
| Tensleep Sandstone | Pennsylvanian | Sandstone and dolostone; eolianite and sabkha | 5205 (1586)/320 (98) | Goose Egg shales and evaporites | Oil |
| Amsden Formation | Pennsylvanian | Limestone; carbonate platform | 5845 (1782)/160 (49) | Dolomicrites | Brine |
| Madison Formation | Mississippian | Limestone; carbonate platform | 6005 (1830)/300 (91) | Dolomicrites and evaporites | Brine |
| Flathead Sandstone | Devonian | Sandstone; braided fluvial | 6865 (2092)/200 (61) | Devonian shales | Brine |

**Table 2.1**: Main oil-bearing and water-bearing reservoir targets (Friedmann & Stamp, 2006).

The three traditional main reservoirs regarding cumulative production are the Shannon Sandstone, member of the Steele Shale Fm., the Fractured Steele Shale and the Second Wall Creek member of the Frontier Fm. All of them are of Upper Cretaceous age. The Lower Cretaceous Dakota and Lakota Fms. and the Jurassic Morrison Fm. are considered prospects for new discoveries. Whereas the Pennsylvanian Tensleep Fm. is the deepest producing interval, and although it has a relatively small cumulative production, Tensleep wells have had the highest IPs (i.e. 820 BOPD) since its exploitation began in mid-70s (Milliken & Koespel, 2002).

#### *2.3.5.1 TENSLEEP FORMATION*

The Tensleep Fm. covers large areas of Wyoming, Montana, and Colorado (Figure 2.9) and it holds two thirds of Wyoming's oil (Nummedal et al., 2003). It is an excellent target for $CO_2$ sequestration because, where oil has not been trapped, there is a thick, continuous, porous, and permeable sandstone aquifer. For example, it is the primary oil-bearing unit at fields such as Rangely, Colorado (the Weber Sandstone is its equivalent), Lost Soldier and Wertz in Wyoming. These fields have received continuous $CO_2$ injections for approximately 20 years (Friedmann and Stamp, 2006).

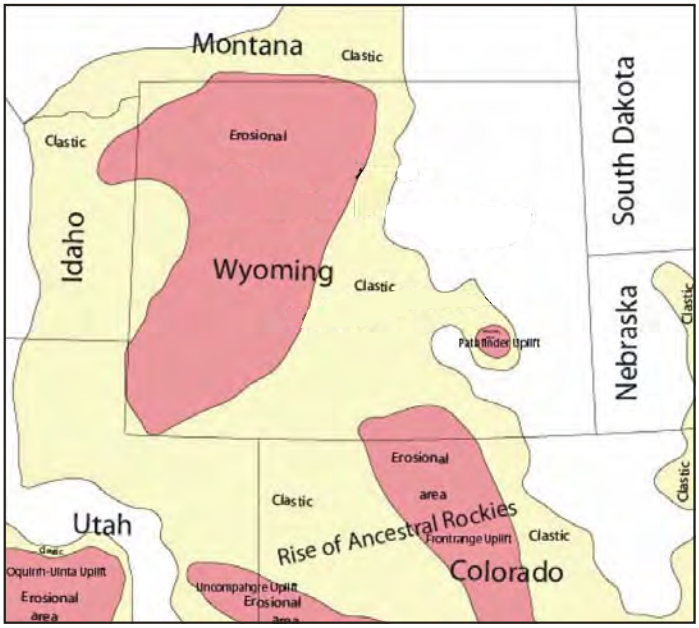


**Figure 2.9**: Paleogeographic map of Early Permian Tensleep extent; dark area represents area of thickest deposition (modified from Miller et al., 1992, Friedmann & Stamp, 2006).

The Tensleep Fm. at Teapot Dome consists of an intercalation of eolian-dune sandstones and inter-dune deposits where the average porosity is 8% and the average permeability is 80 mD. The Tensleep Fm. is divided in several intervals where the B Sandstone is the main producing horizon and the proposed storage interval for the $CO_2$-EOR and sequestration project. Figure 2.10 shows the upper part of the Tensleep Fm. that will be the focus in the present research.

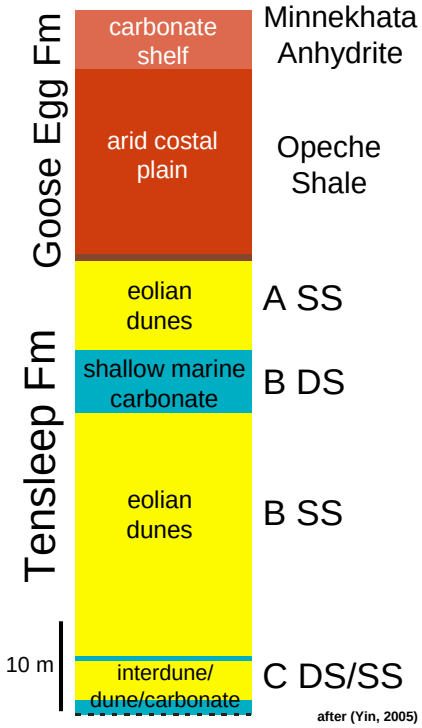


**Figure 2.10**: Schematic stratigraphic column of reservoir (Tensleep Fm.) and caprock (Goose Egg Fm.). SS = sandstone, DS = dolostone.

The dune sandstones are permeable and porous intervals with different levels of cementation, which affects their porosity, permeability and fracture intensity. The inter-dune deposits consist of thin sabkha carbonates, minor evaporates (mostly anhydrite), and thin but widespread extensive beds of very low-permeability dolomicrites (Zhang et al., 2005).

The alternation of dune and interdune deposits represents periods of relative sea level rise, transgressions, followed by exposure and occasionally erosion, which is evidenced by an unconformity on the top of the Tenlseep Fm. Figure 2.11 shows a detailed description of a core in well 54-TPX-10 with the environmental interpretation, and sequence-stratigraphic architecture for the mentioned intervals (Friedmann and Stamp, 2006).

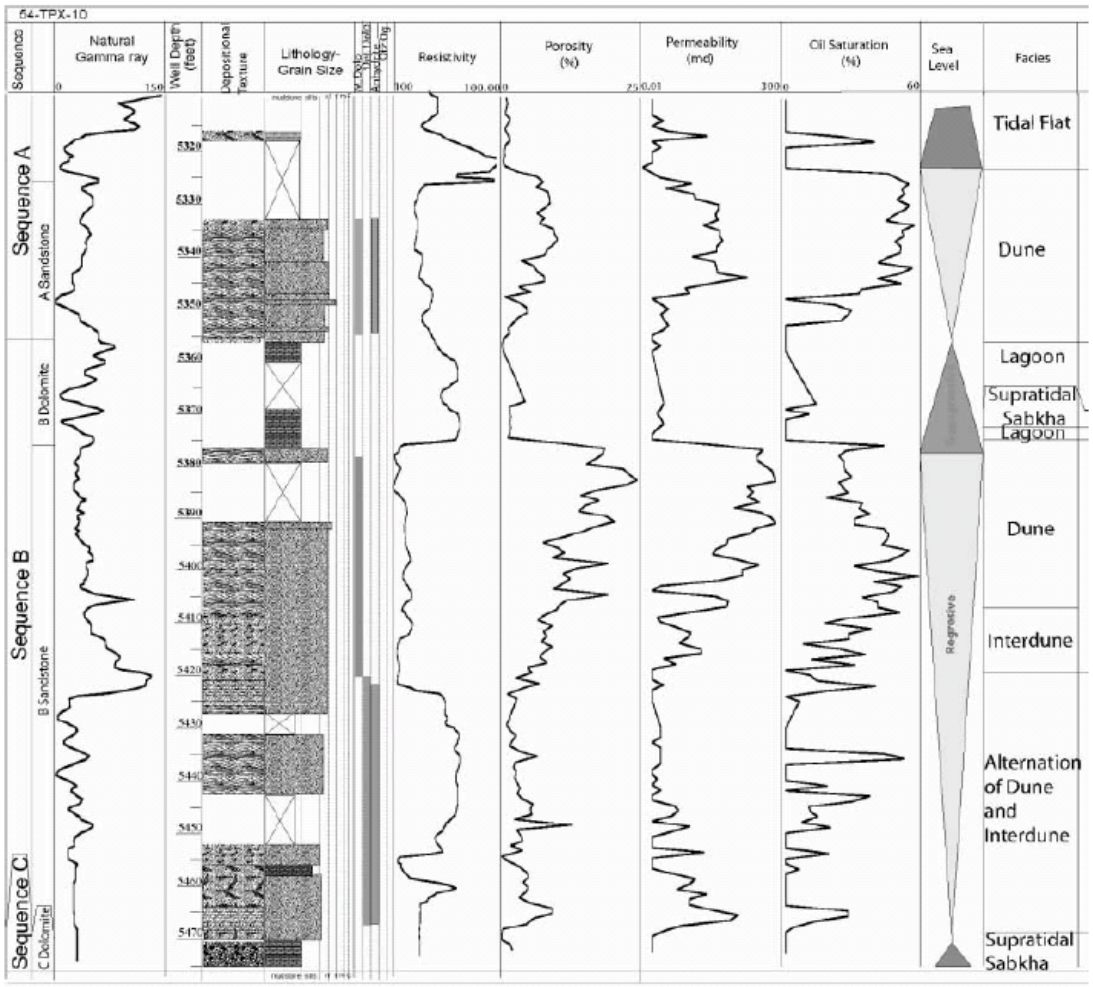


**Figure 2.11**: Core description, environmental interpretation, and sequence-stratigraphic architecture of Tensleep well 54-TPX-10 from within Section 10. Note the variable permeability in the A and B sandstones as a function of cementation and subenvironment (Yin, 2005; Friedmann and Stamp, 2006).

Another factor influencing porosity and permeability variations is the dune architecture. Emmet et al. (1972) established the importance of studying the dune orientation in the Tensleep deposits, because its maximum permeability is oriented parallel to cross bedding. Milliken and Koespell (2002) performed a Tensleep eolian facies analysis on well 67-1-X-10, and although they found that the reservoir character did not only depend on dune cross bedding orientation but also on several other factors (diagenesis, presence of impermeable interdune rocks overlying

permeable dune sands, and fracturing) it will still be important, during a reservoir characterization stage, to consider porosity and permeability anisotropy due to dune orientation.

#### *2.3.5.2 SEAL*

The Permian Phosphoria Fm., locally denominated the Goose Egg Shale, is the regional seal of the Tensleep Fm. throughout Wyoming. At Teapot Dome, consists of more than 90 m (~300 ft) of shale, carbonate, and anhydrite (Minnekahta Member) that has trapped more than 35 million bbl (5.6 million $m^3$) of oil and dissolved natural gas, demonstrating its effectiveness. In particular, in the S1 fault area, the depth of these intervals ranges from ~1600 to ~1750 m below the surface.

A detailed characterization of a 48-X-28 well core, the only Teapot Dome well where the cap-rock has been cored, showed the structure of this interval as consisting of a very tight cemented paleosoil interval overlying a weathering surface on top of the Tensleep Fm (due to the mentioned unconformity) followed by the Opeche Shale member, and the anhydrite on top of it (M. Milliken, personal communication 2006).

### 2.3.6 FRACTURES

The key producing reservoirs at Teapot Dome, and much of the Rocky Mountains, are fractured. In particular, at Teapot Dome, several of the producing zones are in fractured shales, including the Niobrara and Steele shales (Figure 2.8).

Several authors (Lorenz and Cooper, 2004; Schwartz et al., 2005; Lorenz, 2007) have described fractures in the Tensleep Fm., from cores, FMI logs and outcrops. All of them coincide in that most of the fractures are vertical to near vertical. In particular, at Teapot Dome, Lorenz and Cooper (2004) performed a fracture characterization in core samples where they found an average of 1 fracture every 5 ft,

although with increasing cement content, they noted an increase in fracturing. In high porosity sandstones, they described fracture intensity of approximately 1 fracture every 10 ft.; in dolomitic sandstones, 1 fracture every 3 ft.; and in heavily cemented sandstones 1 fracture per ft.

Schwartz et al. (2005) analyzed FMI logs of five wells located approximately parallel to the axis of the anticline and found two main sets of open fractures, where the dominant set has a mean Az = 100° and the secondary one a mean Az = 68°.

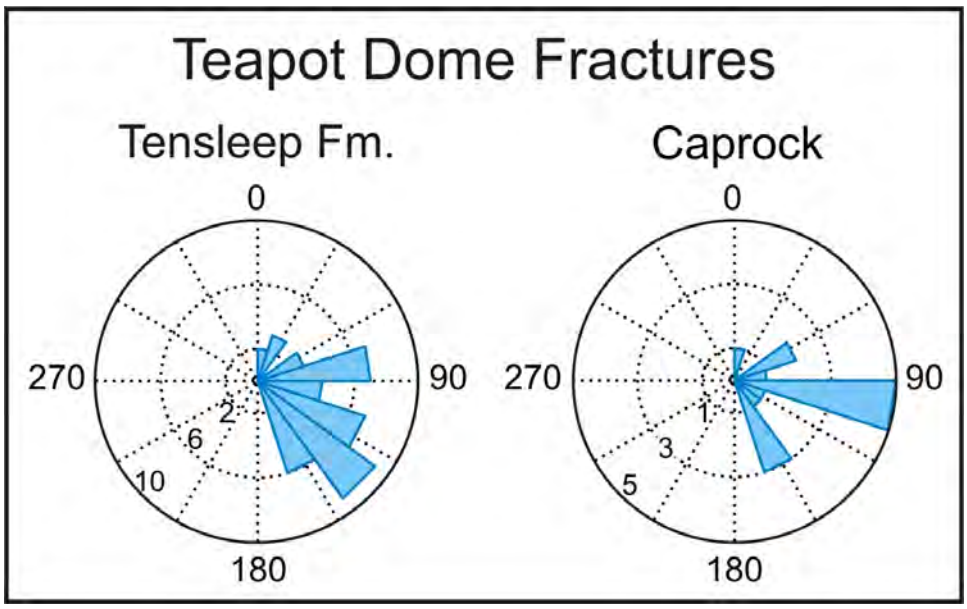


**Figure 2.12**: Fractures in the Tensleep Fm. from wells 25-1-X-14, 61-2-X-15, 67-1-X-10 and 48-X-28 (left); fractrures in the caprock from wells 25-1-X-14, 67-1-X-10 and 48-X-28 (right). See Figure 2.5 for well location.

Figure 2.12 shows the fractures we mapped in the Tensleep Fm. and in the caprock from 4 FMI logs in the area. The role of these fractures will be discussed in the further chapters.

## 2.4 TEAPOT DOME CARBON STORAGE TEST CENTER

Teapot Dome Field Experimental Facility presents an exciting opportunity to conduct $CO_2$ sequestration experiments for several reasons. As mentioned before,

the site is fully owned by the US government and it is operated by the Rocky Mountain Oilfield Testing Center (RMOTC). This Federal ownership provides several significant advantages. It provides a stable platform for long-term scientific investigations in a steady business context without the commercial drivers of a privately owned oil field. In addition, the field has a high density of wells, and the extensive data set from Teapot Dome and all experimental results are in the public domain (Friedmann et al., 2004b).

Field infrastructure includes roads, pipelines, water lines, water-treatment facilities, a gas-processing plant, workover rig, etc. Currently, RMOTC owns and operates 1 drilling rig and 600 pump jacks of varying sizes. Drilling costs for certain work are covered by RMOTC, and an internal committee of scientists and engineers approves drilling programs in coordination with all other efforts (e.g., the current site characterization and $CO_2$ program).

### 2.4.1 DATA SET

The field covers nearly 10,000 ac (40.5 $km^2$) and contains more than 2200 wells total, of which more than 1200 may be accessed (Table 2.2). Of these, about 600 are currently producing, and more than 400 penetrate to a depth greater than 2700 ft (823 m). All cores, well logs, mud logs, completion descriptions, and production data from these wells are in the public domain (RMOTC, 2005a, b, c).

| Data Type | Format | Accessibility |
|---|---|---|
| 3-D seismic volume | Digital | Direct |
| 3-D seismic interpretations, including horizons and faults | Digital | Indirect through vendor |
| Wire-line logs: 423 deep wells (>2700 ft) | Digital | Direct |
| Wire-line logs: 800 shallow wells | Paper and raster format | Direct and indirect (Wyoming Oil and Gas Conservation Commission) |
| Cores | Boxed samples | Direct and indirect |
| Core descriptions | Reports, paper, and raster | Direct and indirect |
| Formation tops and picks | Digital and paper | Direct and indirect |
| Well completion reports | Paper | Direct |
| Well and formation production data | Paper and raster | Direct |
| Reports on field experiments and studies | Raster | Direct |
| Production tests | Raster | Direct |
| Geochemical analyses, including hydrocarbon and brine composition | Paper and raster | Direct |
| Full 3-D flow simulations | Digital and raster | Indirect |
| Static geomodels of Tensleep Sandstone, Section 10 | Digital | Indirect |

**Table 2.2**: Data types and format at Teapot Dome (Friedmann and Stamp, 2006).

#### *2.4.1.1 SEISMIC*

The 3D seismic cube is a post-stack migrated filtered volume (also unfiltered is available). Five horizons have been interpreted (McCutcheon, 2003), as well as the main faults associated with them. The interpreted reflectors are the Second Wall Creek Sandstone, Lakota Sandstone (a good quality reflector that provides mid-level structural control across Teapot Dome), Red Peak Member of Chugwater Fm. (also a good quality reflector), the Tensleep Fm. and the Precambrian basement. Major fault cuts were mapped only in the intersection with the seismic horizons, but systematic correlation of each fault has not been done.

#### *2.4.1.2 WELL LOGS*

Of the 1300 wells at Teapot Dome, around 43 have penetrated the Tensleep Fm., and most of them are in the denominated Section 10 (Figure 2.13). In table 2.3, we summarize the wells in the study area that present the most complete set of logs, including FMI, cores, as well as the sonic logs and drilling reports.

| Well | FMI | SONIC | GR | Resistivity | Caliper | Porosity | Cores | Drilling Reports |
|---|---|---|---|---|---|---|---|---|
| **11-AX-11** | | X | X | X | | X | | |
| **25-1-X-14** | X | X | X | X | X | X | | X |
| **41-2-X-3** | X | X | X | X | X | X | | X |
| **43-TpX-10** | | X | X | X | | X | X | |
| **44-1-TpX-10** | | X | X | | X | X | X | |
| **48-X-28** | X | X | X | X | X | X | X | X |
| **51-CMX-10** | | | X | X | | X | X | |
| **54-TpX-10** | | | X | X | | X | X | |
| **56-TpX-10** | | | X | X | | X | X | |
| **61-2-X-15** | X | X | X | X | X | X | | X |
| **62-TpX-10** | | | X | X | | X | X | |
| **62-TpX-11** | | X | X | X | | X | | |
| **67-1-TpX-10** | X | X | X | X | X | X | | X |
| **71-1-X-4** | X | X | X | X | X | X | | X |

**Table 2.3:** Summary of Tensleep wells with most complete data set in Section 10 (see Figure 2.13 for location).

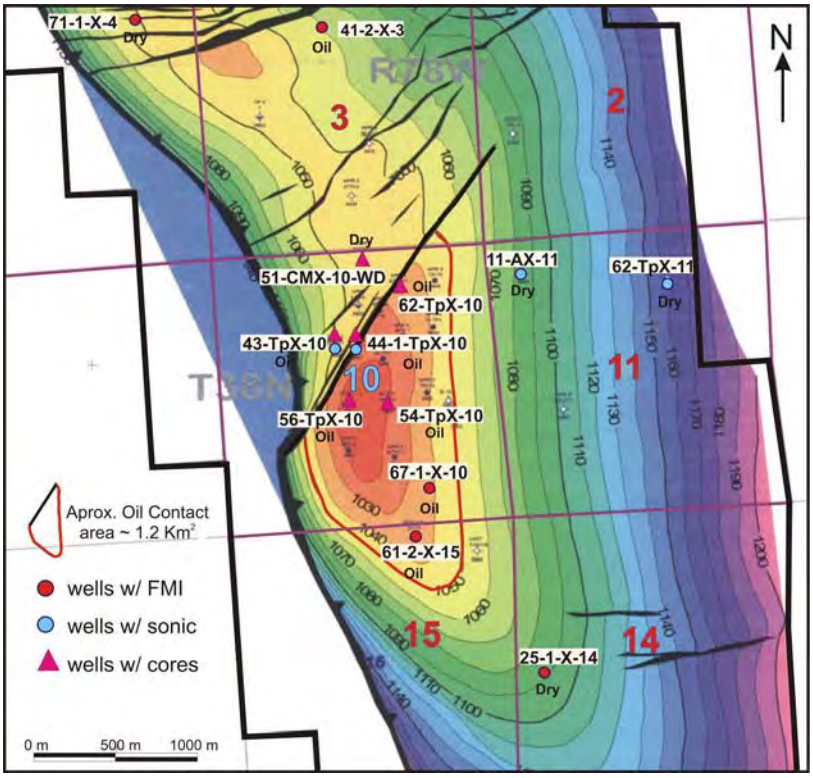


**Figure 2.13**: Study Area with location of wells classified in 3 categories: Wells with conventional+FMI logs, wells with conventional+sonic logs and, wells with conventional logs+Tensleep cores, plotted on a time structure map of the Tensleep Fm. prepared by McCutcheon (2005).

### 2.4.2 PILOT PROJECT

The Tensleep Fm. was chosen as a target for the $CO_2$-EOR and sequestration pilot for the appropriate depth range, relatively small number of wells penetrating the zone, regional extent and oil production significance, excellent cap rock, and local enhanced oil recovery potential (Friedmann and Stamp, 2006).

The $CO_2$-EOR and Sequestration Pilot is planned for early 2009 and will inject 1 million cubic feet per day (MMcfd) or 52 tonnes/day of supercritical $CO_2$ during six weeks, in order to test the $CO_2$-EOR potential of this horizon. If successful, EOR will help to offset the cost of a longer sequestration project.

### 2.4.3 $CO_2$ SOURCE

Wyoming has large $CO_2$ reserves, including the Greater Big Piney–La Barge Area in southwestern Wyoming, one of the world's largest natural sources of $CO_2$ (Nummedal et al., 2003). Presently, Exxon's Shute Creek facility in the La Barge area, is the $CO_2$ supplier for all the EOR projects within the Rocky Mountains. As of October 2006, ~250 MMcfd of $CO_2$ were contracted to Chevron, Anadarko and Merit Energy for use in their fields in Colorado and Wyoming (Figure 2.14) (Hassler, 2006). At Rangely Field, CO, Chevron was injecting 166 MMcfd (Emfi, 2004), whereas Anadarko is currently injecting 48 MMcfd at Monell and 320 MMcfd at Salt Creek (Gaines, 2008). In addition, Merit Energy is currently injecting ~3 MMcfd at Bairoil Fields (Stroud, 2008).

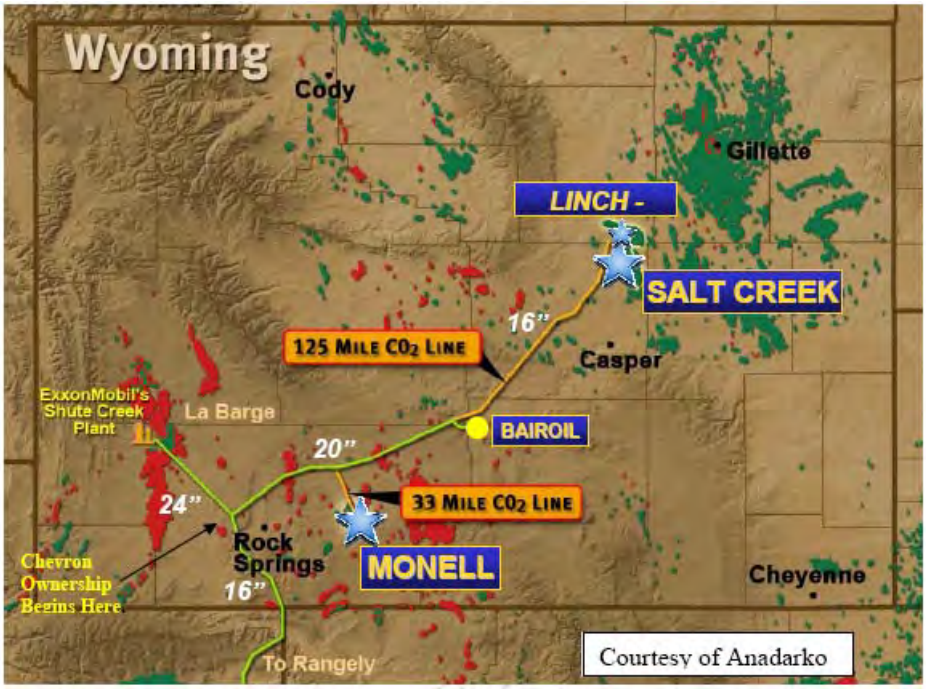


**Figure 2.14**: Existing carbon dioxide infrastructure in the region. Primary infrastructure for $CO_2$ delivery is owned by Exxon, Chevron and Anadarko (or their affiliates). Exxon: from Shute Creek through Rock Springs and on to Bairoil. Chevron: from Rock Springs to Rangely. Anadarko: from Bairoil to Salt Creek (Hassler, 2006).

Exxon Mobil's Shute Creek gas processing facility was built in 1986 and produces $CO_2$ in association with sour natural gas from southwest Wyoming. The plant, that also produces methane, is the largest sulfur-producer in Wyoming and the largest helium producer in the United States (WSGS Carbon Dioxide Group). An average of 207 MMcfd of $CO_2$ was sold in 2007 for enhanced oil recovery, but another 181 MMcfd were vented (Bleizeffer, 2008). This corresponds to a total of $7.33 \times 10^6$ tonnes/yr $CO_2$ separated at Shute Creek.

The Teapot Dome Tensleep pilot will take advantage of the pipeline already constructed from Shute Creek facility to Anadarko's Salt Creek for the Second Wall Creek EOR project. The pipeline supplies Salt Creek with anthropogenic $CO_2$, and since the possibility of constructing a pipeline extension from Salt Creek into Teapot

Dome is not clear yet; $CO_2$ is expected to be delivered by truck for the start of the pilot (Friedmann and Stamp, 2006).

## 2.5 SUMMARY

In this chapter, we presented an overview of Teapot Dome's geology, as well as the characteristics of the National Carbon Storage Test Center and the proposed experiments, which are the focus of this dissertation. Most of the work that will be presented in the following chapters is related to the $CO_2$-EOR and sequestration pilot, planned in the Section 10 area, where the Tensleep Fm. is trapped against the S1 fault.

CHAPTER 3

# SEAL INTEGRITY AND FEASIBILITY OF $CO_2$ SEQUESTRATION IN THE TEAPOT DOME EOR PILOT: GEOMECHANICAL SITE CHARACTERIZATION

## 3.1 ABSTRACT

This paper reports on a preliminary investigation of $CO_2$ sequestration and seal integrity at Teapot Dome oil field, Wyoming, USA, with the objective of predicting the potential risk of $CO_2$ leakage along reservoir-bounding faults. $CO_2$ injection into reservoirs creates anomalously high pore pressure at the top of the reservoir that could potentially hydraulically fracture the caprock or trigger slip on reservoir-

bounding faults. The Tensleep Formation, a Pennsylvanian age eolian sandstone, is evaluated as the target horizon for a pilot $CO_2$ EOR-carbon storage experiment, in a three-way closure trap against a bounding fault, termed the S1 fault. A preliminary geomechanical model of the Tensleep Fm. has been developed to evaluate the potential for $CO_2$ injection inducing slip on the S1 fault and thus threatening seal integrity. Uncertainties in the stress tensor and fault geometry have been incorporated into the analysis using Monte Carlo simulation. We found that even the most pessimistic risk scenario would require ~9 MPa of excess pressure to cause the S1 fault to reactivate and provide a potential leakage pathway. This would correspond to a $CO_2$ column height of ~1500 m, whereas the structural closure of the Tensleep Fm. in the pilot injection area does not exceed 100 m. Therefore $CO_2$ injection is not likely to compromise the S1 fault stability.

## 3.2 INTRODUCTION

For $CO_2$ sequestration to be a viable carbon management solution, one of the main issues to be addressed is the risk of $CO_2$ leakage. From a technical perspective, depleted or mature oil and gas reservoirs hold great promise as sequestration sites because they have hold hydrocarbons for geological periods, implying the presence of effective trap and seal mechanisms. However, it has long been known (*e.g.*, Raleigh *et al.* 1976) that fluid injection causes changes in the pore pressure and stress field that could potentially alter the initial seal of the reservoir by either hydraulically fracturing the cap rock or triggering slip on pre-existing faults by reducing the effective normal stress on the fault plane (see review by Grasso, 1992).

In light of this, a key step in the evaluation of any potential site being considered for geologic carbon sequestration is the ability to predict whether the increased pressures associated with $CO_2$ sequestration are likely to affect seal capacity. Although one possible leakage route in depleted oil and gas fields may be the damaged casings of old or abandoned wells, the focus of the present work is to

evaluate the potential risk of $CO_2$ leakage through natural pathways by inducing slip on faults that are currently sealing and bounding the hydrocarbon reservoirs. It is thus essential to study the relationship between faults and the present-day stress field to predict which faults could be potential leakage routes.

Another way of compromising seal integrity is by hydrofracturing the cap rock, which occurs when the pore pressure at the top of the reservoir is as high as the least principal stress in the overlying unit. In both cases, geomechanical characterization can be used to derive the pressures and rates of injection needed to reach those critical values and can therefore help evaluate the potential risk of leakage.

## 3.3 TEAPOT DOME $CO_2$ EOR-CARBON STORAGE PILOT

The Teapot Dome Field Experimental Facility (Figure 3.1) is owned by the U.S. government and operated by the U.S. Department of Energy (DOE) and the Rocky Mountain Oilfield Testing Center (RMOTC). This federal ownership assures a platform for long-term scientific investigations in a stable business context. The extensive data set of Teapot Dome is in the public domain, thus facilitating research of all kinds. These unique characteristics make Teapot Dome an ideal laboratory to conduct an EOR - Carbon Storage experiment in a mature oil reservoir. To evaluate the scientific and technical feasibility, the project team is working with interested industry and research partners to design the first $CO_2$ injection experiment, a small, short-duration EOR pilot, using existing wells and infrastructure. Project execution will be primarily contingent upon receiving adequate support from RMOTC's industry and research partners. The project envisioned would target the Tensleep Formation, with a minimum of ~60 tons/day $CO_2$ for a minimum of ~1.5 months.

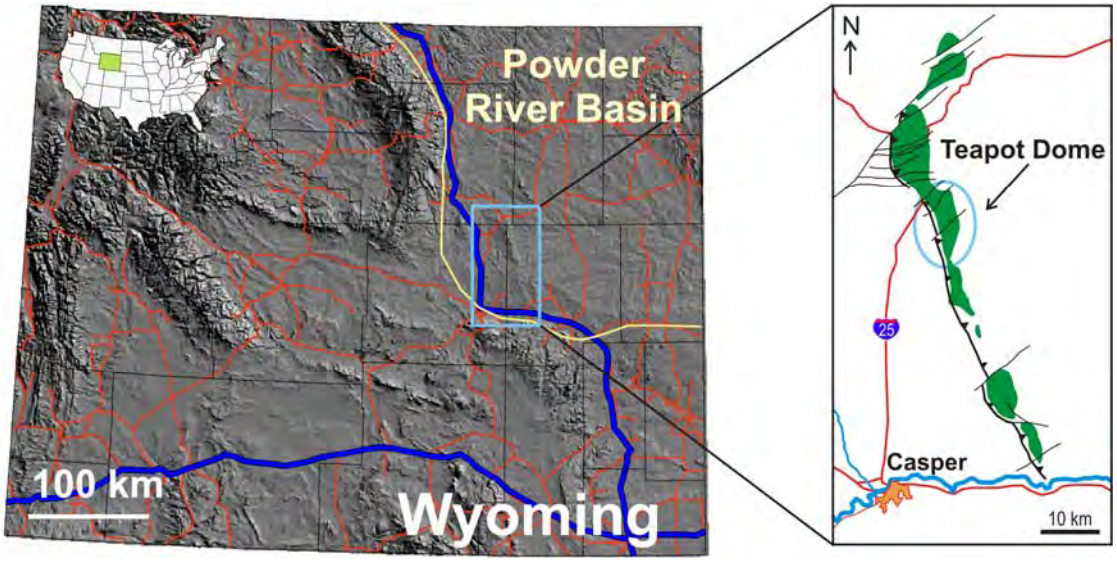


**Figure 3.1**: Location of Teapot Dome. Satellite image of Wyoming (left), Salt Creek structural trend, topographic relief in green (right) (courtesy of RMOTC).

## 3.4 GEOLOGY OF TEAPOT DOME

Teapot Dome is an elongated asymmetrical, basement-cored anticline with a north-northwest axis. It is part of the Salt Creek structural trend (Figure 3.1), located on the southwestern edge of the Powder River Basin (Cooper and Goodwin, 1998, Beinkafner, 1986). The anticline (Figure 3.2) is interpreted as a west verging fault propagation fold, typical of many Laramide age folds in the Rocky Mountain Region (McCutcheon, 2003, Milliken and Koepsell, 2003). It is bounded on the west by a series of high-angle reverse faults of approximately 35° to 40° east-northeast dip (McCutcheon, 2003). The anticline is compartmentalized into several blocks by major oblique strike-slip to normal faults (Figure 3.2) involving the basement. In some cases, these faults are actually a series of smaller faults, subparallel to a major fault. In cross-section they produce what is sometimes called a flower structure (Twiss and Moores, 1992). These faults are well defined in the seismic data and in outcrops. In general, they are oriented along a NE-SW trend, but vary in geometry, displacement, and complexity. The major fault zones have been assigned arbitrary names S1, S2, S3, and S4 (McCutcheon, 2003) as shown in Figure 3.2.

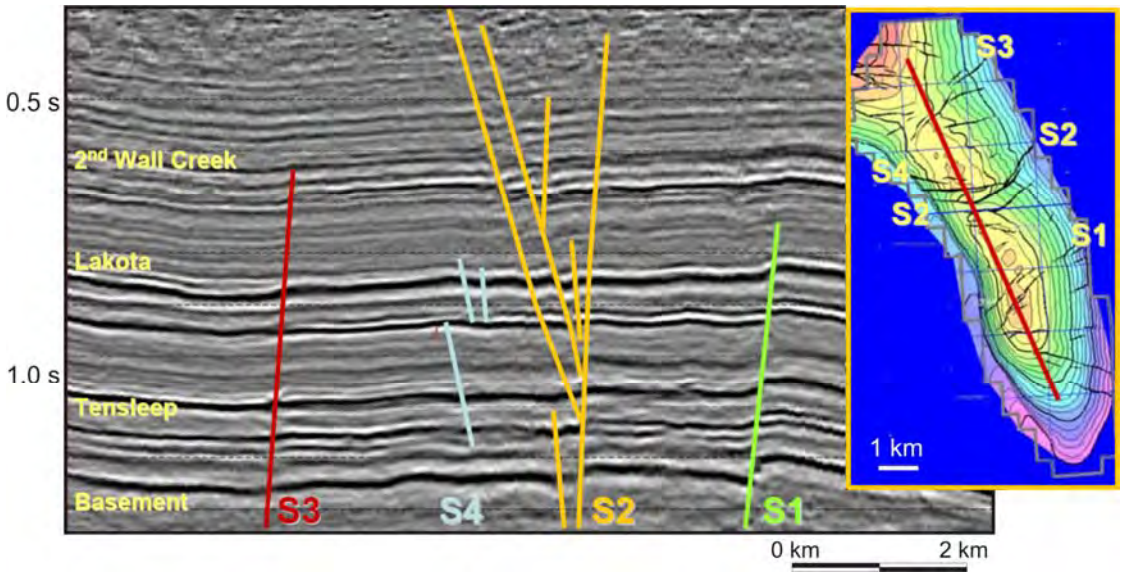


**Figure 3.2**: NW-SE cross section through Teapot Dome (left). Depth-structure map of 2nd Wall Creek Sandstone with locations of seismic line (right) (Friedmann et al., 2004).

The stratigraphy of Teapot Dome consists of Upper Cretaceous to Mississippian strata of diverse origin ranging from offshore sediments to coastal sandstone dunes over a granitic basement. The Tensleep Formation, of Pennsylvanian age, is the deepest hydrocarbon producing interval in the anticline. It contains multiple sequence boundaries in response to frequent and high-amplitude sea level changes (Zhang *et al.,* 2005). In this area it consists of interdune deposits such as eolian sandstones, sabkha carbonates, evaporites (mostly anhydrite), and extensive beds of very low permeability dolomicrites. The average porosity is 10% (5 – 20% range), and the average permeability is 30 mD (10 – 100 mD range). The average net thickness is 15 m. The reservoir has a strong aquifer drive and therefore hydrostatic reservoir pressure, and the reservoir temperature is ~88°C. The Tensleep Formation is divided into several intervals, of which the approximately 30 m thick B-Sandstone is the main producing horizon and the proposed storage interval for this experiment.

The Opeche Shale plus the anhydrite of the Minnekahta Member of the Permian Goose Egg Formation (Figure 3.4) comprise the regional seal of the Tensleep Fm. throughout Wyoming. At the top of the Tensleep Fm. there is a tightly cemented

dolomitic eolian or interdune sandstone, with diagenetic effects possibly related to a long period of subaerial exposure. A major unconformity on this surface is characterized by a sedimentary breccia with clasts of the Tensleep Fm. dolomitic sandstone suspended in a matrix of dolomitic and anhydritic sandstone of the Opeche Member. The two meter thick Opeche Sandstone Member is capped by 17 meters of redbed siltstone and sedimentary breccia of the Opeche Shale Member, deposited in an arid coastal plain setting. Overlying the Opeche Shale there are approximately 5 meters of the Minnekahta Limestone, deposited in a carbonate shelf setting (M. Milliken, personal communication, 2006).

In the area under study, the Tensleep Formation has its structural crest at 1675 m below surface covering an area of approximately 1.2 $km^2$ (Figure 3.3). The reservoir is trapped against a NE-SW trending fault to the north resulting in a three-way closure trap. A three-way trap is one in which the fluids are trapped by structural relief and the top seal on three sides of the trap, and by a sealing fault on the fourth side. The trapping fault, named S1, has been described as an oblique-slip basement-cored right-lateral tear fault (Milliken and Koepsell, 2003). Figure 3.3 is a time-structure map of the Tensleep Formation. In a time-structure map the formation structure is mapped in two-way seismic travel time (TWTT) expressed in milliseconds (ms), instead of depth/elevation. The red line, corresponding to the 1050 ms contour, indicates the oil/water contact. There is approximately 40 ms TWTT of structural closure (approx. 100 m at velocity = 2500 m/s) which is the vertical distance from structural crest to the spill point of structure on this reservoir. This means that around 100 m of fluid column height can be trapped.

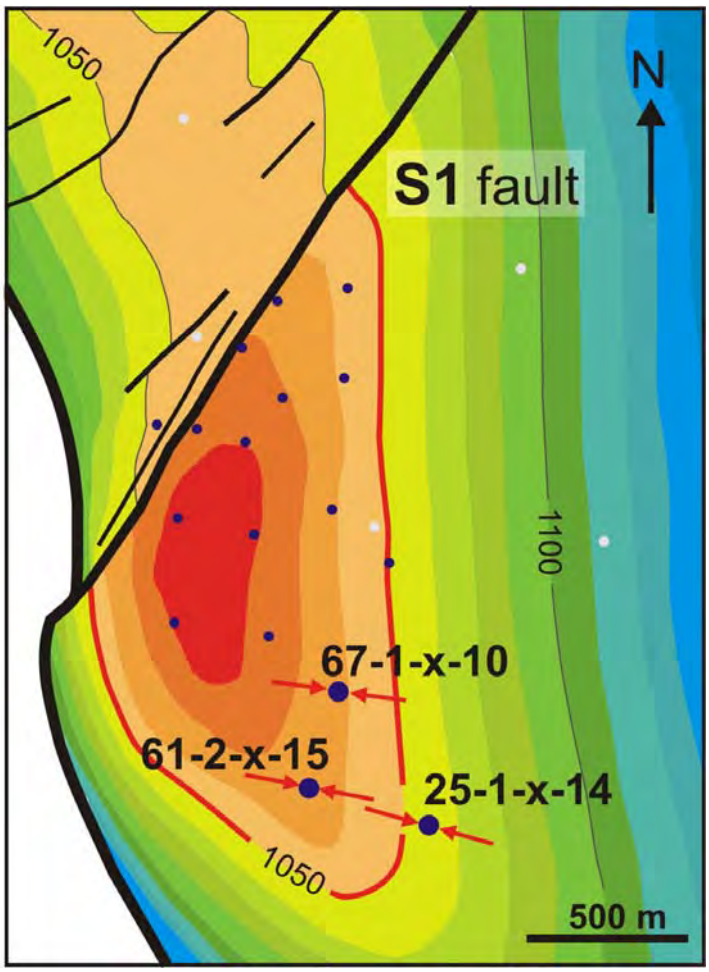


**Figure 3.3**: Time-structure map in milliseconds (ms) of Tensleep Formation in Section 10 area showing the S1 fault, oil-contact area (red contour line), $S_{Hmax}$ direction and analyzed wells (blue dots).

## 3.5 GEOMECHANICAL CHARACTERIZATION

To obtain the geomechanical model and perform a critically stressed fault analysis we follow the methodology of Zoback *et al.* (2003) for assessing the stress state, and Wiprut and Zoback (2002) for assessing fault stability. The parameters needed for a full definition of the stress state are summarized in Table 3.1 along with the data sources used to constrain the parameters.

The magnitude of the vertical stress ($S_v$) is obtained by integration of rock densities taken from density logs from the surface to the depth of interest (see first row of Table 3.1, where $z_0$ is the depth of interest, ρ is the density and $g$ is the gravity

acceleration). Density logs measure the bulk density of the rocks in the wellbore walls through gamma ray emissions. The proportion of gamma rays emitted by the source and back-scattered to the detector depends on the electron density of the formation and therefore its matrix density (Jahn *et al*., 1998).

The least principal stress, $S_3$, which is usually the minimum horizontal principal stress ($S_{hmin}$), can be obtained from the analysis of hydraulic fracturing via either minifracs or extended leak-off tests after the casing is set. Hydraulic fractures allow the determination of $S_3$ orientation and magnitude since they always propagate perpendicular to the least principal stress in the earth (Hubbert and Willis, 1957).

While $S_v$ and $S_3$ are relatively straightforward to estimate, the maximum horizontal stress ($S_{Hmax}$) magnitude can be obtained in different ways by modelling wellbore failure features such as drilling-induced tensile fractures (if $S_v$, $S_{hmin}$ and pore pressure ($P_p$) values are known) or stress-induced wellbore breakouts (if $S_v$, $S_{hmin}$, $P_p$ and the rock strength are known). The orientation of the horizontal principal stresses in vertical wells can be straightforwardly determined from wellbore failure orientations. Drilling-induced tensile fractures propagate parallel to $S_{Hmax}$, whereas breakouts form at the azimuth of $S_{hmin}$. Under normal drilling conditions, the occurrence of drilling-induced tensile fractures in a vertical well usually indicates a strike-slip faulting stress state (Zoback *et al*., 2003).

| Parameter | Data |
|---|---|
| Vertical Stress ($S_v$) | Density logs: $S_v(z_0) = \int_0^{z_0} \rho g dz$ |
| Minimum horizontal Stress ($S_{hmin}$) | LOT, XLOT, minifrac |
| Maximum horizontal Stress ($S_{Hmax}$) | Modeling wellbore failures |
| Stress orientation | Orientation of wellbore failures |
| Pore Pressure | Measure, sonic logs |
| Rock strength | Lab, logs, modeling well failure |
| Faults and fractures | Seismic, wellbore imaging |

**Table 3.1:** Parameters and data needed to define the stress tensor and the geomechanical model.

Density, sonic and Formation Microresistivity Imager (FMI) logs in the 67-1-x-10, 61-2-x-15 and 25-1-x-14 wells (see Figure 3.3 for well locations) were analyzed to quantify the stress tensor ($S_v$, $S_{Hmax}$ and $S_{hmin}$) in the area of interest. A sonic log measures the speed of sound in the wall of the borehole, and is related to both the porosity and lithology of the rock being measured, whereas the FMI log makes a detailed image of the rocks on all sides of the well hole by measuring resisitivity of the rock.

*Stress Orientation from FMI logs*

Drilling-induced tensile fractures were analyzed in FMI logs from the three study wells**.** Interactive image analysis yielded 420 observations of drilling-induced tensile fractures over a depth range of 400 – 1800 m (Figure 3.4). The average maximum horizontal stress ($S_{Hmax}$) direction is 116° ±15° AZ (N64°W). This value is consistent with the $S_{Hmax}$ orientation of 105° AZ (N75°W), observed by Milliken and Koepsell (2003) in well 67-1-x-10. If we consider only the drilling-induced tensile fractures in the Tensleep Fm., the direction of $S_{Hmax}$ is 100° ±15° AZ (N80°W).

Figure 3.4 shows the stratigraphic column and the distribution of tensile fractures on each of these wells. In well 67-1-x-10 tensile fractures are found through most of the column while in well 25-1-x-14 there are surprisingly fewer features, even though the two wells were drilled with similar mud weights. In well 61-2-x-15 only part of the Tensleep Fm. was imaged, where tensile fractures are present as well. Note the lack of breakouts at the depth of the Tensleep Fm.

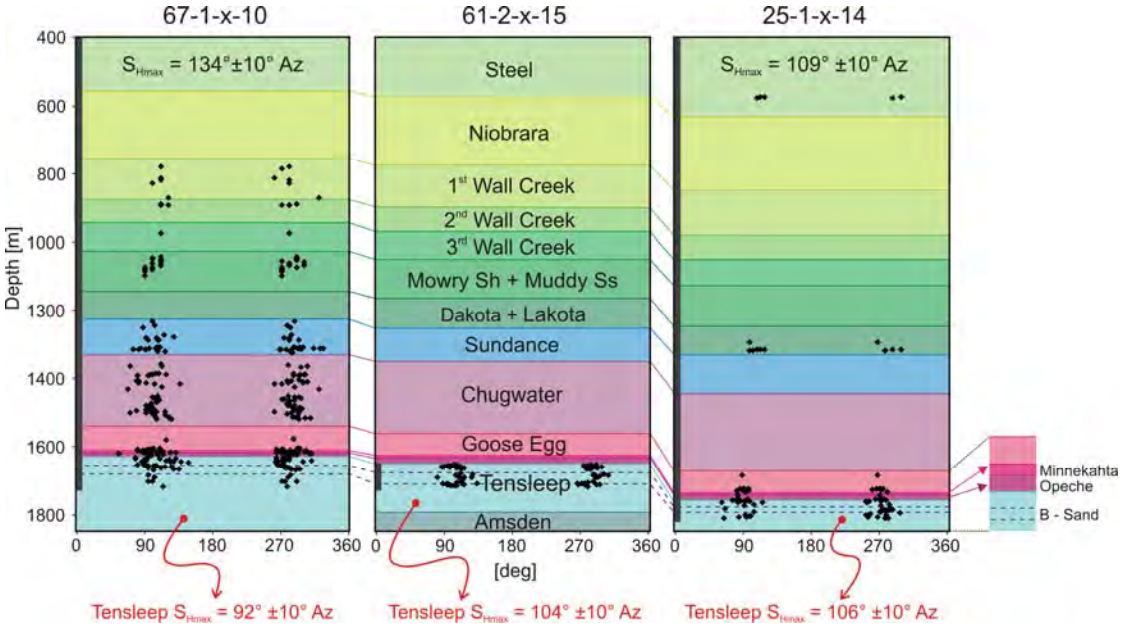


**Figure 3.4**: Observations of drilling-induced tensile fractures in the three study wells. The orientation at the top of each panel indicates the average $S_{Hmax}$ stress orientation from the entire interval studied. The stress orientation in the Tensleep Fm. is indicated at the bottom of each figure. The vertical bar in each panel indicates the range of depths covered by the FMI log. The entire thickness of the Tensleep Fm. is shown in the middle panel, but was not penetrated in the other two wells. The B sand is only ~30 m thick and located near the top of the formation.

The rock strength used in the horizontal stress magnitude estimations was determined from sonic logs using an empirical relationship developed by Chang et al. (2006) for weak and unconsolidated sandstones in the Gulf Coast. The average estimated value of the B-Sandstone rock strength varies from 55 MPa to 65 MPa in the three wells.

Figure 3.5 represents the range of allowable values for the horizontal principal stresses based on Coulomb faulting theory and Anderson's stress and faulting classification system, provided depth, pore pressure and a particular coefficient of friction. The solid black line in Figure 3.5 outlines a polygon that defines the limits of Mohr-Coulomb failure for frictional equilibrium of pre-existing faults. The stress state must be inside of this polygon because the strength of the crust does not allow a larger stress difference between the greatest and least principal stresses. The black solid lines separate the three triangular regions reflecting normal faulting (NF), strike-slip faulting (SS), and reverse faulting (RF) stress conditions. NF implies $S_v = S_1 > S_{Hmax} = S_2 > S_{hmin} = S_3$, SS environment requires $S_{Hmax} = S_1 > S_v = S_2 > S_{hmin} = S_3$ whereas RF implies $S_{Hmax} = S_1 > S_{hmin} = S_2 > S_v = S_3$. The red contours on Figure 3.5 discriminate the permissible stress states for a series of rock strengths whereas the blue contours delimit possible horizontal stress magnitudes based on the tensile strength of the rock (Moos and Zoback, 1990; Zoback et al., 2003).

The magnitudes of $S_{Hmax}$ and $S_{hmin}$ were estimated from observed occurrence of drilling-induced tensile fractures and non-occurrence of wellbore breakouts, following Zoback et al. (2003). The green polygon in Figure 3.5 shows the allowable magnitudes of $S_{Hmax}$ and $S_{hmin}$ for well 67-1-x-10 data at depth = 1656 m (top of Tensleep Fm.), hydrostatic $P_p$ = 16.56 MPa, $S_v$ = 40.6 and compressive rock strength (C) = 55 MPa. Since no breakouts were observed it was assumed that, the calculated rock strength is the lower bound for the actual rock strength and acts as an upper bound for the $S_{Hmax}$ magnitudes, as well as the zero tensile strength blue line. The mud weight and temperature, obtained from the drilling reports, were also considered, and with these constraints, the range of possible stress magnitudes was estimated. From the data in this particular well $S_{Hmax}$ could range from 31.5 to 43.0 MPa and $S_{hmin}$ from 24.5 to 28.5 MPa.

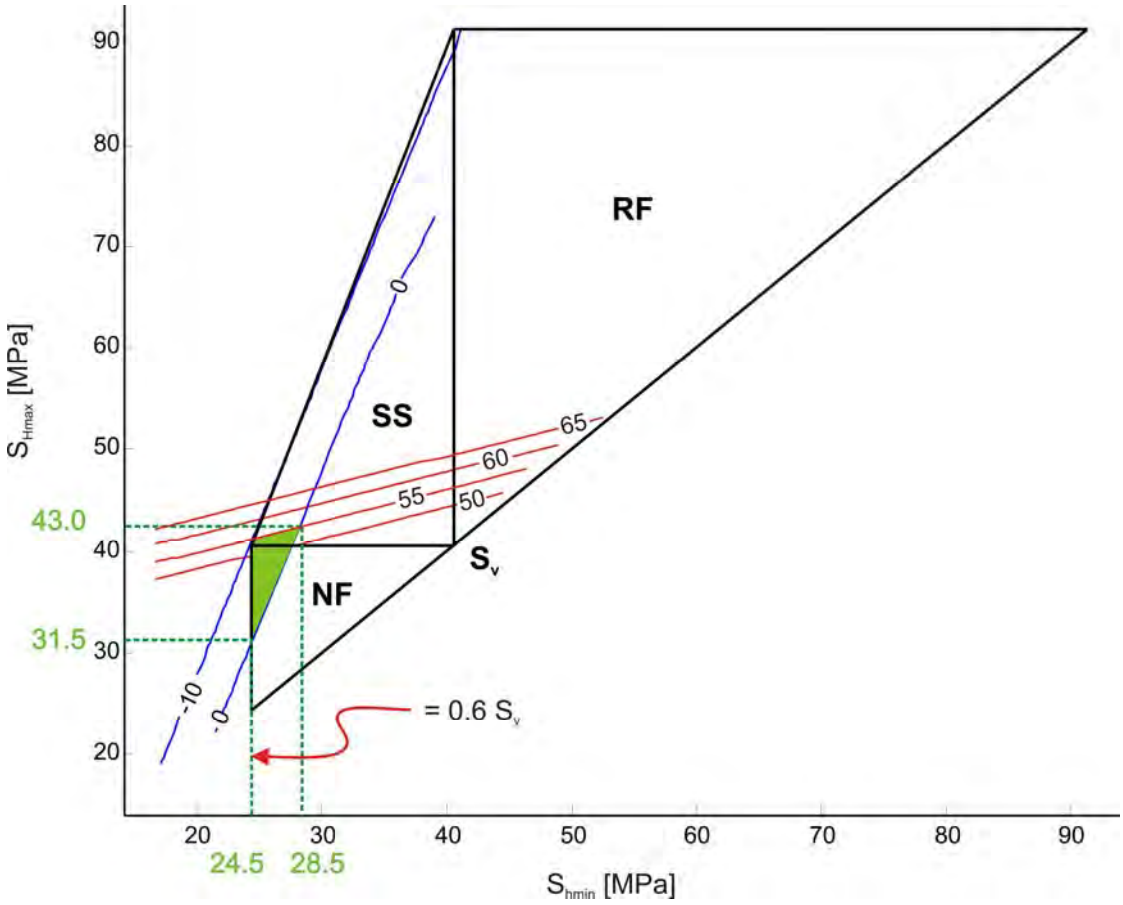


**Figure 3.5**: Stress polygon for well 67-1-x-10 (see explanation in text) at depth = 1656 m (top of Tensleep Fm.), Pp = 16.56 MPa, Sv = 40.6 and compressive rock strength = 55 MPa. Red lines are isovalues of rock strength and blue lines represents isovalues of tensile rock strength.

The analysis of the three studied wells yielded a NF/SS faulting stress state where $S_{Hmax} \approx S_v > S_{hmin}$. This is supported by fault movement observed in the youngest sections of the 3D seismic cube and by the displacements on NE/SW faults observed in the surface outcrops and trenches (Milliken, 2005).

Due to the absence of leakoff or minifrac tests in the Tensleep Fm. to obtain the magnitude of $S_{hmin}$ (which would also better constrain the magnitude of $S_{Hmax}$), the critically stressed fault analysis was first performed with an $S_{hmin}$ gradient of $0.6S_v$ and $S_{Hmax} = S_v$ expected for a NF/SS environment. Available data from a minifrac test performed in the 2nd Wall Creek reservoir confirms $S_{hmin} = 0.6S_v$. This minifrac test was performed in well 71-1-ax-4, roughly 2 km northwest of the area under study,

where the 2nd Wall Creek reservoir is at approximately 900 m depth and 720 m above the top of the Tensleep Fm.

With this information, a 2nd order stress tensor (S) that only varies with depth was defined as the base case scenario to estimate the leakage potential of the S1 fault. Since the present stress state corresponds to a NF/SS environment, $S_1 = S_{Hmax}$, $S_2 = S_v$ and $S_3 = S_{hmin}$ (see Eq. 3.1).

$$S = \begin{bmatrix} S_1 & 0 & 0 \\ 0 & S_2 & 0 \\ 0 & 0 & S_3 \end{bmatrix} = \begin{bmatrix} S_{H\max} & 0 & 0 \\ 0 & S_v & 0 \\ 0 & 0 & S_{h\min} \end{bmatrix} = \begin{bmatrix} S_v & 0 & 0 \\ 0 & S_v & 0 \\ 0 & 0 & 0.6S_v \end{bmatrix} \quad \textbf{(3.1)}$$

## 3.6 FAULT SLIP POTENTIAL USING COULOMB CRITERION

The S1 fault was mapped in the available 3D seismic survey and converted to depth using the seismic dip processing moveout (DMO) velocities. To determine the risk of leakage through the S1 fault, the authors evaluated the state of stress and pore pressure acting on the fault plane following the methodology of Wiprut and Zoback (2002) described below.

It is important to note that the orientation of the S1 fault has an azimuth of 36°, which is nearly perpendicular to $S_{Hmax}$ (see Figure 3.3). Therefore, it immediately appears unlikely that this fault could slip in a NF/SS stress field.

To perform the quantitative analysis, the shear (τ) and normal stresses ($S_n$) were calculated for each element of the fault. Then Coulomb failure criteria were applied to predict the critical pressure ($P_c$) necessary to reactivate fault slip, assuming a coefficient of friction (μ) of 0.6.

$$P_c = S_n - \tau / \mu \quad \textbf{(3.2)}$$

Comparing this $P_c$ with a reference $P_p$, modeled from the pressure data of the field, a critical pressure perturbation ($P_{cp}$) was obtained. $P_{cp}$ indicates the pore pressure change to enable a fault element to slip given the stress state, fault

orientation and reference $P_p$. In this analysis, it is assumed that active faults are potential conduits for fluid migration such that $P_{cp}$ indicates the leakage potential for each portion of the fault (Figure 3.6a). It is worth noting that this is a conservative approach for evaluating likelihood of $CO_2$ leakage along the fault, even though the amount of potential leakage could be quite small if the area of fault slip is small.

For the base case stress scenario defined in the previous section, at the depth of the Tensleep Formation (red line in Figure 3.6a), approximately 16 MPa of excess pressure would be required to cause the fault to slip. This corresponds to a $CO_2$ column height of approximately 2300 m (at a density of 700 kg/m$^3$). Since the average closure of the Tensleep Formation in this area is no more than 100 m, it is anticipated that the S1 fault is not at risk of reactivation and therefore will not be a leakage pathway for $CO_2$ migration.

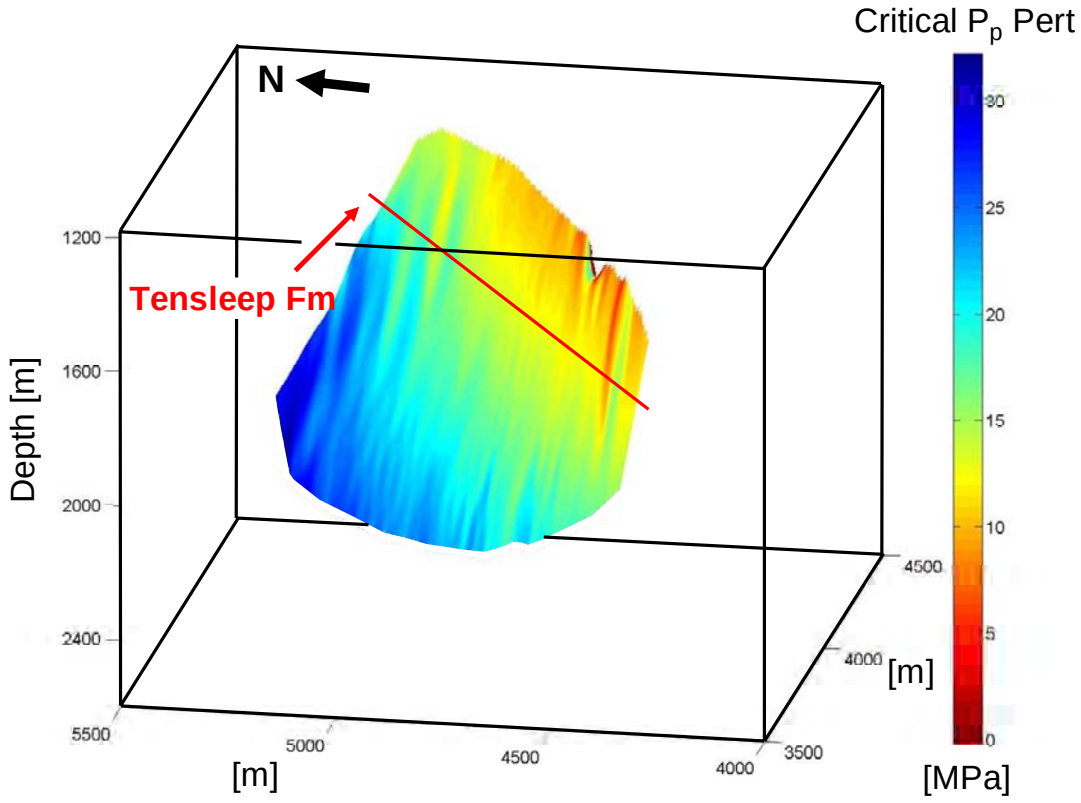


**Figure 3.6a**: Fault surface color-coded with critical pressure perturbation values indicating the fault slip potential. At the Tensleep Fm. (red line), ~16 MPa of excess pressure would be required to cause the fault to slip.

To evaluate how poro-elastic effects impact fault stability, Equation 3.3 was incorporated in the previous analysis. This equation was derived for an isotropic, porous and elastic reservoir that is infinite in extent. Segall and Fitzgerald (1996) showed that this relationship is also valid if the ratio of lateral extent to thickness of a reservoir is greater than 10:1 (which is the present case).

$$\Delta S_{Hor} = \alpha \frac{(1-2\nu)}{(1-\nu)} \Delta P_p \qquad \textbf{(3.3)}$$

$S_{Hor}$ corresponds to both $S_{Hmax}$ and $S_{hmin}$, α is Biot's coefficient and ν is Poisson's ratio (Brown et al., 1994).

$P_{cp}$ was estimated for a potential $CO_2$ injection-induced increase in $P_p$ =10 MPa, α = 1 and ν = 0.25. As shown in Figure 3.6b, the poro-elastic effects increase the amount of extra pressure needed to cause slip in the S1 fault. At the depth of the Tensleep Formation (red line in Figure 3.6b) approximately 20 MPa of excess pressure would be required.

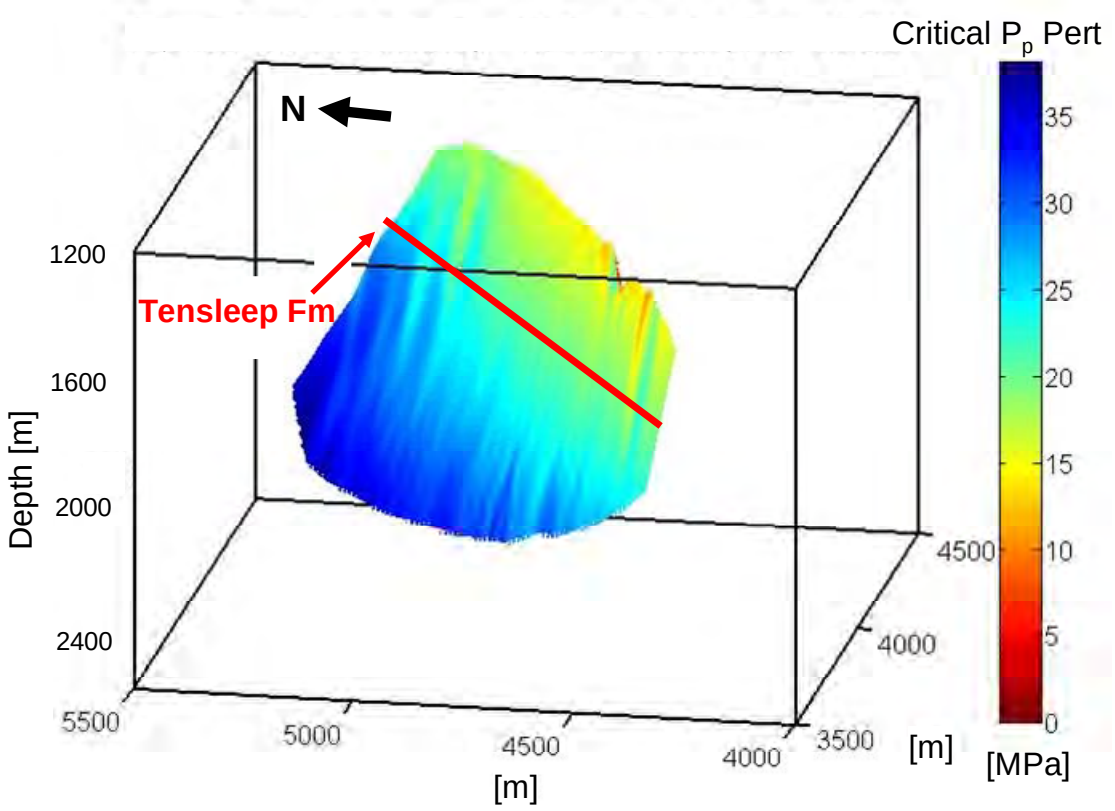


**Figure 3.6b**: Fault surface color-coded with critical pressure perturbation values indicating the fault slip potential considering the poro-elastic effect. At the Tensleep Fm. (red line), ~20 MPa of excess pressure would be required to cause the fault to slip.

## 3.7 CRITICAL PRESSURE PERTURBATION SENSITIVITY ANALYSIS

To evaluate how the uncertainties in the horizontal stress magnitudes and in the strike and dip of the fault with respect to the stress field affect the slip potential of the S1 fault, a sensitivity analysis of those parameters was performed. In the case of the fault orientation we need to account for the limits in the seismic resolution as well as for the uncertainties in the time-depth conversion of the structures mapped. During the seismic acquisition, the travel time of a wave from the surface to the objective at depth is measured. To convert the measured travel time to depth it is necessary to assume the velocity of the wave, from which comes the uncertainty on real depths and geometry of the bodies under consideration.

Random distributions of the components of the stress tensor were generated based on the mean, minimum and maximum stress values estimated for each well. For the base cases of a normal fault ($S_1=S_v$, $S_2=S_{Hmax}$ and $S_3=S_{hmin}$) and strike-slip ($S_1=S_{Hmax}$, $S_2=S_v$ and $S_3=S_{hmin}$), cases were analyzed separately using over 10,000 Monte Carlo Simulations. In the case of normal faulting, $S_{Hmax}$ is less than $S_v$ and greater than $S_{hmin}$. In the strike-slip case, $S_v$ is less than $S_{Hmax}$ and greater than $S_{hmin}$. Figures 3.7 (for normal faulting) and 3.8 (for strike-slip faulting) show the fault slip potential probability as a function of reservoir pressure for variations of the indicated component of the stress tensor (while the others remained fixed). From this analysis, it was established that in 99.9% of the cases a pressure perturbation of more than 9 MPa would be necessary to induce slip on the S1 fault.

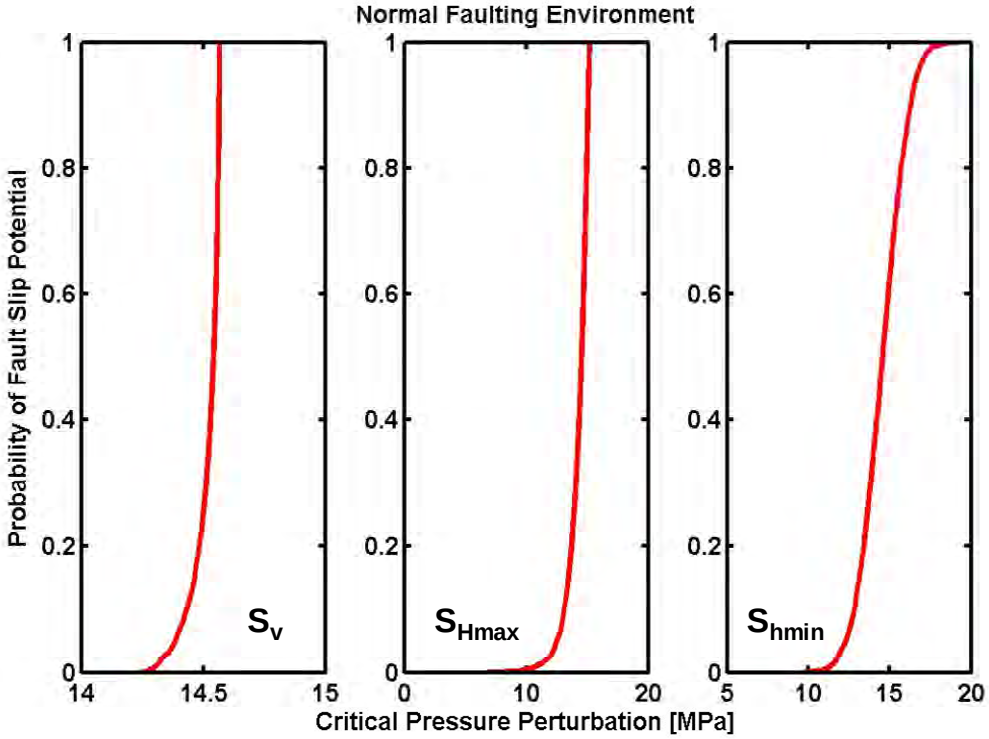


**Figure 3.7**: Fault slip potential probability for Normal Fault environment, as a function of each of the components of the stress tensor, varying $S_v$ (maintaining $S_{Hmax}$ = 34.4 MPa and $S_{hmin}$ = 25.7 MPa fixed) (left); varying $S_{Hmax}$ (maintaining $S_v$ = 39.9 MPa and $S_{hmin}$ = 25.7 MPa fixed) (center) and varying $S_{hmin}$ (maintaining $S_v$ = 39.9 MPa and $S_{Hmax}$ = 34.4 MPa fixed) (right).

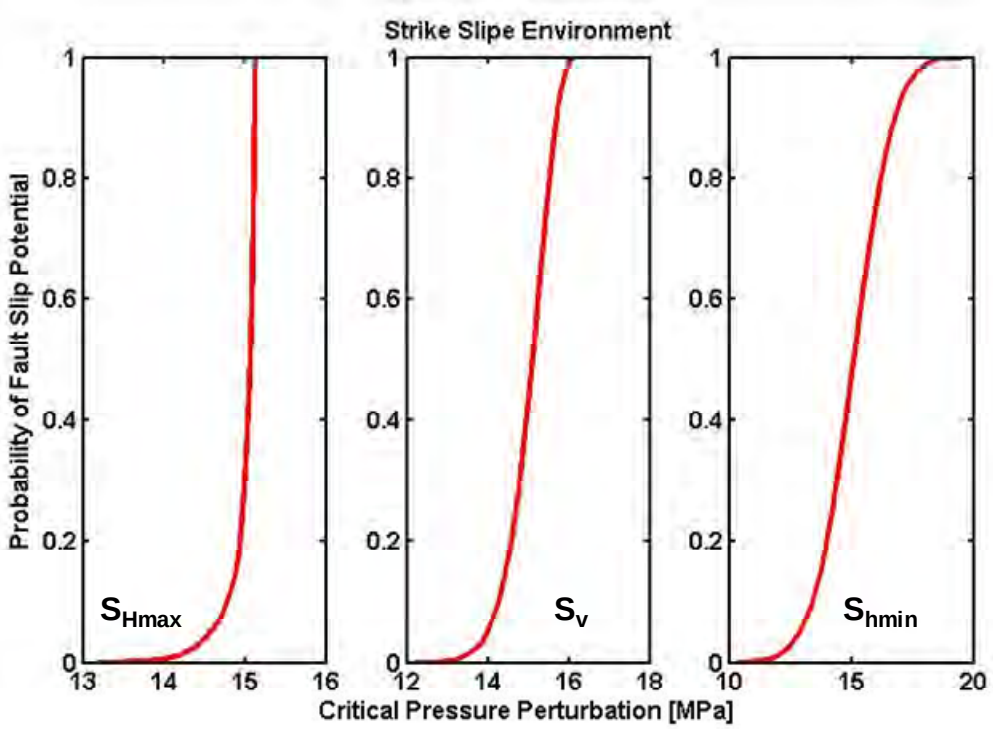


**Figure 3.8:** Fault slip potential probability for Strike-Slip environment, as a function of each of the components of the stress tensor, varying $S_{Hmax}$ (maintaining $S_v$ = 39.6 MPa and $S_{hmin}$ = 25.7 MPa fixed) (left); varying $S_v$ (maintaining $S_{Hmax}$ = 45.5 MPa and $S_{hmin}$ = 25.7 MP fixed) (center) and varying $S_{hmin}$ (maintaining $S_{Hmax}$ = 45.5 MPa and $S_v$ = 39.6 MPa fixed) (right).

To account for the uncertainties with respect to the geometry of the fault, Figure 3.9 evaluates fault slip probability as a function of variations in fault azimuth (Figure 3.9 left) and dip (Figure 3.9 right). These cases were evaluated with the mean values of the stress tensor. The azimuth has bigger impact than the dip angle. However this impact is less than the stress variation and in 99.9% of the test scenarios, the critical pressure perturbation values are above 13 MPa.

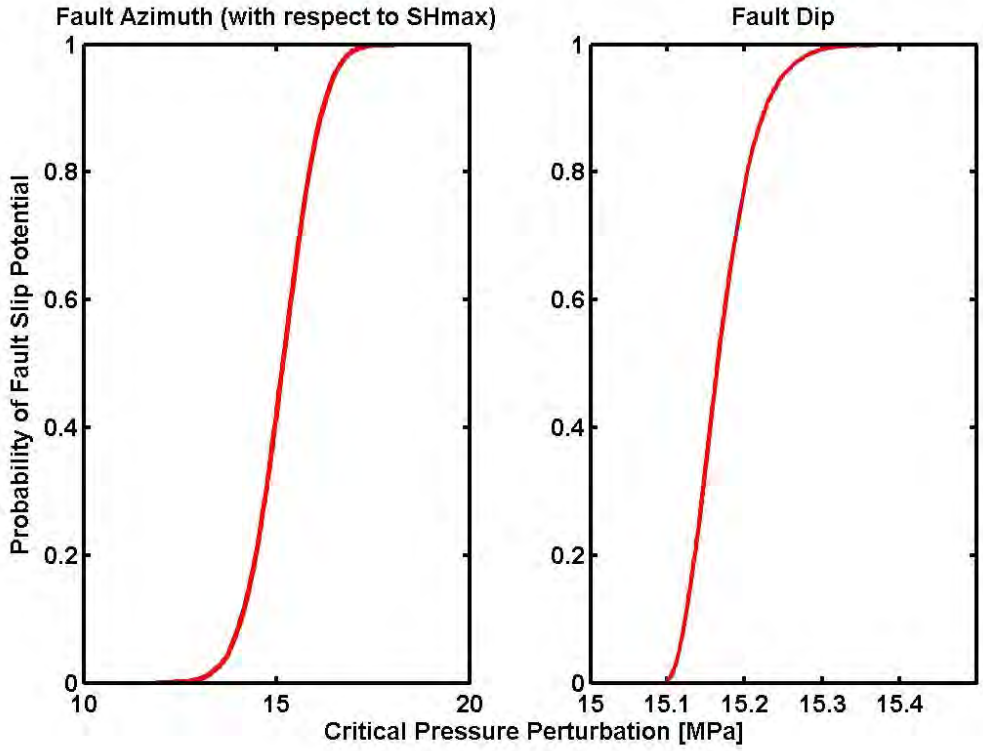


**Figure 3.9**: Fault slip potential probability as function of variation in the fault azimuth (left) and in the fault dip angle (right). The mean value of the stress tensor ($S_v$ = 39.90, $S_{Hmax}$ = 34.40 and $S_{hmin}$ = 25.72 MPa) was used to analyze these scenarios.

Even in the most pessimistic risk scenario, a $CO_2$ column height of approximately 1500 m (using a reasonable average density ~700 kg/m$^3$) is required to reach the lowest estimated $P_{cp}$ value (~10 MPa).

## 3.8 HYDRAULIC FRACTURE LIMIT FOR CAPROCK

Better constraints on the least principal stress ($S_{hmin}$) in both the reservoir and the caprock are necessary not only to more precisely estimate the magnitudes of $S_{hmin}$ and $S_{Hmax}$, but also to get more exact values for the maximum pressure increase at the top of the structure that the reservoir could sustain before hydrofracturing the overlying unit.

Knowledge on the hydraulic fracture limit of the caprock is important for two reasons. It is useful for evaluating the risk of leakage, and it provides a constraint on the maximum $CO_2$ column height that the reservoir can contain if hydraulic fracturing of the overlying unit occurs before the column reaches the spill point of the structure. In other words, the hydraulic fracture limit helps to evaluate whether there is a dynamic constraint for the $CO_2$ column in the area under study (e.g. Finkbeiner et al., 2001).

In order to better estimate the value of $S_{hmin}$ we need either a leak-off test or minifrac in the caprock. In the drilling reports of the three studied wells, no fluid loss information was recorded and no leak-off test or minifrac test data are available at Teapot Dome, other than the one mentioned in the 2$^{nd}$ Wall Creek reservoir.

With the better constrained value of $S_{hmin}$ it will be possible to evaluate whether the hydrofracture limit of the Tensleep Formation or the caprock could be a lower constraint in the sustainable injection pressure than the estimated $P_{cp}$ on the fault. However, from the estimated range of plausible values for the stress tensor it was estimated that the value of $S_{hmin}$ could be in between 23 to 32 MPa.

## 3.9 FRACTURES AT TEAPOT DOME

Several authors (Lorenz and Cooper, 2004; Schwartz et al., 2005; Lorenz, 2007) have described fractures in the Tensleep Fm., from cores, FMI logs and outcrops, as vertical to near vertical. In particular at Teapot Dome, Lorenz and Cooper (2004) performed a fracture characterization in core samples where they found an average of 1 fracture every 5 ft, although with increasing cement content, they noted and increase in fracturing. In high porosity sandstones they described a fracture intensity of approximately 1 fractures every 10 ft, in dolomitic sandstones 1 fractures every 3 ft and in heavily cemented fractures 1 fracture per ft.

These values of fracture intensity correspond to a fractured reservoir and careful consideration must be given to these features and their relationship with the present

day stress field to estimate their contribution to the risk of $CO_2$ leakage. Our previous geomechanical characterization yielded a NF/SS regime with a maximum horizontal stress ($S_{Hmax}$) direction of ~116° Az (red arrow in Figure 3.1). In a NF stress regime, the optimal direction for slipping is parallel to $S_{Hmax}$, which is represented by the green line in Figure 3.11. In the case of a SS regime, there are potentially two optimal directions for slip, each of them at 30° with respect to $S_{Hmax}$, represented as blue lines in Figure 3.10.

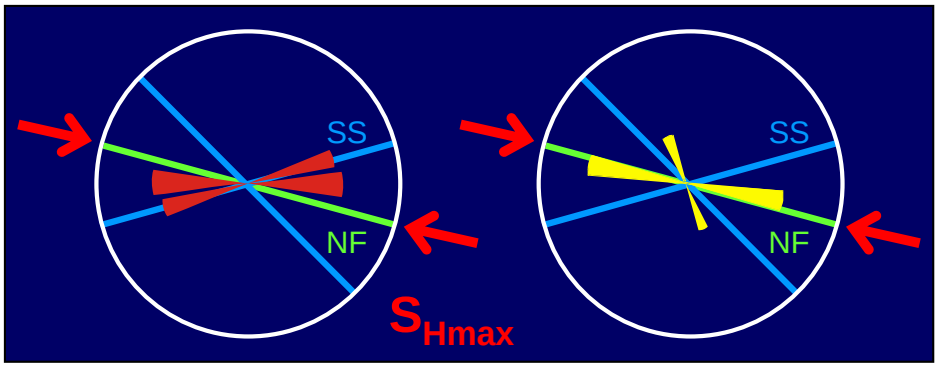


**Figure 3.10:** Strike orientation of main fractures sets in the Tensleep Fm. from Lorenz (2007) (left) and Schwartz et al. (2005) (right).

Figure 3.11 also shows the dominant sets of open fractures described by Schwartz et al. (2005) (right) and Lorenz (2007) (left) for the Tensleep Fm. at Teapot Dome. Comparing the strike of these open fracture sets with the optimal directions for slip in a NF/SS regime, we can observe that at least three of these sets are parallel to one of these optimal directions. In Figure 3.11 the poles of these fractures are plotted in a stereo net color coded with the critical pressure needed for a fracture to slip. Fracture sets a, b and c are very close to the critical pressure needed for reactivation.

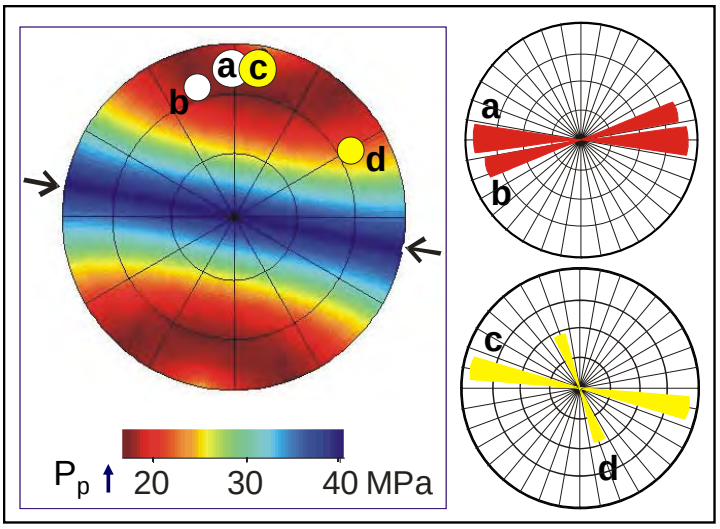


**Figure 3.11**: Rose diagrams of the dominant fracture sets at the Tensleep Fm. (right) and the poles of these sets color-coded with the critical pressure needed to reactivate them (left). Note the black arrow in the bottom indicating the hydrostatic pore pressure (~16.5 MPa).

We performed a fracture characterization in the FMI logs used in the previous sections, where we mapped several fractures sets in the reservoir as well as in the caprock (Figure 3.12). Some of these sets coincide with previous fracture characterizations as the ones mentioned in the previous paragraph.

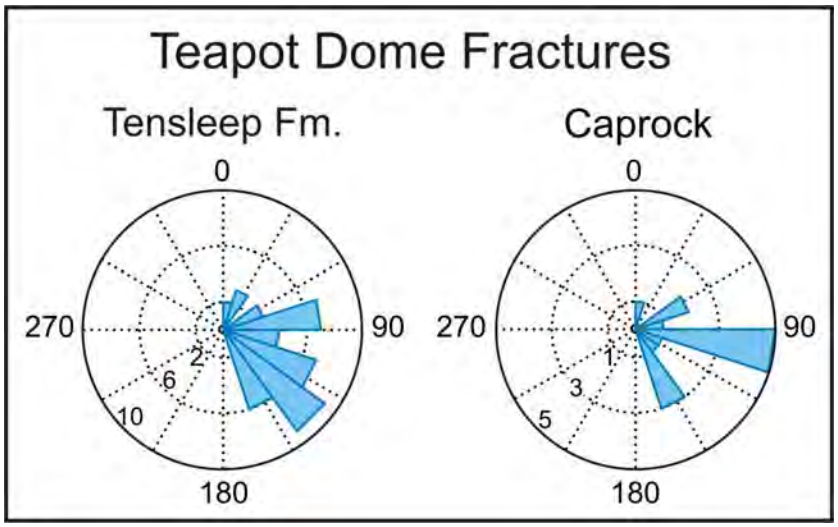


**Figure 3.12**: Fractures sets mapped in three FMI well logs in the S1 area.

Figure 3.13 shows plots of the coulomb failure function (CFF) as a function of fracture pole orientation for the caprock and the Tensleep. When the CFF is close to zero, it indicates that the fracture is critically stressed (white dots).

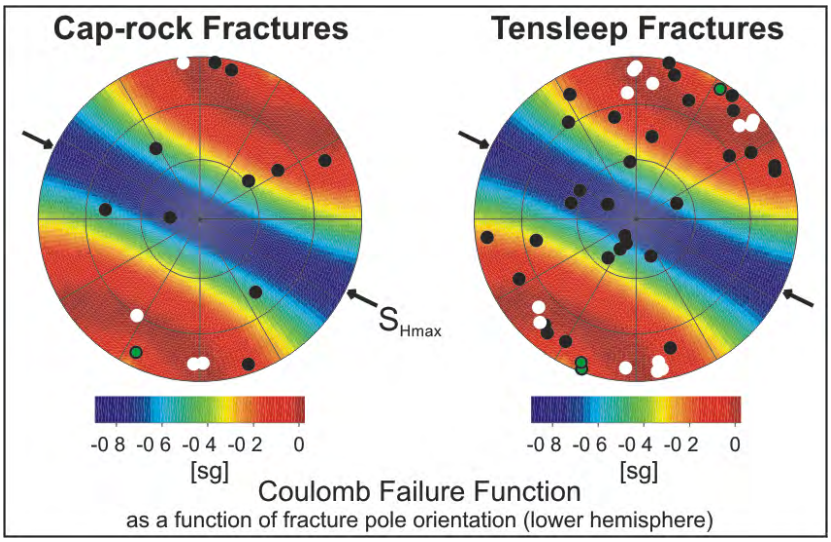


**Figure 3.13**: Observed Tensleep Fm. fractures (right) and caprock fractures (left) form three wells of the area under study. The white dots are the poles of the fractures that are critically stressed.

Several of these fractures are critically stressed, which could have a positive impact in reservoir permeability and injectivity but constitutes a potential risk for seal integrity, either if the caprock fractures are reactivated or if the reservoir fractures propagate into the caprock.

If any of these two scenarios occur, the reactivation of these minor faults will most likely result in microseismic activity. This microseismicity could be monitored to map the vertical $CO_2$ migration and identify potential leakages.

## 3.10 S2 FAULT ZONE STABILITY ANALYSIS FOR A POTENTIAL LEAKAGE EXPERIMENT

As mentioned in the previous chapter, a second experiment has been proposed at Teapot Dome. This second test plans to perform a controlled leakage experiment in the S2 fault zone.

The objective is to inject small amounts of $CO_2$ at the depth of the 2$^{nd}$ Wall Creek, ~930 m, in this structurally complex area, to study the potential occurrence of leakage and methods to monitor it.

To confirm that the S2 fault area would be suitable for this experiment, we performed a similar fault stability analysis than the one described in the previous sections in three branches of the S2 fault. To the previous geomechanical characterization, we incorporated drilling induced tensile fracture orientations from wells 71-1-X-4 and 48-X-28 (Figure 3.14) that yielded very similar stress orientations than previously determined. Also, there is a leak-off test in well 71-1-X-4 at the depth of the 2$^{nd}$ Wall Creek that confirms the NF-SS present day stress tensor.

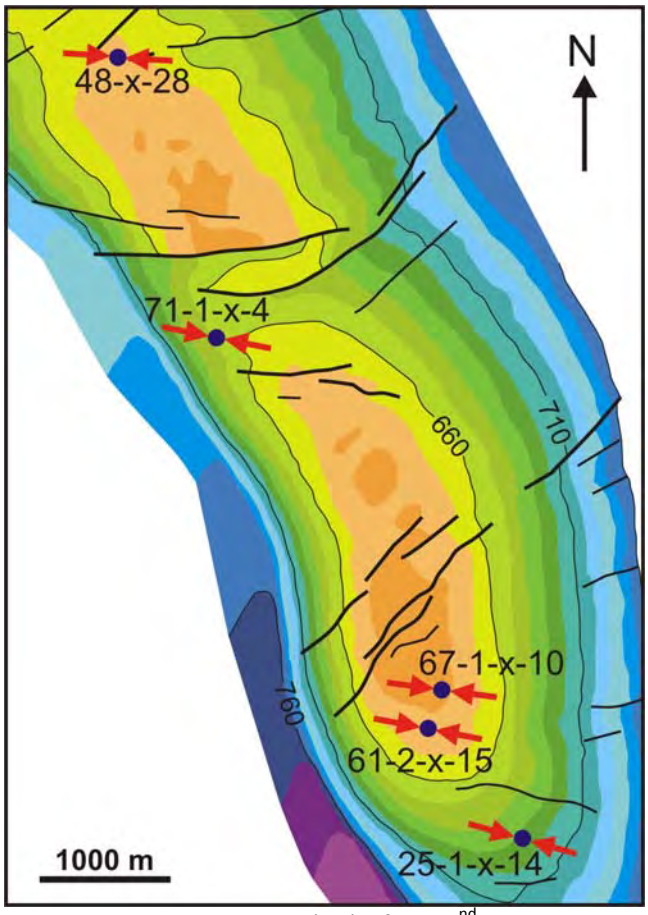


**Figure 3.14**: Time-structure map in milliseconds (ms) of the 2nd Wall Creek showing $S_{Hmax}$ directions and analyzed wells (blue dots). In addition, the S1 fault (to the south) and the S2 fault zone north of well 71-1-X-4.

Figure 3.15 shows the result of the fault stability analysis confirming that these faults are critically stress and therefore a small increase in pressure ( < than 5 MPa) due to the $CO_2$ injection could cause this faults to reactivate, potentially inducing leakage.

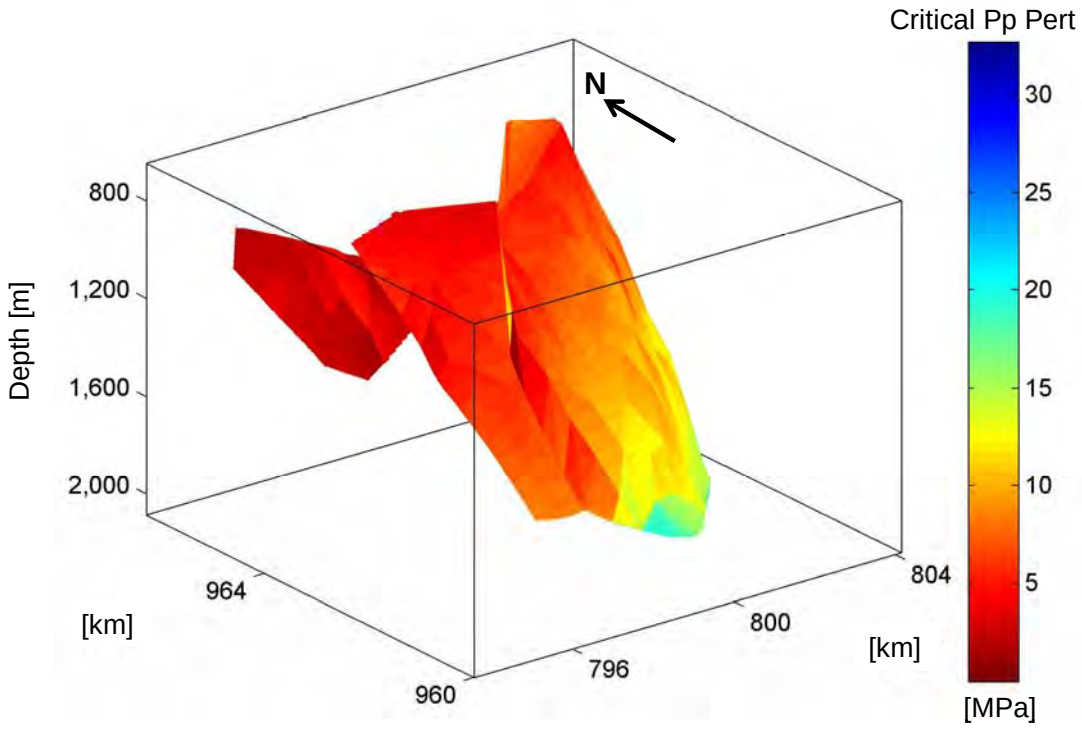


**Figure 3.15**: S2 fault surfaces color-coded with critical pressure perturbation values indicating the fault slip potential. At the Tensleep Formation (red line), ~16 MPa of excess pressure would be required to cause the fault to slip.

## 3.11 SUMMARY

A comprehensive geomechanical model for the Tensleep Fm. was generated in the context of providing the technical foundation required for RMOTC and its partners to consider and design a $CO_2$ injection project at Teapot Dome. This model allows the project team to quantitatively estimate the pore pressure at which the S1 fault would slip, and therefore supports predictions about the risk of leakage in the target storage unit.

The components of the stress tensor as well as the geometry of the fault were considered in a probabilistic sensitivity analysis, from which it was established that for even the most pessimistic scenario, 99.9% of the cases would require at least 10 MPa of excess pressure to cause the S1 fault to reactivate. This pressure would be seen at the top of a $CO_2$ column of approximately 1500 m in height. As the average closure of the Tensleep Fm. structure in this area does not exceed 100 m, the S1 fault

does not appear to be at risk of reactivation and therefore providing a leakage pathway for $CO_2$ under the present stress field.

Planned refinements to this analysis are direct measurements of $S_{hmin}$ in the Tensleep Fm. as well as in the caprock. These data will provide more reliable estimates for the maximum sustainable pressure before hydrofracturing the caprock, as well as for the maximum $CO_2$ column height that this structure could support. The possible presence of faults with smaller displacements than the one detectable by the seismic (but potentially more favorable orientations for reactivation) will have to be evaluated.

A fracture characterization was performed in three FMI logs in the area, where some of these fractures where found critically stressed, both in the Tensleep Fm. and in the caprock. The presence of these minor faults enhances formation permeability and injectivity of $CO_2$. However, the potential for slip on these faults could eventually compromise the top seal capacity of the Tensleep Fm. if these minor faults extend up into the cap rock.

Finally, a fault stability analysis was performed in the S2 fault zone to corroborate if this area is suited for a proposed controlled leakage experiment. The results indicate that these faults are critically stressed and inducing small increases in pressure could reactivate them and potentially creating leakage.

# CHAPTER 4

# 3D STOCHASTIC RESERVOIR MODEL AND FLUID FLOW SIMULATION OF THE TENSLEEP FORMATION

## 4.1 ABSTRACT

Mature oil and gas reservoirs are attractive targets for geological sequestration of $CO_2$ because of their potential storage capacities and the possible cost offsets from enhanced oil recovery (EOR).

In this work, we develop a 3D reservoir model and fluid flow simulation of the Tensleep Formation using geomechanical constraints in advance of a proposed $CO_2$-EOR and sequestration pilot at Teapot Dome Oil Field, WY. The objective of this work is to model the migration of the injected $CO_2$ as well as to obtain limits on the rates and volumes of $CO_2$ that can be injected, without compromising seal integrity.

In the present chapter, we combine our previous geomechanical analysis, geostatistical reservoir modeling, and fluid flow simulations to investigate critical questions regarding the feasibility of the $CO_2$-EOR and sequestration project in the Tensleep Fm. The analysis takes in consideration the initial trapping and sealing mechanisms of the reservoir, the consequences of past and present oil production on the system, and the potential effect of the $CO_2$ injection on the reservoir and the seal. Finally, we also assess the storage capacity of the Tensleep Fm. in this particular trap.

The EOR and sequestration project will consist in the injection of 1 million cubic feet (MMcfd) of supercritical $CO_2$ for six weeks. The results of the simulations indicate that the injected $CO_2$ will rapidly rise to the top layers, above the main producing interval, and will accumulate in the fractures (almost none will get into the matrix). A well control strategy, consisting of shutting in and re opening wells, will be necessary to improve oil recovery without circulating $CO_2$. Incremental oil production is predicted to be less than 10% and this value could go up to almost 30% if double the amount of $CO_2$ is injected in twice the amount of time.

The results suggest that the present trap could eventually hold 2 wells injecting 1 MMcfd each, during 15 years. This will sequester ~$5x10^5$ tonnes of $CO_2$ corresponding to a small power plant of ~37,800 tonnes per year.

A sensitivity analysis was conducted to estimate the response of the pilot performance to several parameters such as fracture permeability, porosity and spacing, relative permeability curves, matrix porosity and permeability, and grid size. However, in the present scheme of well control, when wells shut-in at different times in each scenario, that changes the distribution of the $CO_2$ and the conditions of the simulation. This also affects the resultant oil production and complicates the direct comparison among scenarios. Therefore, a different approach to the sensitivity analysis is also taken, where there is no limit on the amount of gas that each well can produce. This approach allows comparing the impact on the system of each of the analyzed parameters, but it does not allow comparing the amount of produced oil or sequestered $CO_2$.

## 4.2 INTRODUCTION

In previous stages of this project, the Tensleep Formation has been analytically evaluated as the target horizon for a pilot $CO_2$-EOR and carbon storage experiment in a three-way closure trap against a bounding fault, termed the S1 fault. From the comprehensive geomechanical analysis, we estimated the geomechanical constraints we use in the fluid flow simulation described in this chapter.

It was found that the S1 fault does not appear to be at risk of reactivation and it was estimated that caprock integrity is not a risk by the buoyancy pressure of the maximum $CO_2$ column height that the formation can hold. Besides, we established the presence of critically stressed minor faults and fractures in the reservoir and caprock. If these minor faults are reactivated, they could enhance the permeability of the reservoir, creating permeability anisotropy inside it.

In this chapter, we develop a stochastic 3D reservoir model of the Tensleep Formation, as input of a fluid flow simulation, using these geomechanical constraints. Our objective is to model the migration of the injected $CO_2$, as well as to obtain limits on the rates and volumes of $CO_2$ that can be injected, without compromising seal integrity.

## 4.3 3D STOCHASTIC RESERVOIR MODEL

In the lifetime of an oil field, models play a fundamental role in understanding and predicting the main geological, geophysical, and engineering reservoir components. Reservoir modeling is never a goal on its own. It takes the geological model as an input and delivers a product that will then be the input for a flow simulation. Good model building requires focus on the end goal, whether it is the estimation of the original oil in place (OOIP), the optimal placement of a well, the design of secondary recovery methods, the prediction of water breakthrough, or the optimization of a $CO_2$-EOR and Sequestration project, etc. (Caers, 2005).

The objective of 3D modeling is to provide one or several alternative numerical models intended to represent those geological, geophysical and reservoir engineering aspects of the subsurface that matter for the particular goal of the study. These numerical models are used to estimate key reservoir parameters, predict production performance, and provide uncertainty statements when needed. The uncertainty statements of these reservoir parameters are as important as providing estimates of the parameters themselves (Caers, 2005). A stochastic simulation will provide different equiprobable numerical reservoir models (different realizations) that when processed by the flow simulator will yield a distribution of reservoir forecasts. This allows the transfer of uncertainty from the geological/petrophysical model to the final forecast (Journel, 1994).

Gringarten (2005) summarized the main parts involved in stochastic 3D modeling, which consist of a series of hierarchical steps starting with the visualization and analysis of the data, followed by building the structural model, creating a velocity model to perform the time-depth conversion, and gridding the structural model. Once the reservoir is gridded, geostatistics is used to populate the grid with the petrophysical reservoir properties. A common applied technique in this step is Sequential Gaussian Simulation (SGS), which is a simple method for simulating continuous properties (porosity, permeability) requiring only knowledge of a variogram and histogram (Caers, 2005). In this simulation process, numerous equally probable realizations are created to quantify the uncertainty of the model. The final step once the grid is populated is to upscale it to the chosen flow simulation grid. In the present study, this process was carried out with a commercial software application: Earth Decision Suite 2.1.6 – Gocad.

### 4.3.1 RESERVOIR CHARACTERIZATION IN SECTION 10 (S1 FAULT AREA)

As mentioned in Chapter 2, the Tensleep Fm. consists of an intercalation of eolian-dune sandstones and inter-dune deposits. The dune sandstones are permeable and porous intervals with different levels of cementation that affects their porosity, permeability, and fracture intensity. The inter-dune deposits consist of thin sabkha carbonates, minor evaporates (mostly anhydrite), and thin but widespread extensive beds of very low-permeability dolomicrites (Zhang et al., 2005). The caprock for the Tensleep Fm. consists of two intervals of the Goose Egg Fm., the Opeche Shale member and the Minnekhata member. The depth of these intervals ranges from ~1600 to ~1750 m below the surface. Figure 4.1 shows the schematic stratigraphic column of the reservoir and caprock, following Yin (2005), that we use to construct the reservoir model.

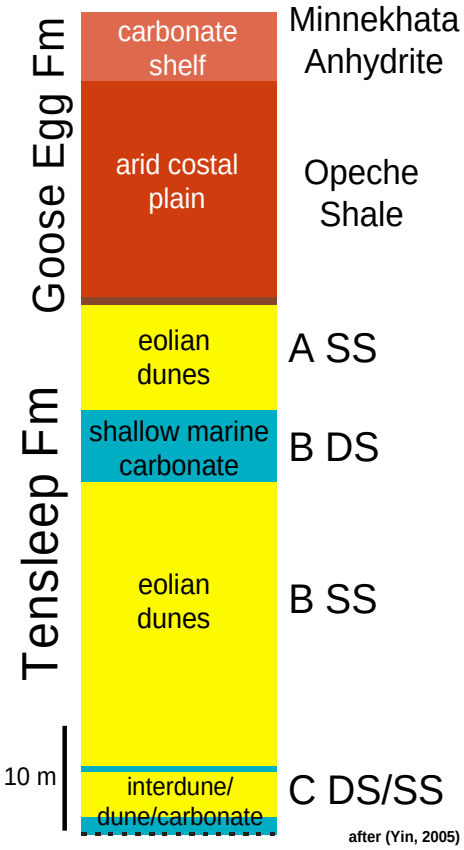


**Figure 4.1**: Schematic stratigraphic column of reservoir (Tensleep Fm.) and caprock (Goose Egg Fm.). SS = sandstone, DS = dolostone (after Yin, 2005).

The geometry of this model is based on time structure maps from the 3D seismic volume at the top of the Tensleep Fm. (A-Sandstone) and at the top of the main producing interval (B-Sandstone) interpreted by McCutcheon (2003). We converted the time-structure maps to depth using a linear velocity model obtained from the Dip-moveout (DMO) velocity analysis performed during the 3D seismic processing. This velocity model was adjusted with the corresponding well-log tops from ~36 wells along the anticline (Figure 4.2, left). We then segmented these surfaces at the intersection with the reservoir-bounding fault, S1, to construct a detailed model focusing in the Section 10 area (Figure 4.2 right).

To build the detailed model we also used well log tops of the Minekhata Member, Opeche Shale Member, A-Sandstone, B-Dolostone, B-Sandstone, C1-Dolostone, and C1-Sandstones from ~26 wells in the Section 10 area (Figure 4.2 right). Furthermore, we divided the B-Sandstone in two intervals, where the upper one is more porous and permeable than the lower one. The subdivision was based on detailed correlations of density, neutron and porosity logs of the mentioned wells in the area. The lowest and water filled C2-Sandstone interval was incorporated as an explicit aquifer layer beneath the reservoir.

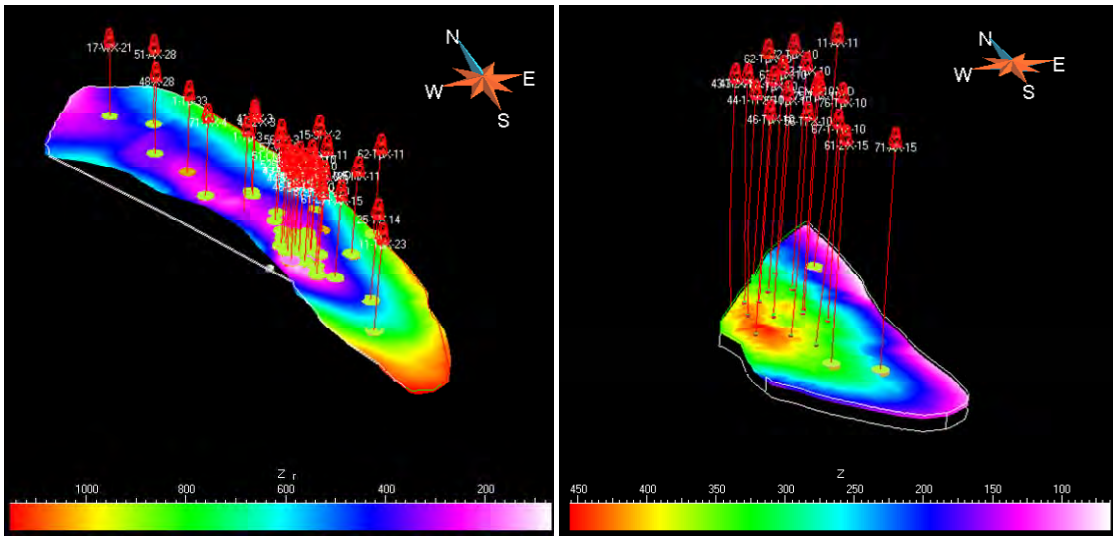


**Figure 4.2**: Depth-structure map of the Tensleep Fm. displaying the 36 wells used to adjust the time-depth conversion.

The 11 grid-layers correspond to the 9 stratigraphic units shown in Figure 4.1. The Upper and Lower B-Sandstones are represented in the gird by two layers each, allowing for more detailed characterization in the main producing intervals. In order to account for the permeability anisotropy caused by fractures, described in Chapter 3, we oriented the grid blocks in a direction approximately parallel to the $S_{Hmax}$ direction, 116° Az. This scenario would correspond to a normal faulting (NF) environment.

We built a ~1.5x3x0.15 km, 11-layer grid, where each cell is ~10 by 10 m and their heights vary from ~1 to 50 m, depending on the thickness of the corresponding horizon. This grid contains 515,361 cells (161x291x11).

After populating the original grid with porosity and permeability distributions, which will be described in the following section, we upscaled it to a coarser grid to optimize running time in the fluid flow simulator, trying to minimize loss of detail. The upscaled grid has cell dimensions of ~50 by 100 m, but maintaining their original height. This corresponds to a total of 8,976 (17x48x11) grid cells (Figure 4.3). For the upscaling process, we used a geometric mapping method and an arithmetic average algorithm for continuous properties, built in Gocad.

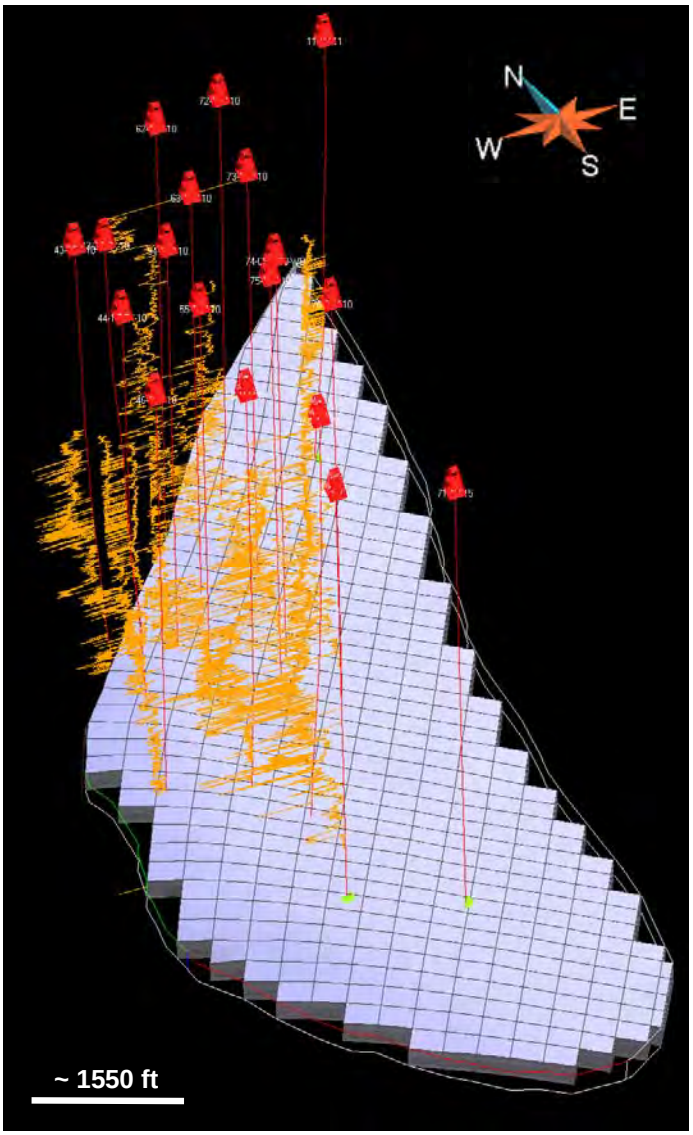


**Figure 4.3**: 3D Upscaled grid aligned parallel to $S_{Hmax}$ Az = 116°, showing wells in the area and their porosity logs.

### 4.3.2 USING GEOSTATISTICS TO POPULATE THE 3D MODEL WITH POROSITY AND PERMEABILITY DISTRIBUTIONS

One of the biggest challenges in building a 3D geological model is that hard data is limited and the few available pieces of information come from different sources at different scales and with various degrees of reliability. The major contribution of geostatistics is, therefore, data integration. It combines different types of data, taking

in consideration their uncertainty, and transferring such uncertainty to the final forecast (Journel, 1994).

In the present study, we use the sequential Gaussian simulation (SGS) method (Isaaks, 1990) to produce equally probable realizations of porosity and permeability that reflect the data variability and spatial statistics. Hard data from wells was incorporated in the interval where it existed, such as porosity data from density, neutron, and sonic logs as well as from cores from four different wells. Soft data was incorporated as well, including porosity-permeability correlations from core measurements, and porosity and permeability distribution from the reservoir lithofacies defined by Yin (2005b) for the Teapot Dome Tensleep Sandstones. Table 4.1 summarizes the values used in the base case simulations (see example in Figure 4.4).

| Poro [%] | | | | K [mD] | | | | Corr.Coeff. |
|---|---|---|---|---|---|---|---|---|
| Interval | MEAN | Min | Max | Interval | MEAN | Min | Max | K - Poro |
| MNKT | 0 | 0 | 0 | MNKT | 0 | 0 | 0 | 0 |
| OPCH | 0 | 0 | 0 | OPCH | 0 | 0 | 0 | 0 |
| ASand | 6.13 | 1.30 | 10.30 | ASand | 2.82 | 0.02 | 30.00 | 0.33 |
| Bdolo* | 3.03 | 0.20 | 8.20 | Bdolo* | 0.21 | 0.01 | 1.78 | 0.74 |
| Upper BSand | 15.38 | 7.80 | 24.00 | Upper BSand | 62.58 | 0.02 | 240.00 | 0.75 |
| Lower BSand | 5.01 | 0.70 | 12.70 | Lower BSand | 0.17 | 0.02 | 1.10 | 0.37 |
| Cdolo* | 4.35 | 0.70 | 10.10 | Cdolo* | 1.06 | 0.02 | 15.00 | 0.74 |
| C1Sand | 4.38 | 0.70 | 12.70 | C1Sand | 0.23 | 0.02 | 1.10 | 0.26 |
| C2Sand | *Idem than C1Sand* | | | C2Sand | *Idem than C1Sand* | | | *Idem than C1Sand* |

*from core values

**Table 4.1:** Porosity and Permeability values from Yin's lithofacies analysis (2005b).

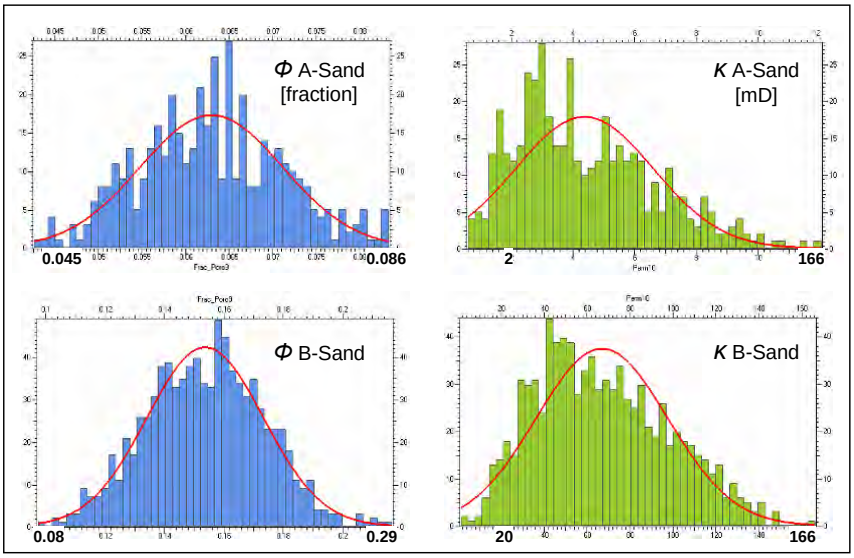


**Figure 4.4**: Example of porosity (blue) and permeability (green) geostatistical distribution for A-Sand and upper B-Sand intervals.

We also populated the grid with porosity and permeability distributions from existing cores in 8 wells in the area. Table 4.2 summarizes the values that will be used in simulations during the sensitivity analysis stage. The mentioned wells are 11-AX-11, 43-TPX-10, 44-1-TPX-10, 54-TPX-10, 55-TPX-10, 56-TPX-10, 62-TPX-10, and 71-AX-15.

| Poro [%] | | | | K [mD] | | | | Corr.Coeff. |
|---|---|---|---|---|---|---|---|---|
| Interval | MEAN | Min | Max | Interval | MEAN | Min | Max | K - Poro |
| MNKT | 0 | 0 | 0 | MNKT | 0 | 0 | 0 | 0 |
| OPCH | 0 | 0 | 0 | OPCH | 0 | 0 | 0 | 0 |
| ASand | 4.74 | 0.20 | 14.60 | ASand | 3.69 | 0.01 | 186.00 | 0.33 |
| BDolo | 3.03 | 0.20 | 8.20 | BDolo | 0.21 | 0.01 | 1.78 | 0.74 |
| Upper BSand | 10.54 | 0.56 | 28.80 | Upper BSand | 29.31 | 0.01 | 570.00 | 0.75 |
| Lower BSand | 6.95 | 3.60 | 9.95 | Lower BSand | 3.45 | 0.04 | 9.98 | 0.37 |
| CDolo | 4.35 | 0.70 | 10.10 | CDolo | 1.06 | 0.02 | 15.00 | 0.74 |
| C1Sand** | 4.38 | 0.70 | 12.70 | C1Sand | 0.23 | 0.02 | 1.10 | 0.26 |
| C2Sand | *Idem than C1Sand* | | | C2Sand | *Idem than C1Sand* | | | *Idem than C1Sand* |

**from Yin facies

**Table 4.2:** Porosity and Permeability values from core plugs from 8 wells in Section 10.

The spatial variability of the properties was incorporated into the SGS algorithm using two different types of semivariograms. One was modeled so as to consider the porosity and permeability heterogeneity due to the dune configuration, and the second one represents a more homogeneous pattern corresponding to inter-dune deposits. Milliken and Koepsell (2002), from the analysis of FMI logs in well 67-1-X-14, interpreted a paleo-wind direction ~N-S. Therefore, if we assume that dune

propagation was indeed perpendicular to the wind direction, this will correspond to porosity and permeability anisotropy in the E-W direction. For the sandstone intervals, we chose a spherical variogram with a 0.5 nugget effect, 15.71 sill and an anisotropic range of 1749 and 233 ft, with 85° Az for the principal axis. For the dolostones we chose a spherical variogram with a 0.5 nugget effect, 5.39 sill and an isotropic range of 1160.3 ft. Due to the lack of data, the choice of these variograms is highly subjective; however, it represents reasonable values of dune sizes found in the literature and the more homogeneous spatial correlation expected in the interdune deposits. In total, we created 20 porosity and permeability distributions. Figure 4.5 shows one of the permeability realizations at the B-Sandstone level (left) and at the B-Dolostone level (right).

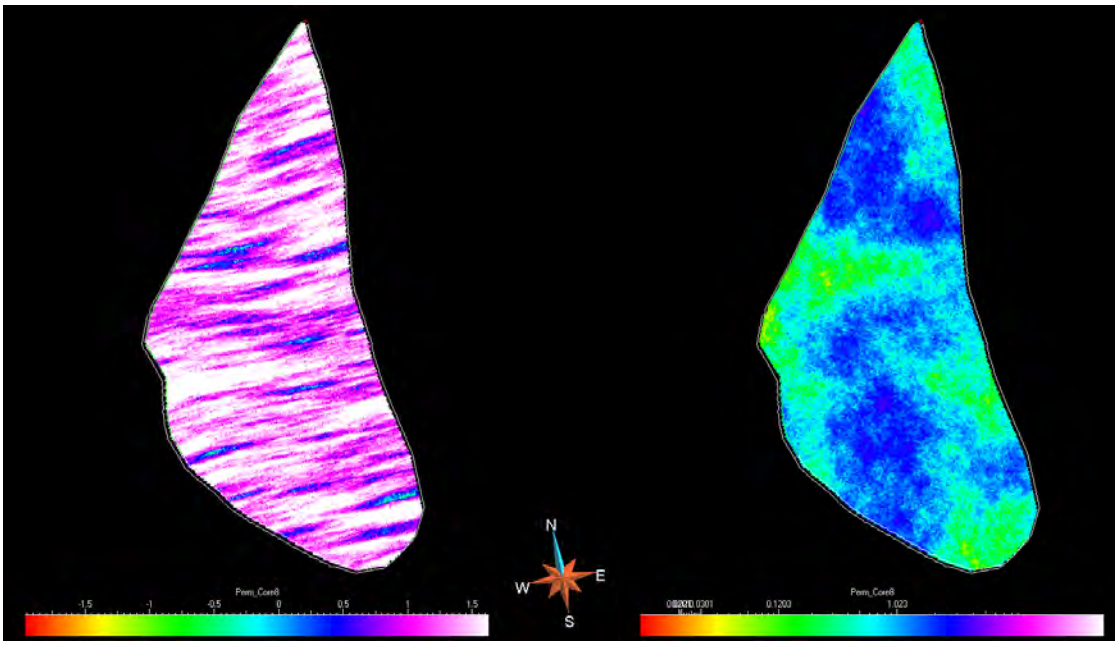


**Figure 4.5**: Map showing one of the permeability realizations at the B-Sandstone level (left) and at the B-Dolostone level (right).

As mentioned before, once we populated the grid with porosity and permeability distributions the final step was to upscale it to a coarser grid more suitable for the fluid flow simulation. Figure 4.6 shows a SSW-NNE cross-section of the upscaled 3D

reservoir model color-coded with one of the porosity realizations. Figure 4.7 displays a map of the upscaled grid showing one of the permeability realizations at the B-Sandstone level (left) and at the B-Dolostone level (right).

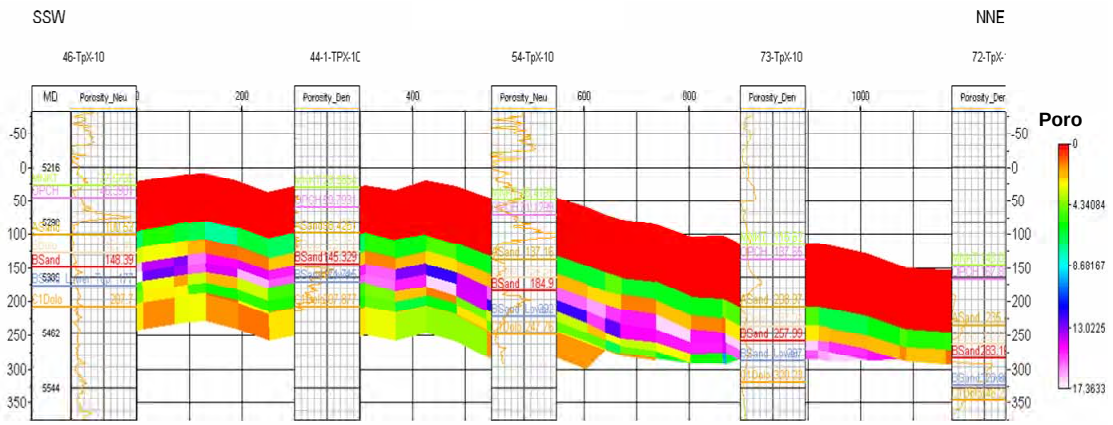


**Figure 4.6**: SSW – NNE Cross section of upscaled grid, showing one of the porosity realizations, and the porosity logs and well tops of five of the used wells.

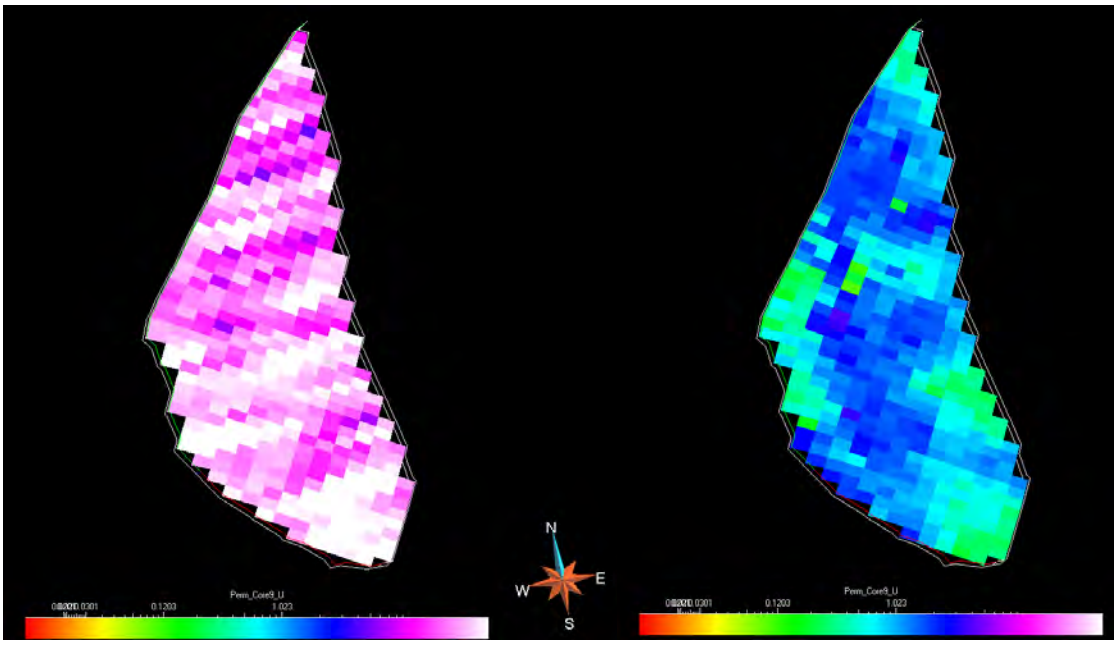


**Figure 4.7**: Map of the upscaled grid showing one of the permeability realizations at the B-Sandstone level (left) and at the B-Dolostone level (right).

Even if some detail is lost, it is still possible to notice the ~E-W permeability anisotropy in the sandstone interval (right).

## 4.4 MODELING $CO_2$-EOR PROCESSES IN A FRACTURED RESERVOIR

$CO_2$ injection has been used as a commercial process for enhanced oil recovery (EOR) since the 1970s and is the second-most applied EOR process in the world (Jarrell et al., 2002). As a result, in the oil industry there is considerable experience regarding the execution of this type of projects. Traditionally, the goal has been to recover the higher amount of oil from the reservoir injecting the minimum amount of gas, because the cost of $CO_2$ affects the profitability of the project. However, when the objective is to combine EOR and $CO_2$ sequestration, different $CO_2$ flooding designs will have to be implemented in order to increase the amount of $CO_2$ left behind when production stops (Kovscek, 2005).

The behavior of the $CO_2$ in the reservoir, although different from the oil behavior, has enough similarities to allow us to use analogous techniques to better understand, predict, and manage a $CO_2$-EOR project. The most common technique in practice in the oil industry is the use of Fluid Flow Simulation, where the concept is to apply the conservation of mass over each block of a gridded reservoir; flow rate is computed for each of these blocks by a discrete form of Darcy's Law (Aziz and Settari, 1979). It considers a set of initial boundary conditions and solves second order non-linear partial differential equations using finite difference and/or matrix algebra (Melzer, 2007).

Some of the most commonly used simulators are based on a 3 phase, 3D, fully implicit black oil models, but there is a number of other simulators available that incorporate compositional or thermal effects. For example, in $CO_2$-EOR applications the modified black-oil simulator and the fully compositional simulator are the two principal types used for predicting $CO_2$ flood performance. The first one is an approximate technique that accounts for oil displacement by $CO_2$. The fully compositional one uses an Equation-of-State (EOS) to predict the development of miscibility between $CO_2$ and oil. According to Jarrell et al. (2002), this approach is more rigorous, but it requires more computation time.

In order to accurately predict a $CO_2$ flood with this type of simulators, previous production history of the field should be simulated (and validated) to have the correct distribution of oil components at the start of the $CO_2$ flood to be simulated.

Pruess et al. (2004) studied the capabilities of several numerical simulation codes, including the GEM code of the Computer Modeling Group (CMG), and although pointing out that several improvements needed to be done, they concluded that the current simulation codes were shown capable of modeling the problems related to the $CO_2$ sequestration in geologic reservoirs.

### 4.4.1 PREVIOUS $CO_2$-EOR PROJECTS

$CO_2$ injection has been used for EOR applications since the 1970s. By 2005, 20,000 tons per day of $CO_2$ were used in oil fields for EOR projects, where approximately 10 bbl of oil were produced for every ton of $CO_2$ injected. To date, most of the $CO_2$ utilized is still not anthropogenic, although some of it might be, coming mainly from purification of natural gas (Jensen et al., 2005).

The traditional focus of these type of projects have been on reservoir with light to medium density oils (29° to 48° API) and depths from 760 to 3700 m. In the US, $CO_2$-EOR operations are mainly in the Permian and Rocky Mountain basins (Texas, New Mexico, and Colorado). (Jensen et al., 2005).

In the Rocky Mountains, in particular in Wyoming, this technology started with Amoco's Lost Soldier and Wertz $CO_2$ miscible floods in the late 1980s. They are still in operation and they had had a substantial incremental oil production. For example, in the Tensleep reservoir at Lost Soldier the EOR has been estimated in 24 million barrels of oil, which represents 9.9% of the estimated OOIP (EPRI, 1999). The total EOR at Wertz as a percentage of OOIP is approximately the same, although incremental production is less substantial. In Colorado, Chevron-Texaco started the Rangely field, $CO_2$-based EOR since the mid-1980s with an additional recovery of 10.5% of the estimated OOIP. The project is still in operation.

### 4.4.2 PREVIOUS FLUID FLOW SIMULATIONS AT TEAPOT DOME:

Wadleigh (2005) performed an in-house simple reservoir simulation for RMOTC during the first planning stages of the $CO_2$-EOR pilot in the Tensleep. This simulation was done with GEM compositional simulator, which was modeled as a dual-porosity, dual permeability system. The equation of state (EOS) was modeled after laboratory oil-$CO_2$ tests.

The grid was 14x14x5 (980 blocks) and the layers had constant porosity and permeability values. From this model, 30 to 40% increase in oil recovery was predicted (Friedmann and Stamp, 2006).

In the present study, we use the EOS from Wadleigh's work.

Gaviria (2005) compared fully compositional and pseudo-miscible black oil fluid models to test a $CO_2$-EOR and sequestration project at Teapot Dome. Based on quarter pattern simulations, he concluded that the pseudo-miscible model could not be used to represent the $CO_2$ injection process in the Tensleep, and that dual porosity models with variable fracture permeability provided a better reproduction of historic oil and water rates; although history matching in fully-compositional field-scale simulations could not be achieved.

### 4.4.3 $CO_2$ PROCESS MECHANISMS

$CO_2$ is effective for EOR operations due to its density and viscosity. At super critical conditions, its density approaches liquid density values, but its viscosity remains low.

$CO_2$ and oil are multiple-contact miscible, i.e. they require many contacts where components of the oil and $CO_2$ can transfer continuously. At the beginning, $CO_2$ condenses into the oil making it lighter. Usually, methane is driven out of it. Then, the higher components of the oil vaporize into the $CO_2$ rich phase, making it denser and more like the oil, therefore increasing its solubility in the oil. This process continues until the oil-enriched $CO_2$ cannot be distinguished from the $CO_2$-enriched oil and

there is no interface between the $CO_2$ and the oil (one hydrocarbon phase) (Jarrel et al., 2002).

Miscibility is a function of temperature and pressure, but in isothermal reservoirs, only pressure becomes important. The pressure at which miscibility occurs is called the minimum miscibility pressure (MMP).

### 4.4.4 OPTIONS FOR $CO_2$ FLOOD DESIGN

There are five basic injection processes that combine continuous, alternating, and chase fluid injection schemes (Jarrell et al, 2002) (Figure 4.8):

- Continuous $CO_2$ injection without any other injected fluid. This is generally used in gravity-drainage reservoirs ($CO_2$ injected at top of reservoir).
- Continuous $CO_2$ chased with water, it is similar to the continuous $CO_2$ flood but with chase water at the end. The immiscible water displaces the mobile and miscible $CO_2$-oil mix. This design is more effective in reservoirs that are more homogeneous.
- Conventional alternating $CO_2$ and water, chased with water: Alternating cycles of equal volumes of $CO_2$ and Water (WAG) at a constant gas/water ratio (WAG ratio). At the end, a chase of continuous water is started. This approach is used in highly stratified heterogeneous reservoirs where the goal is to reduce the amount of $CO_2$ entering the high-velocity layers.
- Tapered alternating $CO_2$ and water (sometimes chased with water): $CO_2$ and water are injected in alternating unequal cycles, where the water cycles are always increasing. The purpose of this design is to reduce the purchase cost of $CO_2$ but it can also reduce near-term revenues.
- Alternating $CO_2$ and water chased with gas: This is similar to conventional WAG, but is then chased with a less expensive gas after the total volume of $CO_2$ is injected. It can also be combined with water chase in between or at the

end of the gas chase. This option is good to avoid the use of water on water-sensitive lithologies.

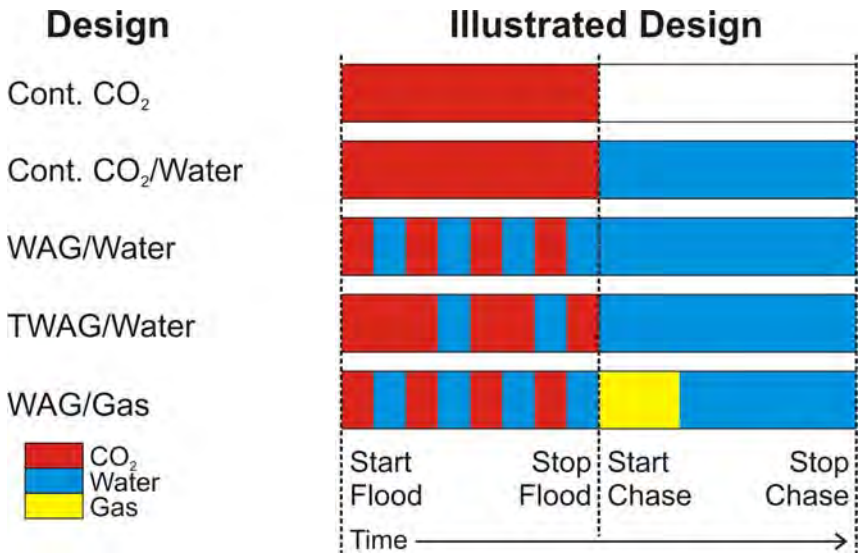


**Figure 4.8**: Illustration of typical $CO_2$ Flood designs. Cont. $CO_2$ = Continuous $CO_2$ flood; Cont. $CO_2$/Water = Continuous $CO_2$ flood chased with water; WAG/Water = Conventional alternating $CO_2$ and water chased with water; TWAG/Water = Tapered alternating $CO_2$ and water chased with water; WAG/Gas = Alternating $CO_2$ and water chased with gas (Modified from Jarrell et al, 2002).

Since the goal of our study is to co-optimize both oil recovery and $CO_2$ sequestration, all the options designed to reduce the amount of $CO_2$ to inject will not serve the objectives of this project.

With respect to the designs that use water to displace the oil-$CO_2$ mix, or that use it to control mobility of the $CO_2$, perhaps they would have been quite useful in this project. However, it has been shown that WAG schemes do not contribute to maximizing $CO_2$ storage, since some of the pore space is filled with water that otherwise could be occupied by $CO_2$ (Kovscek and Cakici, 2005). Similarly, the injection of water can have a negative effect in a thick highly permeable layer, since the injected $CO_2$ might flow to the top of the layer, while the water could gravitate to the bottom, seriously influencing mobility ratios. In addition, even if water has little effect on the phase equilibrium of $CO_2$/oil, $CO_2$ dissolution in water may prevent

some of the $CO_2$ from contacting the oil and can affect the water formation volume factor and viscosity of water, ultimately reducing the concentration of $CO_2$ that can contact the oil (Jarrell et al, 2002).

Therefore, we try the well control process approach that shuts in wells with $CO_2$ breakthroughs and re-opens them after a certain condition is given (i.e. reservoir pressure increases or gas saturations decreases). This has been suggested as the most successful strategy for co-optimization in EOR and sequestrations projects (Kovscek and Cakici, 2005).

## 4.5 FLUID FLOW SIMULATION

For our fluid flow simulations we use the Generalized Equation-of-State Model Compositional Reservoir Simulator (GEM, version 2007.15). We initially model the projected $CO_2$-EOR and sequestration pilot in the Tensleep using a continuous $CO_2$ flood pattern. The parameters of these simulations are described in the following sections.

### 4.5.1 RESERVOIR DATA

The original oil in place of the Tensleep Fm. has been estimated as 3.8 million bbls (0.6 million $m^3$) of oil and 11 MMscf (0.31 million $m^3$) of natural gas. It is a lower gravity sulfurous oil of 32 °API, of this, more than 1.8 million bbl (0.29 million $m^3$) have been produced together with more than 170 million bbl (27 million $m^3$) of water. Reservoir pressure is 16.2 MPa (2350 psi) and reservoir temperature is 88 °C (190 °F). $CO_2$ swelling tests suggested that a Tensleep Sandstone $CO_2$ flood would be miscible or near miscible. These test showed excellent response to $CO_2$, including oil swelling of more than 20%, interfacial tension reduction of 90%, and five fold viscosity reduction (Friedmann and Stamp, 2006).

Water production rates indicate the influence of a strong aquifer that has maintained almost constant reservoir pressure during the history of the field. Therefore, water drive is considered as the primary producing mechanism in the reservoir (Gaviria, 2005, Friedmann and Stamp, 2006).

| **Reservoir Property** | **Value** |
|---|---|
| Formation | Tensleep |
| Producing area | 1.8 $km^2$ (0.7 $mi^2$) |
| Average Depth | 1670 m (5500 ft) |
| Gas-oil Contact | No present |
| Water-oil Contact | ~100 m (350 ft) ss |
| Average Matrix Permeability of Main Producing Interval | ~30 mD |
| Average Matrix Porosity of Main Producing Interval | ~10% |
| Oil Gravity | 31 °API |
| Reservoir Temperature | 88 °C (190 °F) |
| Primary Production Mechanism | Water Drive |
| Original Reservoir Pressure | ~16 MPa (2300 psi) |
| Bubble Point Pressure | 0.3 - 0.5 MPa (40 - 70 psi) |
| Average Pressure at start of $CO_2$ injection | ~16 MPa (2300 psi) |
| Solution GOR at original pressure | 4 SCF/BBL |
| Oil Viscosity at 60 °F and 42 psi | 3.5 cp |
| Minimum Miscibility Pressure (MMP) | 9 MPa (1300 psi) |

**Table 4.3**: Basic reservoir and fluid data (modified from Gaviria, 2005).

Teapot Dome field had its first production well from First Wall Creek sandstone interval in 1908, but the development and exploration program at Teapot Dome started only on 1976. In 1996, a high number of wells were drilled, 27 of them targeted the Tensleep Fm. (Gaviria, 2005). Figure 4.9 shows the historical oil and water production from the Tensleep.

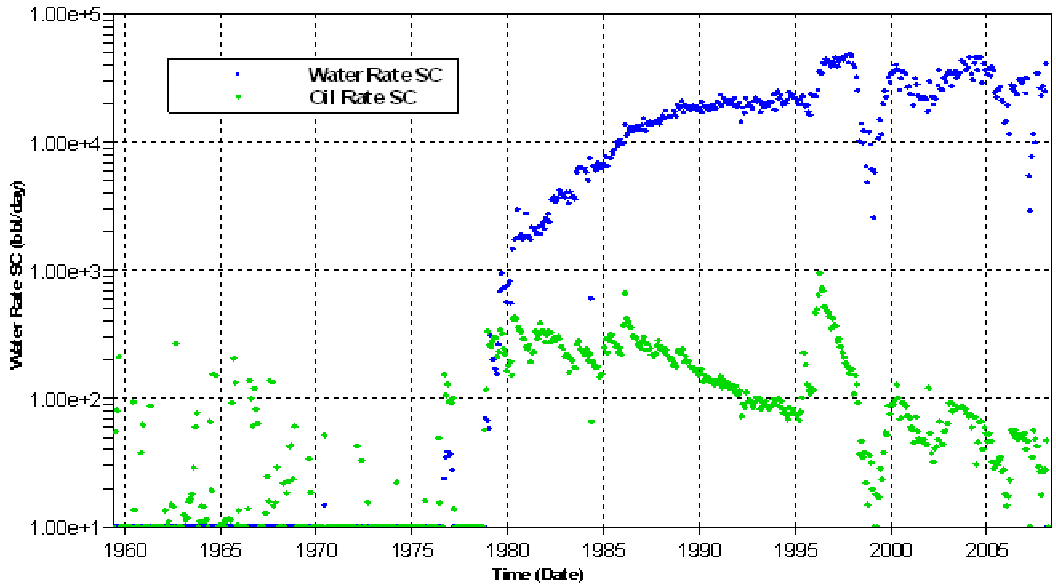


**Figure 4.9**: Historic oil and water production from Tensleep Fm. at Teapot Dome, from 1959 – 2008.

## 4.5.2 SIMULATION SET UP

### *4.5.2.1 MODEL*

The chosen model to run in the simulator is the upscaled model from the program Gocad (see Figure 4.7). It has 8,976 blocks where 3,679 of them are active. Since the caprock is considered impermeable in these simulations, they are set up as Null.

### *4.5.2.2 MATRIX POROSITY AND PERMEABILITY*

The matrix porosity and permeability distributions for the initial fluid flow simulations are one of the geostatistical realizations from Yin's (2005) facies analysis. In the sensitivity analysis of the final results we consider the variation that takes place due to different geostatistical realizations as well as from using porosity and permeability values measured in core samples in some of Section 10 wells.

#### *4.5.2.3 FRACTURE POROSITY AND PERMEABILITY*

We have very little control on fracture porosity and permeability, since no measurements have been done to get some insight in that respect. We use fracture porosity values from Wadleigh (2005) and tried different fracture permeability values during the history matching process. The final chosen values for the base case scenario (Table 4.21) are approximately one order of magnitude greater than the matrix permeability, which is a reasonable assumption for sedimentary rocks.

#### *4.5.2.4 FRACTURE SPACING*

We assign fracture spacing values (Table 4.21) based on the fracture characterization performed by Lorenz and Cooper (2004) in a core sample of well 48-X-28. They found and average of one fracture every feet of core. They defined fracture intensity as cumulative fracture height over core length. The average fracture intensity they found for all cored facies was 20 ft of fracture height per 100 ft of core, which is equivalent to the average fracture count. Therefore, we translated their fracture intensity values to determine the fracture spacing in each of the layers. We used the following values: for high porosity sandstones (such as BSand) 1 fracture every 10 ft.; in dolomitic sandstones (such as A or CSand), 1 fractures every 3 ft; and in heavily cemented intervals (such as the interdune deposits), 1 fracture per ft.

#### *4.5.2.5 MATRIX RELATIVE PERMEABILITY*

We use relative permeability curves determined by Gavira (2005), which were obtained from laboratory tests performed in four Tensleep samples. One sample from well 62-TPX-10 (sample A at 5443') and three samples from well 43-TPX-10 (sample B at 5486', sample C at 5492' and sample D at 5500'). The tests were performed using simulated reservoir brine and mineral oil with a viscosity of 30 cP. All samples showed similar composition, hard rock with fine to very fine grains;

however, relative permeability experiments showed important differences in the endpoints. Initial water saturations (Swi) were between 12.5% to 22.1% and residual oil saturations (Sro) were between 28.7% and 56.3% (Figure 4.10). The maximum oil relative permeability is 0.65 at connate water saturation (Swc = 15%). At 60% water saturation, the oil relative permeability is almost zero. As water saturation increases in the reservoir, the water relative permeability also increases, reaching a maximum value of 0.04 at 94% water saturation.

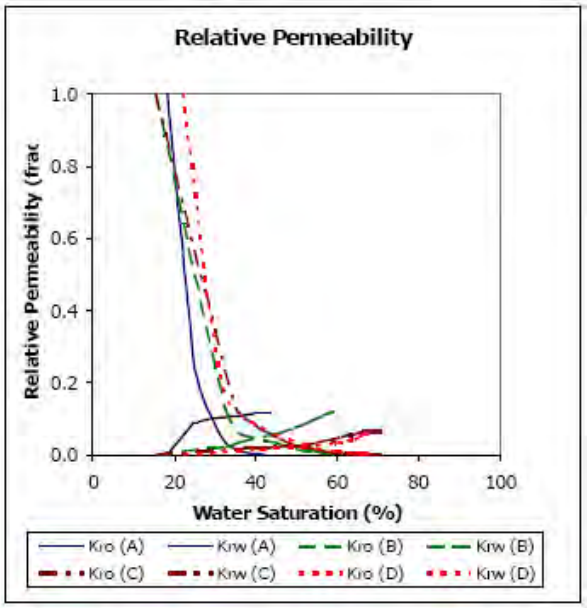


**Figure 4.10**: Water-oil relative permeability curves as a function of water saturation measured in four Tensleep samples (Gaviria, 2005).

During the process of history matching, we tried with different matrix relative permeability curves and the one estimated from sample A had the better performance. Figure 4.11 shows the relative permeability curves issued in our simulations. Hysteresis effect is not considered since this is a water-wet system (Jarrell et al., 2002).

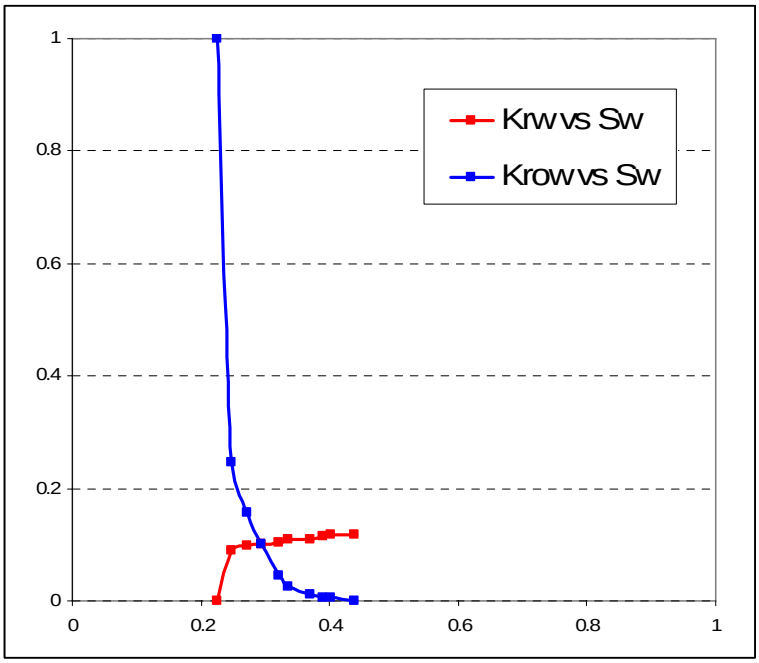


**Figure 4.11a**: Water-oil relative permeability curves, from Sample A, used in the base case scenario as a function of water saturation.

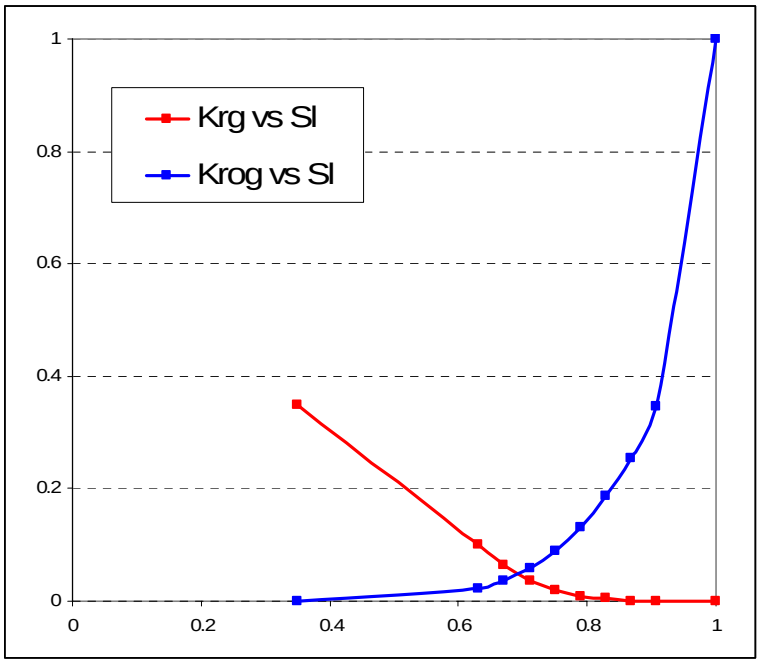


**Figure 4.11b**: Gas-oil relative permeability curves, from Sample A, used in the base case scenario as a function of water saturation.

GEM allows the use of Stone's first and second models, as modified by Aziz and Settari (1979), to obtain three phase relative permeability functions from two phase data (GEM 2007.11, Aziz and Settari, 1979). In our simulations, we used Stone's first model.

#### *4.5.2.6 FRACTURE RELATIVE PERMEABILITY*

It is normally assumed that fracture relative permeability curves are straight lines; although these might not be the best representations since fracture aperture changes due to compaction, mineralization, and other factors that affect fluid flow. Similarly, roughness, capillary pressure, and wettability influence fluid flow interference. If very high fracture permeability values are considered, then straight line relative permeability curves might be reasonable assumptions.

Since no data was available for fracture relative permeability curves, during the history matching process we tried several arbitrary curves, close to straight lines configuration. However, it was difficult to match the total produced water without having to use extreme values of fracture permeabilities. Since this is an unconstrained problem, where the only data available for history matching is historic productions of water and oil, we decided to use the same relative permeability curve for both matrix and fracture during the history matching stage. Later, we tested the sensitivity on the results to different fracture permeability curves during the prediction stage.

#### *4.5.2.7 $CO_2$ RELATIVE PERMEABILITY*

In the case of an immiscible flood (reservoir pressure < MMP) $CO_2$ will remain in a gas phase which is non-wetting compared to the oil and water. Therefore, usual three phase relative permeability models will apply to the oil, water, and gas relative permeabilities (Jerrell et al., 2002).

In the case of a miscible flood above the MMP the $CO_2$-rich phase is a solvent that has similar properties to the oil and initially follows the oil relative permeability curve. Here the solvent would be the intermediate wetting phase if the reservoir is oil-wet, and the solvent relative permeability will be affected by the reduction in pore space occupied by oil and water. Or eventually, if the solvent is less wet than water, water blocking could happen (Jerrell et al., 2002).

Since $CO_2$ is a multiple contact solvent, when injected, it leaves behind a small residual oil saturation that interferes with subsequent flows of solvent and causes the solvent ($CO_2$-rich phase) relative permeability to be lower than the oil relative permeability (Chopra et al., 1999, Jarrell et al, 2002). This effect was described for oil-wet or mixed-wet reservoirs.

In the case of a strong water-wet reservoir, oil is the intermediate wetting phase and the $CO_2$-rich phase is the non-wetting phase. Here the solvent relative permeability will be reduced by residual oil.

However, measurements of steady-state relative permeability for solvent, oil, and water for a water-wet dolomite showed that the solvent relative permeability was almost the same as the oil (Dria, et al, 1993, Jerrell et al., 2002).

In a case as the present one, a water-wet reservoir where no measurements of solvent relative permeability are available, we assume that $CO_2$ relative permeability is equal to oil relative permeability, as recommended by Jerrell et al. (2002).

#### *4.5.2.8 CAPILLARY PRESSURE*

The capillary pressure (Figure 4.12) we used in our simulation is an average curve obtained from three Tensleep samples (Gavira, 2005). Two of them were extracted from well 56-TPX-10 (samples E at 5391' and F at 5400') and one from well 44-1-TPX-10 (sample G at 5538'). Capillary pressure curves in these three samples show low displacement pressure (approximately 1 psi), which suggests a good reservoir with very good sorting and big pore throats (Gaviria, 2005).

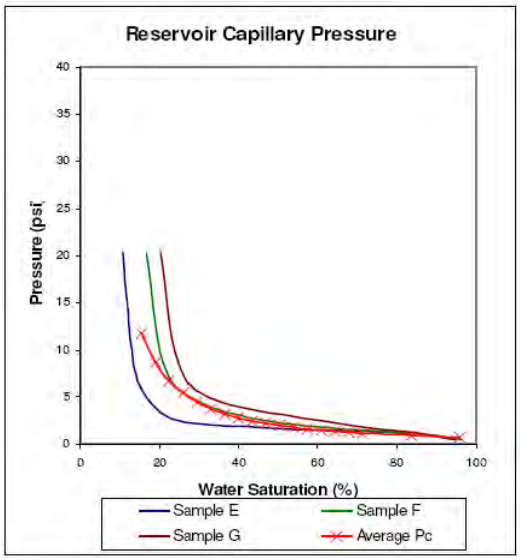


**Figure 4.12**: Laboratory and average capillary pressure curves from Gaviria (2005). The average curve (red line) is the one used in our simulations.

#### *4.5.2.9 WETTABILITY*

The wettability was determined by testing a core sample from well 62-TPX-10 (5418') at reservoir temperature (190 °F or 88 °C). Synthetic brine and crude oil were flushed through the sample. The analysis of the test results yielded a water-wet indicator of 0.402 versus oil-wet indicator of 0.033 (Gaviria, 2005). The water-wet indicator is a relationship between volume of oil displaced spontaneously when the oil saturated rock sample is submerged in synthetic brine, and the total oil volume displaced by injecting brine in the sample up to residual oil saturation conditions.

#### *4.5.2.10 EQUATION OF STATE*

Tensleep Formation oil samples were gathered from well 72-TPX-10 and analyzed by Hycal Energy Research Laboratories in 2004. The solvent impact of $CO_2$ was measured in the laboratory (Figure 4.13). The results indicate that the oil swells up to 30% as $CO_2$ contacts dissolves into oil and that the oil viscosity reduces to approximately one-third of its unprocessed reservoir condition, which is very supportive of an EOR application. They describe that the Tensleep oil is very low in

light hydrocarbon components (methane and ethane), which could dilute injected $CO_2$ and detract from the solvent impact of a $CO_2$ project. Therefore, most $CO_2$ added to the reservoir is estimated to be dissolved into the oil phase for oil recovery improvement (Hycal, 2004).

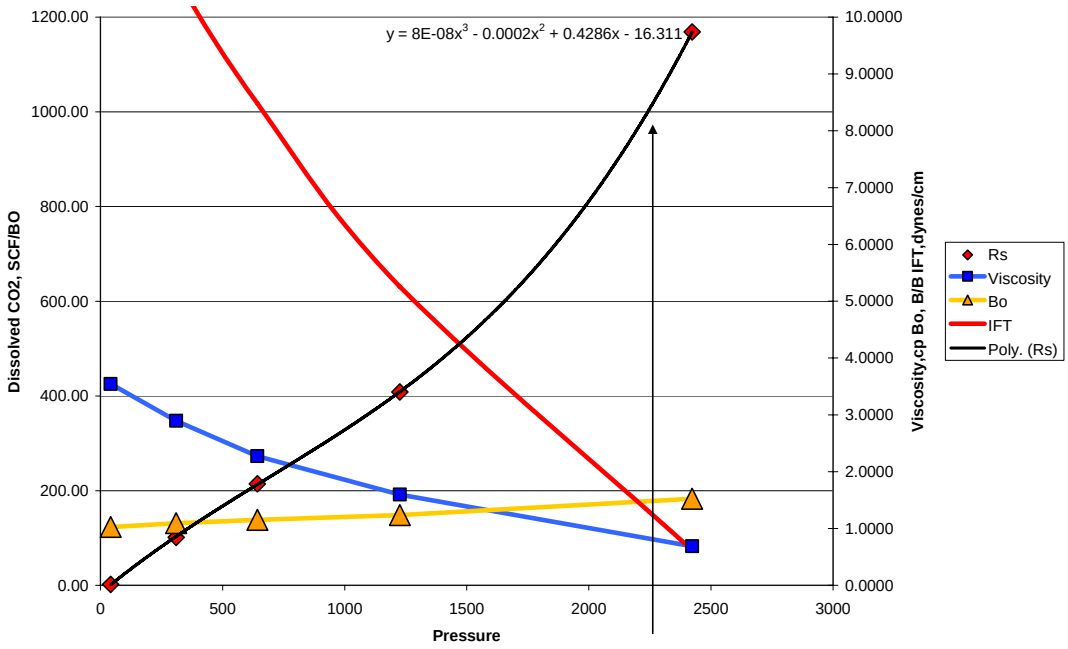


**Figure 4.13**: This plot shows laboratory measured increase in oil volume and reduced viscosity as the $CO_2$ in solution increased beyond the 1000 SCF/BO saturated condition at a reservoir pressure of 2336 psi (190 °F). Estimated IFT values are also plotted to illustrate the near-miscible condition that develops (Hycal, 2004).

Due to the low light-hydrocarbon composition, it was recommended to use a 6-component EOS described in Table 4.4 (Wadleigh, 2005).

| Component | Mw (g/gmole) | Pc (atm) | Tc (°k) | Omega A | Omega B | Accentric Factor |
|---|---|---|---|---|---|---|
| **C1 to N2** | 26.41700 | 35.146050 | 134.37819 | 0.457236 | 0.0777961 | 0.035733 |
| **CO2** | 44.01000 | 52.732012 | 304.20000 | 0.457236 | 0.0777961 | 0.225000 |
| **C2 to IC5** | 58.66350 | 31.282130 | 348.47099 | 0.457236 | 0.0777961 | 0.167679 |
| **C6 to C10** | 114.13127 | 27.586230 | 488.61317 | 0.457236 | 0.0777961 | 0.266720 |
| **C11 to C14** | 168.41008 | 27.276990 | 780.50523 | 0.457236 | 0.0777961 | 0.783660 |
| **C15 to C22** | 400.95423 | 12.589630 | 1018.30460 | 0.457236 | 0.0777961 | 1.012090 |

**Table 4.4**: Six-component EOS definition (Wadleigh, 2005).

#### *4.5.2.11 AQUIFER*

Initially, we used an analytical aquifer to represent the strong water influx in the reservoir. No information is available on the extension and strength of the real aquifer since pressure data have not been collected from the reservoir. Therefore, we used the Carter-Tracy aquifer model (Dake, 1978) connected at the bottom of the simulation grid with the following arbitrary parameters: 3000 ft thickness, 15% porosity, 500 mD permeability, and 30000 ft radius size. However, with only this analytical aquifer, it was extremely hard to match the total produced water during the history of the field.

Since most of the water flows through the fractures, it was necessary to add a fractured aquifer, C2Sand, at the bottom of the simulation grid (K. Aziz, personal communication, 2008). The fracture permeability of the C2Sand in the base case scenario is set to 4000 mD.

### 4.5.3 INITIAL CONDITIONS

We ran the simulations in a dual porosity (dual permeability) mode.

The initial conditions were set to: reservoir pressure of 2370 psi at a reference depth of 200 ft sub-sea; reservoir temperature of 190 °F; oil-water contact at 350 ft sub-sea. The initial water saturation from the relative permeability curve was 0.225 and the initial oil saturation within the grid blocks was 0.775.

### 4.5.4 HISTORY MATCHING

History matching (HM) was performed using historical oil production rates as a constraint and comparing the simulation results to match historical water rates. The few available pressure data in this area consists of pre-production DST from wells 54-TpX-10, 56-TpX-10, and 44-1-TpX-10. Due to the very limited constrain in the system, we did a HM on the production and water rates at a field scale. Therefore, sensitivity analysis of the simulation results will be essential.

#### *4.5.4.1 SENSITIVITY ANALYSIS TO HM PARAMETERS:*

During the trial and error process of history matching we tried different parameters such as grid size, fracture permeability (*k*F), fracture porosity (øF), fracture spacing (spF), initial oil saturation ($S_{io}$), capillary pressure ($P_c$) and relative permeability curves ($k_{rel}$). Below we present a series of sensitivity analysis that we conducted for these parameters along the process of HM. Each parameter is compared to one of three Scenarios, which were the best cases at the time of performing the sensitivity analysis. All these three scenarios were run with matrix porosity and matrix permeability from Yin's facies analysis (see section 4.3.2); relative permeability curves from Sample A (Figure 4.11); $S_w$ = 0.225; oil-water contact = 350 ft sub-sea and the parameters shown in Table 4.5.

| Scenario I | | | | | | | | |
|---|---|---|---|---|---|---|---|---|
| | Fracture *k* [mD] | | | øFrac [frac] | spFrac [ft] | Grid Size [ft] | Wells BHP [psi] | No. Layers |
| | I | J | K | | | | | |
| **All Grid** | 500 | 100 | 500 | | | | 28 | 11 |
| **MNKT** | - | - | - | - | - | 300x200x21 | | 1 |
| **OPCH** | - | - | - | - | - | 300x200x63 | | 1 |
| **ASand** | 100 | 50 | 100 | 0.5 | 3 | 300x200x27 | | 1 |
| **BDolo** | | | | 0.1 | 5 | 300x200x20 | | 1 |
| **BSand_U** | | | | 1 | 10 | 300x200x20 | | 2 |
| **BSand_L** | | | | 0.5 | 3 | 300x200x16 | | 2 |
| **C1Dolo** | | | | 0.1 | 5 | 300x200x2 | | 1 |
| **C!Sand** | | | | 0.5 | 2 | 300x200x45 | | 1 |
| **C2Sand** | 1000 | 500 | 1000 | 1 | 2 | 300x200x168 | | 1 |

| Scenario II |
|---|
| All parameters are the same as in **Scenario I** except for BHP<br>All Wells BHP [psi] = 500 |

| Scenario III |
|---|
| All parameters are the same as in **Scenario II** but incorporating $P_c$ |

**Table 4.5**: Parameters of the three case scenarios used in the history matching sensitivity analysis.

Three tables are presented below with the parameters subjected to sensitivity analysis as well as the percentage comparison of total cumulative water produced with respect to the corresponding scenario.

GRID SIZE

Three cases were tested to see the effect of grid size. The first one divided each original cell size in 3 in the horizontal plane (I and J directions), therefore creating 9 new grid cells while conserving their thickness. Not a significant variation in total amount of water produced was observed there with respect to Scenario I. The other

two cases explore the effect of dividing the vertical layers in 2 and 3, and here the impact was significantly more important.

| Analyzed Parameter | Description | CW % difference to BC | Running time [hrs] |
|---|---|---|---|
| Grid size | Original grid size split in 3 (I & J directions) | 92.99 | 10.78 |
| | Original layers split in 2 (K direction) | 42.64 | 2.76 |
| | Original layers split in 3 (K direction) | 26.86 | 5.26 |

**Table 4.6**: Sensitivity analysis on some HM parameters compared against Scenario I (see Table 4.5). Running time of Scenario I is 1.35 hours.

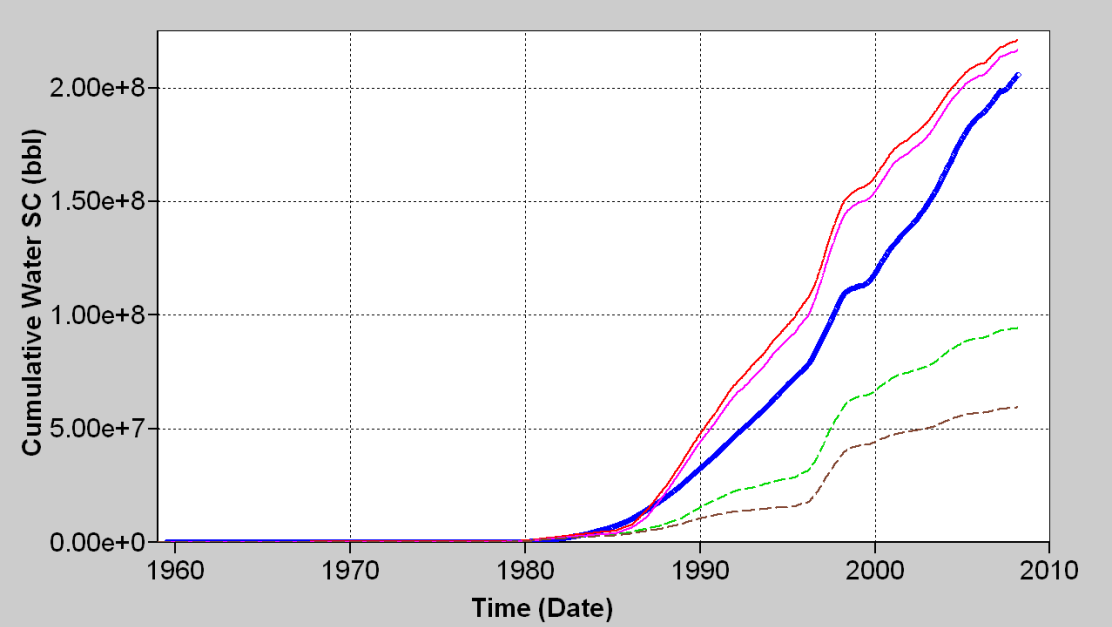


**Figure 4.14**: History matching sensitivity to grid size. Curves show cumulative water production [bbl] of Scenario I (red), horizontal refinement case (magenta), vertical refinement by 2 case (green), vertical refinement by 3 case (brown) and field data (blue).

The simulations done using the parameters shown in Table 4.7 are compared to the simulation of Scenario II (Table 4.5):

| Analyzed Parameter | Description | CW % difference to BC | Running time [hrs] |
|---|---|---|---|
| Fracture Permeability (*k*F) | Double *k*F | 120.17 | 1.58 |
| | Half *k*F | 65.16 | 1.25 |
| Fracture Porosity (øF) | Double øF | 62.23 | 1.04 |
| | Half øF | 114.55 | 1.91 |
| Fracture Spacing (spF) | Double spF | 99.62 | 1.31 |
| | Half spF | 98.98 | 1.33 |
| Initial Water Saturation ($S_w$) | $S_{io}$ 0.22 | 86.54 | 1.34 |
| | $S_{io}$ 0.23 | 111.35 | 1.45 |
| Capillary Pressure ($P_c$) | including $P_c$ | 58.26 | 2.80 |

**Table 4.7**: Sensitivity analysis on some HM parameters compared against Scenario II (see Table 4.5). Running time of Base Case II is 1.08 hours.

### FRACTURE PERMEABILITY & POROSITY

Fracture permeability and porosity are some of the parameters with greater impact in the model, since we are using a dual porosity-permeability simulator. Fracture permeability values can be obtained from the analysis of pressure build-up tests, where the permeabilities are adjusted to match production rates and bottom-hole pressures in the tested wells (Gaviria, 2005). Nevertheless, as mentioned before, there is no available pressure data in the Tensleep, therefore these are some of the most unconstrained parameters that we have to deal with and sensitivity analysis of the final results will be essential.

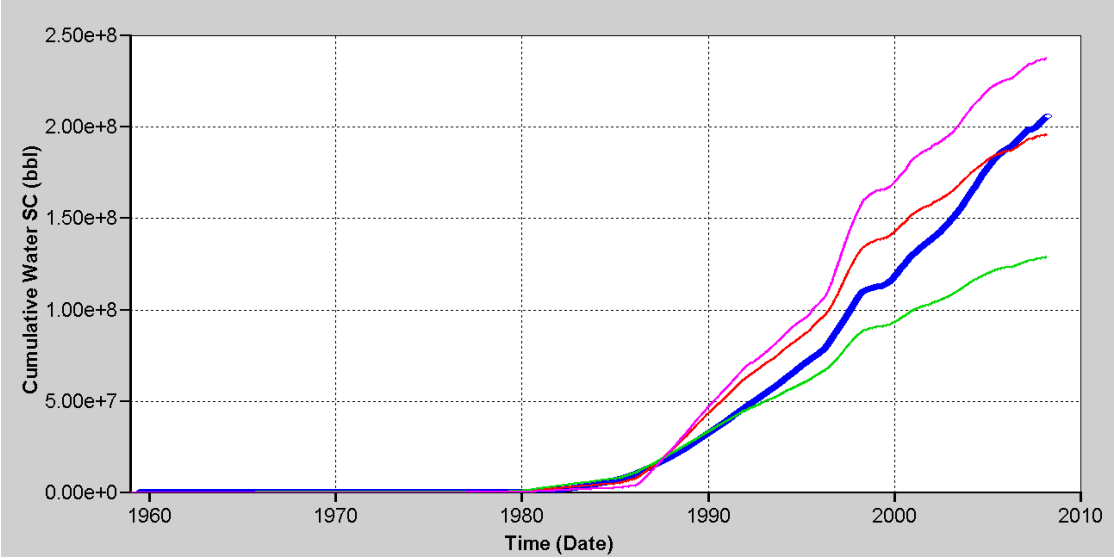


**Figure 4.15**: History matching sensitivity to Fracture Permeability. Curves showing cumulative water production [bbl] of Scenario II (red), double-*k*F case (magenta), half- *k*F case (green) and field data (blue).

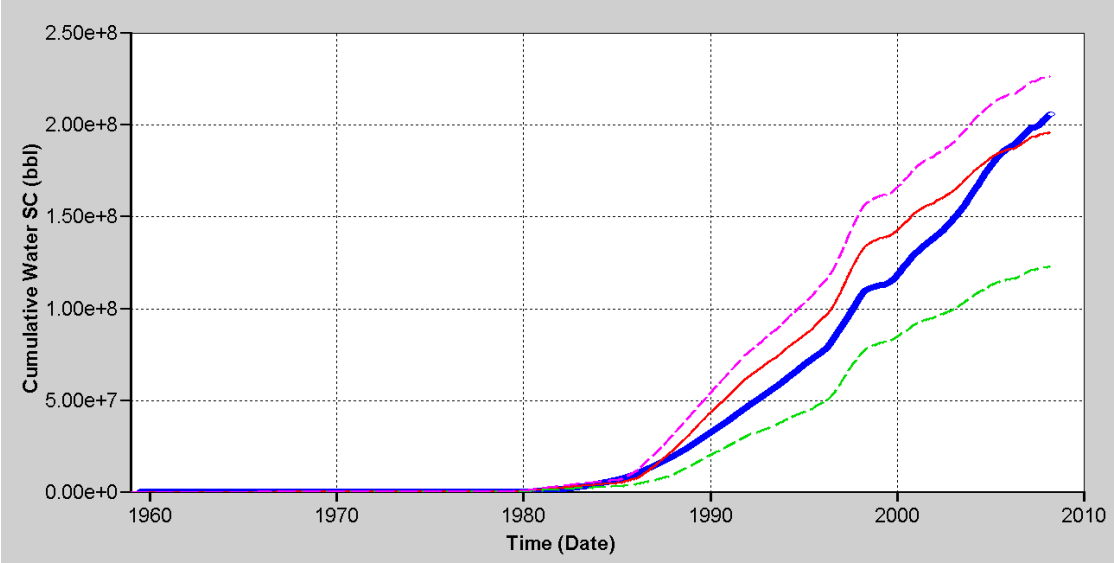


**Figure 4.16**: History matching sensitivity to Fracture Porosity. Curves showing cumulative water production [bbl] of Scenario II (red), double-øF case (magenta), half- øF case (green) and field data (blue).

### FRACTURE SPACING

Fracture spacing is one of the parameters with less impact in the model.

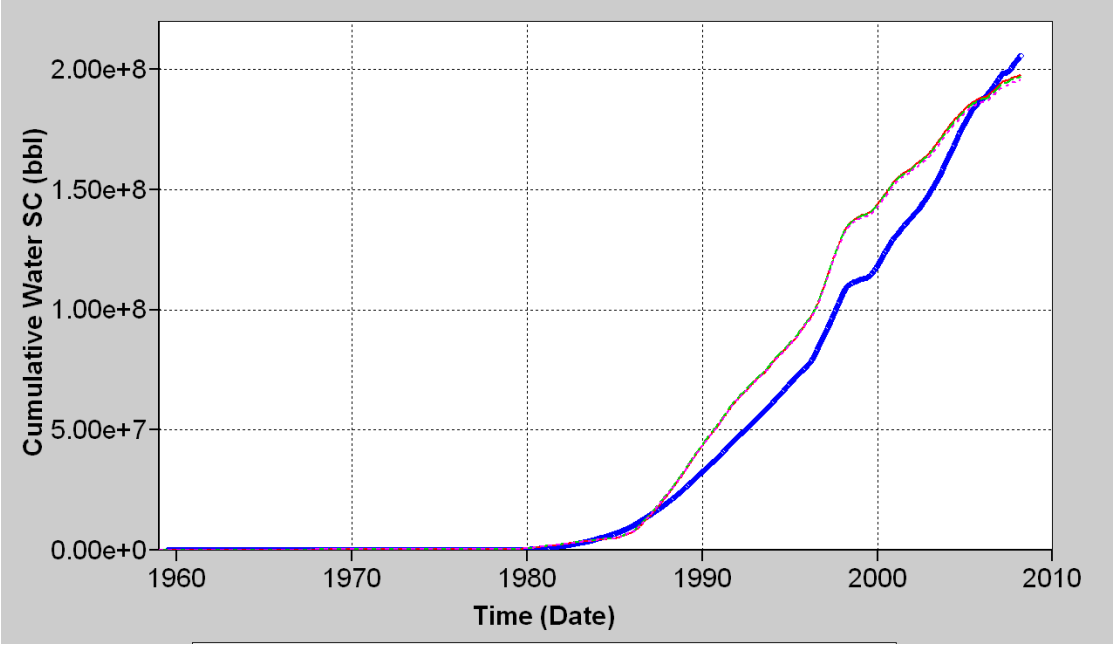


**Figure 4.17**: History matching sensitivity to Fracture Spacing. Curves showing cumulative water production [bbl] of Scenario II (red), double-spF case (green), half-spF case (magenta) and field data (blue).

### INITIAL FLUID SATURATION

A fluid saturation of 0.225 initially over predicts water production and is also not in agreement with tests performed in five samples of the Tensleep, where water saturations were found in between 0.125 and 0.221.

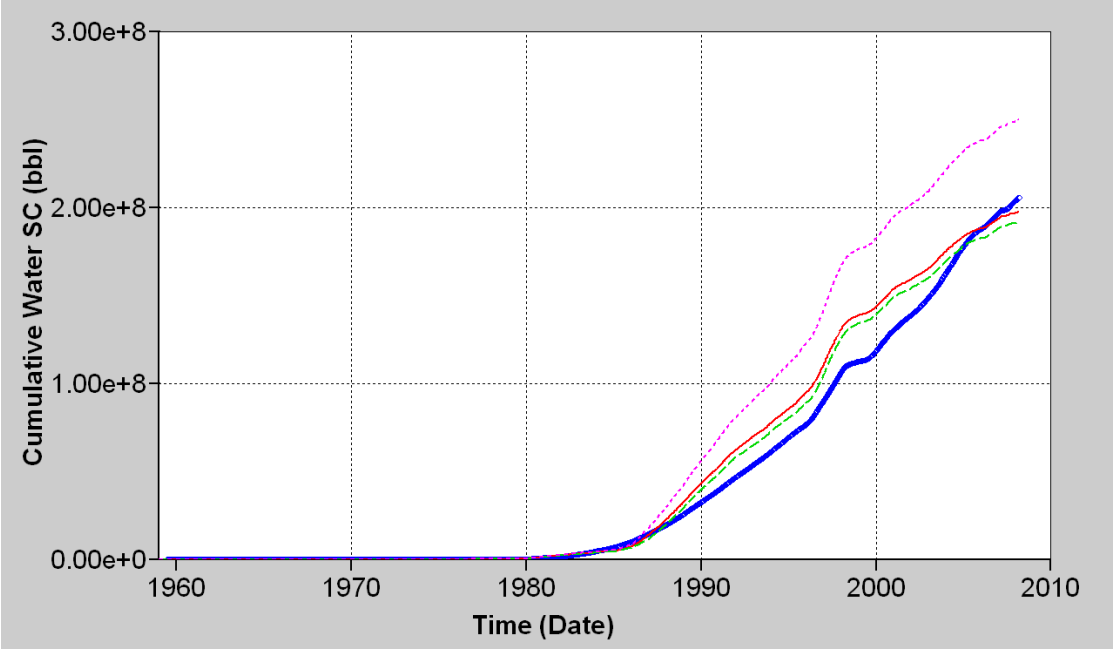


**Figure 4.18**: History matching sensitivity to Initial Water Saturation. Curves showing cumulative water production [bbl] of Scenario II where $S_w$ = 0.225 case (red), $S_w$ = 0.23 case (magenta), $S_w$ = 0.22 case (green) and field data (blue)

### CAPILLARY PRESSURE

Capillary pressure is an important parameter for low permeability, fractured sandstones, as most of the Tensleep Fm. (A. Kovscek, personal communication, 2008). Therefore, we performed a new history matching after incorporating $P_c$ leading to Scenario III (see Table 4.5).

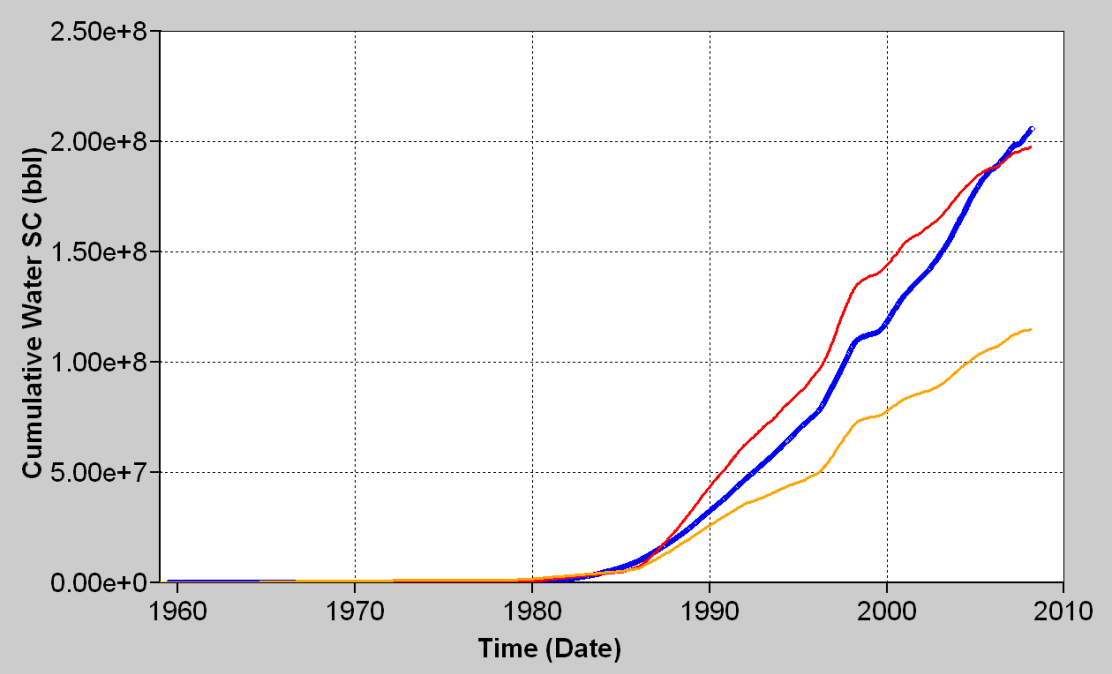


**Figure 4.19**: History matching sensitivity to $P_c$. Cumulative produced water in Scenario II (red); case including $P_c$ (orange) and field data (blue).

### RELATIVE PERMEABILITY CURVES

These simulations compare the impact of a different relative permeability curve instead of the one we used in the other two scenarios (Sample A). The new $K_{rel}$ curve (Ave. $K_{rel}$) is the average of the relative permeability curves of 4 Tensleep samples, including Sample A (Gaviria, 2005). We also tested, the impact of a different initial water saturations $S_w$ = 0.15, instead of $S_w$ = 0.225 as in all other cases. These simulations were done after incorporating $P_c$ so they are compared with Scenario III (see Table 4.5).

| Analyzed Parameter | Description | CW % difference to BC | Running time [hrs] |
|---|---|---|---|
| $K_{rel}$ Curves | Ave. $K_{rel}$ & $S_w$ = 0.15 | 3.69 | 2.34 |
| | Ave. $K_{rel}$ & $S_w$ = 0.225 | 4.25 | 2.35 |

**Table 4.8**: Sensitivity analysis of relative permeability curves ($K_{rel}$) compared with Scenario III (see Table 4.5). Running time of Base Case III is 3.01 hours.

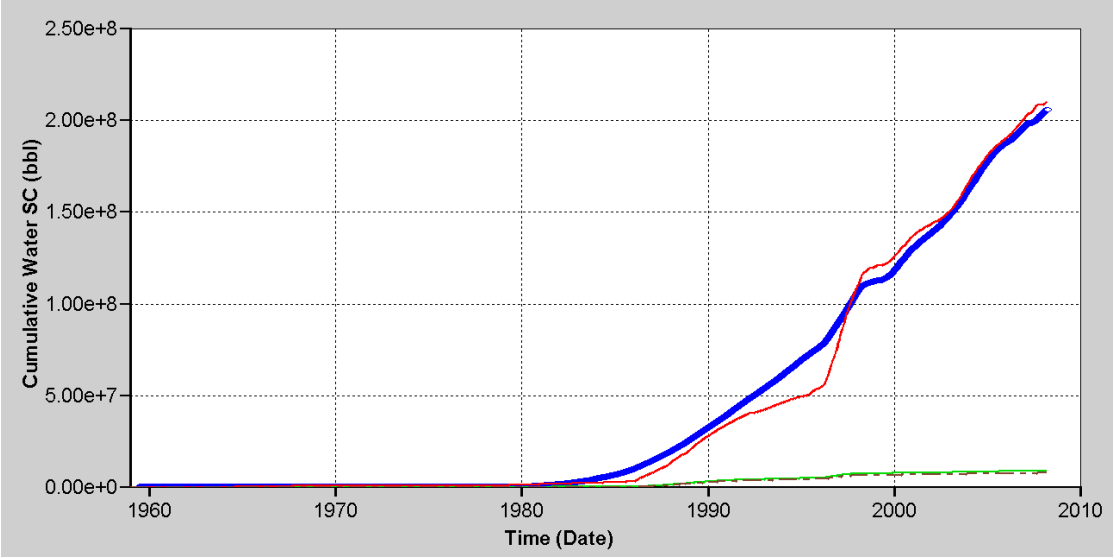


**Figure 4.20**: History matching sensitivity to relative permeability curves. Scenario III with $K_{rel}$ from Sample A (red), case with $K_{rel}$ from Gaviria, (2005) and $S_w$ = 0.225 (green), case with $K_{rel}$ from Gaviria, (2005) and $S_w$ = 0.15 (brown) and field data (blue).

### 4.5.5 BASE CASE SCENARIO:

After the HM process, the parameters for the base case scenario (BC) where chosen. The BC was run with matrix porosity and matrix permeability from Yin's facies analysis (see section 4.3.2); relative permeability curves from Sample A (Figure 4.11); $S_w$ = 0.225 (even if initially over predicts water production); oil-water contact = 350 ft sub-sea and the parameters shown in Table 4.9.

| | *k*Frac I [mD] | *k*Frac J [mD] | *k*Frac K [mD] | øFrac | spFrac - [ft] | Grid Size [ft] | No. of Layers |
|---|---|---|---|---|---|---|---|
| All Grid | 800 | 400 | 800 | | | | 11 |
| MNKT | - | - | - | - | - | 300x200x21 | 1 |
| OPCH | - | - | - | - | - | 300x200x63 | 1 |
| ASand | 200 | 100 | 200 | 0.5 | 3 | 300x200x27 | 1 |
| BDolo | | | | 0.1 | 5 | 300x200x20 | 1 |
| BSand_U | | | | 1 | 10 | 300x200x20 | 2 |
| BSand_L | | | | 0.5 | 3 | 300x200x16 | 2 |
| C1Dolo | | | | 0.1 | 5 | 300x200x2 | 1 |
| C!Sand | | | | 0.5 | 2 | 300x200x45 | 1 |
| C2Sand | 4000 | 4000 | 4000 | 1 | 2 | 300x200x168 | 1 |

**Table 4.9**: Properties of the Base Case Scenario: Fracture permeability (*k*F) in I, J and K direction, Fracture Porosity (øF), Fracture spacing (*sp*F), grid size of each layer and No. of layers per stratigraphic unit. *sp*F is the same in the I and J direction while it is 0 in the K direction is since there are no horizontal fractures in the model.

The simulation with the base case scenario produces a total of $1.96 \times 10^8$ bbl of water at surface conditions, which is 99.23% of the total cumulative water produced in the field. Figure 4.21 shows the comparison between the base case scenario and the field data, both for water rate (left) and water cut (right) at surface conditions. In Figure 4.22 cumulative water production is plotted.

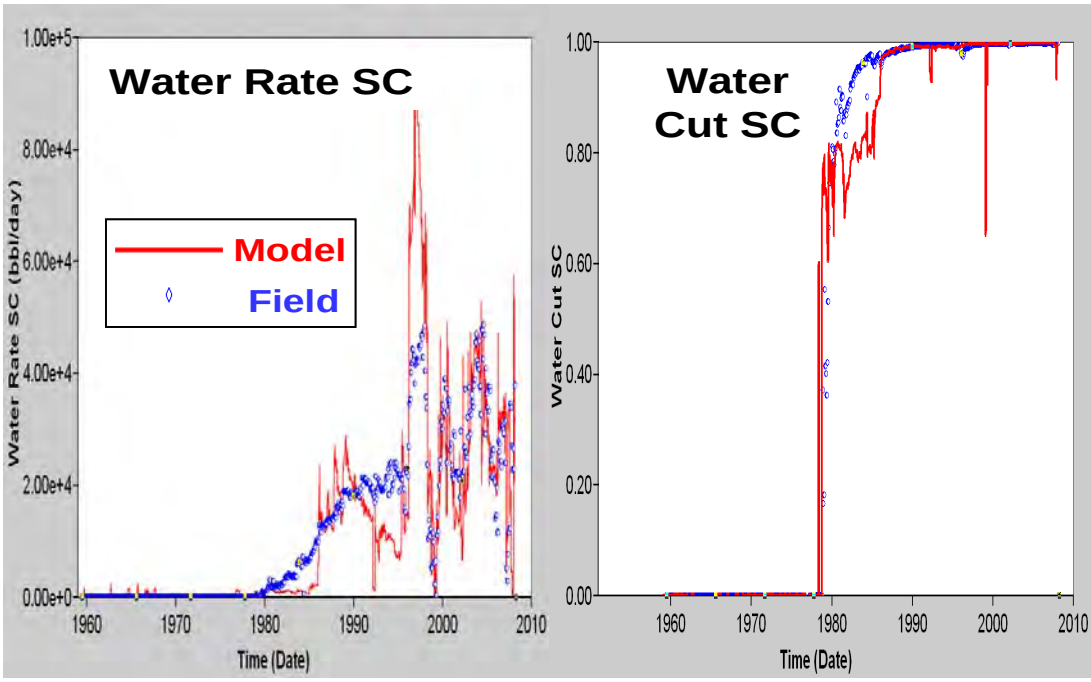


**Figure 4.21**: Comparison between the base case scenario (red) and the field data (blue). Left: water rates at surface condition; Right: water cut at surface conditions.

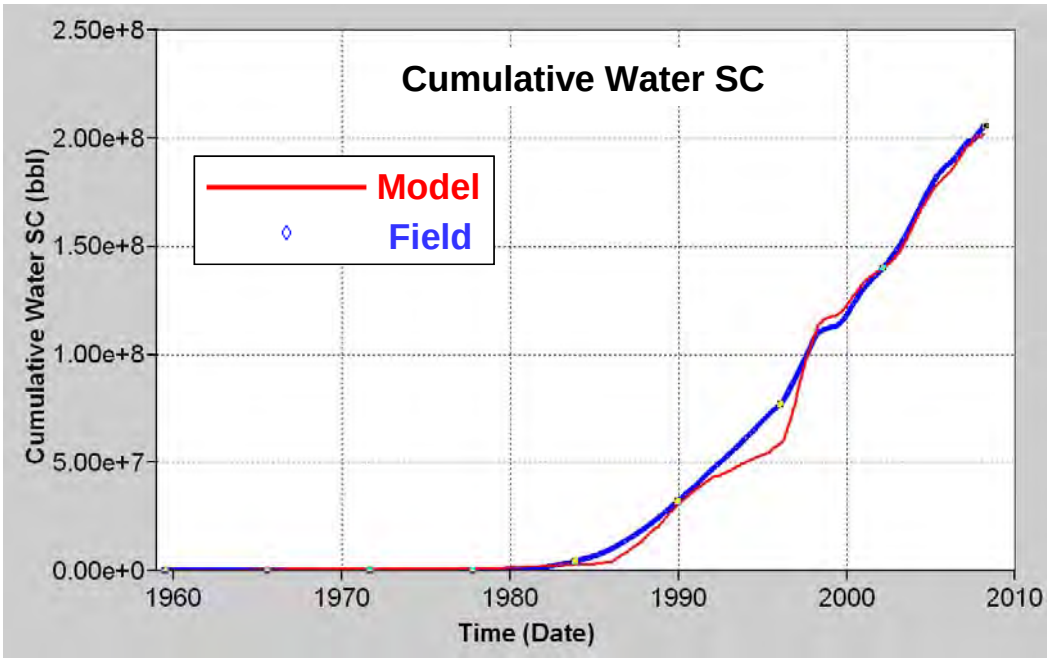


**Figure 4.22**: Cumulative water at surface conditions (SC) of base case scenario (red) and field data (blue). Total water produced with the Base Case simulation is 99.23% of total water produced in the field.

### 4.5.6 PILOT $CO_2$-EOR SIMULATIONS

The projected $CO_2$-EOR pilot will inject 52 tonnes/day or 1 MMcfd of supercritical $CO_2$ during six weeks.

The $CO_2$ will be injected in the crest of the anticline in a gravity stable flood where the objective is for the $CO_2$ to replace the water in the fractures (high in the structure). It is expected to interact with the oil in the adjacent matrix pores, reducing its viscosity and interfacial tension to be drained into the fracture system for production at wells lower in the structure (Friedmann and Stamp, 2006).

We simulated this scenario as well as three alternative ones and compared these predictions with the simulated primary production in the field, without any $CO_2$ injection. The simulated scenarios are listed below:

- Base Case: injection of 1 MMcfd during 6 weeks
- Case 2: injection of 1 MMcfd during 12 weeks
- Case 3: injection of 2 MMcfd during 6 weeks
- Case 4 injection of 2 MMcfd during 12 weeks
- Primary Production Case without $CO_2$ injection

At the time of starting our predictions, there are 10 producing wells, out of the 14 during the history matching process. Five of these wells are in an area of approximately ¼-mile radius around well 44-1-TpX-10, the injector well (Figure 4.26). These wells are the ones expected to respond during the injection pilot.

$CO_2$ is injected in the Upper BSand and the upper half of the Lower BSand (Figure 4.23). The results obtained from these simulations highlight several important factors that will affect the performance of the flood.

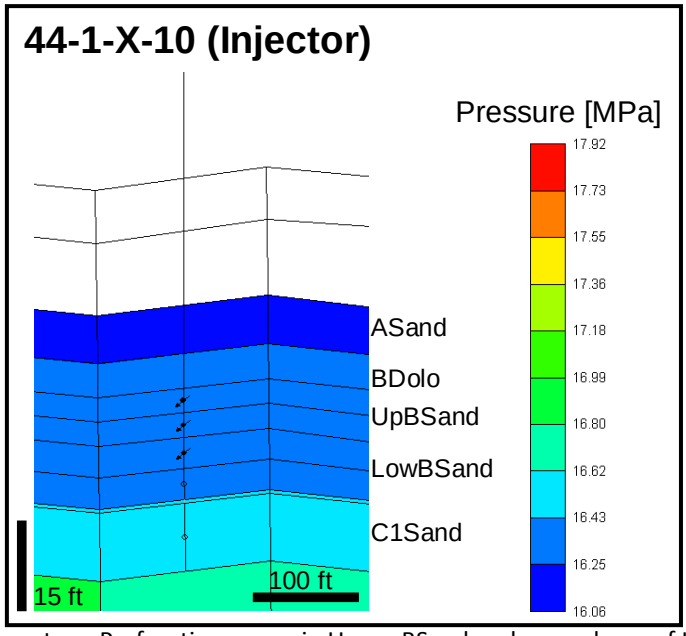


**Figure 4.23**: Injector set up. Perforations open in Upper BSand and upper layer of Lower BSand.

First, that $CO_2$ rapidly rises (2 -3 days) through the highly permeable fracture network (Figure 4.24, see crossection location on Figure 4.26) due to buoyancy forces. It accumulates in the fractures at the top layers (ASand and BDolo) almost without penetrating in the matrix pores. Contrary to the expected positive effect of a high permeable fracture network, this rapid buoyancy presents a problem, since the $CO_2$ migrates away of the main producing interval (BSand) where is being injected, and where it was expected to remain to allow enough time to be dissolved into the oil.

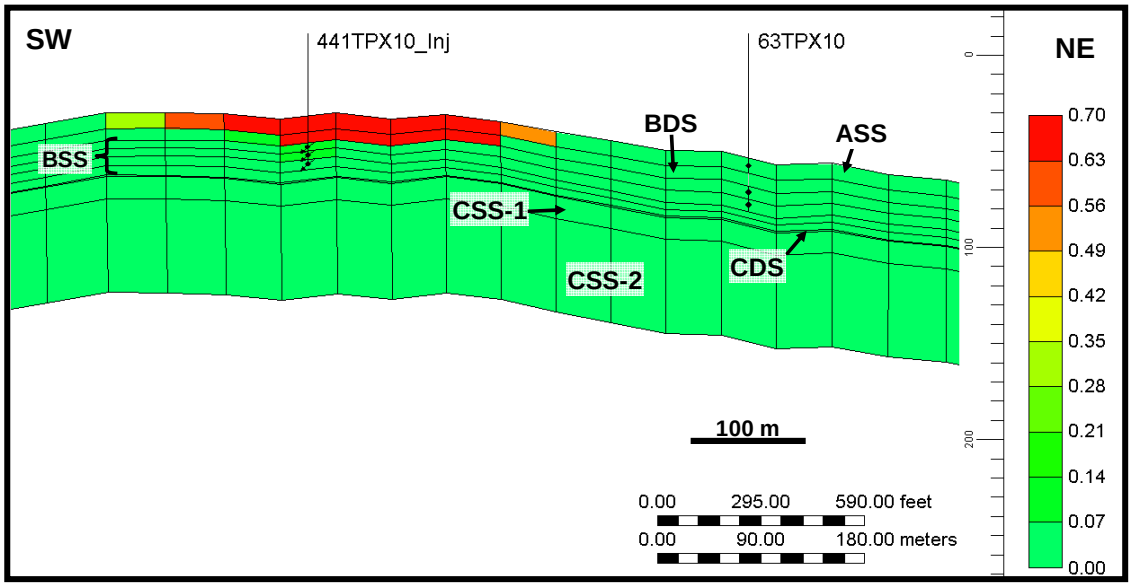


**Figure 4.24**: Gas Saturation in the fractures after 6 weeks of injection.

Another problem caused by these high permeability conduits is gas breakthrough times. In the base case simulation (Figure 4.25) $CO_2$ breakthrough occurs in well 55-TpX-10 at 16 days after the start of injection. Wells are set up to shut in when the $CO_2$ rate goes above 5000 cfd, since there are no gas recycling facilities in the field. This brings an important production loss.

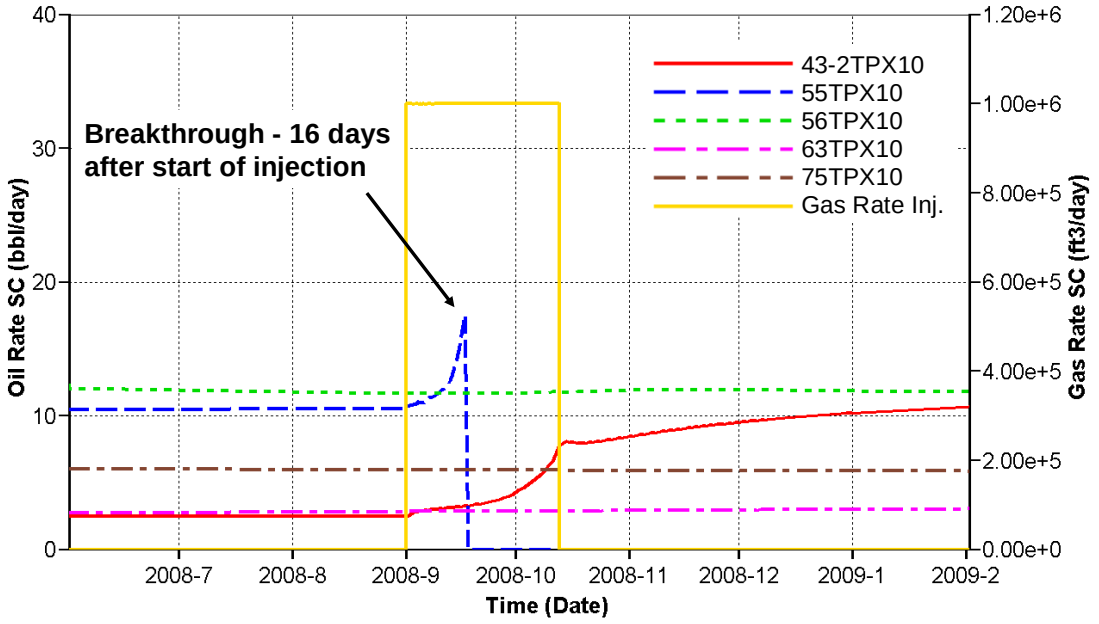


**Figure 4.25**: Base Case: Injection of 1 MMcfd of $CO_2$ for 6 weeks. Oil rate at surface conditions is plotted for the 5 closest wells to the injector. Injected gas rate is plotted in yellow.

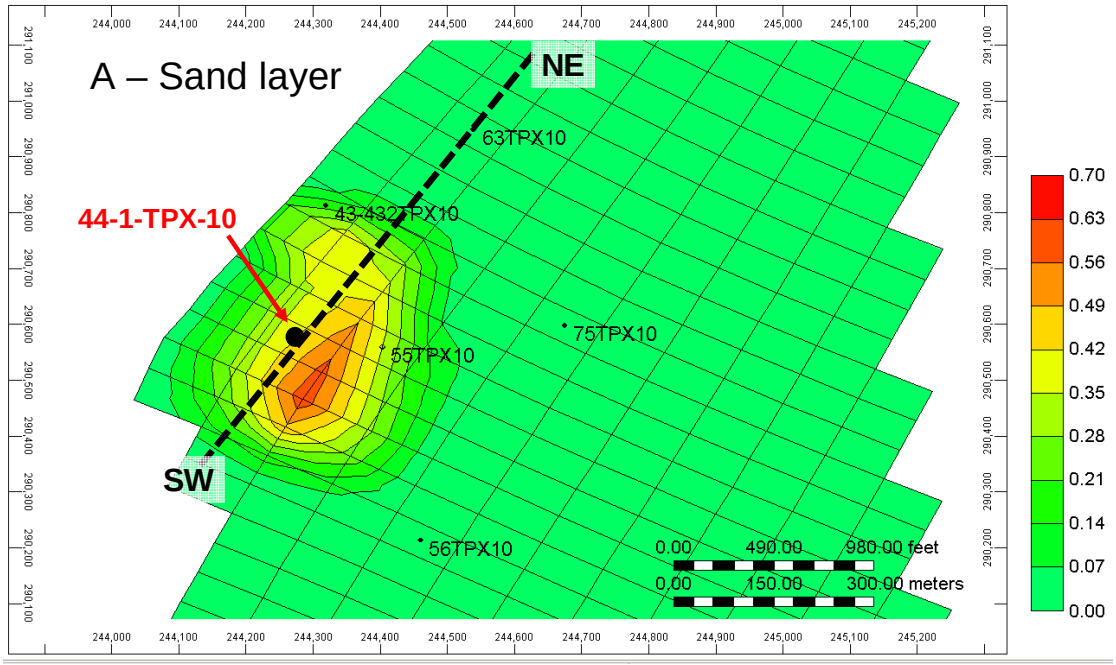


**Figure 4.26**: Base Case: Injection of 1 MMcfd of $CO_2$ for 6 weeks: Gas Saturation in fractures after 6 weeks of injection in the uppermost layer, ASand.

In all the simulated cases, the gas saturation in the other layers is very small. Besides, in all of them, the pressure change is insignificant, less than 0.20 MPa. At

this injection rates there is no risk to either fault stability or seal integrity. The maximum allowable injection pressure is set up to 22.75 MPa (3300 psi), below the estimated lower boundary for $S_{hmin}$, However, in none of the cases the injection pressure ever rose above 2520 psi.

Table 4.10 summarizes the incremental oil recovery at 6 weeks, 12 weeks and five years after the start of injection compared to the primary production scenario, without EOR (Figure 4.27). The reason why most of these cases recover less oil than in the primary production case is due to the closure of wells with high gas oil rations (GOR). In the first two cases, the main producing well (55-TpX-10) is shut-in at 16 days after start of injection. In the last two cases the same well is shut-in at 9 days after the start of injection. In the last case, wells 56-TpX-10 and 43-2-TpX are also shut-in at 43 and 60 days respectively.

| Injection period | Injected $CO_2$ | % of recovered oil after 6 weeks | % of recovered oil after 12 weeks | % of recovered oil after 5 years |
|---|---|---|---|---|
| 6 weeks | 1 MMcfd | 90.7 | 90.1 | 90.1 |
| 12 weeks | 1 MMcfd | 82.3 | 97.5 | 99.4 |
| 6 weeks | 2 MMcfd | 77.3 | 99.1 | 99.0 |
| **12 weeks** | **2 MMcfd** | **72.6** | **103.5** | **63.1** |

**Table 4.10**: Percentage of oil recovered in each of the cases compared to primary injection without $CO_2$.

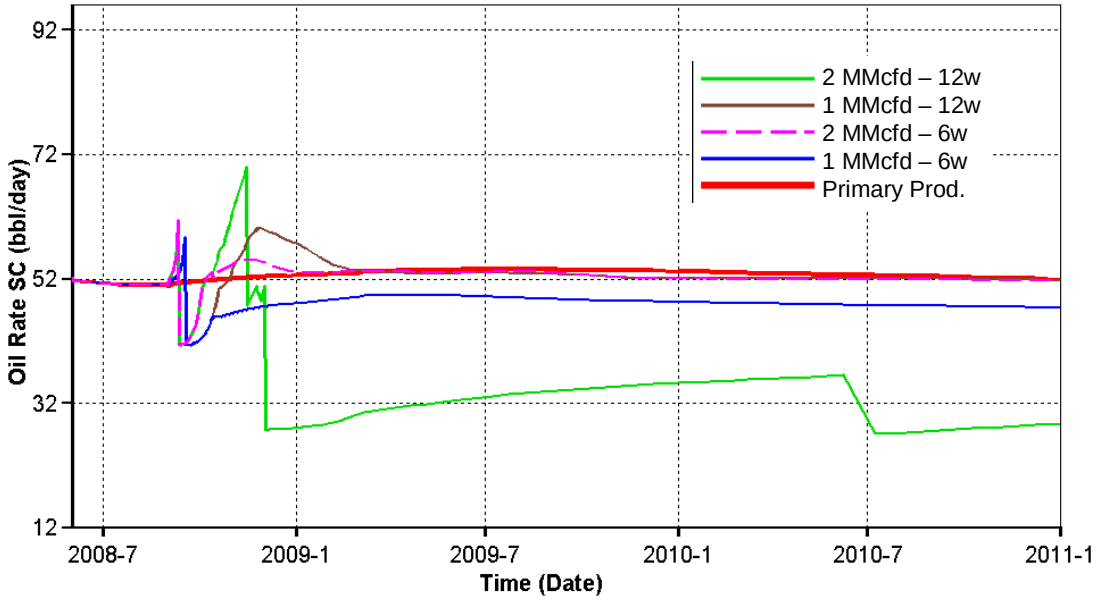


**Figure 4.27**: Oil rate in each of the cases as well as primary production without $CO_2$. Detail over a year and 2.5 years.

To solve the production loss due to well closure, a $CO_2$ mobility control strategy should be implemented. As we mentioned in Section 4.4.4, WAG is not recommended for the co-optimization between EOR and storage that we want to achieve. Therefore, a well control strategy of re-opening shut-in wells after certain time (when gas saturation had lower around the well) is tested in the simulation described in the next paragraphs. With these schemes, oil recovery improved noticeably. Table 4.11 and Figure 4.28 illustrate these results.

| Injection period | Injected $CO_2$ | % of recovered oil after 6 weeks | % of recovered oil after 12 weeks | % of recovered oil after 5 years |
|---|---|---|---|---|
| 6 weeks | 1 MMcfd | 91.6 | 90.6 | 108.2 |
| 12 weeks | 1 MMcfd | 91.6 | 97.9 | 117.6 |
| 6 weeks | 2 MMcfd | 94.4 | 99.3 | 117.6 |
| 12 weeks | 2 MMcfd | 94.4 | 103.7 | 128.1 |

**Table 4.11**: Percentage of oil recovered in each of the cases with well control strategy compared to primary injection without $CO_2$.

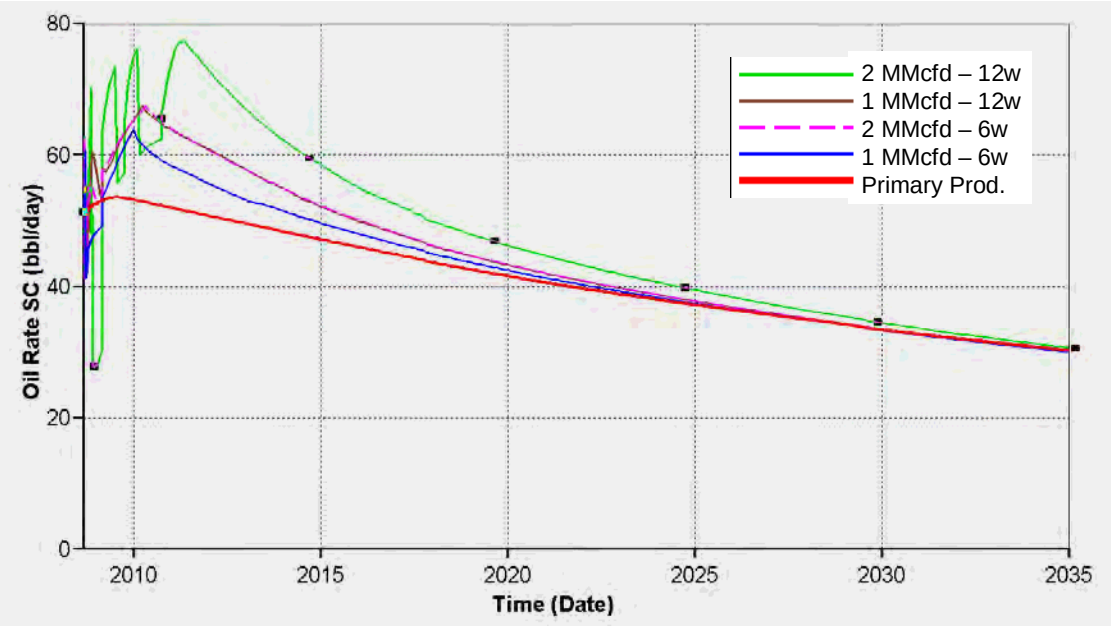


**Figure 4.28**: Incremental oil recovery of each of the cases, with a well control strategy. Compared to primary production without $CO_2$.

### 4.5.7 SEQUESTRATION POTENTIAL

The pilot $CO_2$-EOR is an experiment designed to test the short term EOR potential of $CO_2$ in this formation. However, simulations with larger amounts of injected $CO_2$ and longer periods of injection time are necessary if we want to understand the storage capacity of the Tensleep, and to make an impact in sequestering $CO_2$.

To have an idea of how much 52 tonnes a day (1 MMcfd) represent, we can compare it to the total emissions from different power plants. For example the highest emitter US power plant produces $6.30 \times 10^4$ tonnes a day (1,217 MMcfd) and Shute Creek, the $CO_2$ source for this project produces $2.10 \times 10^4$ tonnes a day (388 MMcfd). Of course, the Tensleep Fm. in this context has a small trap that does not offer enough reservoir volume to sequester such high amounts of $CO_2$. But a more reasonable fit for this size of traps, is the 100 highest emitter power plant in the US, which produces $6.30 \times 10^4$ tonnes a day (6.3 MMcfd) (Center for Global Development, 2007).

| US Power Plants | tonne/yr | tonne/day | MMcfd |
|---|---|---|---|
| Highest emitter: Scherer, GA | $2.30 \times 10^7$ | $6.30 \times 10^4$ | 1,216.9 |
| ExxonMobil's Shute Creek | $7.33 \times 10^6$ | $2.01 \times 10^4$ | 388 |
| 100 highest emitter: Miami Fort, OH | $6.86 \times 10^6$ | $1.88 \times 10^4$ | 6.3 |

**Table 4.12**: $CO_2$ emissions from power plants in the US (Center for Global Development, 2007)

#### *4.5.7.1 TESTING STORAGE CAPACITY OF RESERVOIR*

The capacity of the Tensleep was investigated through a series of simulations summarized in Table 4.13. The injection rates range from 1 MMcfd to 388 MMcfd.

The first tested example extends the Base Case Scenario (BC) injection (1 MMcfd) during 15 years, and after that, the simulation continued for 227 years (until year 2350). Similarly to the BC, the increase in pressure is also insignificant, no greater than 0.7 MPa. As mentioned before, the $CO_2$ rises rapidly through the fractures to the top layers, ASand and BDolo, and it takes almost a year for it to start saturating the fractures in the BSand. Gas saturation in the matrix starts being evident in the ASand approximately a year and three months after the start of injection, and it takes two years before it starts saturating the matrix of the BSand. By the end of the simulation, the gas saturations in matrix and fractures are almost equilibrated, although not completely.

We also simulated the injection of 6.3 (Miami Fort power plant scenario), 10, 15, 20, 58 (Shute Creek gas processing plant scenario), and 388 (Scherer power plant scenario) MMcfd for the same period of time. However, in all of these cases the maximum allowable bottom-hole injection pressure was reached much before the planned 15 years. The increase in pressure in all of them is approximately 7.4 MPa. The pressures did not go further up, since by the time these pressure were reached the injector BHP reached the limit, therefore, dramatically lowering the injection rates.

| Injected $CO_2$ [MMcfd] | Max. Pressure Increase [MPa] | Time of max. BHP reached | Total Injected $CO_2$ [tonnes] |
|---|---|---|---|
| 1 | < 0.7 | Not reached (injected 15 yrs) | $2.97x10^5$ |
| 4.2 (in 2 wells) | < 0.7 | 3y & 5m (well 1)<br>2y & 5m (well 2) | $3.85x10^5$ |
| 6.3 | < 7.4 | 1 yr, 8 months | $2.25x10^5$ |
| 10 | < 7.4 | 8 months | $1.60x10^5$ |
| 15 | < 7.4 | 5 months | $1.54x10^5$ |
| 20 | < 7.4 | 3 months, 21 days | $1.55x10^5$ |
| 58 | < 7 | 1 month, 4 days | $1.12x10^5$ |
| 388 | < 7 | 4 days | $1.37x10^5$ |

**Table 4.13**: Summary of simulations to test the Tensleep Fm. storage capacity, y = years, m = months.

In order to test the best scenario for a sequestration only project, we also simulated the injection of 1 MMcfd in 2 and 3 simultaneous injectors as well as 2 MMcfd in 1, 2 and 3 injectors (Figure 4.29). The best scenario sequesters ~$1.19x10^6$ tonnes of $CO_2$ by injecting 2 MMcfd in only one well. This would correspond to a small power plant of ~40,000 tonnes per year.

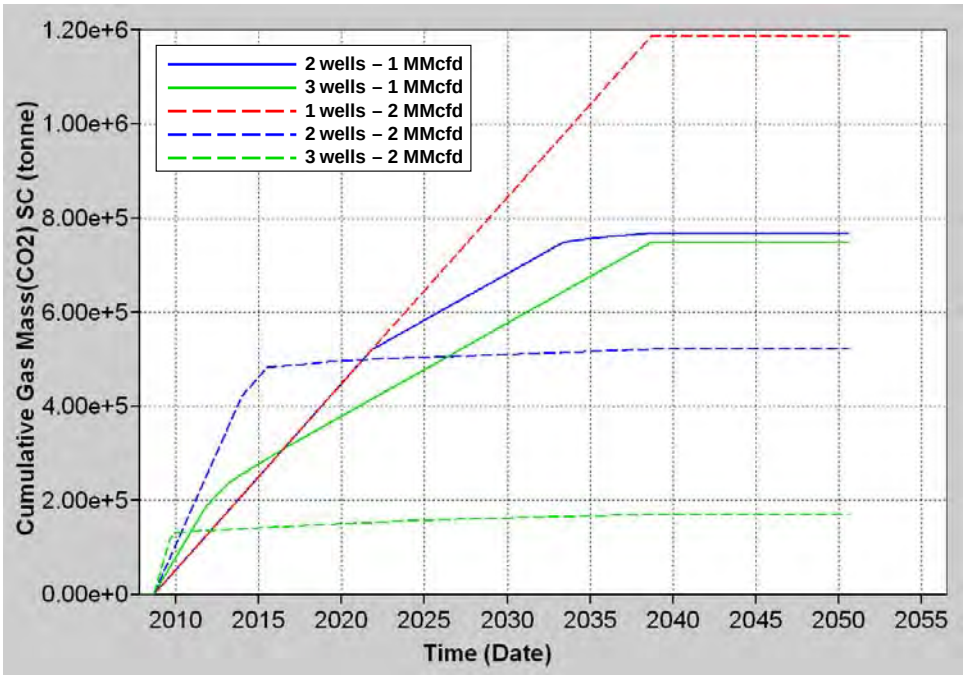


**Figure 4.29**: injection of 1 MMcfd in 2 and 3 simultaneous injectors (solid lines) as well as 2 MMcfd in 1, 2 and 3 injector (dashed lines).

## 4.5.8 SENSITIVITY ANALYSIS OF PILOT $CO_2$-EOR

The sensitivity analysis was performed with the Base Case scenario (BC) described in the previous section, but keeping the injection time for 5 years in order to be able to observe long term variations.

### *4.5.8.1 FRACTURE PERMEABILITY (KF)*

Fracture permeability is, as expected, one of the factors that most affects the system. Sensibility cases were ran with 10, 4, 2, 0.5 and 0.25 times the permeability values of the BC scenario. Well control is not applied at this stage.

Although higher permeabilities improve oil recovery considerably in the short term, they also cause earlier gas breakthroughs and therefore, the loss of oil production from the shut-in wells. As a result, there is an overall decrease in oil recovery in the long term. However, if well control is extended beyond the pilot-injection period, these results might change. In the cases of lower permeability

scenarios, even if the breakthrough times are delayed lower values of permeability also reduce the amount of recovered oil (Table 4.14).

| *k*F factor | % Oil recovered after 6 weeks | % Oil recovered after 12 weeks | % Oil recovered after 5 years |
|---|---|---|---|
| 10 | 350.3 | 265.0 | 96.0 |
| 4 | 192.3 | 183.0 | 100.7 |
| 2 | 131.3 | 125.3 | 107.1 |
| 0.5 | 87.7 | 82.5 | 72.8 |
| 0.25 | 81.0 | 69.0 | 61.7 |

**Table 4.14**: Effect of fracture permeability in oil recovery compared to the BC after 6 and 12 weeks, and 5 years of 1 MMcfd $CO_2$ injection.

#### *4.5.8.2 Fracture Porosity (øF)*

Fracture porosity has almost zero impact in oil recovery during the first three month and has very little impact in later dates. Five different scenarios were compared with 10, 4, 2, 0.5 and 0.25 times the original fracture porosity used for the BC scenario. However, it does not appear to be a systematic correlation in between fracture porosity and produced oil, or in between fracture porosity and breakthrough times.

#### *4.5.8.3 Fracture Spacing (spF)*

Five different scenarios were produced with 10, 4, 2, 0.5 and 0.25 times the original fracture spacing used for the BC. Table 4.15 summarizes the percentage oil recovery difference from the BC. The impact is less important than with fracture permeability, and its effect is not obvious. The loss of production from some of the shut-in wells affects the incremental recovery more than the tested parameter it self.

| *sp*F factor | % Oil recovered after 6 weeks | % Oil recovered after 12 weeks | % Oil recovered after 5 years |
|---|---|---|---|
| 10 | 125.1 | 132.2 | 102.0 |
| 4 | 106.2 | 112.3 | 112.0 |
| 2 | 101.0 | 103.5 | 102.8 |
| 0.5 | 100.5 | 100.0 | 102.2 |
| 0.25 | 103.1 | 99.1 | 96.4 |

**Table 4.15**: Effect of fracture spacing on oil recovered compared to the BC after 6 and 12 weeks, and 5 years of 1 MMcfd $CO_2$ injection.

#### *4.5.8.4 Relative Permeability Curves ($K_{REL}$)*

Four scenarios were created to test the effect of the relative permeability curves in the model compared to the BC. In the base case scenario we use the same $K_{rel}$ for the matrix than the one used in the history matching process while the fracture $K_{rel}$ have the same saturations than the matrix, but with the typical X shape of fracture $K_{rel}$. The sensitivity scenarios include:

1. Fracture $K_{rel}$ of BC is used for both the matrix and the fracture system.
2. Matrix $K_{rel}$ is used for both matrix and fractures, as it was the case during the history matching process (Figure 4.11).
3. Same matrix $K_{rel}$ than in the BC and X shaped fracture $K_{rel}$ with 0 initial water saturation.
4. Average $K_{rel}$ curves described by Gaviria (2005) (Figure 4.30).

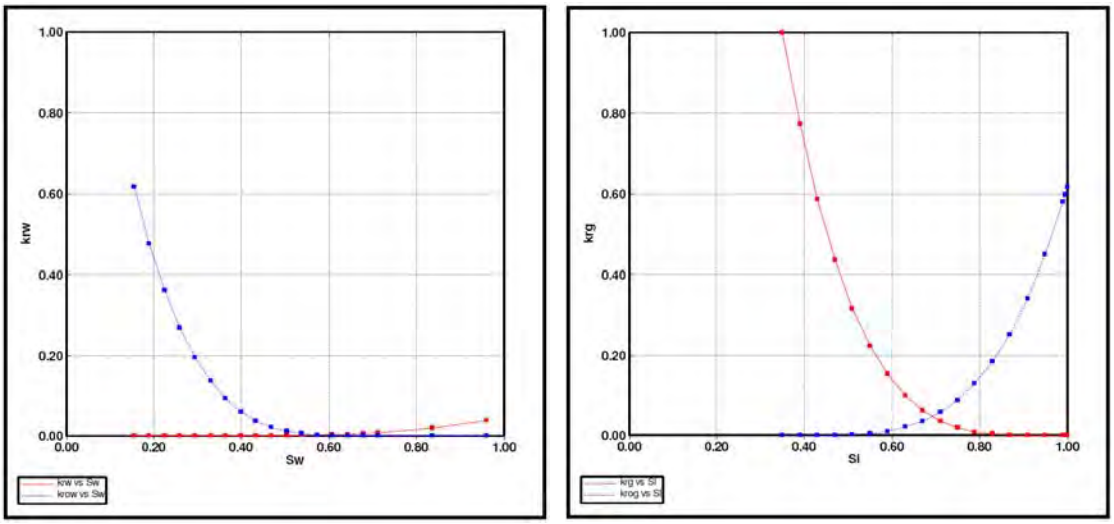


**Figure 4.30**: Average $K_{rel}$ curves described by Gaviria (2005). Water-oil relative permeability curves (left); Gas-oil relative permeability curves (right).

The difference in oil recovered form all the scenarios is insignificant during the pilot stage, and it becomes slightly noticeable in later dates; but it is still not significant in terms of cumulative oil recovery. Table 4.16 shows the comparison of recovered oil. Scenarios 1, 2, and 3 are almost equal during the first year injection and they are very similar to the BC (red line). The most notorious difference is with the average *Krel.*

| $K_{rel}$ | % Oil recovery after 6 weeks | % Oil recovery after 12 weeks | % Oil recovery after 5 years |
|---|---|---|---|
| Case 1 | 100 | 100 | 97.3 |
| Case 2 | 100 | 100 | 97.3 |
| Case 3 | 100 | 100 | 97.3 |
| Case 4 | 105.6 | 111.1 | 102.5 |

**Table 4.16**: Effect of $K_{rel}$ curves on oil recovered compared to the BC after 6 weeks, 12 weeks, and 5 years of 1 MMcfd $CO_2$ injection.

#### *4.5.8.5 MATRIX POROSITY & PERMEABILITY*

Several scenarios were tested with different distributions of porosity and permeability. In all of them there was little variation during the initial stages of injection in the amount of oil recovered. Figure 4.31 shows and example of it, where after the first month the results start varying due to the different timing of gas breakthrough.

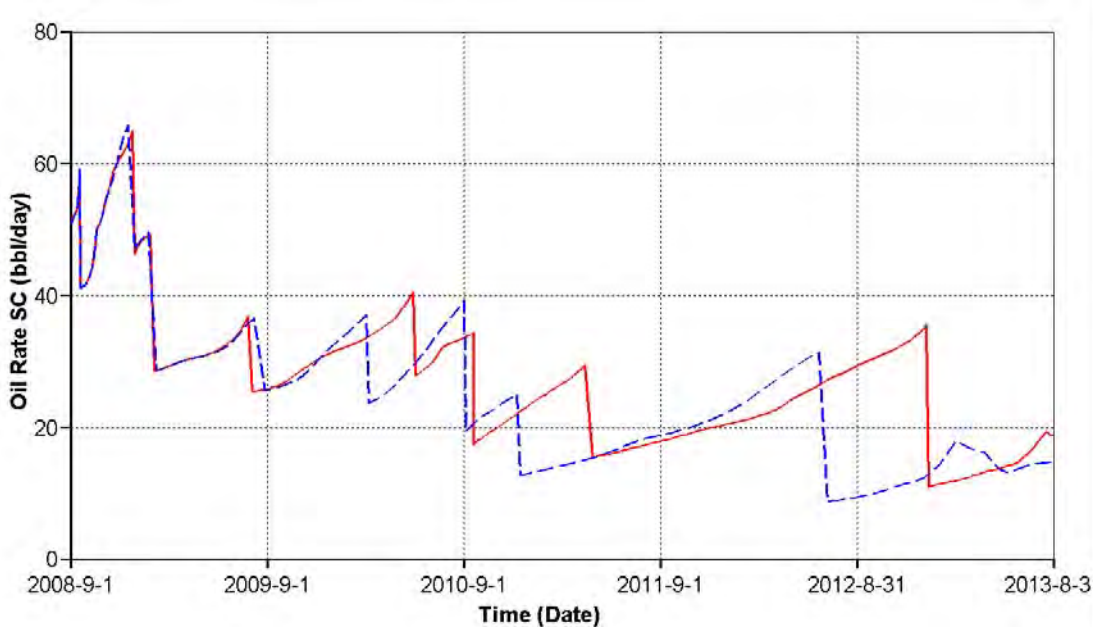


**Figure 4.31**: Oil rate comparison between BC (red line) and a case run with a different matrix porosity and permeability distribution.

#### *4.5.8.5 GRID SIZE*

As with the other tested parameters, grid size changes the $CO_2$ breakthrough times in different wells, complicating the possibility to make any valid quantitative observations on how this refinements influence the system. For example, in the case in which the grid was refined horizontally (I and J directions) by a factor of three, it is possible to observe an increment in oil rates at the beginning of the injection. Cumulative oil after 6 weeks of injection was 167.2% of the BC cumulative oil, while

in 12 weeks of injection it was 129.8%. However, breakthrough times diminished, causing the closure of wells sooner than in the BC, and after 5 years of injection the cumulative oil was 80.7% of the BC one.

However, it was clear from the simulations that in order to be able to resolve the $CO_2$ plume geometry we need a more refined grid both vertically and horizontally.

### 4.5.9 SENSITIVITY ANALYSIS OF PILOT $CO_2$-EOR WITHOUT GAS CONSTRAINTS

From the sensitivity analysis described in the previous section, it is extremely difficult to drive any conclusion because the tested parameters greatly affect gas breakthrough times, which also affects the resultant oil production and complicates the direct comparison among scenarios. The imposed constraint in a well is to shut-in when gas rate is higher than 5000 cfd. Therefore, when the first well shuts-in at different times in each scenario, the distribution of the $CO_2$ and the conditions of the simulation change.

For these reasons, a different approach for the sensitivity analysis was taken; the wells were allowed to produce without any gas production constraints. This permits to analyze the effect of each tested parameter in the system. Nevertheless, the resultant production is not the real production expected in the field and therefore, this sensitivity analysis does not provide a range of possible outcomes regarding oil production and $CO_2$ storage.

The sensitivity simulations described in the previous sections were re-run under these new conditions.

Among all the parameters tested, fracture permeability is, as expected, one of the factors that greater affects the system. Where in general, more oil is recovered with higher fracture permeabilities (Figure 4.32). The other parameter that has a high influence on the results is the relative permeability (Figure 4.33). On the other hand, fracture spacing and specially fracture porosity are the factors that less influence have on the results (Figures 4.34 and 4.35).

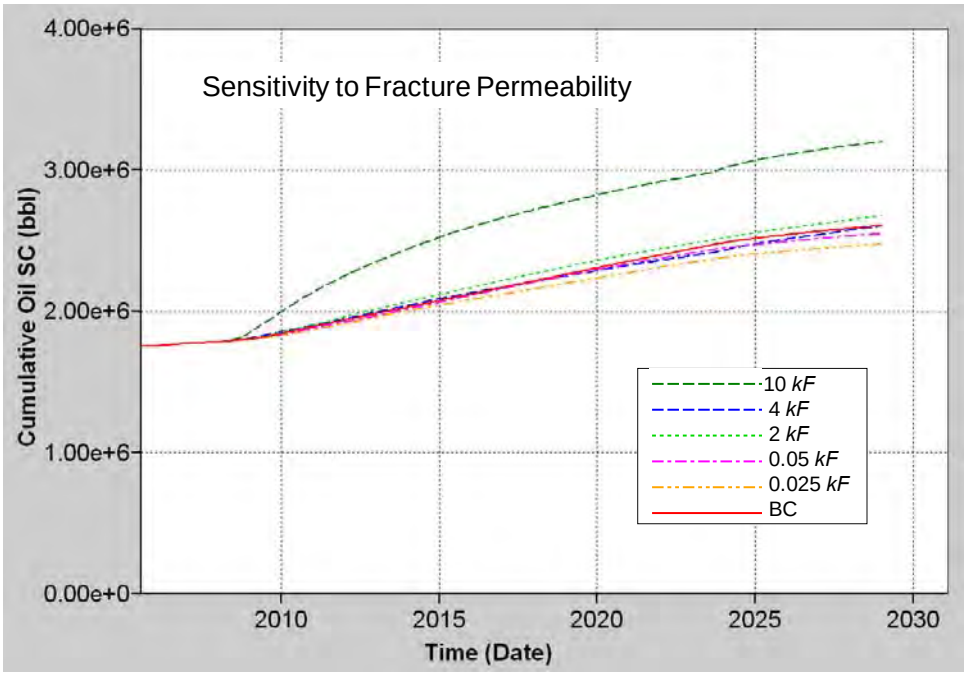


**Figure 4.32**: Cumulative Oil comparison between BC (red line) and 10, 4, 2, 0.5, and 0.25 times the original fracture permeability.

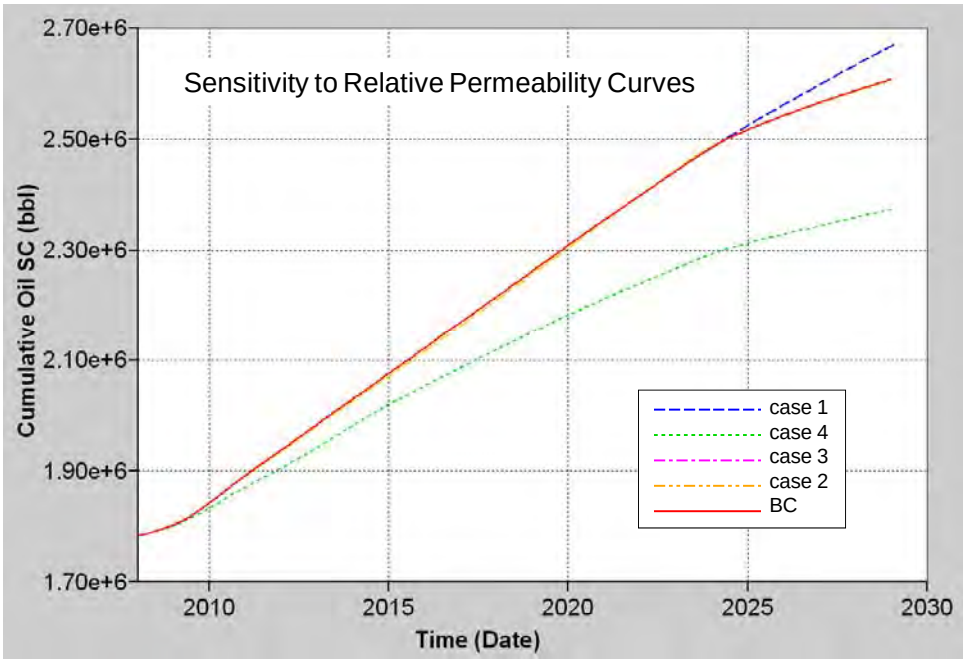


**Figure 4.33**: Cumulative Oil comparison between BC (red line) and four different relative permeability curves: case 1 - Fracture Krel of BC is used for both the matrix and the fracture system; case 2 - Matrix Krel is used for both matrix and fractures, as it was the case during the history matching process (Figure 4.11); case 3 - Same matrix Krel than in the BC and X shaped fracture Krel with 0 initial water saturation; case 4 - Average Krel curves described by Gaviria (2005) (Figure 4.30).

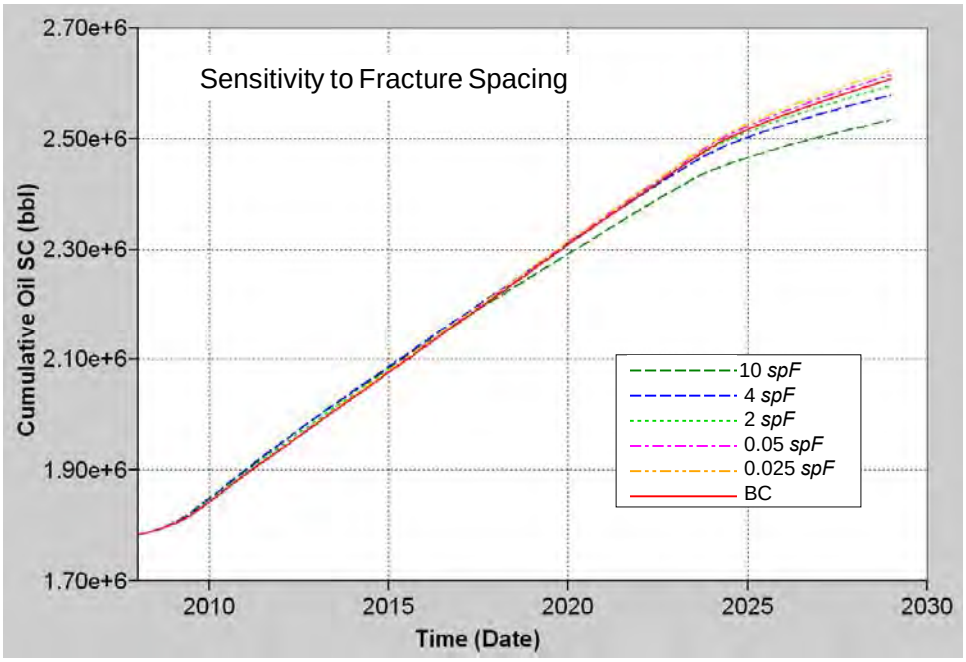


**Figure 4.34**: Cumulative Oil comparison between BC (red line) and 10, 4, 2, 0.5, and 0.25 times the original fracture spacing.

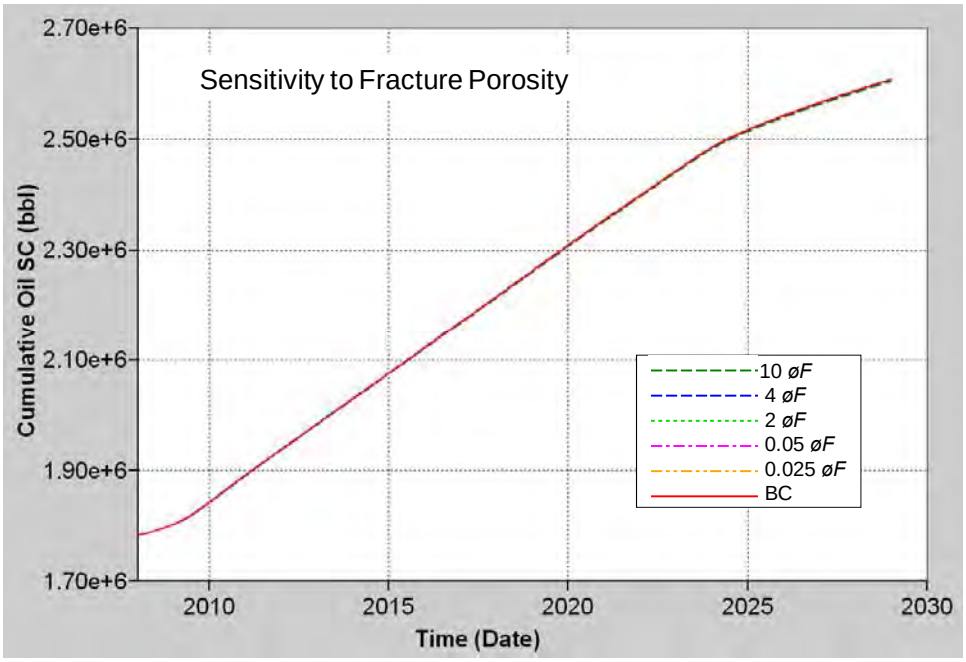


**Figure 4.35**: Cumulative Oil comparison between BC (red line) and 10, 4, 2, 0.5, and 0.25 times the original fracture porosity.

We also run the new sensitivity analysis on matrix porosity and permeability. We first tested the values obtained from Yin's lithofacies analysis (see section 4.3.2) keeping the same matrix porosity than in the BC and using 10 different matrix

porosity realizations from the geostatistical analysis (Figure 4.36). Similarly, we tested 10 different matrix porosity realizations keeping the same in matrix permeability used in the BC case (Figure 4.37). We repeated this analysis using the matrix porosity and permeability values obtained from core samples (Figures 4.38 and 4.39).

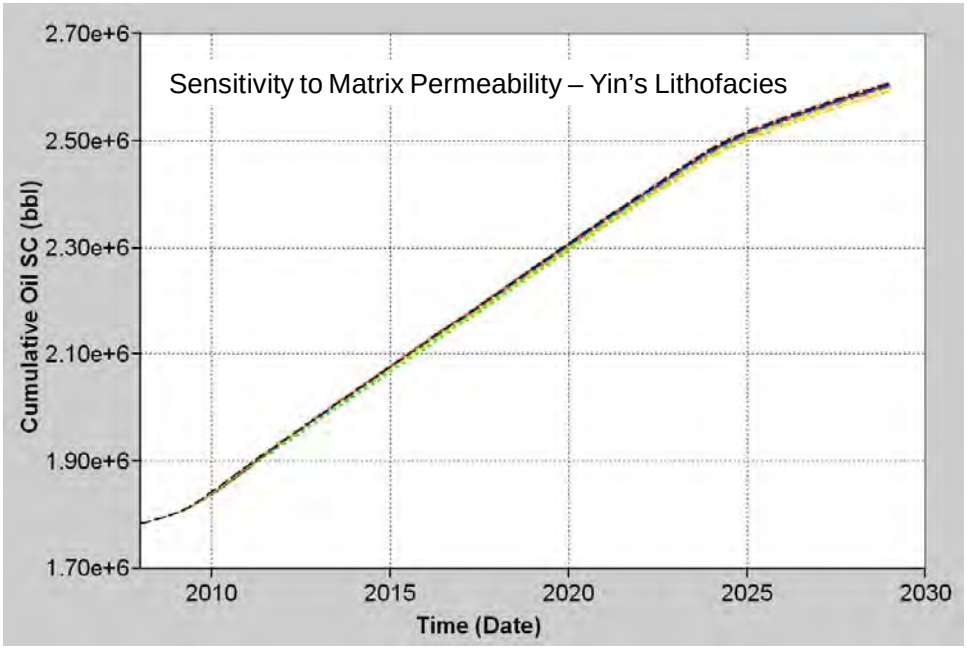


**Figure 4.36**: Cumulative Oil comparison between BC (black line) and 10 simulations with different realizations of matrix permeability obtained from the geostatistical analysis using Yin's lithofacies values (see Section 4.3.2).

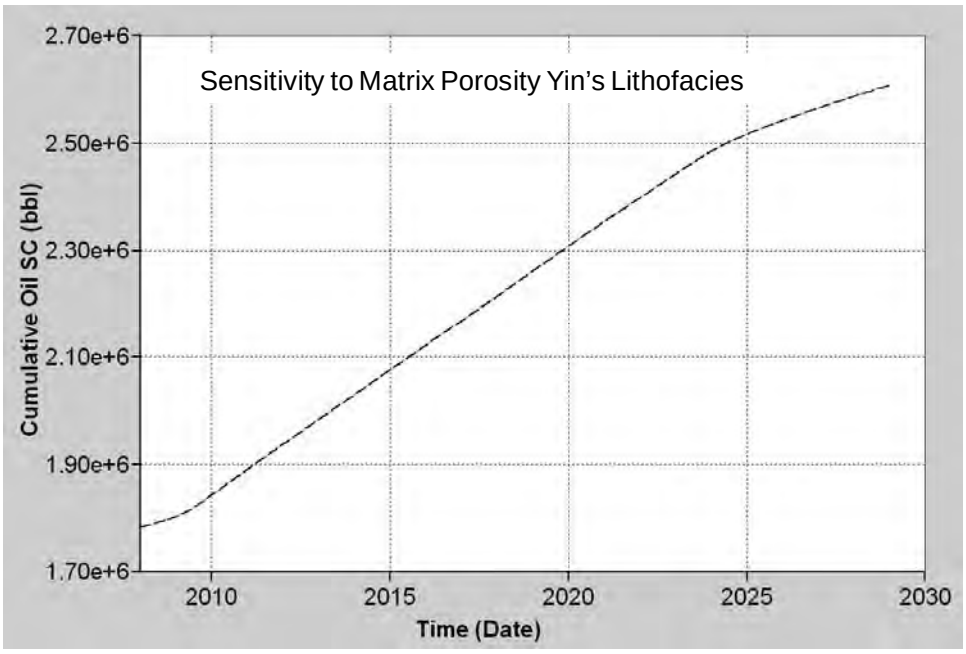


**Figure 4.37**: Cumulative Oil comparison between BC (black line) and 10 simulations with different realizations of matrix porosity obtained from the geostatistical analysis using Yin's lithofacies values (see Section 4.3.2).

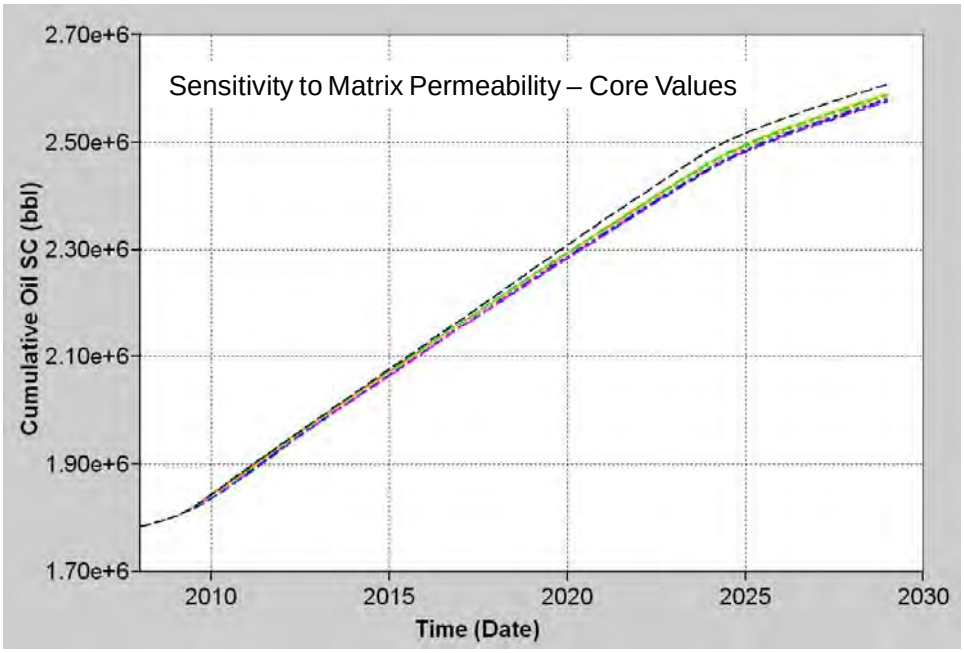


**Figure 4.38**: Cumulative Oil comparison between BC (black line) and 10 simulations with different realizations of matrix permeability obtained from the geostatistical analysis using core values (see Section 4.3.2).

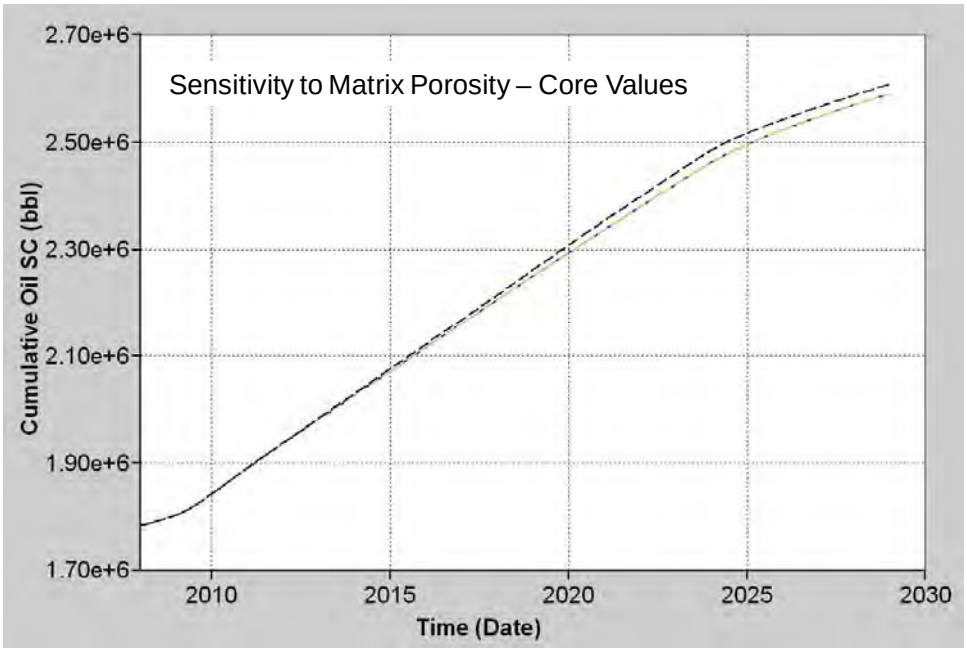


**Figure 4.39**: Cumulative Oil comparison between BC (black line) and 10 simulations with different realizations of matrix porosity obtained from the geostatistical analysis using core values (see Section 4.3.2).

In both cases (Yin's lithofacies and core values), matrix porosity barely modified the results where matrix permeability, although producing slightly more variations, did not produced great differences either. However, running the simulations with matrix porosity and permeability realizations obtained from core values produced more pessimistic outcomes than the ones run with Yin's lithofacies analysis.

## 4.6 SUMMARY

In order to test the feasibility of the $CO_2$-EOR pilot project at Teapot Dome, we performed a 3D stochastic reservoir model and fluid flow simulation of the fractured Tensleep Fm. in a three-way trap against the S1 fault. The geological model was based on a structural and stratigraphic seismic interpretation, well logs, and core data. We used geostatistics to populate the model with porosity and permeability distributions. The fluid flow simulation incorporated the geomechanical constraints developed in Chapter 3. These constraints established the maximum allowable injection rates as well as pressure limits to be avoided at the top of the reservoir and

at the fault boundary. Similarly, we also incorporated a fracture permeability anisotropy subparallel to the $S_{Hmax}$ direction. We history matched our model with historic oil and water rates from the field.

The results of the fluid flow simulation showed that the pressure increase is minimal during the pilot project not constituting a risk for fault stability or seal integrity. However, buoyancy and mobility of $CO_2$ could represent a problem for the EOR performance. $CO_2$ was injected in the main producing interval (BSand) to dissolve in the oil, but almost immediately rose to the top layers through the high permeability fracture network, taking almost a year to start saturating the fractures in the BSand. The mobility of the gas results in early breakthroughs in the closer wells with their consequent shut-in and loss of production.

Four different scenarios were tested as potential schemes for the projected $CO_2$-EOR pilot, which consisted on the injection of: 1) 1 MMcfd for 6 weeks, 2) 1 MMcfd for 12 weeks, 3) 2 MMcfd for 6 weeks and 4) 2 MMcfd for 12 weeks. In all of them, oil recovery was less than the predicted from a pure primary production scenario due to the mentioned closure of wells with high GOR. However, when a well control strategy (re-opening wells after a certain period of time) was implemented, incremental oil recovery went up from 8%, in case 1, to 28%, in case 4, of the BC production.

The amount of $CO_2$ planned to be injected in the initial pilot project is modest in the context of making an impact in sequestering carbon dioxide. The storage potential of the Tensleep was tested injecting higher amounts of $CO_2$, which are comparable to daily emissions of different size power plants. The results suggest that the present trap could eventually hold an injection scheme of 2 MMcfd in a single well during at least 30 years, sequestering ~$1.2x10^6$ tonnes of $CO_2$ corresponding to a small power plant of ~40,000 tonnes per year. Due to the small size of the trap, there seems not to be any advantage on injecting in multiple wells at the same time.

During the sensitivity analysis, we studied the impact on the system of several parameters that included fracture permeability, porosity and spacing, relative permeability curves, matrix porosity and permeability, and grid size. The results

suggested that several factors would influence the performance of a $CO_2$ injection. However, it is extremely difficult to drive any conclusion from this sensitivity analysis because these parameters greatly affect gas breakthrough times (the imposed constraint in a well is to shut it in when gas rate is higher than 5000 cfd). Therefore, when the first well shuts-in at different times in each scenario, the distribution of the $CO_2$ and the conditions of the simulation change, making the quantitative sensitivity analysis meaningless.

A different approach for the sensitivity analysis was also taken, where the wells were allowed to produce without any gas production constraints. This allowed us to analyze the effect of these parameters in the system. But, since these are not the real production conditions on the field, this approach would not provide a range of possible outcomes regarding oil production and $CO_2$ storage. Qualitatively, it was observed that fracture permeability is the parameter that most influenced the $CO_2$ and oil behavior where, $K_{rel}$ curves also have an important impact on the results. Conversely, fracture porosity, fracture spacing, matrix porosity and matrix permeability, seemed to have much less influence.

## CHAPTER 5

# FRACTURE DETECTION USING AMPLITUDE VERSUS ANGLE AND AZIMUTH AT TEAPOT DOME OIL FIELD, WY

## 5.1 ABSTRACT

In this chapter we describe an Amplitude Versus Angle and Azimuth (AVAZ) analysis performed at Teapot Dome to identify the presence of fractures using wide-azimuth 3D seismic data. The objective of the present analysis is to expand the 1D scattered fracture characterization previously performed, to a 3D characterization of the fracture network on both the reservoir and the caprock that will allow for a more

accurate assessment of the impact of these fractures in reservoir permeability and in the risk of $CO_2$ leakage.

In previous stages of this project, geomechanical analysis demonstrated that $CO_2$ sequestration will neither induce slip on the reservoir-bounding fault, nor fracture the caprock. However, various sets of pre-existing minor faults in the reservoir are critically stressed (i.e., active) in the current stress field. Hence, raising pore pressure during sequestration will activate slip on these minor faults. The presence of these minor faults enhances formation permeability and injectivity of $CO_2$. However, the potential for slip on these faults could potentially compromise the top seal capacity of the Tensleep if these minor faults extend up into the cap rock.

The AVAZ analysis uses amplitude variations in the long shot/receiver offsets of P-wave seismic data, to determine the orientation and magnitude of the seismic anisotropy that could be correlated with the orientation and intensity of fractures.

The AVAZ results are calibrated with fracture intensity and orientations obtained from FMI logs recorded in the area, as well as stress orientation, the macro fault network of the anticline and the macro sedimentary structures. During the analysis of these results, we did not found enough evidence to indicate whether the anisotropy in the reservoir and caprock is influenced by stress, structural or sedimentary features.

## 5.2 INTRODUCTION – MOTIVATION

As discussed in Chapters 2 and 3, the Tensleep Fm. is an eolian sandstone highly fractured, where various sets of pre-existing minor faults in the reservoir, and fewer in the caprock, were found to be critically-stressed (i.e., active) in the current stress field.

The occurrence of these small faults in the caprock and the potential for slip on these features could potentially compromise the top seal capacity of the Tensleep. Similarly, the presence of these minor faults enhances formation permeability and

injectivity of $CO_2$ in the reservoir. However, the fluid flow simulations discussed in Chapter 4 showed that these fractures could provide conduits for the buoyant $CO_2$ to rapidly migrate to the top layers, away from the main producing interval, where the $CO_2$ was expected to dissolve into the oil to enhance its recovery. For this reason, it will be extremely important to be able to discriminate areas in the reservoir with higher fracture density from areas with lower fracture density in order to design spatially more efficient $CO_2$ injection schemes.

Traditional methods of fracture characterization are 1D (well logs or cores) or 2D (outcrop analogs), but we need a technique that will allow us to spatially characterize these features to better asses their contribution to reservoir permeability and the potential risk of $CO_2$ leakage in the caprock. These faults are below the resolution limit of conventional 3D seismic imaging methods; yet, they are usually aligned in sets that create anisotropy in seismic velocities (and permeabilities). Therefore, with a 3D seismic cube it is possible to map seismic anisotropy and its spatial variability, and obtain information on direction and density of these fractures (Gray and Head, 2000; Hall et al., 2002; Gray, 2008).

In this chapter we describe the study we conducted using Amplitude Versus Angle and Azimuth (AVAZ) analysis to identify the presence of fractures in the reservoir and caprock based on wide-azimuth 3D seismic data, which is based on azimuthal anisotropy measurements.

## 5.3 SEISMIC ANISOTROPY

Seismic anisotropy has been recognized as a widespread phenomenon in the upper crust and even in the upper mantle. There are several causes for this effective seismic anisotropy, but in the crystalline upper crust it can be related to two main mechanisms: stress-related anisotropy and structural anisotropy (Boness, 2005).

Stress-related anisotropy is the response to an anisotropic tectonic stress. The mechanisms proposed to cause this effect are the preferential closure of fractures,

perpendicular to the maximum horizontal compressive stress ($S_{Hmax}$) in a randomly fractured crust (Boness and Zoback, 2004); or the presence of $S_{Hmax}$ aligned liquid-filled microcracks (Crampin, 1985). In both cases, a seismic wave propagating in the vertical plane will be polarized with a fast direction parallel to $S_{Hmax}$ (Bonnes, 2005). Structural anisotropy will be the result of aligned parallel macroscopic fractures and faults, parallel sedimentary planes and the alignment of minerals and/or grains. Here the fast polarization direction will be parallel to the strike of the structural fabric (Boness, 2005).

Traditional analyses of crustal anisotropy are based on shear waves (shear-wave splitting analysis). When a shear-wave enters a zone of effective seismic anisotropy, it splits into two or more phases with different velocities and polarizations. The polarization is controlled by the three dimensional symmetry of the anisotropy, and the delay between them is proportional to the differential slowness of the shear wave in the direction of the ray path and the length of the path through the anisotropic material (Crampin, 1984).

A very common cause of seismic anisotropy is the presence of fractures. Therefore, several methods have been developed for fracture characterization in reservoirs. The goal of this analysis is to obtain Thomsen's coefficient γ, which is the fractional difference between velocities of split shear waves at vertical incidence. γ is related to crack density, which is also related to the permeability of the fracture network, and it can be obtained from the difference in shear-wave travel times and normal-incident reflection amplitudes. However, this methodology is difficult to implement at a reservoir scale because high-quality shear data could be very difficult and expensive to obtain (Rüger and Tsvankin, 1997).

The influence of azimuthal anisotropy on P-wave propagation is not as dramatic as for shear waves, but it still can be considerable. It has been demonstrated that fracturing causes significant azimuthal variation in recorded seismic signatures, and since traditional seismic exploration data is much more common and available, the

characterization of fractured reservoirs using surface seismic data became an increasingly important exploration problem (Rüger and Tsvankin, 1997).

Rüger and Tsvankin (1997) showed the Amplitude-variation-with-offset (AVO) response of fractures reservoirs. AVO analysis consists in extracting reflection coefficients (ratio of amplitudes of reflected and incident seismic waves) from seismic data, and interpreting it in terms of the change in medium parameters. They illustrated that P-wave amplitudes could be sensitive even to relatively weak anisotropy of the rock, and they showed how the azimuthally dependent AVO signature can be interpreted and combined with normal-moveout and shear-wave-splitting analyses (if available) to constrain the crack density and other medium parameters.

## 5.4 AVAZ METHOD IN FRACTURED RESERVOIRS

The AVAZ analysis uses amplitude variations in the long shot/receiver offsets of P-wave seismic data to determine the intensity and orientation of fractures (Gray et al., 2003). It is a sample-by-sample fitting of the amplitudes in the prestack seismic gather to an equation derived by Rüger (1996):

$$R(i,\varphi) = A + [B^{iso} + B^{ani}\cos^2(\varphi - \varphi_{sym})]\sin^2 i$$

where $R$ is the reflectivity (amplitude) of the $P$ wave, $A$ is the AVO intercept, $B^{iso}$ is the isotropic AVO gradient, $B^{ani}$ is the anisotropic gradient (or crack density), $i$ is the incident angle of the seismic wave and $\varphi$ is the azimuth of the ray path, and $\varphi_{sym}$ is the azimuth of the direction, perpendicular to the fracture strike. This equation describes how the amplitude of reflected P-wave on the interface between two azimuthal anisotropic media varies at different incident angles and azimuths (Figure 5.1, left) of the ray path (Zheng et al. 2004).

Rüger showed that the AVO gradient can be split into both isotropic and anisotropic ($B^{iso}$ & $B^{ani}$ ) parts for a Horizontally Transverse Isotropic (HTI) medium (Figure 5.1, right). Such a medium can be created by a group of open vertical fractures encased in an isotropic background material. The fractures parallel to the maximum horizontal stress will be open, whereas those parallel to the minimum horizontal stress will be closed. If an azimuthally isotropic material overlies this layer, then Rüger's equation indicates the fracture properties of the underlying fractured medium and the anisotropic part of the AVO gradient describes the strike and crack density of the fractures (Rüger, 1996, Jenner, 2001 and 2002, Gray et al, 2003, Gray and Todorovic-Marinic, 2004).

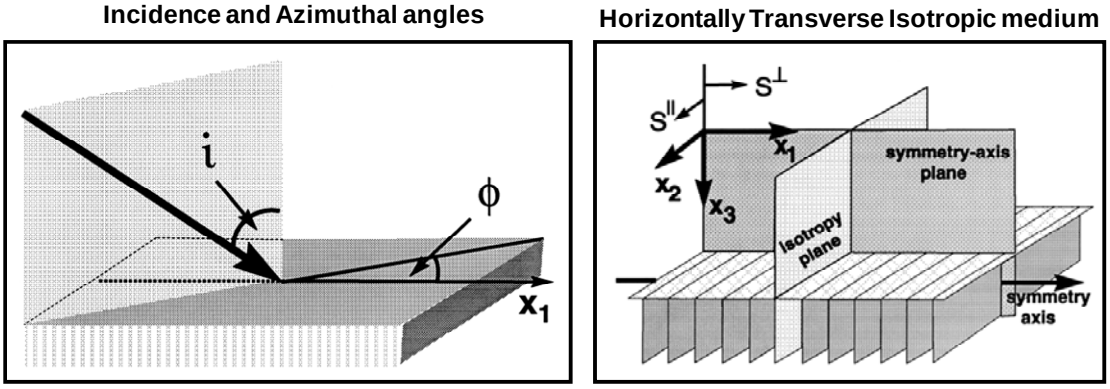


**Figure 5.1**: Left - Incidence and azimuthal angles: the reflection response from fractured reservoir depends on two angles: (1) the polar (incidence) angle $\vartheta$ between the vertical and the slowness vector of the incident wave and (2) the azimuthal angle $\varphi$ defined with respect to the symmetry axis. Right – HTI medium: Different P-wave reflection amplitudes in the two vertical symmetry planes, the symmetry-axis plane and the isotropy plane, lead to azimuthally dependent AVO response. As indicated by the arrows, shear waves polarized parallel and normal to the isotropy plane have different vertical velocities (modified from Rüger & Tsvankin, 1997).

Figure 5.2 shows an example of the multi-linear regression fit to the pre-stack amplitudes of the seismic as explained above. An estimate of the reflecting angle and an estimate of the azimuth of the incident seismic ray at the reflection point are the predictor variables (Gray et al, 2003). The multi-linear regression analysis is done at every seismic sample to estimate the parameters of Rüger's equation.

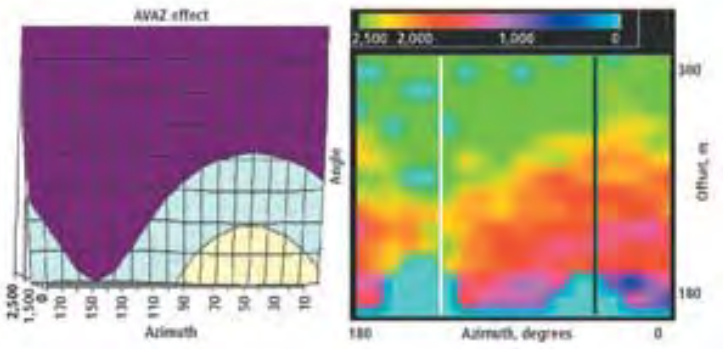


**Figure 5.2**: Top view of Rüger's model (left) compared to the amplitudes of a real seismic gather sorted into offset and azimuth (right). The amplitude correlation in the model with respect to those in the real data (blues are dead traces), suggests that the model is sufficient in itself to explain these amplitude variations (Gray et al., 2003).

These attributes contain different information that may be relevant for the identification of fracturing if the reflection comes from an HTI layer overlain by a layer that is horizontally isotropic. If so, the anisotropic gradient is closely related to seismic crack density in the underlying layer, and the azimuth of the anisotropic gradient, anisotropy azimuth, could be then the strike of the fractures in an HTI medium (Gray et al, 2003).

According to Zheng et al. (2004) the fracture density extracted from seismic data is relatively stable. However, the extracted fracture orientation is sensitive to the phase of the seismic data and the types of geological interfaces. They discovered that fracture orientation rotates 90° when the AVO intercepts polarity changes and there is no specific tie between the polarity of AVO intercept and the correct fracture orientation. Therefore, in the cases of thin layers, such as two of the ones analyzed here, the anisotropy azimuth have a 90° ambiguity that can only be resolved with additional data such as fault, fractures or stress orientation.

The assumptions taken in this analysis are the following:

- Small contrasts in elastic parameters, P-wave velocity, S-wave velocity & density, between reservoir and surrounding rock.
- Weak seismic anisotropy (Thomsen, 1986).

- The reservoir behaves as an HTI medium overlain by a horizontally isotropic medium.
- The seismic wave strikes the reservoir at small incidence angles (<35°) from the vertical.

## 5.5 APPLICATION TO TEAPOT DOME – RESULTS ANALYSIS

In this section, we present the results of the AVAZ analysis and we compare them to the fault, fracture, stress directions and macro sedimentary framework to determine whether the observed anisotropy can be related to the present day stress state or to structure (i.e. faults and fractures) or sedimentary features. The AVAZ results are presented for three seismic reflectors that correspond to three horizons: 1) top of the Tensleep Fm, here referred as Tensleep; 2) top of the Tensleep B sandstone, referred as TensleepB, which is located ~ 15 m below the Tensleep; and 3) top of the caprock, referred as Opeche, which is located ~ 20 m above the Tensleep.

The results are compared to the present day stress orientation determined in Chapter 3, from FMI logs of 5 wells in the anticline (Figure 5.3). They are also compared to fracture distributions (Figures 5.4 and 5.5) characterized in 4 of these wells, where digital FMI logs were available. Finally, they are compared to the macro fault network of the anticline, mapped by McCutcheon (2003) from the seismic volume (Figure 5.6). As explained in Chapter 3, it was determined that the present day stress state at Teapot Dome is in the limit of a normal faulting (NF) and strike-slip faulting (SS) environment. In a NF environment, the direction parallel to $S_{Hmax}$ is the optimal direction for slip; consequently, faults parallel to $S_{Hmax}$ are critically stressed and therefore permeable (Zoback, 2007). While in an SS environment, the optimal direction for slip is at 30° from $S_{Hmax}$, in either direction. We also compared the AVAZ results to $S_{Hmax+30}$ and $S_{Hmax-30}$ directions, considering that critically stressed fault will be opened and filled with fluids therefore detectable with this type of analysis.

Figure 5.3 show the wells used to calibrate the AVAZ results. Three of these wells are located in the S1 fault area (Section 10): 25-1-X-14, 67-1-X-10, and 61-2-X-15. Well 71-1-X-4 is located in the S2 area, but there was no digital FMI log available for this well, so, there is no fracture information from this borehole. The fifth well, 48-X-28, is located ~4 km north of Section 10. It has an FMI log that fully imaged the caprock and the Tensleep Fm., and has the longest continuous core in the field. Unfortunately, the core is not oriented; therefore, little information on fracture orientation can be extracted.

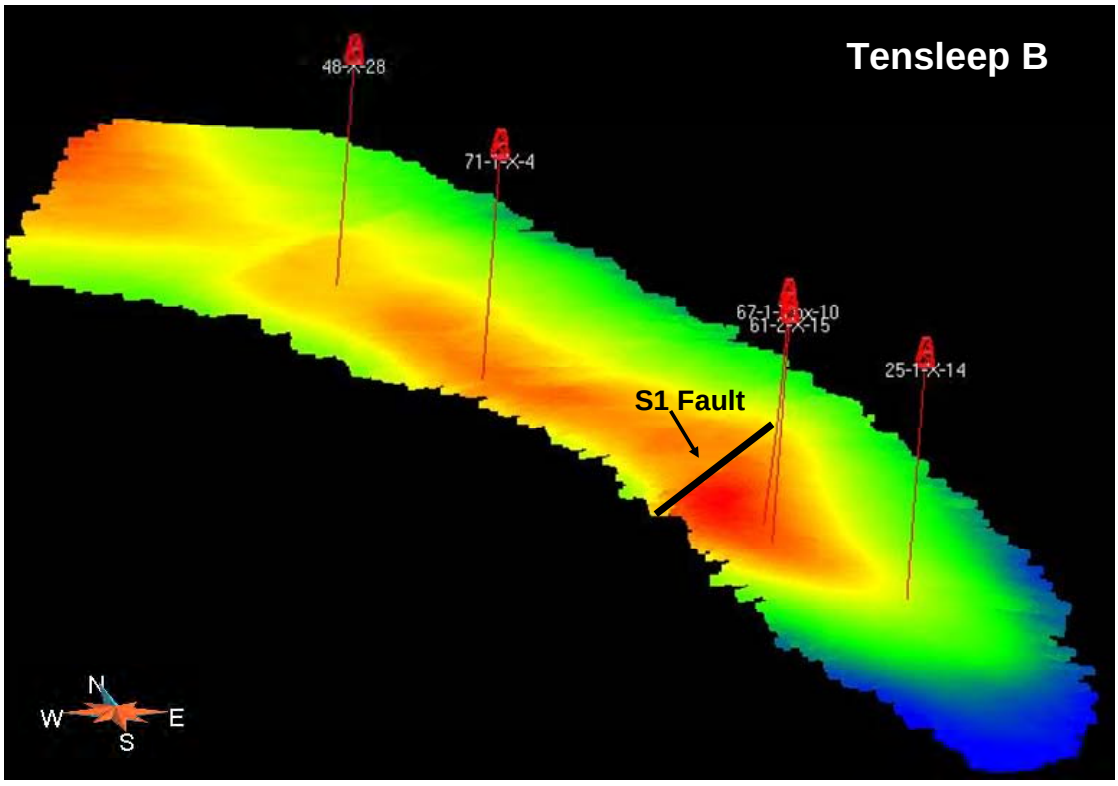


**Figure 5.3**: Time-structure map of Tensleep B showing the location of the wells used to calibrate the AVAZ results.

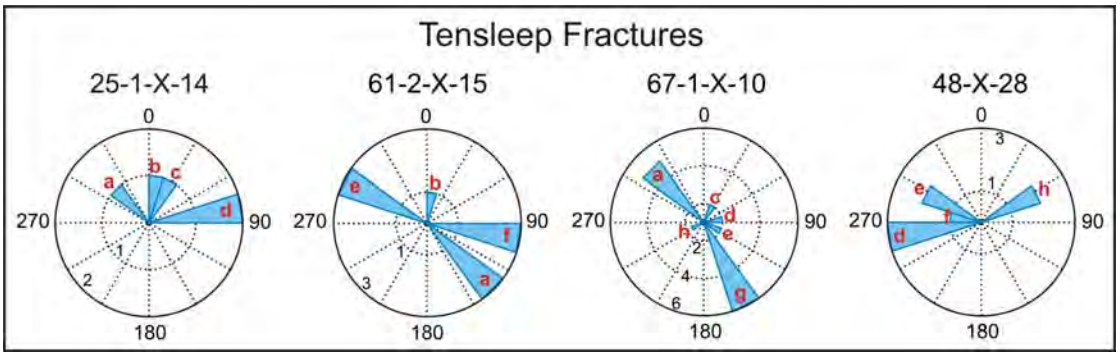


**Figure 5.4**: Rose diagrams of Tensleep Fm. fractures (including the two intervals analyzed here, Tensleep and TensleepB). The letters indicate fractures sets with different orientations. The numbers inside the plots indicate number of fractures.

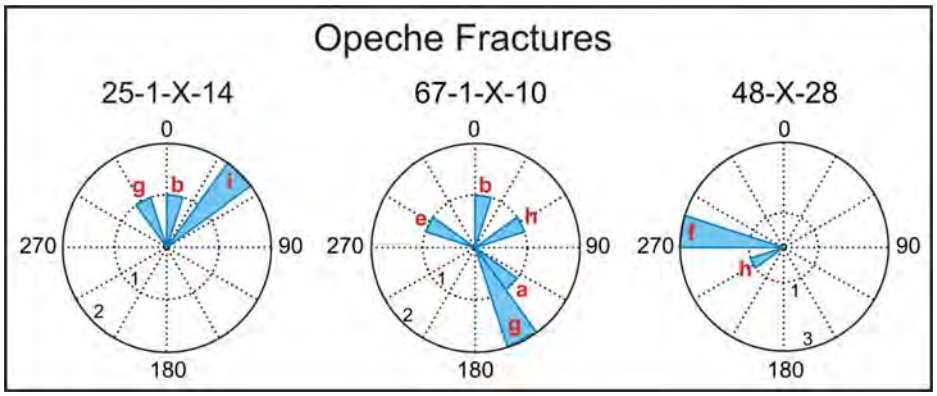


**Figure 5.5**: Rose diagrams of Opeche fractures. The letters indicate fractures sets with different orientation. The numbers inside the plots indicate number of fractures.

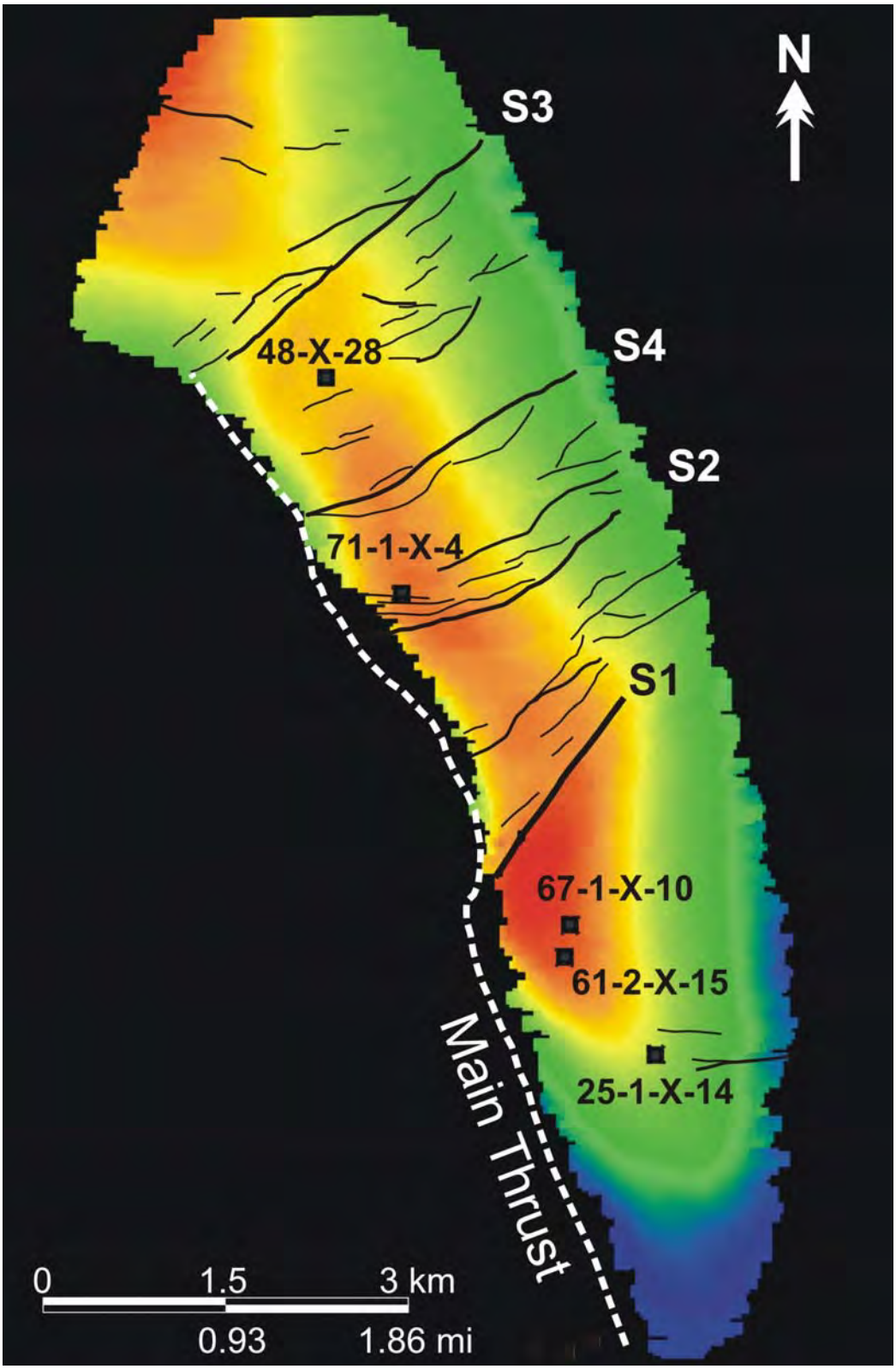


**Figure 5.6**: Time-structure map of Tensleep B showing the structural framework of the Tensleep Fm. at Teapot Dome (modified from McCutcheon, 2003).

As it can be seen in the following figures, the observed anisotropy azimuth is extremely variable throughout the anticline (Figures 5.7, 5.8 and 5.9), and preferential directions are not easily determined. Figure 5.10 shows histogram plots of anisotropy azimuth in the three horizons, where the azimuths are presented in a -90° to 90° angle scale. In this plots it appears to be a very slightly preferential direction at Az 150° ± 15° (-30° in the figure) in the Tensleep and TensleepB. This orientation also seems slightly preferential in the caprock, but in this case, the orientation Az 90° seems to be also a common. However, little conclusion can be extracted at this scale; therefore, we performed a detailed comparison analysis in the areas around the wells with stress and fracture information. We also have to consider the 90° ambiguity described in the methodology section.

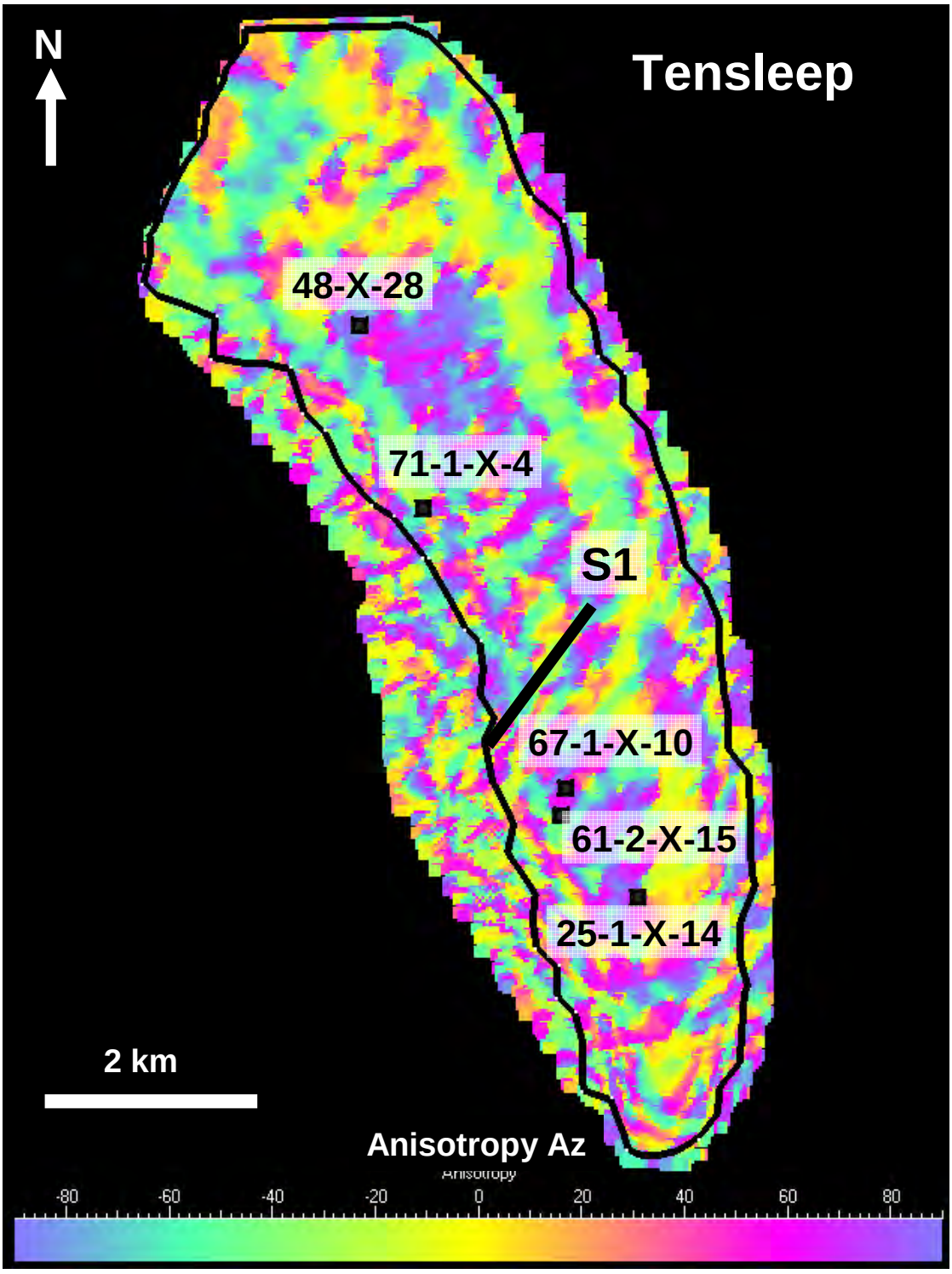


**Figure 5.7**: Azimuth of the anisotropy at the top of the Tensleep Fm. The black contour line represents approximately the limit for the seismic data. Outside of this boundary there is no meaningful anisotropy information.

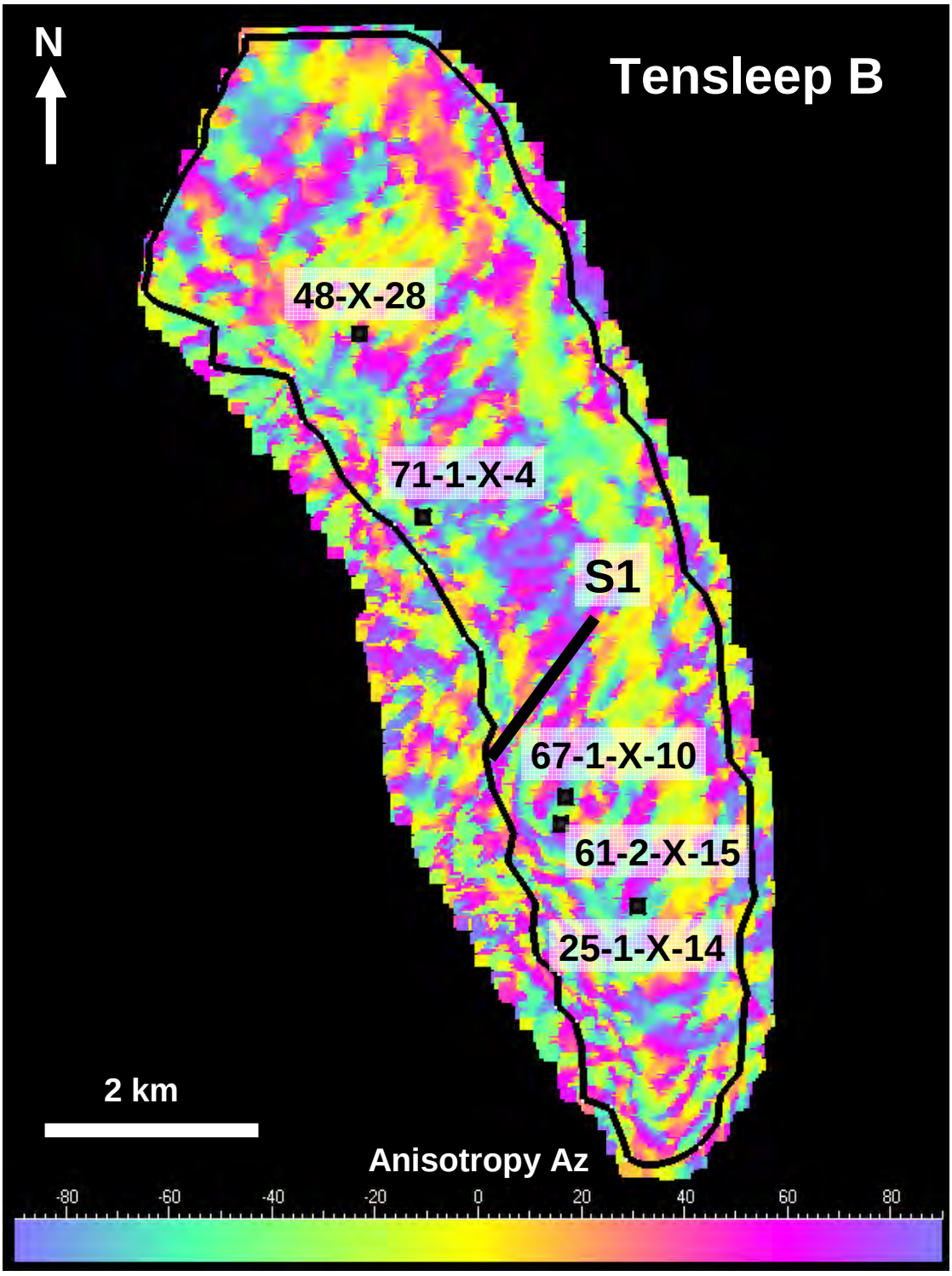


**Figure 5.8**: Azimuth of the anisotropy at the top of the TensleepB interval. The black contour line represents approximately the limit for the seismic data. Outside of this boundary there is no meaningful anisotropy information.

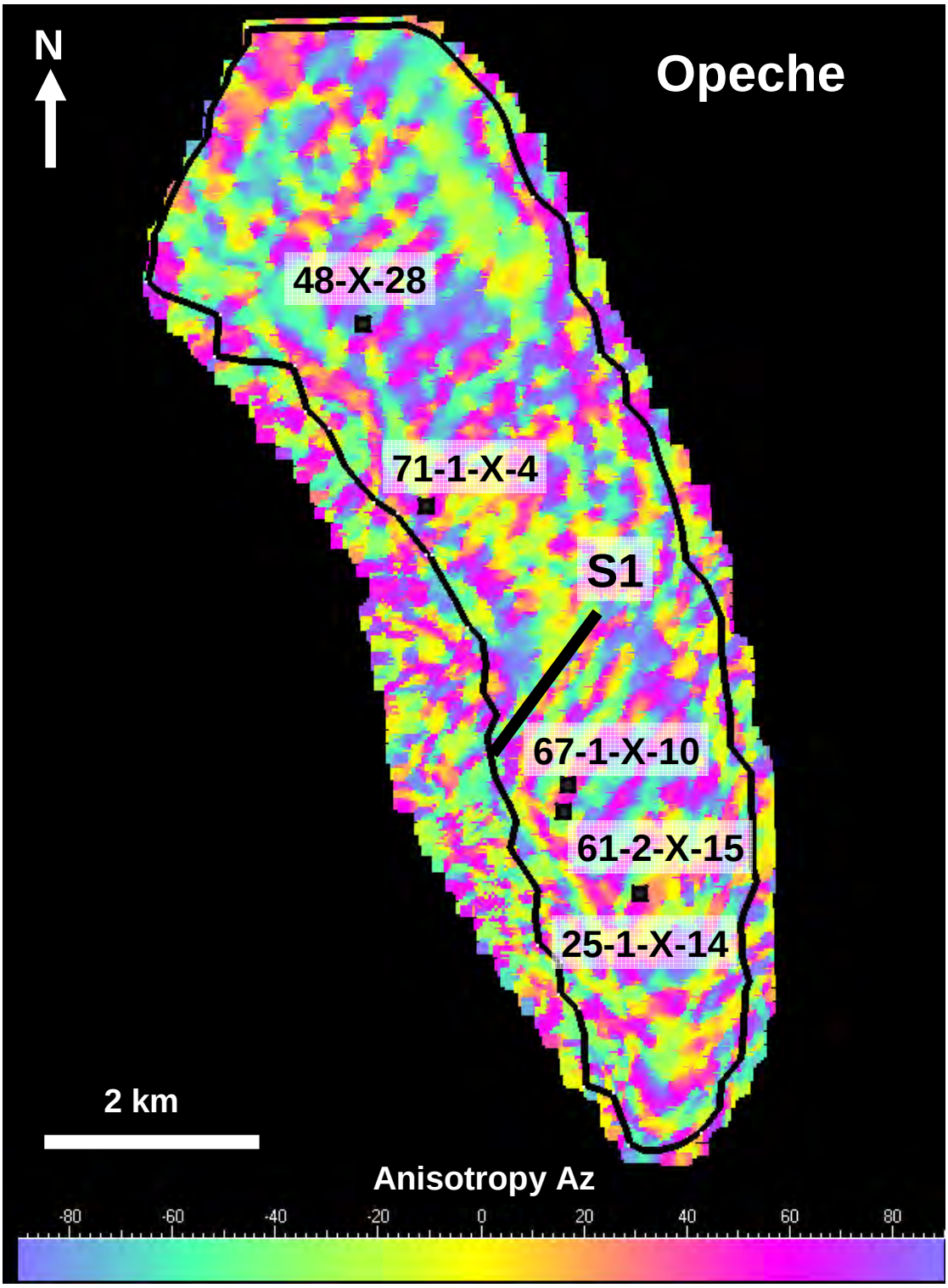


**Figure 5.9**: Azimuth of the anisotropy at the top of the caprock. The black contour line represents approximately the limit for the seismic data. Outside of this boundary there is no meaningful anisotropy information.

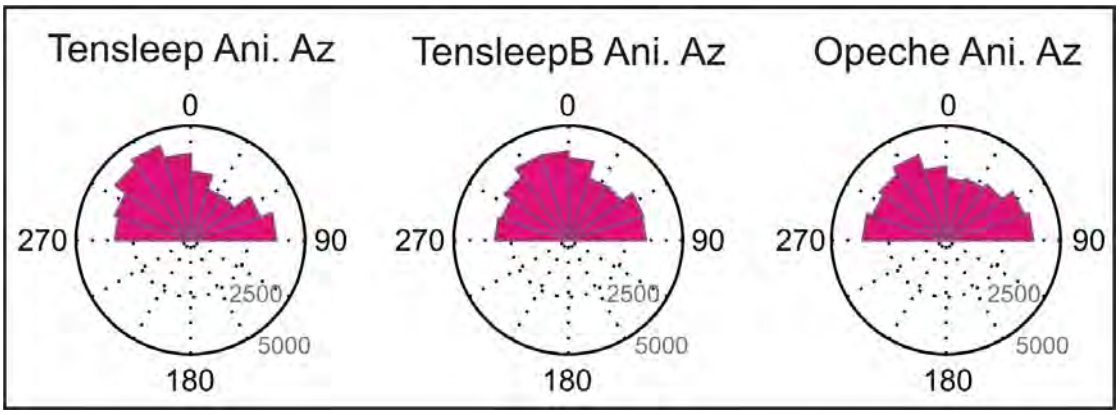


**Figure 5.10**: Angular histogram of Anisotropy Azimuth in the three horizons. Gray numbers indicate number of samples.

## 5.5.1 TENSLEEP ANISOTROPY

### *5.5.1.1 SECTION 10 – S1 FAULT AREA*

In the area denominated Section 10 there are three wells that we use to calibrate the AVAZ results: 25-1-X-14, 67-1-X-10, and 61-2-X-15. This area is south of the S1 fault network , which at the depth of the Tensleep Fm. it consist of a principal fault with a very uniform trend of Az = 36°. There is also a small synthetic fault, Az = 48°, just north of the S1, and two small faults almost E-W (Az 79° and 93°) to the south (Figure 5.7).

Figure 5.11 summarizes the comparison of the AVAZ anisotropy and the orientation of the stress, faults, and fractures around well 25-1-X-14. A detailed map is shown (bottom center) where the anisotropy azimuth is represented as vectors with different sizes indicating their abundance. The magnitude of the anisotropy is also illustrated by the color of the background, where warm colors designate higher values than cold ones. The azimuth direction is only shown if the magnitude is above an arbitrary minimum value. The figure also presents a section of the time-structure map of the Tensleep Fm. (upper left) to facilitate the comparison with the macro structural framework. Finally, the angular plot in the upper right side of the figure

shows all the orientations observed from the well and seismic: $S_{Hmax}$(red line) $S_{Hmax+30°}$ and $S_{Hmax-30°}$ (dashed red lines); major fault orientations, in this case, the S1 fault (black line) and minor fault orientations (dashed black lines); fracture sets observed in the well are represented as blue triangles. Figure 5.12 compares this mentioned directions with a rose diagram (or angular histogram) of the anisotropy azimuth in the portion represented in Figure 5.11. Even at this scale the orientation of the anisotropy is still highly variable.

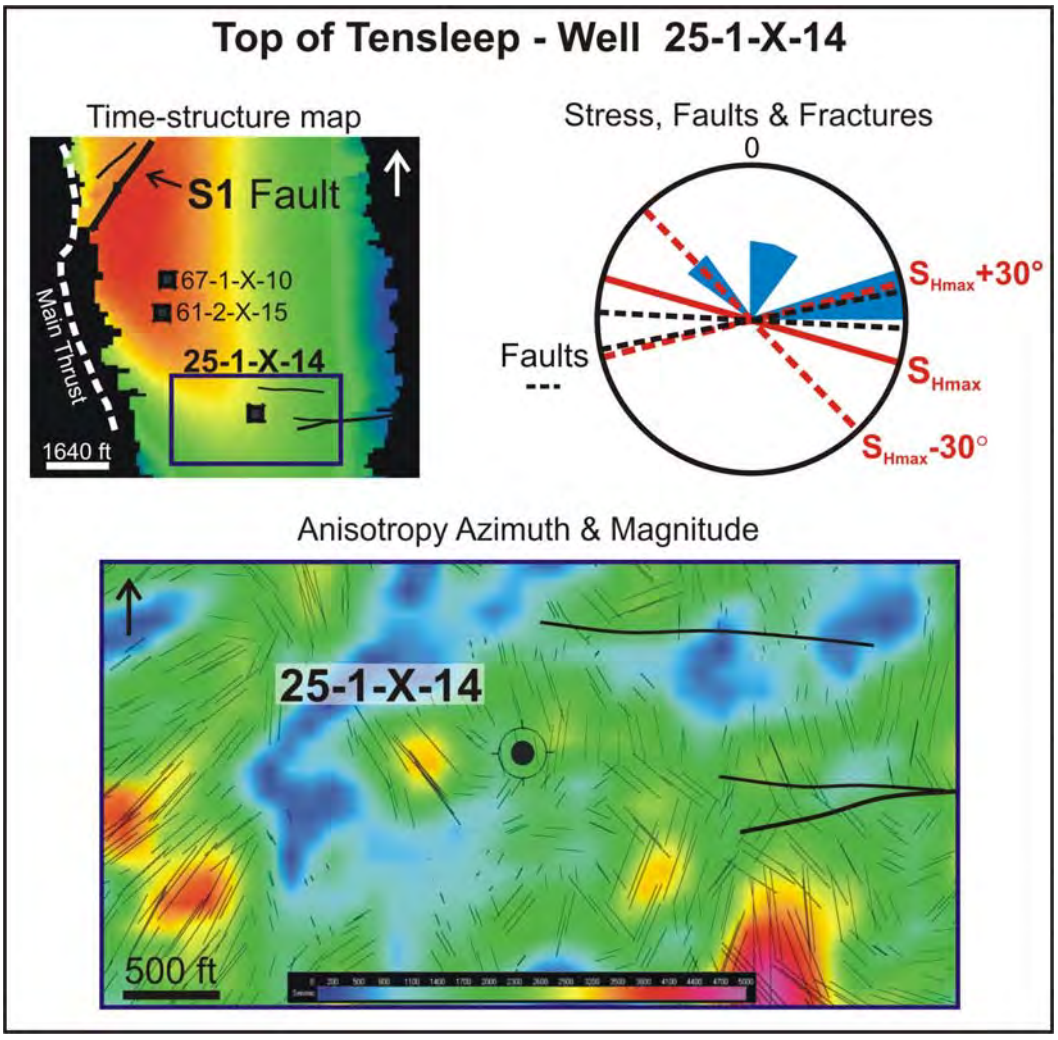


**Figure 5.11**: Tensleep Anisotropy around well 25-1-X-14. Top left: Time-structure map of Tensleep Fm. showing the faults present in the area, the location of the analyzed well and the location of the anisotropy map (blue square). Bottom center: Map representing anisotropy azimuth (thin black lines) and anisotropy magnitude (relative color scale with warm colors higher than cold colors). Top right: Angular plot of faults (from time structure map) and fractures and stress orientation (from well analysis).

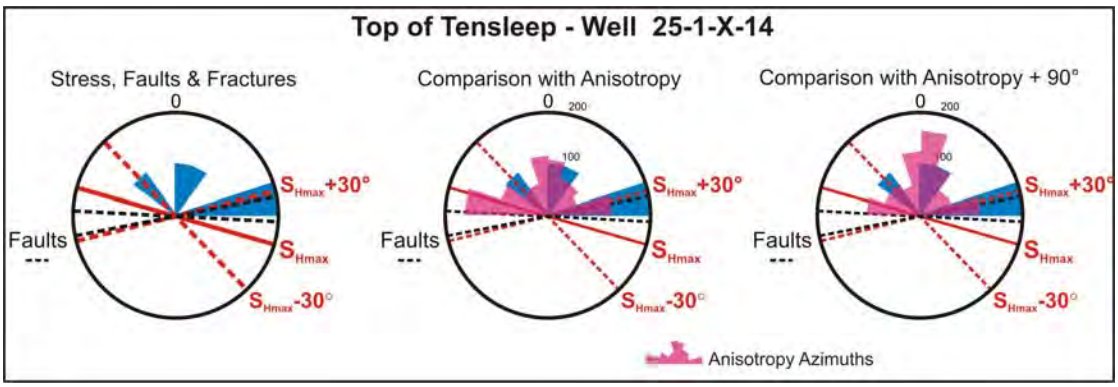


**Figure 5.12**: Comparison of AVAZ anisotropy azimuths (magenta) with stress fracture and fault orientation from seismic and well data in the area around well 25-1-X-14 (see Figure 11). The anisotropy orientations are also rotated 90° to account for the sign ambiguity.

We performed similar comparisons as the one described in the previous paragraphs for all the wells in each of the three horizons (Figure 5.13 to 5.38). In some cases there were no available digital FMI logs, as in well 71-1-X-4, or the interval was not imaged, as in the case of the caprock in well 61-2-X-15. Therefore, no well fracture information was available, and the AVAZ results calibration was done only with the stress and faults orientations. In all the cases the results were similar, the orientation of the AVAZ cracks contained at least one of the stress related directions and orientations related with either faults, fractures or both. Table 5.2 summarizes these results.

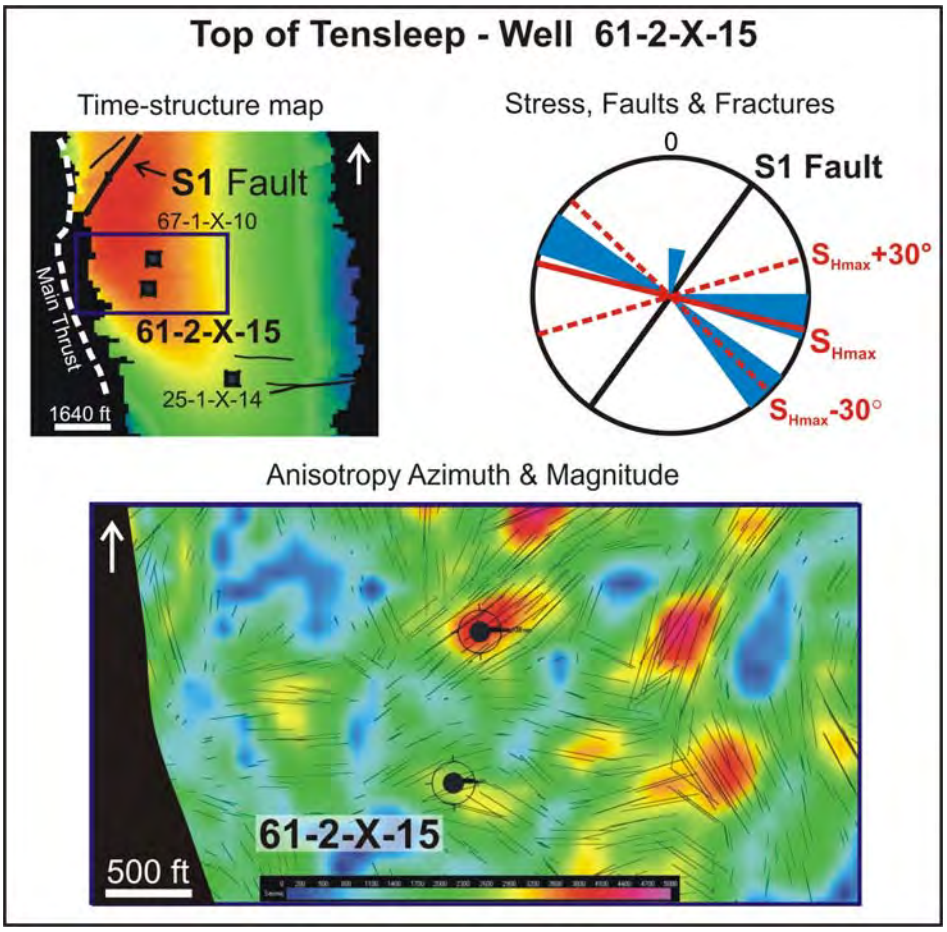


**Figure 5.13**: Tensleep Anisotropy around well 61-2-X-15. Top left: Time-structure map of Tensleep Fm. showing the faults present in the area, the location of the analyzed well and the location of the anisotropy map (blue square). Bottom center: Map representing anisotropy azimuth (thin black lines) and anisotropy magnitude (relative color scale with warm colors higher than cold colors). Top right: Angular plot of faults (from time-structure map) and fractures and stress orientation (from well analysis).

.

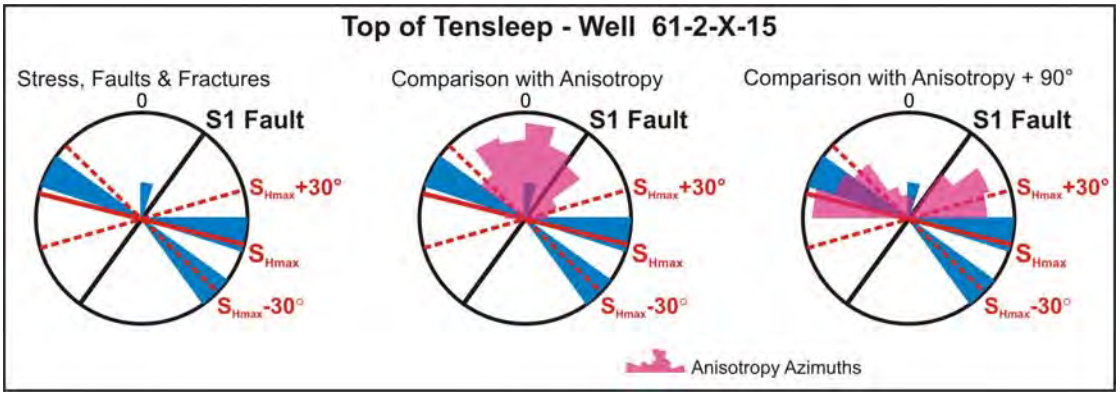


**Figure 5.14**: Comparison of AVAZ anisotropy azimuths (magenta) with stress fracture and fault orientation from seismic and well data in the area around well 61-2-X-15 (see Figure 5.13). The anisotropy orientations are also rotated 90° to account for the sign ambiguity.

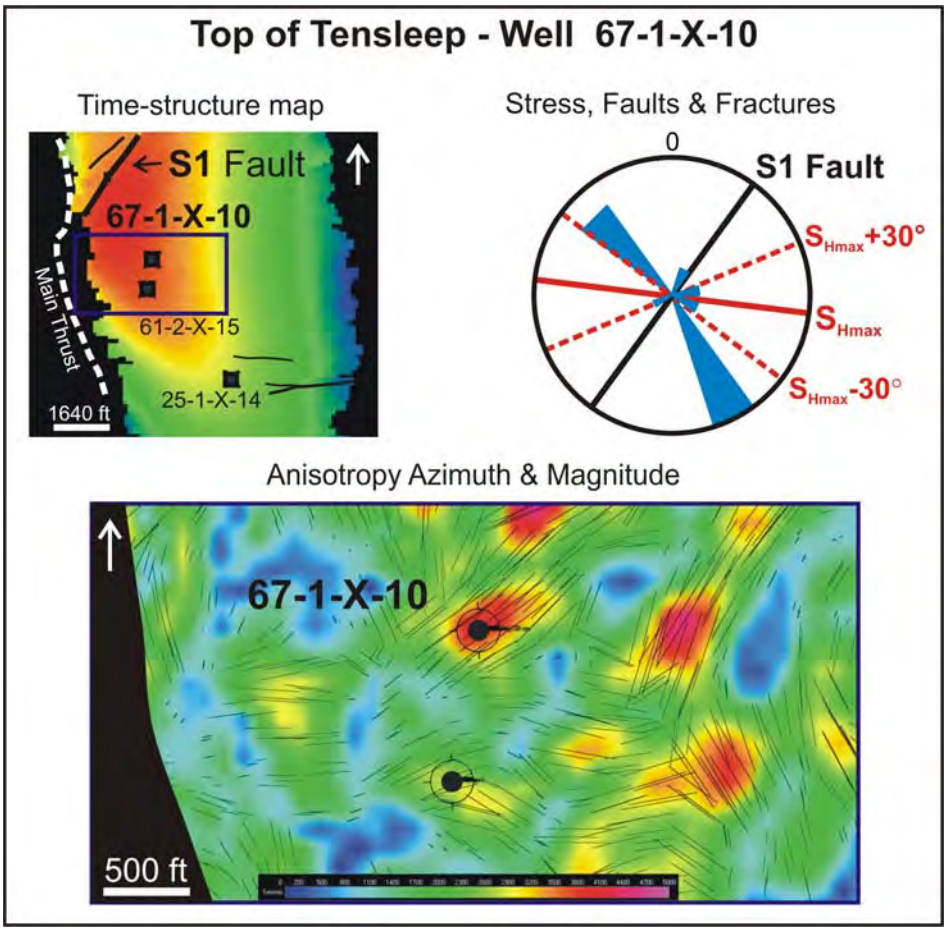


**Figure 5.15**: Tensleep Anisotropy around well 67-1-X-10. Top left: Time-structure map of Tensleep Fm. showing the faults present in the area, the location of the analyzed well and the location of the anisotropy map (blue square). Bottom center: Map representing anisotropy azimuth (thin black lines) and anisotropy magnitude (relative color scale with warm colors higher than cold colors). Top right: Angular plot of faults (from time-structure map) and fractures and stress orientation (from well analysis).

.

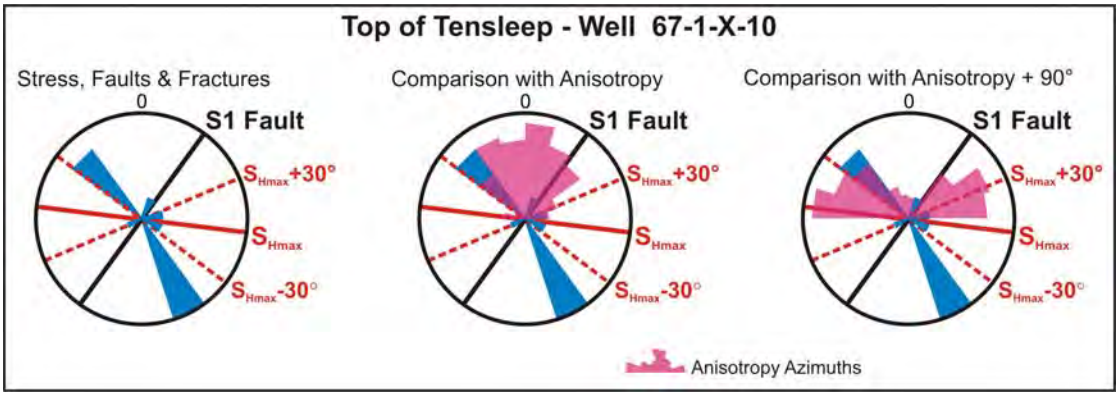


**Figure 5.16**: Comparison of AVAZ anisotropy azimuths (magenta) with stress fracture and fault orientation from seismic and well data in the area around well 67-1-X-10 (see Figure 5.15). The anisotropy orientations are also rotated 90° to account for the sign ambiguity.

*5.5.1.2 S2 FAULT AREA*

Well 71-1-X-4 is located on the S2 fault zone close to northern S4 fault zone. This area is structurally much more complex than Section 10. There is not a distinct main fault, but rather a set of faults with a different azimuths ranging from approximately 36° Az (similar to the S1 fault) to 95° Az; however, the general trend is closer to the E-W direction. It is noticeable in the anisotropy map at the Tensleep level (Figure 5.17) how the crack orientations seem to follow this high range of azimuth almost circling around the well. As mentioned before, there is not fracture characterization in this well to compare it with.

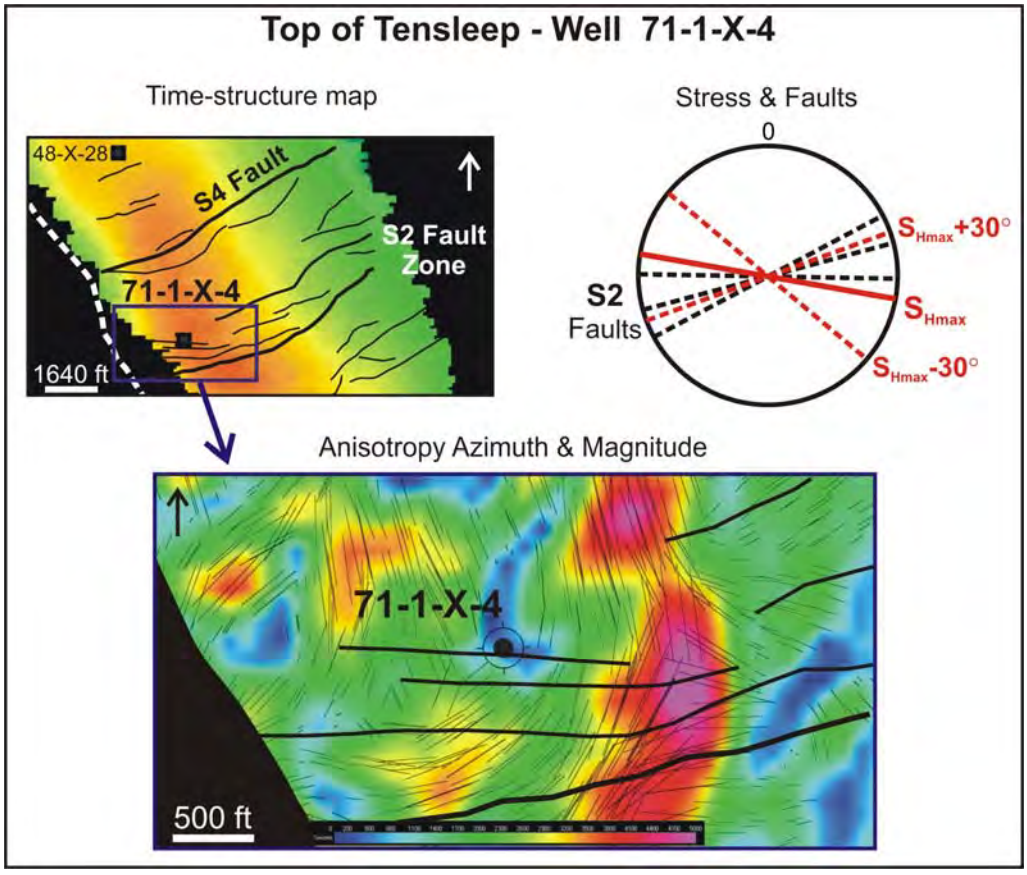


**Figure 5.17**: Tensleep Anisotropy around well 71-1-X-4. Top left: Time-structure map of Tensleep Fm. showing the faults present in the area, the location of the analyzed well and the location of the anisotropy map (blue square). Bottom center: Map representing anisotropy azimuth (thin black lines) and anisotropy magnitude (relative color scale with warm colors higher than cold colors). Top right: Angular plot of faults (from time structure map) and fractures and stress orientation (from well analysis).

.

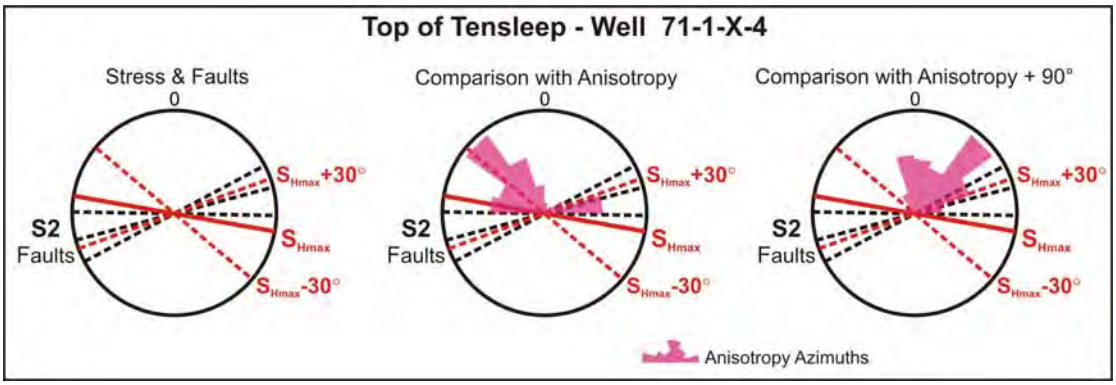


**Figure 5.18**: Comparison of AVAZ anisotropy azimuths (magenta) with stress fracture and fault orientation from seismic and well data in the area around well 71-1-X-4 (see Figure 5.17). The anisotropy orientations are also rotated 90° to account for the sign ambiguity.

#### 5.5.1.3 S3-S4 FAULT AREA

Well 48-X-28 is located in between the S3 and S4 fault zones. Even if less structurally complex than the S2 fault area, there is still a range of azimuths in the faults. However, the anisotropy seems to be less significant than in the previous cases, and its orientation is more uniform.

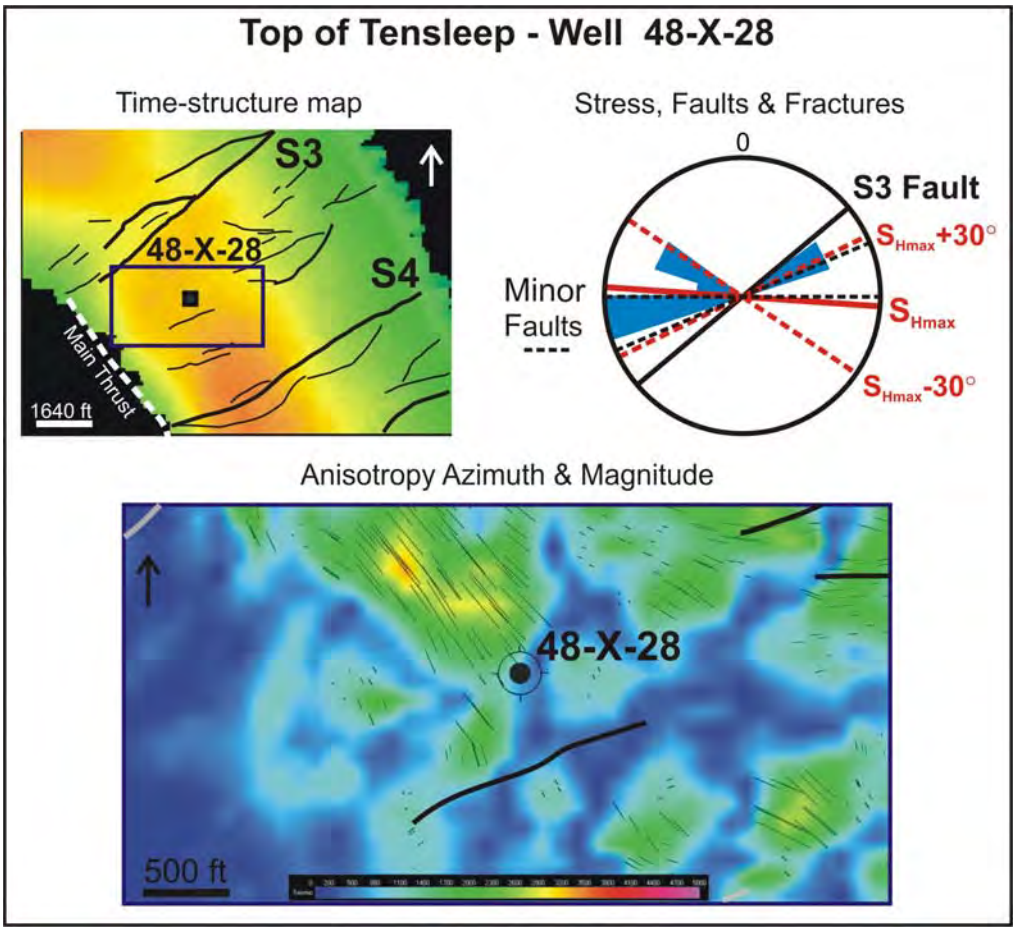


**Figure 5.19**: Tensleep Anisotropy around well 48-X-28. Top left Time-structure map of Tensleep Fm. showing the faults present in the area, the location of the analyzed well and the location of the anisotropy map (blue square). Bottom center: Map representing anisotropy azimuth (thin black lines) and anisotropy magnitude (relative color scale with warm colors higher than cold colors). Top right: Angular plot of faults (from time-structure map) and fractures and stress orientation (from well analysis).

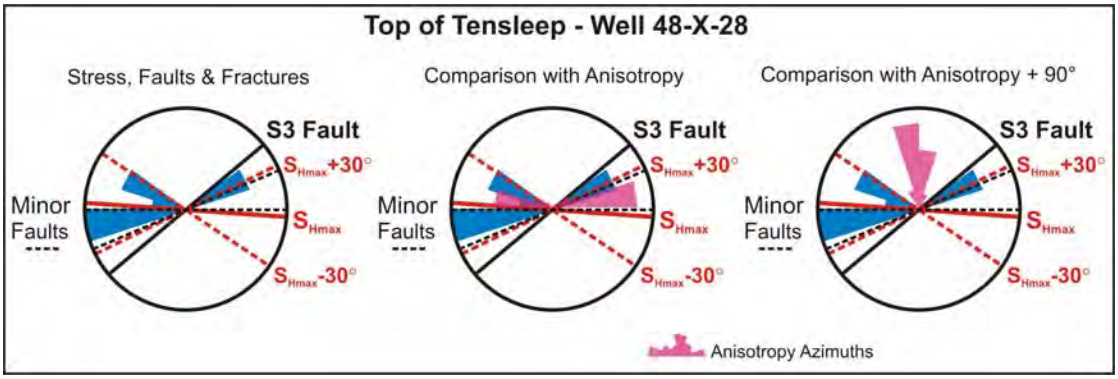


**Figure 5.20**: Comparison of AVAZ anisotropy azimuths (magenta) with stress fracture and fault orientation from seismic and well data in the area around well 48-X-28 (see Figure 5.19). The anisotropy orientations are also rotated 90° to account for the sign ambiguity.

We visually compared anisotropy magnitude with fracture count to see if there is any correlation among them. We observed that well 67-1-X-10 is the one located in the highest magnitude region, which is in agreement with the fracture characterization data (Table 5.1), where this well is also the one that presents the highest fracture count. Following a similar reasoning, well 48-X-28 is the one located in the lowest crack density region, however, it is not the one which presents the lower fracture count.

| | **No. of Total Fractures Tensleep Fm.** | **No. of Total fractures Opeche interval** |
|---|---|---|
| **25-1-X-14** | 5 | 4 |
| **61-2-X-15** | 10 | - |
| **67-1-X-10** | 18 | 6 |
| **48-X-28** | 8 | 4 |

**Table 5.1**: Total number of fractures mapped from the FMI logs in each of the wells.

### 5.5.2 TENSLEEPB ANISOTROPY

The anisotropy in the TensleepB seems to have a little less scatter than in the Tensleep interval, but again it shows anisotropy directions parallel to both of the stress and faults and fracture orientations.

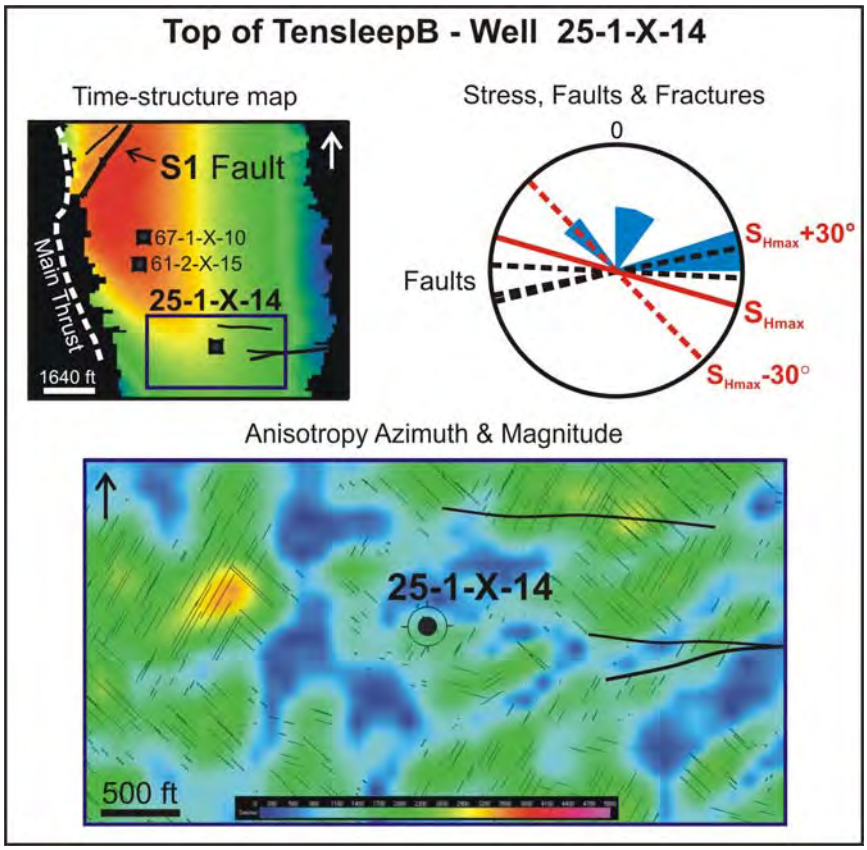


**Figure 5.21**: TensleepB Anisotropy around well 25-1-X-14. Top left: Time-structure map of Tensleep Fm. showing the faults present in the area, the location of the analyzed well and the location of the anisotropy map (blue square). Bottom center: Map representing anisotropy azimuth (thin black lines) and anisotropy magnitude (relative color scale with warm colors higher than cold colors). Top right: Angular plot of faults (from time-structure map) and fractures and stress orientation (from well analysis).

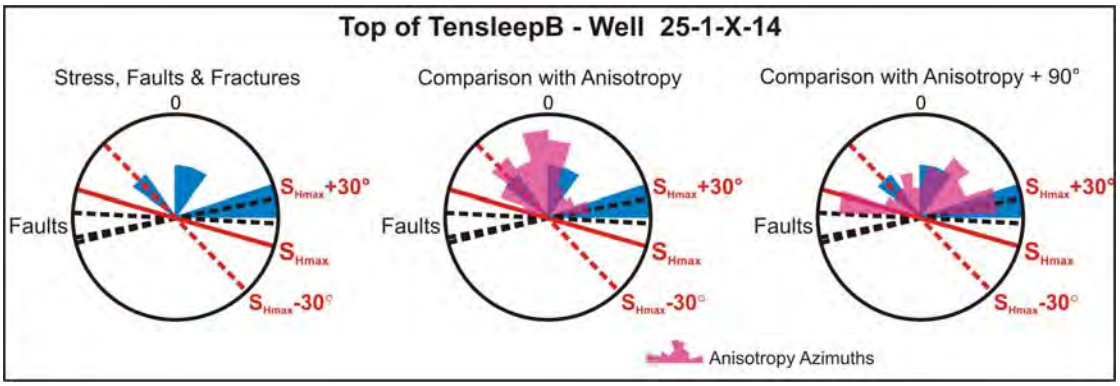


**Figure 5.22**: Comparison of AVAZ anisotropy azimuths (magenta) with stress fracture and fault orientations from seismic and well data in the area around well 25-1-X-14 (see Figure 5.21). The anisotropy orientations are also rotated 90° to account for the sign ambiguity.

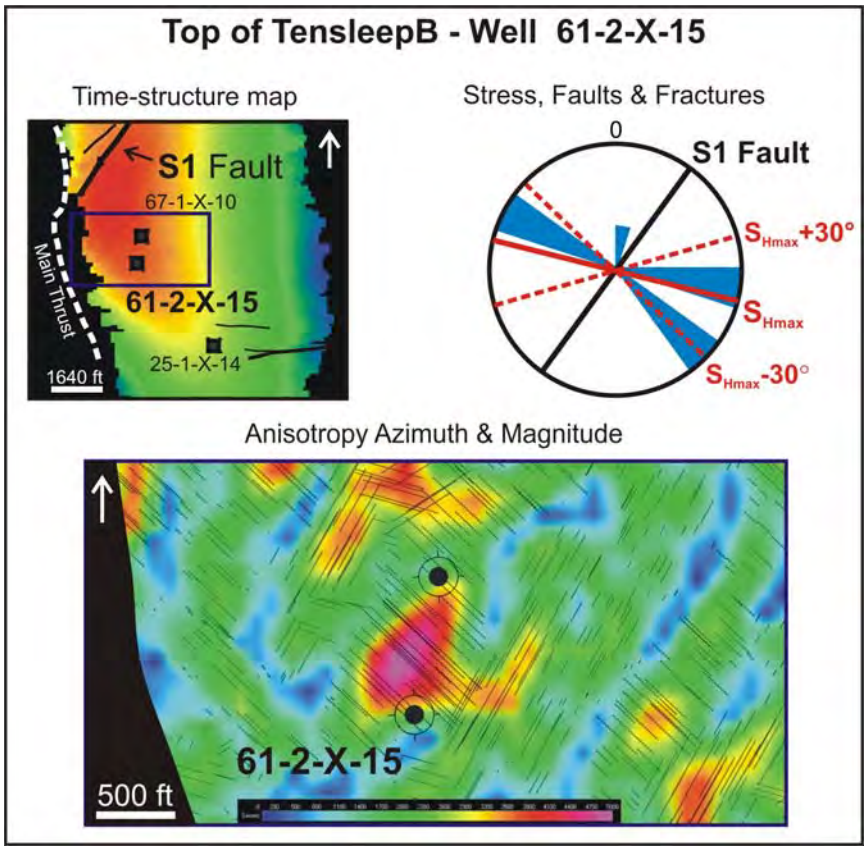


**Figure 5.23**: TensleepB Anisotropy around well 61-2-X-15. Top left: Time-structure map of Tensleep Fm. showing the faults present in the area, the location of the analyzed well and the location of the anisotropy map (blue square). Bottom center: Map representing anisotropy azimuth (thin black lines) and anisotropy magnitude (relative color scale with warm colors higher than cold colors). Top right: Angular plot of faults (from time-structure map) and fractures and stress orientation (from well analysis).

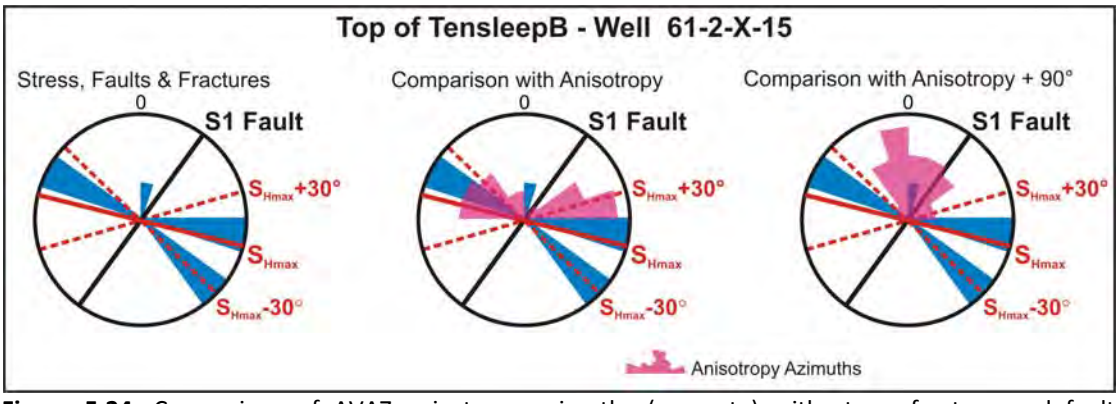


**Figure 5.24**: Comparison of AVAZ anisotropy azimuths (magenta) with stress fracture and fault orientations from seismic and well data in the area around well 61-2-X-15 (see Figure 5.23). The anisotropy orientations are also rotated 90° to account for the sign ambiguity.

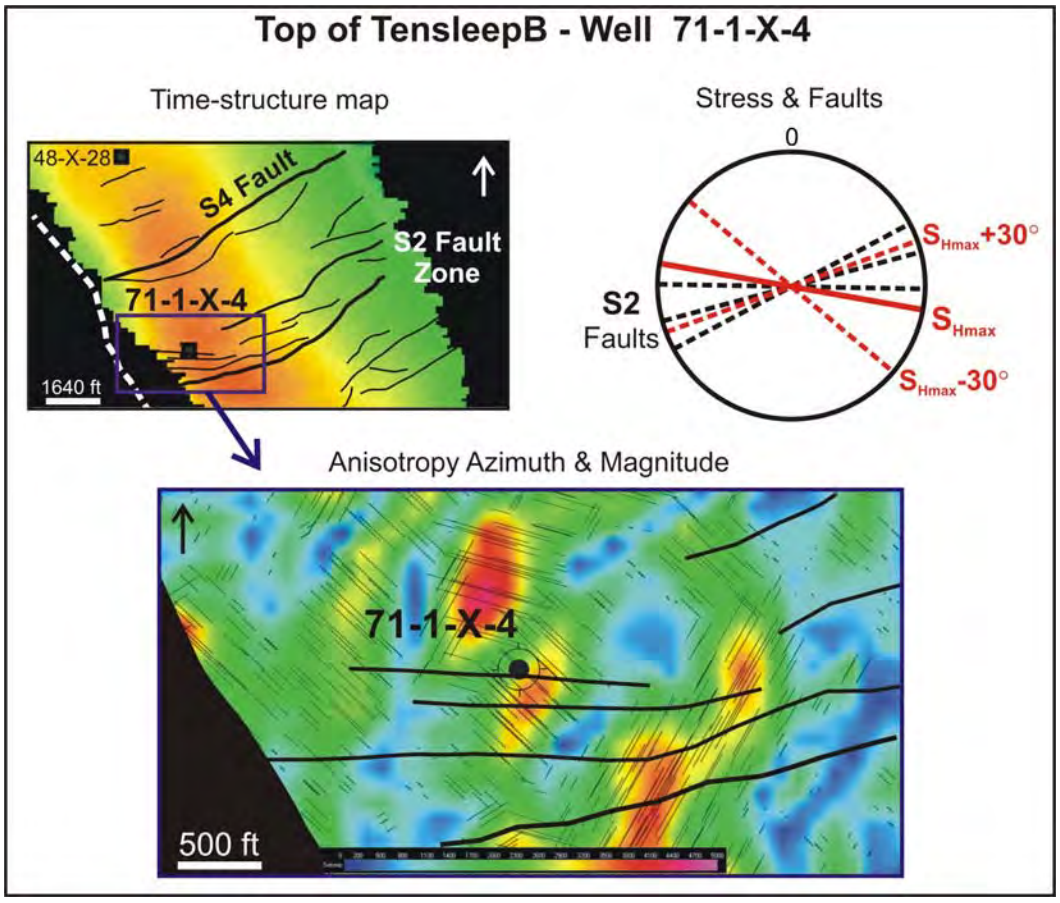


**Figure 5.25**: TensleepB Anisotropy around well 71-1-X-4. Top left: Time-structure map of Tensleep Fm. showing the faults present in the area, the location of the analyzed well and the location of the anisotropy map (blue square). Bottom center: Map representing anisotropy azimuth (thin black lines) and anisotropy magnitude (relative color scale with warm colors higher than cold colors). Top right: Angular plot of faults (from time structure map) and fractures and stress orientation (from well analysis).

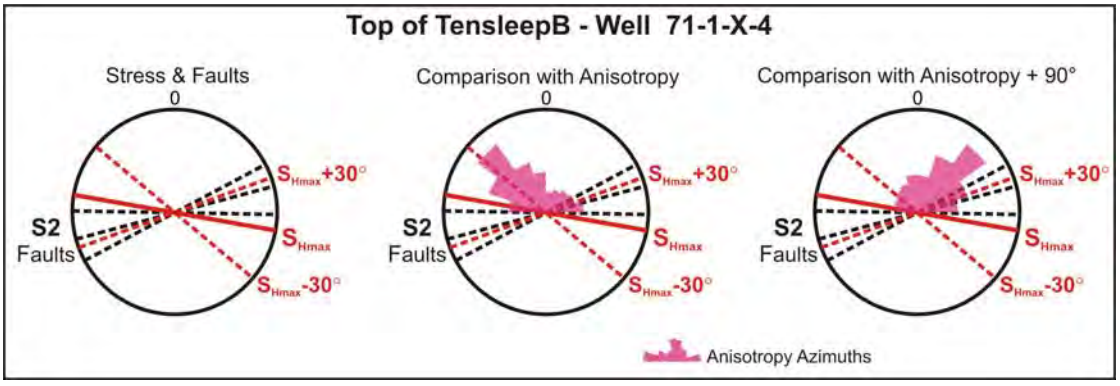


**Figure 5.26**: Comparison of AVAZ anisotropy azimuths (magenta) with stress fracture and fault orientations from seismic and well data in the area around well 71-1-X-4 (see Figure 5.25). The anisotropy orientations are also rotated 90° to account for the sign ambiguity.

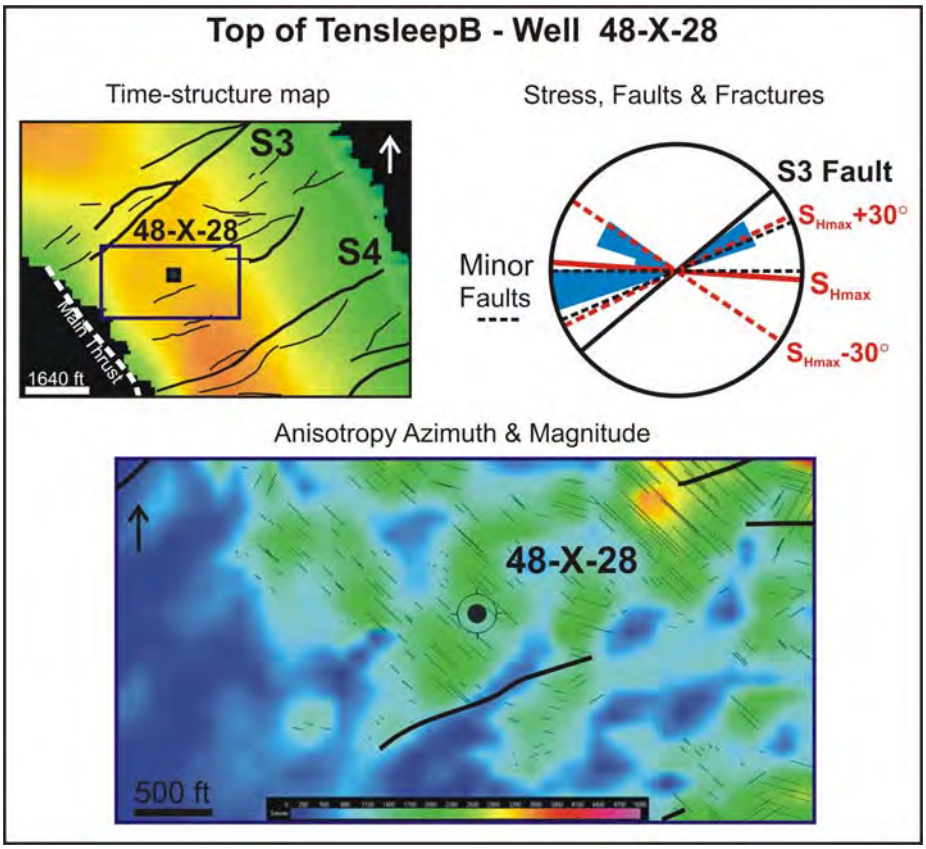


**Figure 5.27**: TensleepB Anisotropy around well 48-X-28. Top left: Time-structure map of Tensleep Fm. showing the faults present in the area, the location of the analyzed well and the location of the anisotropy map (blue square). Bottom center: Map representing anisotropy azimuth (thin black lines) and anisotropy magnitude (relative color scale with warm colors higher than cold colors). Top right: Angular plot of faults (from time-structure map) and fractures and stress orientation (from well analysis).

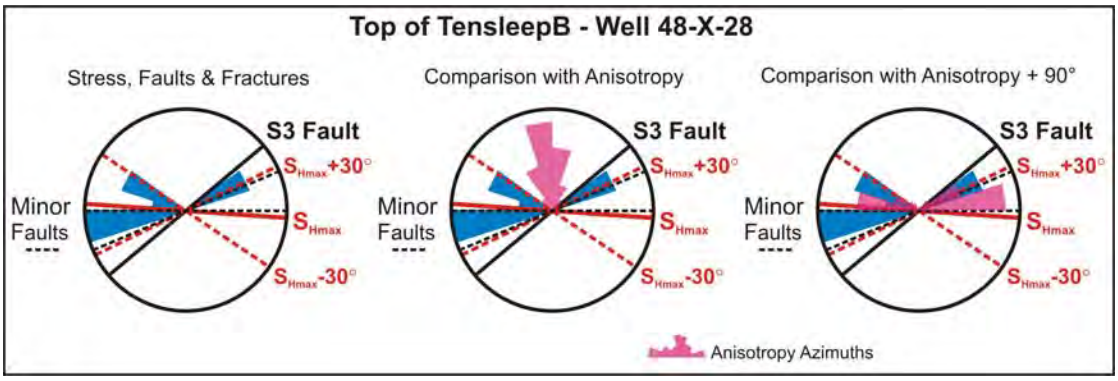


**Figure 5.28**: Comparison of AVAZ anisotropy azimuths (magenta) with stress fracture and fault orientations from seismic and well data in the area around well 48-X-28 (see Figure 5.27). The anisotropy orientations are also rotated 90° to account for the sign ambiguity.

Comparing anisotropy magnitude in the TensleepB to total fracture count in the Tensleep Fm. (Table 5.1), well 61-1-X-15 and 67-1-X-10 are located in very similar and highest regions, and are the two wells with highest fracture counts. However, well 67-1-X-10 has almost double fracture count and that is not reflected in the AVAZ magnitude values. Likewise, well 25-1-X-14 and well 48-X-28 are located in similar and lower crack density regions, and are also the ones with the lowest fracture count.

### 5.5.3 OPECHE ANISOTROPY

The comparison of azimuth orientation to stress, fault and fracture orientations in the Opeche, follows the same pattern than in the other two horizons. The anisotropy azimuths coincide with both stress and structural related orientations.

The magnitudes, however, seem higher than expected. This is particularly notorious in Section 10 where the existing hydrocarbon accumulation suggests that caprock integrity has not been compromised in the near past, as it could have been if the Opeche was highly fractured as these results hint. But again, crack density from the AVAZ results is a model dependent relative parameter that would need to be numerically calibrated against measured crack densities in the field. From the few data points we have in the Opeche interval, there is little difference in the fracture count of wells 25-1-X-14, 67-1-X-10 and 48-X-28 (Table 5.1), and they are located also in similar regions regarding anisotropy magnitude. Unfortunately, we do not have information about the fracture count in well 71-1-X-4, which is the one located at the minimum crack density region from the AVAZ results to see whether this was correlated with well data.

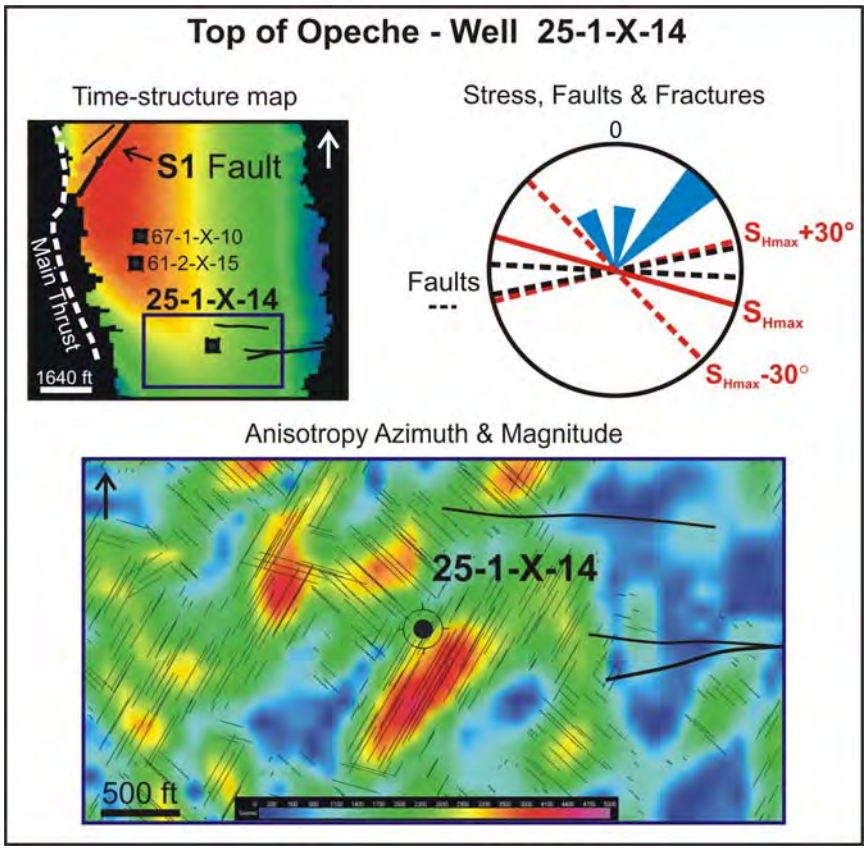


**Figure 5.29**: Opeche Anisotropy around well 25-1-X-14. Top left: Time-structure map of Tensleep Fm. showing the faults present in the area, the location of the analyzed well and the location of the anisotropy map (blue square). Bottom center: Map representing anisotropy azimuth (thin black lines) and anisotropy magnitude (relative color scale with warm colors higher than cold colors). Top right: Angular plot of faults (from time structure map) and fractures and stress orientation (from well analysis).

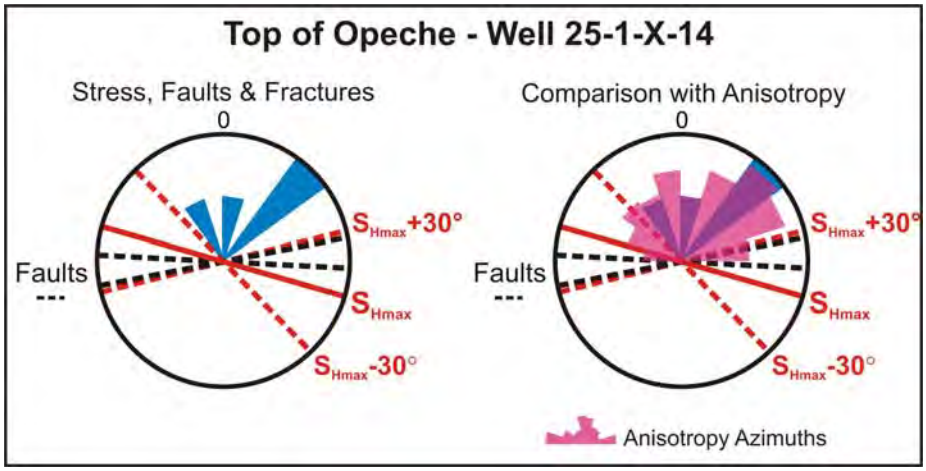


**Figure 5.30**: Comparison of AVAZ anisotropy azimuths (magenta) with stress fracture and fault orientations from seismic and well data in the area around well 25-1-X-14 (see Figure 5.29). The anisotropy orientations are also rotated 90° to account for the sign ambiguity.

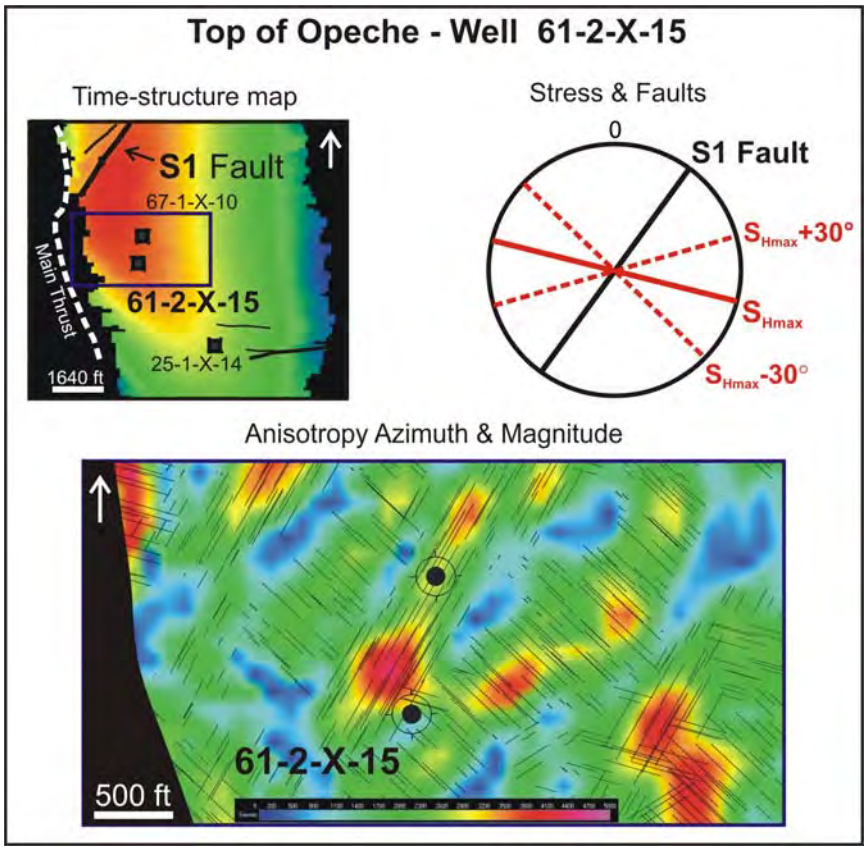


**Figure 5.31**: Opeche Anisotropy around well 61-2-X-15. Top left: Time-structure map of Tensleep Fm. showing the faults present in the area, the location of the analyzed well and the location of the anisotropy map (blue square). Bottom center: Map representing anisotropy azimuth (thin black lines) and anisotropy magnitude (relative color scale with warm colors higher than cold colors). Top right: Angular plot of faults (from time structure map) and fractures and stress orientation (from well analysis).

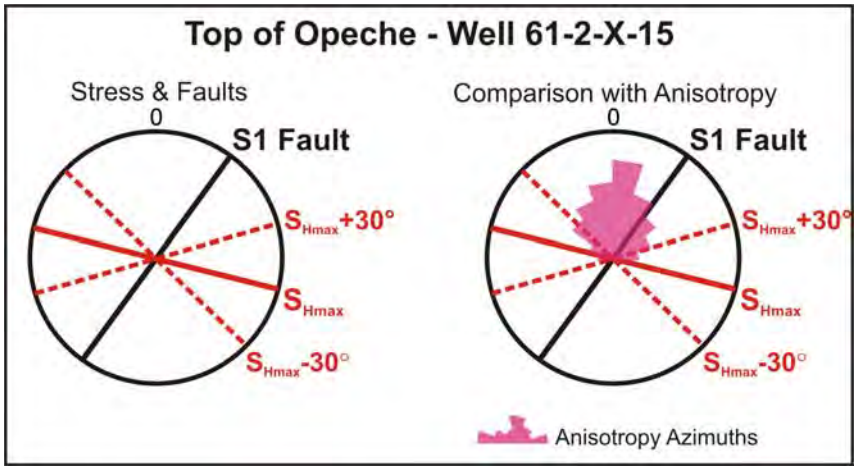


**Figure 5.32**: Comparison of AVAZ anisotropy azimuths (magenta) with stress fracture and fault orientations from seismic and well data in the area around well 61-2-X-15 (see Figure 5.31). The anisotropy orientations are also rotated 90° to account for the sign ambiguity.

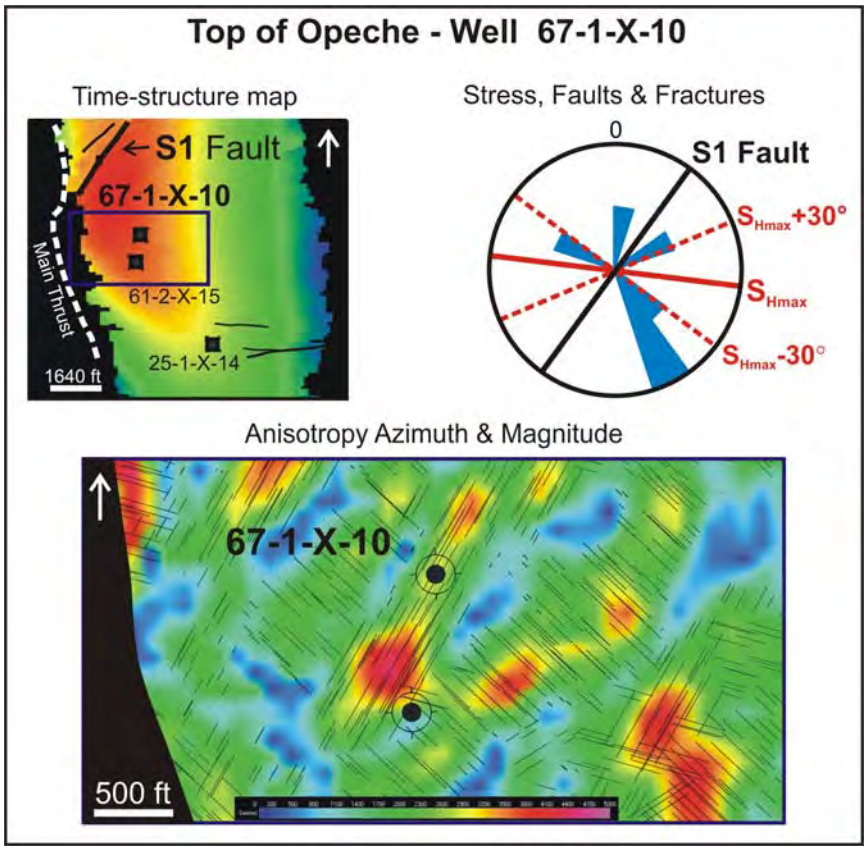


**Figure 5.33**: Opeche Anisotropy around well 67-1-X-10. Top left: Time-structure map of Tensleep Fm. showing the faults present in the area, the location of the analyzed well and the location of the anisotropy map (blue square). Bottom center: Map representing anisotropy azimuth (thin black lines) and anisotropy magnitude (relative color scale with warm colors higher than cold colors). Top right: Angular plot of faults (from time structure map) and fractures and stress orientation (from well analysis).

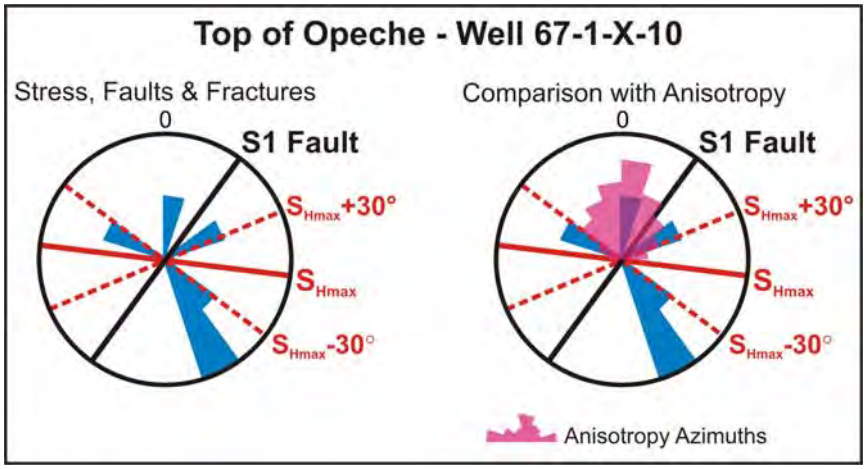


**Figure 5.34**: Comparison of AVAZ anisotropy azimuths (magenta) with stress fracture and fault orientations from seismic and well data in the area around well 67-1-X-10 (see Figure 5.33). The anisotropy orientations are also rotated 90° to account for the sign ambiguity.

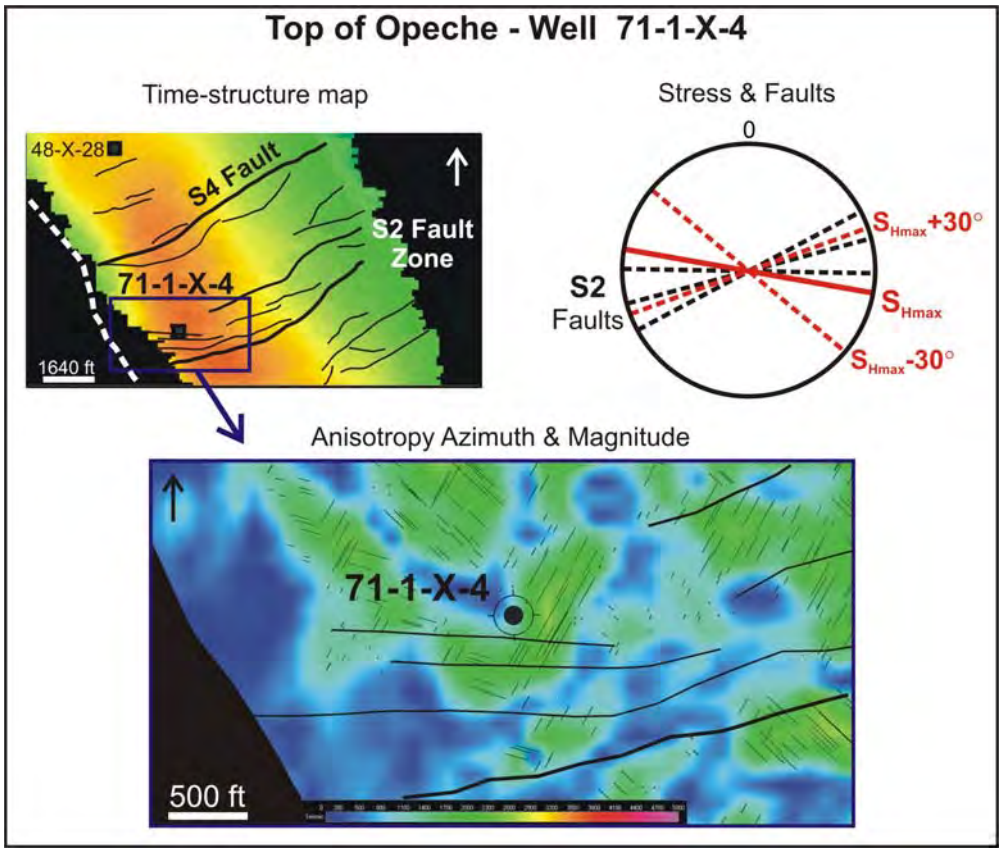


**Figure 5.35**: Opeche Anisotropy around well 71-1-X-4. Top left: Time-structure map of Tensleep Fm. showing the faults present in the area, the location of the analyzed well and the location of the anisotropy map (blue square). Bottom center: Map representing anisotropy azimuth (thin black lines) and anisotropy magnitude (relative color scale with warm colors higher than cold colors). Top right: Angular plot of faults (from time structure map) and fractures and stress orientation (from well analysis).

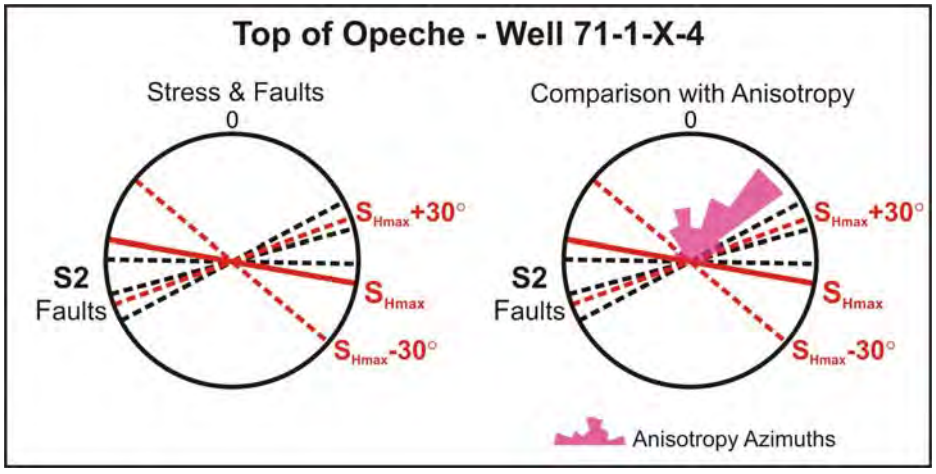


**Figure 5.36**: Comparison of AVAZ anisotropy azimuths (magenta) with stress fracture and fault orientations from seismic and well data in the area around well 71-1-X-14 (see Figure 5.35). The anisotropy orientations are also rotated 90° to account for the sign ambiguity.

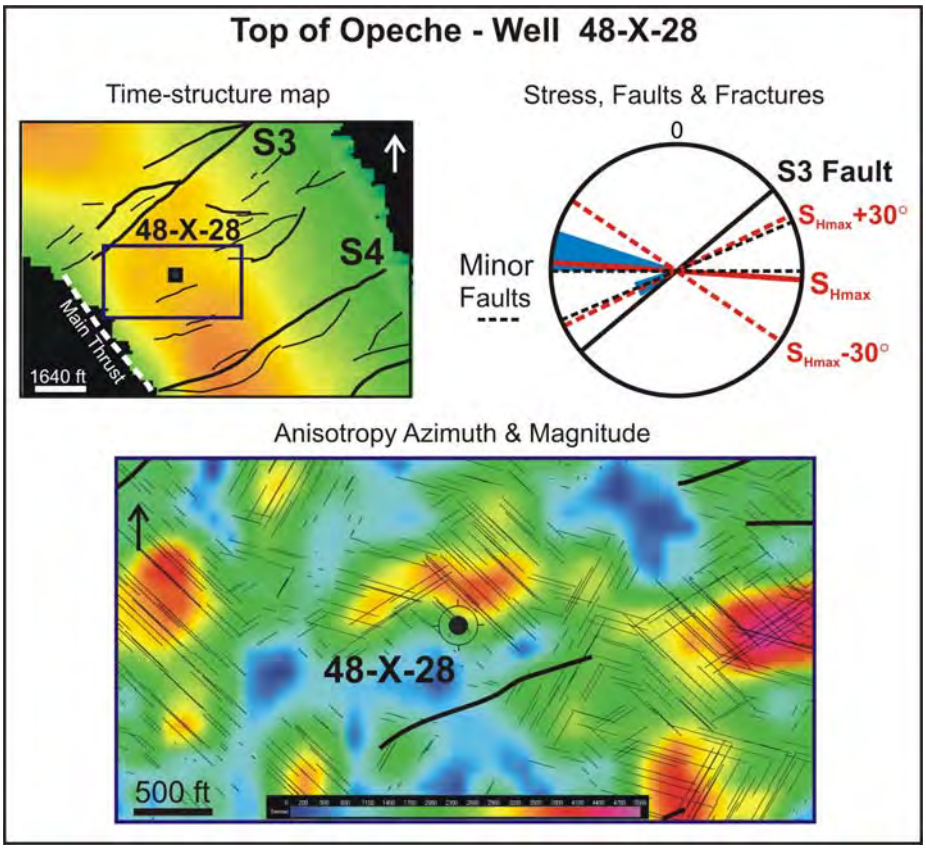


**Figure 5.37**: Opeche Anisotropy around well 48-X-28. Top left: Time-structure map of Tensleep Fm. showing the faults present in the area, the location of the analyzed well and the location of the anisotropy map (blue square). Bottom center: Map representing anisotropy azimuth (thin black lines) and anisotropy magnitude (relative color scale with warm colors higher than cold colors). Top right: Angular plot of faults (from time structure map) and fractures and stress orientation (from well analysis).

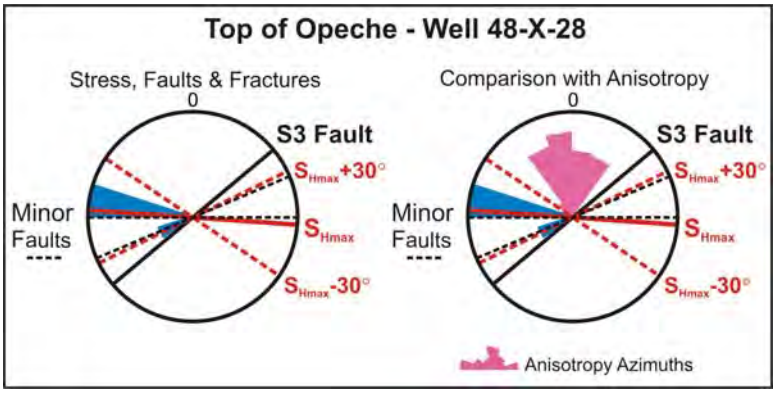


**Figure 5.38**: Comparison of AVAZ anisotropy azimuths (magenta) with stress fracture and fault orientations from seismic and well data in the area around well 48-X-28 (see Figure 5.37). The anisotropy orientations are also rotated 90° to account for the sign ambiguity.

### 5.5.4 DUNE MORPHOLOGY AND ACQUISITION PATTERN

Dune morphology and the seismic acquisition pattern were also examined to evaluate their potential impact on the AVAZ observed anisotropy.

An eolian system such as the one where the Tensleep Fm. was deposited, could easily develop dunes of ~1.5 km or bigger. As an example of an equivalent system, Figure 5.39 shows Kocurek's (1981) interpretation of bedforms structure and dimensions of the Entrada Sandstone (northern Utah and Colorado). The red letters in this figure correspond to different facies, where TPX, TX are different types of dune deposits.

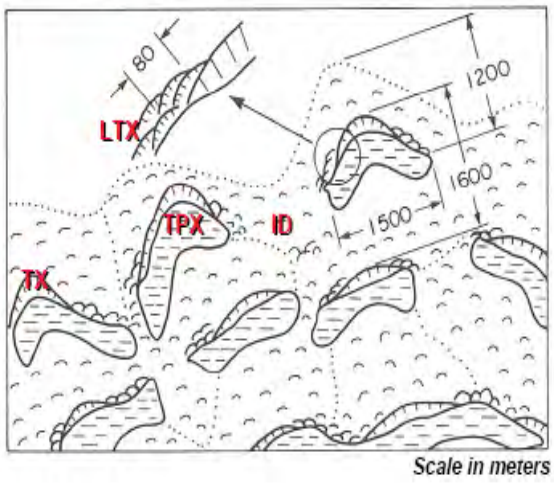


**Figure 5.39**: Bedforms structure and dimensions of the Entrada Sandstone (northern Utah and Colorado). The red letters in this figure correspond to different facies, where TPX, TX, and LTX are different types of dune deposits (Kocurek, 1981).

Dune deposits present porosity and permeability anisotropy parallel and perpendicular to the transport direction. This can lead to an anisotropic cementation as well. Considering the estimated magnitude of the Tensleep bedforms, there is a reasonable likelihood that the observed AVAZ anisotropy could be generated by dune structure.

Figure 5.40 shows an amplitude time-slice at the depth of the Tensleep Fm. In this figure, it is possible to observe that the orientations of the amplitudes more-or-less parallels region paleo-wind pattern in the Pennsylvanian (i.e., from the northeast),

which would make the amplitude patterns parallel to wind direction, and therefore they might be interpreted as arising from 'longitudinal dune' forms (S. Graham personal communication, 2008).

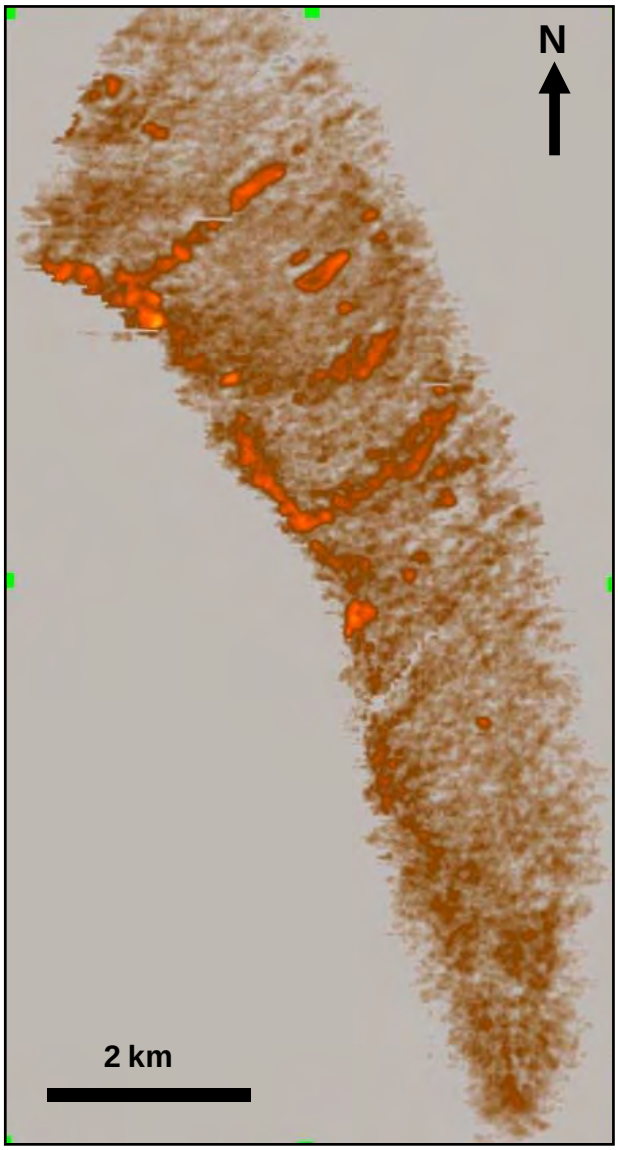


**Figure 5.40**: Amplitude time-slice at the depth of the Tensleep Fm.

However, in order to test this hypothesis, better understanding of dune morphology and paleo wind directions at Teapot Dome would be needed.

On the other hand, the amplitude patterns shown in Figure 5.40 also parallels the seismic acquisition pattern (Figure 5.41). The AVAZ method is very sensitive to

footprint, so one of the first steps is to analyze the acquisition prior to doing any analysis. This helps narrow down the parameterization and eventually reject surveys that are unsuitable.

The footprint effects are reduce by superbinning, and in the case of the Teapot Dome 3D volume, a 7 inlines by 15 crosslines superbin was indicated to alleviate the possibility of footprint. Since this was applied pre-migration, the potential for smear across structure is lessened (D. Gray personal communication, 2008).

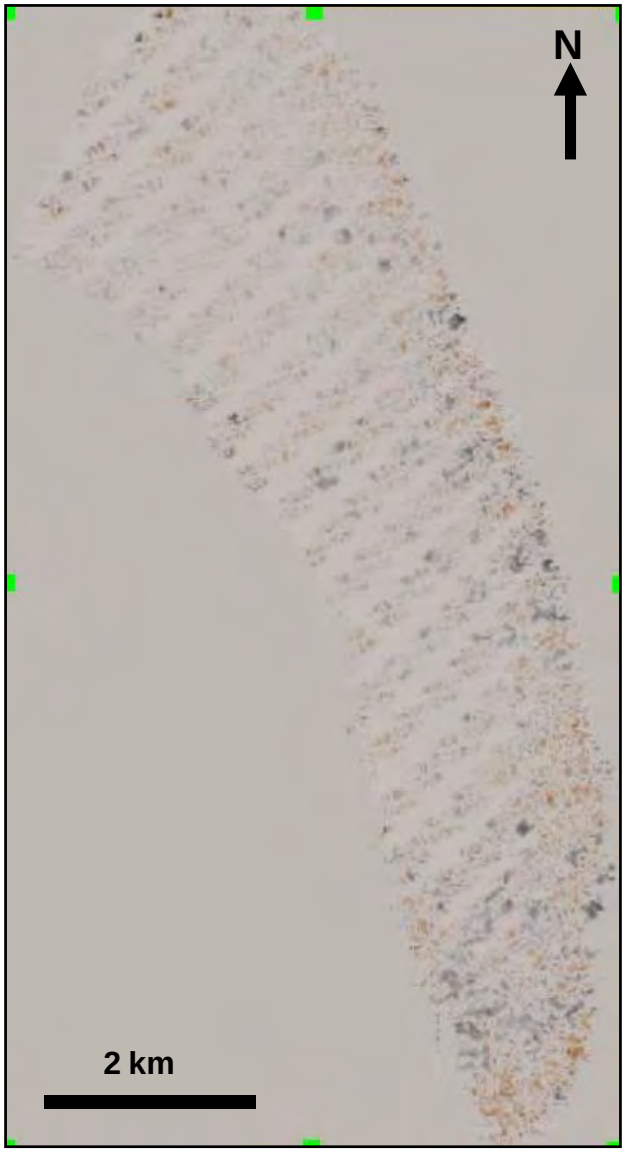


**Figure 5.41**: Amplitude time-slice showing the acquisition pattern of the Teapot Dome 3D seismic volume.

### 5.5.5 SUMMARY OF OBSERVATIONS

As a summary of the observations presented in the previous figures we see that in all of the cases, the azimuth of the anisotropy is parallel to both stress directions and to fault and fracture orientations (Table 5.2). The only exceptions occur in an area of radius ~150 ft around few of the wells, indicating that it is a local phenomenon.

| Interval | Well | Only stress | | Only Structural | | Stress & Structural | |
|---|---|---|---|---|---|---|---|
| | | Area | Well | Area | Well | Area | Well |
| Tensleep | 25 | | | | | Y | Y |
| | 61 | | | | | Y | Y |
| | 67 | | | | | Y | Y |
| | 71 | | | | Y | Y | |
| | 48 | | | | | Y | |
| Tensleep B | 25 | | | | | Y | Y |
| | 61 | | | | | Y | Y |
| | 67 | | | | | Y | Y |
| | 71 | | Y | | | Y | |
| | 48 | | | | | Y | Y |
| Opeche | 25 | | | | | Y | Y |
| | 61 | | | | | Y | Y |
| | 67 | | | | Y | Y | |
| | 71 | | | | | Y | Y |
| | 48 | | | | Y | Y | |

No digital FMI log

**Table 5.2**: Summary of observations in different areas surrounding the wells.

Some other observations (Table 5.3):

- In all the wells, at least part of the anisotropy is parallel to $S_{Hmax}$. However, in most of these areas this $S_{Hmax}$ direction is also subparallel to some structural feature (fault or fracture set).
- At the Tensleep level, both the $S_{Hmax+30}$ and $S_{Hmax-30}$ directions appear in the anisotropy in all wells, except one; whereas in the TensleepB and the Opeche only the $S_{Hmax-30}$ directions are present in all the wells, except one.

| | | $S_{Hmax}$ | $S_{Hmax+30}$ | $S_{Hmax-30}$ |
|---|---|---|---|---|
| Tensleep | 25 | Y | Y | Y |
| | 61 | Y | Y | Y |
| | 67 | Y | Y | Y |
| | 71 | Y | Y | Y |
| | 48 | Y | N | Y |
| Tensleep B | 25 | Y | N | Y |
| | 61 | Y | N | Y |
| | 67 | Y | N | Y |
| | 71 | Y | N | Y |
| | 48 | Y | Y | Y |
| Opeche | 25 | Y | N | Y |
| | 61 | Y | N | Y |
| | 67 | Y | N | Y |
| | 71 | Y | N | Y |
| | 48 | Y | Y | Y |

**Table 5.3**: Summary of observations in different areas surrounding the wells.

## 5.6 SUMMARY

In summary, it is not currently possible to differentiate among the several factors that could be influencing the observed anisotropy in the AVAZ analysis.

It is possible that the method does not work with this data set, because particularities of this setting do not follow the assumptions of the method. For example, one of these assumptions is that the analyzed horizon behaves as Horizontally Transverse Isotropic (HTI) medium, which means that it has only one set of parallel vertical fractures. Most of the descriptions of fractures in the Tensleep indicate that they are vertical, but there is a significant scatter in their azimuths. It is also possible that the observed anisotropy could be influenced by the dune morphology. Evaluation of this hypothesis is beyond the scope of this thesis.

However, at this point these are just speculations and we do not have enough data to indicate the origin of the observed anisotropy, neither to indicate the degree of confidence in the success of this method for the Tensleep Fm. at Teapot Dome.

# CHAPTER 6

# USING MICROSEISMIC STIMULATION TO ENHANCE PERMEABILITY IN TIGHT FORMATIONS

## 6.1 ABSTRACT

Deep saline formations have great potential for geologic sequestration of $CO_2$. As such formations are widespread in many parts of the U.S., they are in theory, easily accessed from point sources of $CO_2$, such as power plants, factories, refineries, cement plants, etc. As typical of deep mature basins, many deep saline formations of the mid-continental U.S. appear to have very low porosity and permeability

compared to those encountered in large oil reservoirs, resulting in limited injectivity and storage capacities.

A demonstration $CO_2$ sequestration project was performed in the Michigan Basin, the Otsego County Test Site, where potential targets for sequestration include several Paleozoic reservoirs. In particular we analyze the Silurian Bass Island dolomite (BILD) at approximately 1050 m depth. The source for this project is the associated $CO_2$ removed from the Antrim Shale gas at 6 centralized gas-processing plants in the Otsego County and other adjacent counties, which averages ~1.2 million metric tons per year. A preliminary simple fluid flow simulation indicates that under the present condition ~50% of this $CO_2$ could be stored in the BILD.

During an injection-induced microseismicity stimulation experiment, a total of more than 10,000 metric tons of supercritical $CO_2$ were injected into the BILD formation during a period of 40 days. The objectives of the injection experiment were to evaluate microseismic monitoring technologies and establishing the storage capacity and suitability of the BILD, and potentially enhance the permeability and injectivity of the target reservoir.

Microseismic stimulation is initiated by increasing the fluid pressure in the target formation, thus reducing the effective normal stress on optimally-oriented faults and fractures triggering slip, and creating high-permeability pathways within the reservoir. This technique is a frequent and safe practice for imaging hydraulic fracturing operations in the oil and gas industry, and enhancing permeability in geothermal resources.

We have developed a preliminary geomechanical characterization as a base for the proposed experiment. To develop the geomechanical model, we analyzed formation micro-image (FMI), density and sonic logs from two wells, as well as leak-off tests and pore pressure measurements from wells in the vicinity. This analysis also provided us with the theoretical pressure needed to hydrofracture the target formation and the expected fracture direction propagation.

Seismic monitoring of the injection was achieved by two downhole seismometer arrays that consisted of eight, three-component sensors each. The arrays were deployed in two nearby monitoring wells directly above the target horizon at 150 m and 550 m lateral distance to the injection point, respectively. The sensor spacing was 15 m. Calibration shots in the injection well were used to determine the orientation of the sensors at each depth in the two monitoring wells.

The analysis of the obtained microseismic data and the understanding of the spatial-temporal behavior of the induced microearthquakes are related to the hydraulic parameters such as injection rate and well-head pressure, which provide valuable information on the resultant fluid-flow network of the reservoir.

## 6.2 INTRODUCTION

One of the biggest challenges for $CO_2$ sequestration in deep saline formations is the very low porosity and permeabilities often shown, that translates into limited injectivity and storage capacities.

Injection-induced microseismicity has been frequently used in the oil industry to enhance permeability. Increasing fluid pressure following hydraulic fracturing, reduces the effective normal stress on optimally-oriented faults and fractures, therefore inducing slip and creating high-permeability paths within the reservoir. The induced failure is mainly triggered by a diffusive process of pore pressure perturbation and often occurs as a sequence of many small events.

The volume of rock stimulated by hydraulic fracturing can be imaged by locating these microearthquakes induced by the injection (Albright and Pearson, 1982) that can be relocalized to show the geometry of slipping fractures. In addition to the permeability enhancement and characterization of hydraulic fracture network, microseismicity can potentially be used for the estimation of hydraulic properties of rocks over large scales such as hydraulic diffusivity and permeability (Shapiro et al., 2002).

Some examples of fluid induced microseismicity can be found in sedimentary environments such as the Frio sandstone or the Cotton Valley tight gas sands. In carbonate settings some examples include the Austin chalk and low porosity Ordovician carbonate rocks in Clinton County, Kentucky. In crystalline rocks, examples can be found in hot-dry-rock geothermal sites such as Fenton Hill, New Mexico or Soultz, France (Phillips et al., 2002). Another remarkable example is the Yufutsu oil and gas field, Japan, where injectivity was increased eight times after the stimulation (Tezuka, 2006).

Therefore, it was proposed the use of microseismic stimulation to enhance the permeability and injectivity in a tight formation; as well as the use of seismic monitoring to gather information about the permeability and the fracture network of the reservoir.

Passive seismic monitoring (PSM) started in the 30s and its growth was the result of the interest in quantifying earthquake phenomena. The most notorious examples in the use of this technique count Richter's earthquake magnitude scale for regional events in CA (1935) and the discovery of earthquake frequency-magnitude relation (Gutenberg and Richter, 1941). In the 60s, technical developments in seismic networks and modern data processing allowed the application of PSM to detect and analyze earthquakes over a broad range of magnitudes.

PSM is a tool used in a variety of applications such as mapping active faults at different scales for hazard estimation, investigation of large earthquake phenomena along plate-bounding faults, and characterization of hydrocarbon and geothermal reservoirs (Bohnhoff et al, *in press*). Recently, this technique has started to be developed and tested to monitor underground storage of $CO_2$ as in the project described in this chapter.

## 6.3 OTSEGO COUNTY TEST SITE – MI

The experiment took place in Otsego County in the Michigan Basin, as part of an ongoing project of the Midwest Region Carbon Sequestration Partnership (MRCSP), founded by the Department of Energy/National Energy Technology (DOE/NETL), where the objective was to investigate $CO_2$ sequestration potential in Upper Silurian to Middle Devonian strata. The proposed injection interval is the Bass Island dolomite (BILD) at 1048 m depth.

A pilot well, State Charlton 4-30 (Figure 6.1) was drilled in November 2006 at the Core Energy gas fields near a DTE ENERGY gas processing plant (Turtle Lake).

.


**Figure 6.1**: Satellite image of Michigan area. The white square indicates the Otsego County, and the location of the test well Charlton 4-30 is indicated by the yellow dot.

The source for this project is the associated $CO_2$ removed from the Antrim Shale gas at 6 centralized gas-processing plants in the Otsego Country and other adjacent counties, which averages ~1.2 million metric tons per year. The $CO_2$ is delivered to the test site through an existing $CO_2$ pipeline that Core Energy utilizes for several $CO_2$-EOR projects that has been going at least since 2004 in the Otsego County. This EOR projects targets the Paleozoic reefs at ~5000 ft depth, they are relatively small floods involving 2 or 3 wells (Oil and Gas Journal Report, 2004). One of these floods occurs just in these pilot areas ~1500 ft deeper and ~2000 ft north of one of the monitoring wells.

### 6.3.1 TEST SITE GEOLOGY

Figure 6.2 shows the schematic stratigraphic column at well State Charlton 4-30 from borehole logs, sidewall and conventional cores. The storage interval comprises the BILD (injection target) and the Bois Blanc Formation, whereas the seal is the Amherstburg Formation.

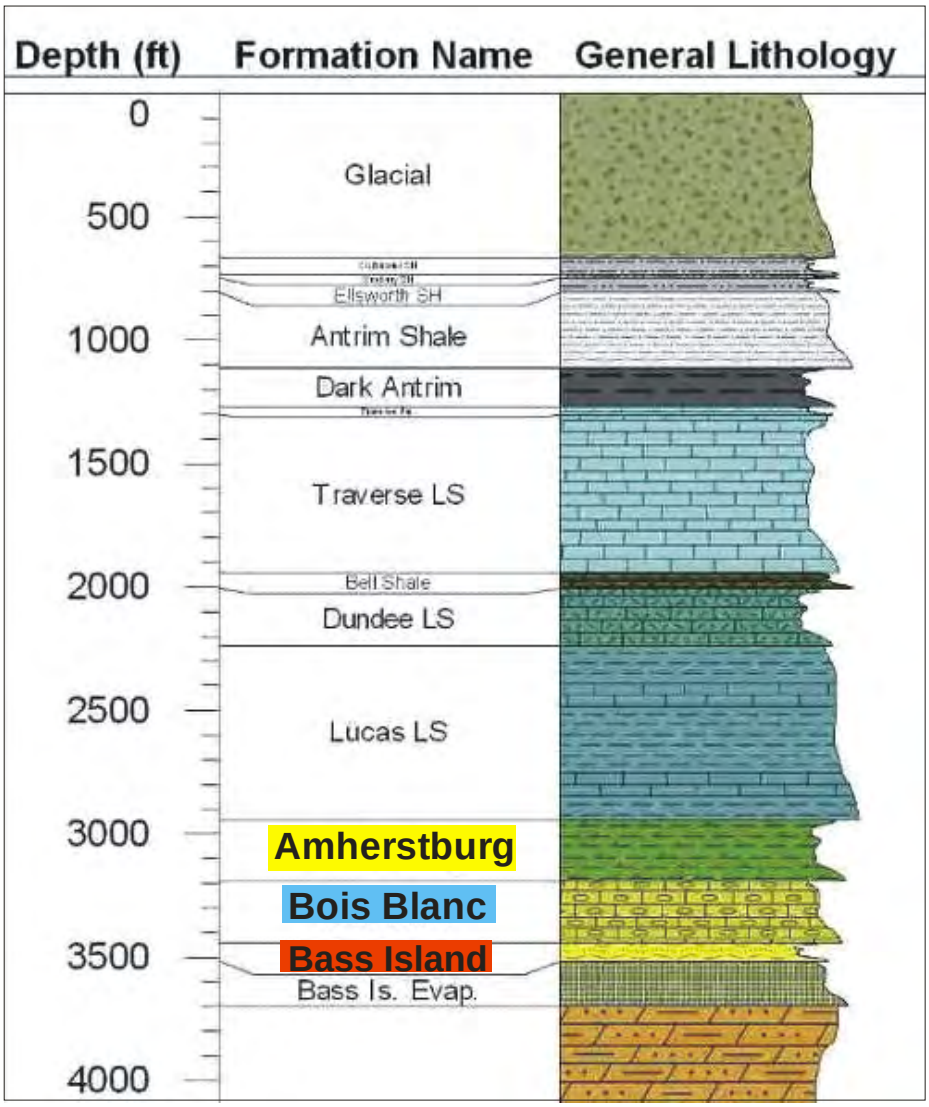


**Figure 6.2**: Stratigraphic column of the test site. In red, it is highlighted the injection target interval: Bass Island dolomite, which together with the Bois Blanc Fm. constitutes the total storage interval (figure courtesy of Battelle).

The BILD interval is a porous dolostone at the top of the Silurian Bass Islands "Group" at 1048 m depth (3440 ft). It is 22 m thick in this well, but approximately 15 m thickness average in the Michigan Basin, where it is laterally very persistent (Figures 6.3 and 6.4) without structural complexities (note the large vertical exaggeration in Figure 6.4).

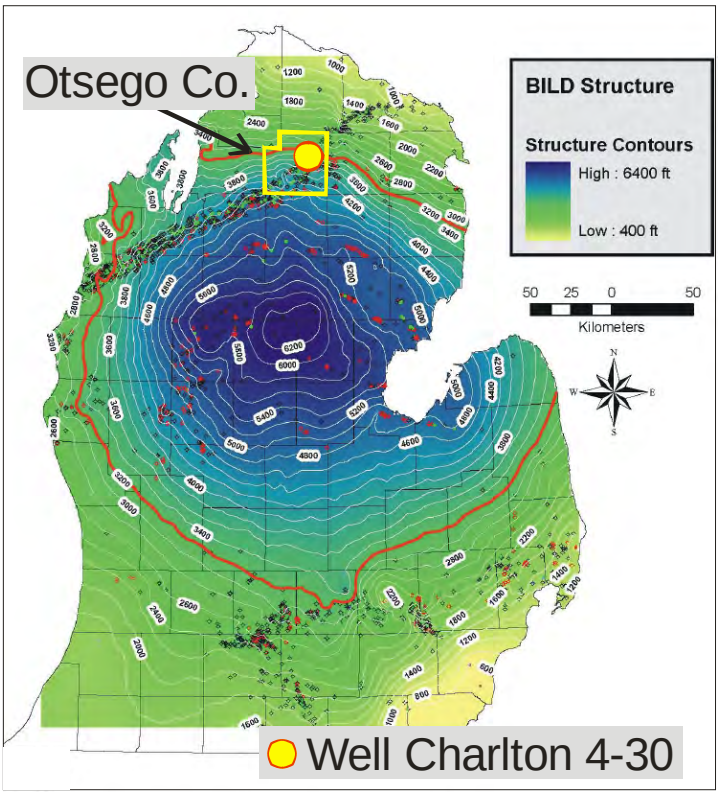


**Figure 6.3**: Structural map of Bass Island dolomite in Michigan, showing the location of Otsego Co. and Well Charlton 4-30. Modified from Barnes et al. (in press).

Porosity in the BILD ranges from less than 5% to more than 25%, and the average porosity is 15%. The average permeability is less than 13 mD. Barnes *et al.* (*in press*) performed a preliminary interpretation based on cores from the well State Charlton 4-30, in which they suggested that this unit was deposited in a restricted marine, possibly tidal flat to sabhka environment, with periodic and possibly protracted subaerial exposure surfaces, that resulted in repeated karsted intervals. They indicated that mineralized natural fractures are common.

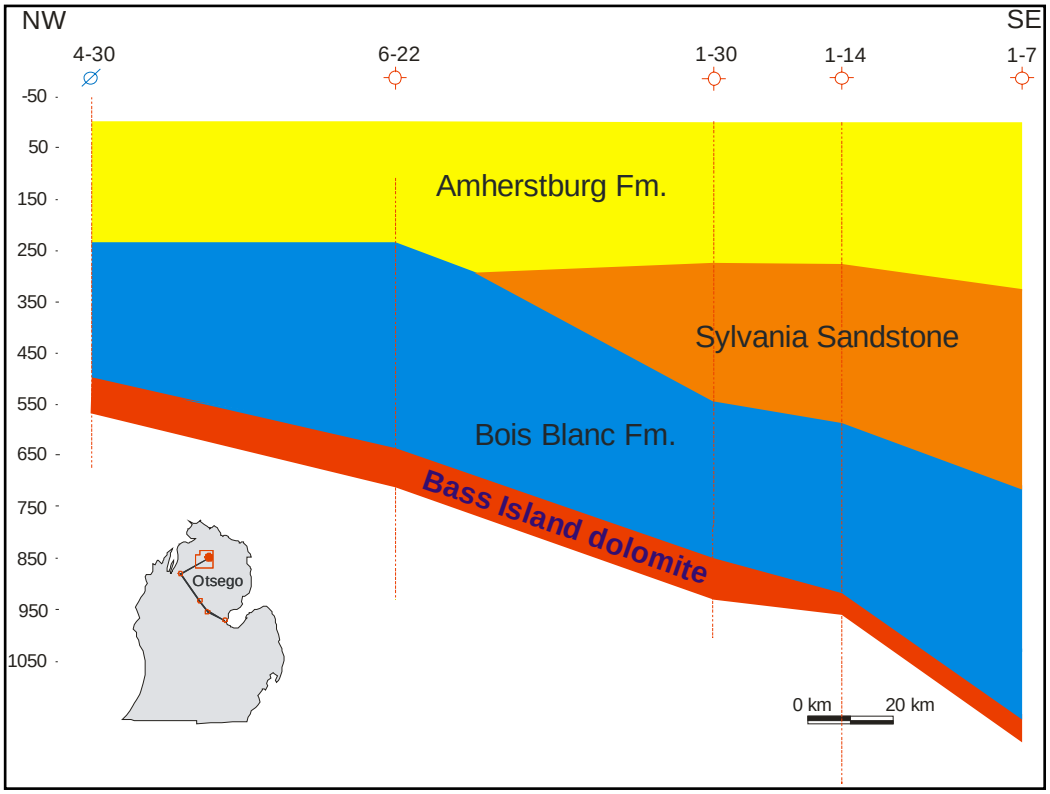


**Figure 6.4**: Regional Stratigraphic cross section showing the lateral continuity of the Bass Island dolomite (red). The cross section was generated from ~100 modern open hole logs. Note the large vertical exaggeration (vertical scale is in meters). Modified from Barnes *et al*, *in press*.

The Bois Blanc Formation is described as cherty carbonate strata, 78 m thick that overlies the BILD. Although it apparently lacks suitable injectivity potential in the well State Charlton 4-30, and therefore it could be locally considered a seal, it has been mentioned in other parts of the basin as a potential storage target, and here it is considered as part of the storage interval (Barnes *et al., in press*).

The Amherstburg Fm., the primary caprock, is a dense limestone with very low porosity and permeability which is also laterally very persistent, has uniform thickness and it is usually found through the entire Michigan basin. Porosity values are lower than 10% and most of them are less than 5%. Preliminary mini-permemeter measurements showed very low permeability where most measurement are less than 1 millidarcy. This unit was described from cores as a

fossiliferous, dense, skeletal wackestone to mud-rich packstone unit that shows good potential as an effective caprock (Barnes *et al*., *in press*).

## 6.4 PRELIMINARY GEOMECHANICAL CHARACTERIZATION

We performed a preliminary geomechanical characterization analyzing FMI, density and sonic logs from the well State Charlton 4-30 and State Charlton 3-30 as well as a leak-off test and pore pressure measurements from wells in the vicinity.

The magnitude of the vertical stress ($S_v$) was obtained by integration of rock densities, taken from the density logs, from the surface to the top of the BILD (1048 m). The least principal stress $S_3$, which is usually the minimum horizontal principal stress ($S_{hmin}$), can be obtained from the analysis of hydraulic fracturing via either minifracs or extended leak-off tests. Due to the lack of such data in the two mentioned wells we used the fracture gradients from a deep well in central Michigan described by Haimson (1978). The maximum horizontal stress ($S_{Hmax}$) magnitude was obtained by modeling wellbore failure features (drilling-induced tensile fractures in this case), as well as the magnitudes of $S_v$, $S_{hmin}$, pore pressure ($P_p$) and rock strength values.

The orientation of the horizontal principal stresses in a vertical well, like the State Charlton 4-30 is determined from the drilling induced fractures orientations (Figure 6.5), since they propagate parallel to $S_{Hmax}$. Under normal drilling conditions, the occurrence of these drilling-induced tensile fractures (in a vertical well) usually indicates a strike-slip faulting stress state (Zoback *et al.,* 2003).

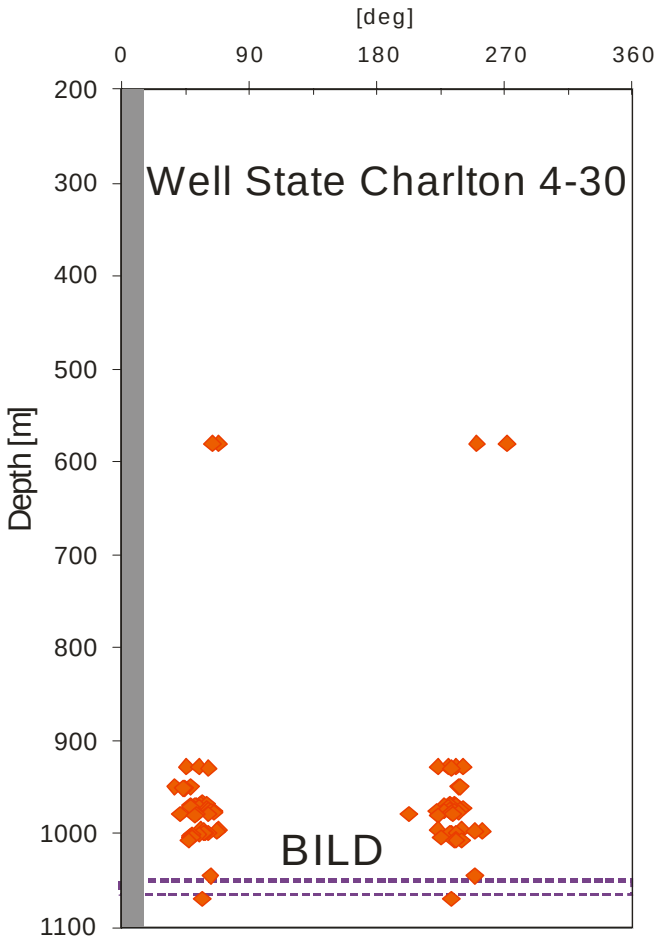


**Figure 6.5**: Distribution of tensile fractures in well State Charlton 4-30. The purple dotted line indicates the Bass Island dolomite (top and base), and the gray rectangle on the left of the plot indicates the imaged portion of the well.

More than 80 drilling-induced tensile fractures were analyzed in the FMI log of well State Charlton 4-30 over a depth range of 580 – 1080m (Figure 6.5), and the average maximum horizontal stress ($S_{Hmax}$) direction obtained is 55º±10º Az. This value is consistent with the regional $S_{Hmax}$ directions in the area, which are summarized in Figure 6.6 (Reinecker *et al*., 2005).


**Figure 6.6**: Regional Stress map modified from Reinecker et al, (2005). The red arrow indicates the $S_{Hmax}$ direction determined in the present study.

The rock strength used in the horizontal stresses magnitude estimations was determined by empirical relationships for carbonate rocks (Chang *et al*., 2006). The BILD rock strength varies from 58 MPa to 72 MPa whether we use relationship 1 or 2 respectively.

$$UCS = 143.8\exp(-6.95\phi) \quad (1)$$

$$UCS = 135.9\exp(-4.8\phi) \quad (2)$$

In summary, the analysis of the studied wells indicates a Strike Slip faulting stress state (Figure 6.7), where $S_{Hmax}$ ≈ 33 MPa, $S_v$ = 26.6 MPa, $S_{hmin}$ ≈ 17.9 MPa (Haimson, 1978), and $S_{Hmax}$ orientation = 55º ±10º Az. The pore pressure used in this analysis is $P_p$ = 10.8 MPa, slightly over hydrostatic.

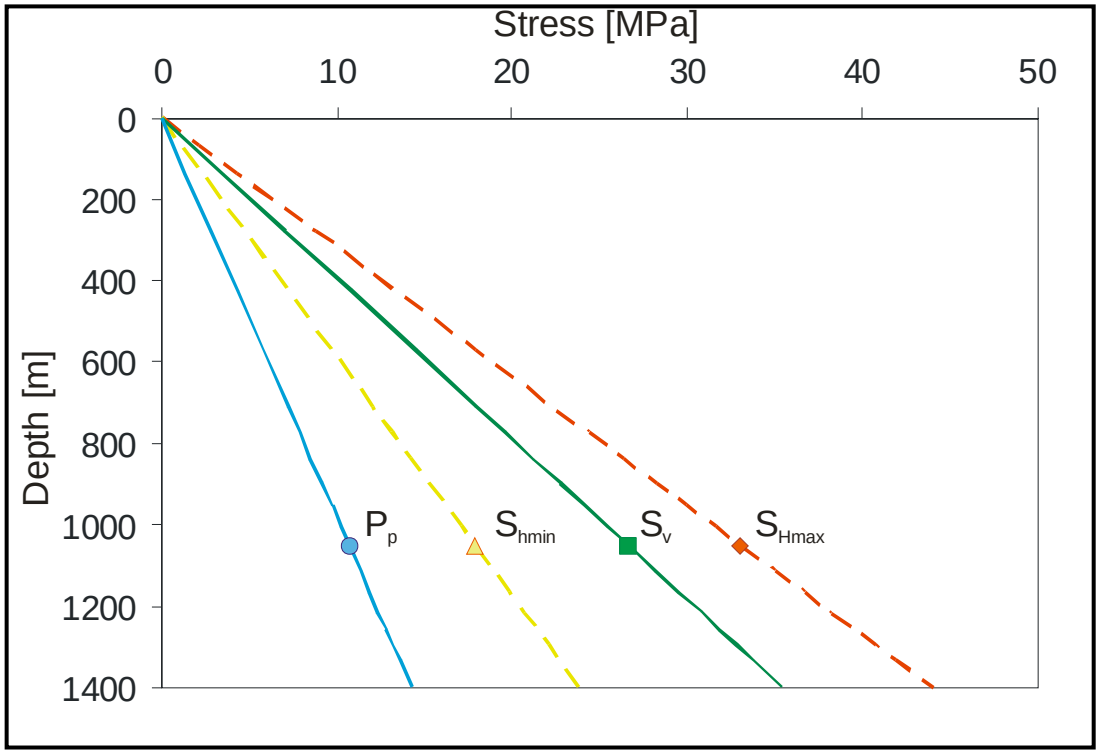


**Figure 6.7**: Stress summary plot for well State Charlton 4-30. At 1048 m depth (top of Bass Island dolomite): $P_p$ = 10.8 MPa (blue dot), $S_{Hmax}$ ≈ 33 MPa (red diamond), $S_v$ = 26.6 MPa (green square), $S_{hmin}$ ≈ 17.9 MPa (yellow triangle).

Under the present stress conditions, if the fluid pressure in the well exceeds the magnitude of the least principal stress ($S_{hmin}$), a vertical hydraulic fracture should propagate in the plane normal to the $S_{hmin}$ direction, since they always propagate perpendicular to the least principal stress in the earth (Hubbert and Willis, 1957).

Once the induced seismicity experiment takes place, we will have the empirical value of $S_{hmin}$, which is the upper-bound pressure value to avoid hydrofracture the formation during the sequestration phase.

## 6.5 PRELIMINARY PRE-INJECTION FLUID FLOW SIMULATION

A very simple preliminary fluid flow simulation was performed to gain insight on the potential injectivity of the Bass Island dolomite.

The BILD was modeled over an area of 5 $km^2$ and 15 m height. We built a 200x200x5 grid (200,000 grid blocks), where one grid block has 25 m on each side and 3 m height. The inclination of the BILD is very gentle in the Michigan Basin, therefore, for this exercise we considered it to be zero. The grid was centered on one injection well.

We used sequential Gaussian simulation (SGS) method (Isaaks, 1990) to generate equally probable realizations of porosity (Figure 6.8) and permeability based on the values obtained from the mentioned core (Figure 6.9). We used a beta porosity distribution and a log normal permeability distribution where the porosity mean value is 0.128 with a standard deviation of 0.067. In the case of the permeability, the mode value is 0.001 mD and the mean is 13.88 mD with a standard deviation of 27.31 mD. To account for the spatial variability of the data, we used a theoretical spherical variogram expecting a certain amount of lateral correlation in the properties, considering we were in a sedimentary basin.

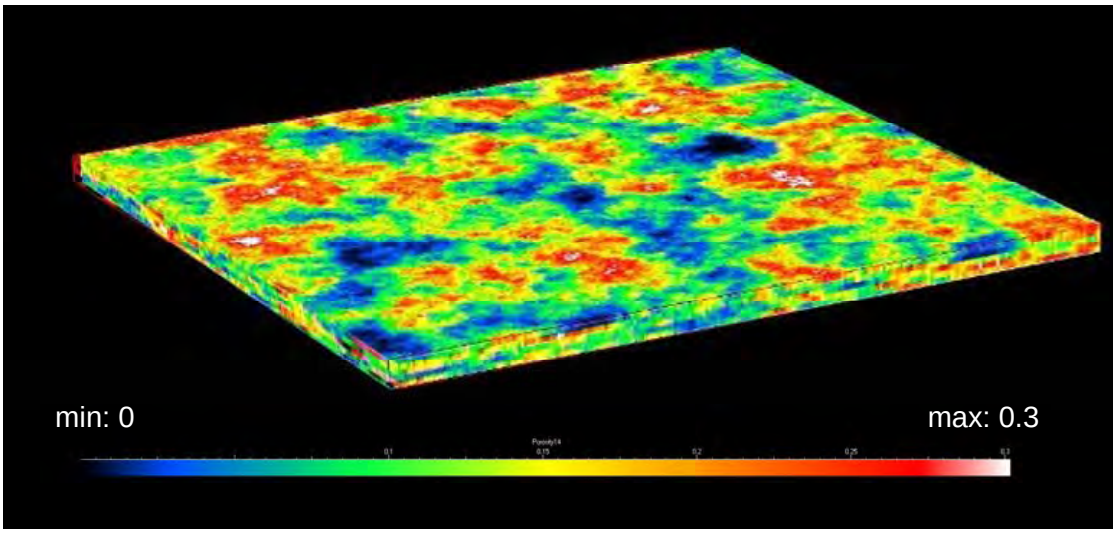


**Figure 6.8**: 200x200x5 grid of the BILD, showing one of the porosity realizations performed with the SGS method. Porosity mean value is 0.128 with a standard deviation of 0.067.

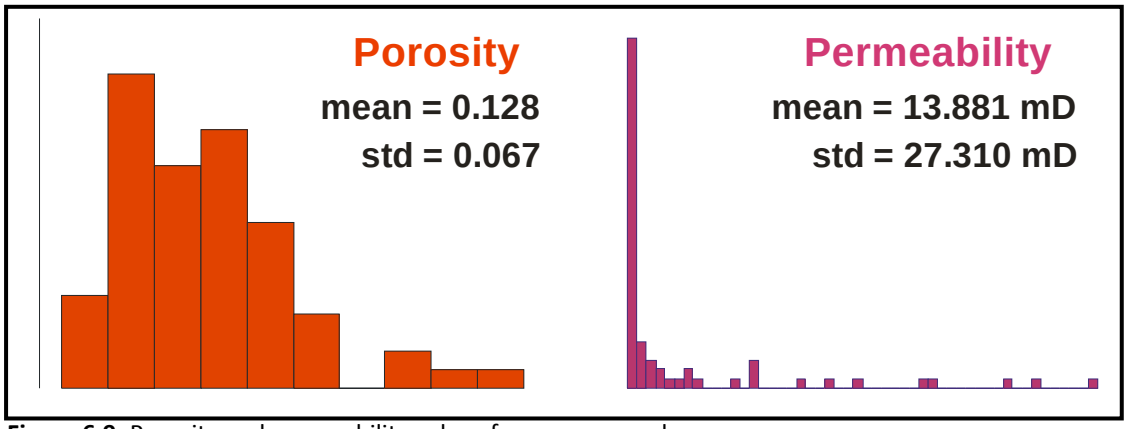


**Figure 6.9**: Porosity and permeability values from core samples.

For this preliminary simulation, we used a commercial black-oil simulator (IMEX – CMG) where water was modeled as oil and $CO_2$ as gas, in order to allow for the $CO_2$ to dissolve in the brine. A constant pressure boundary condition was enforced to simulate an open reservoir system. The reservoir temperature is 28.9 °C. The simulations were run with a bottom hole pressure (BHP) constraint slightly below the fracture gradient (17 MPa). Although the objective of the field test was to inject ~10,000 tons of $CO_2$ during a short period of time, we simulated $CO_2$ injection for 10 years in order to have an approximate idea of how much $CO_2$ could be sequestered in this site, considering the permeability before enhancement.

We also simulated the real experiment injecting ~10,000 tons of $CO_2$ during 40 days, and we did not observe $CO_2$ breakthrough in any of the monitoring wells, which was confirmed from fluid monitoring at those wells during the experiment (J. Gerst personal communication, 2008).

From the results of this preliminary simulation, considering injecting in a single well over a ten year period, we found that the amount of $CO_2$ that can be injected in the BILD averages approximately 60,724 metric tons per year (see Figure 6.10 and 6.11), which over 10 years is roughly half of the $CO_2$ emissions from the gas-processing plants in the Otsego and adjacent counties (~1.2 million metric tons/year)

in one year (Barnes *et al., in press*). Formation pressure stays below the theoretical $S_{hmin}$ magnitude (Figure 6.12) over these 10 years.

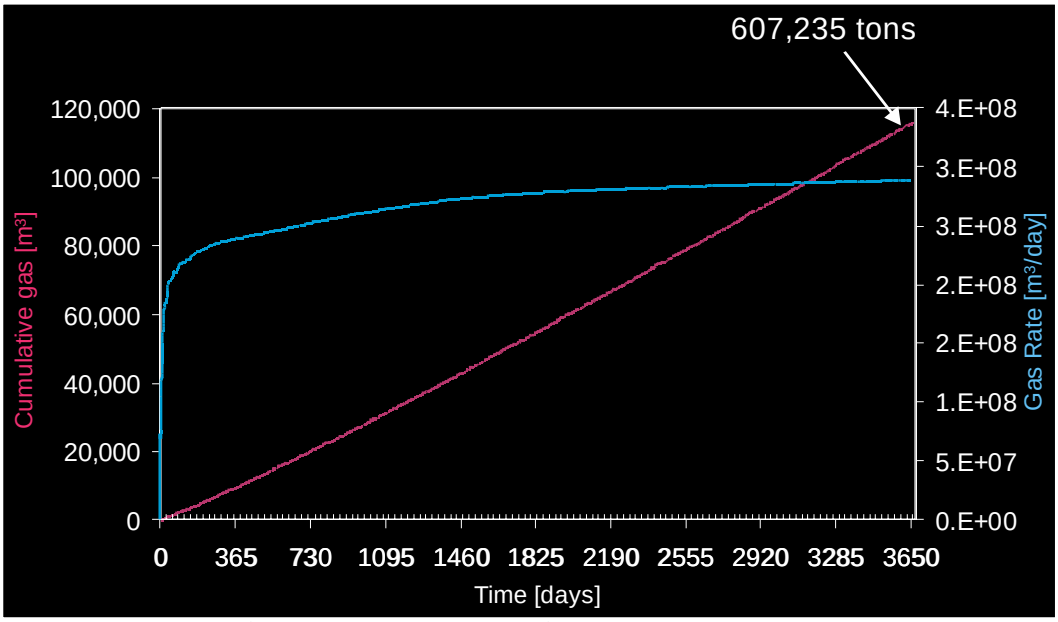


**Figure 6.10**: Total $CO_2$ [$m^3$] and $CO_2$ injection rate [$m^3$/day] over a ten year period. The total amount of $CO_2$ injected in the BILD is 607,235 metric tons.

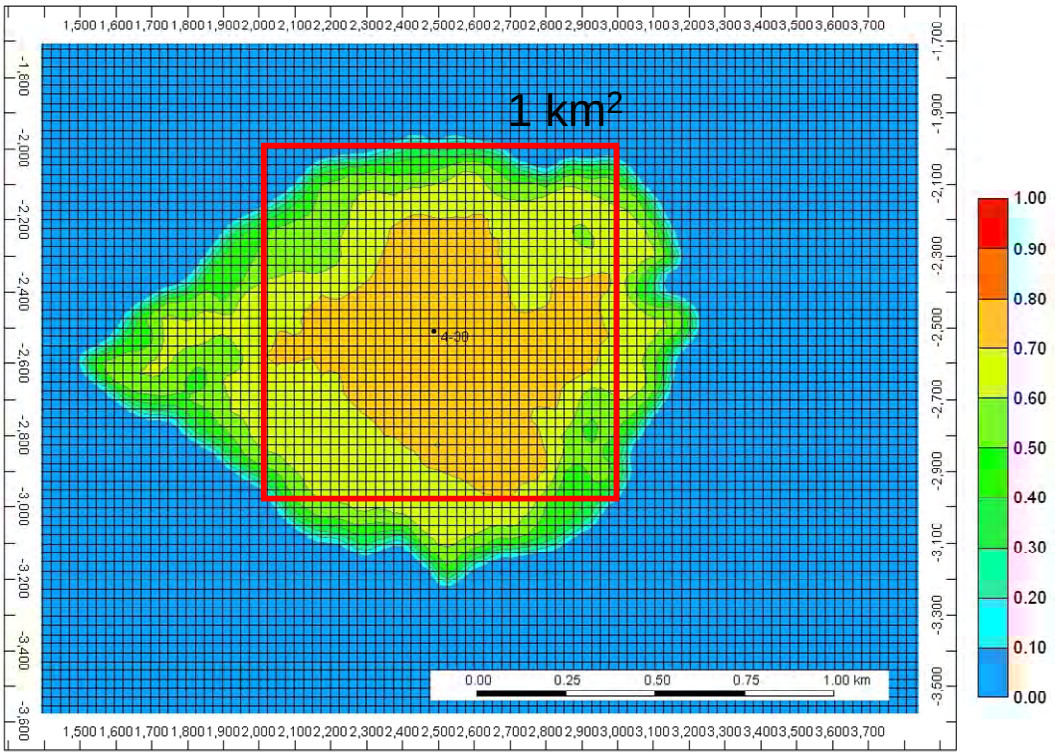


**Figure 6.11**: Detail of BILD grid showing $CO_2$ saturation after 10 year of injection. For reference, the red square represents 1 $km^2$.

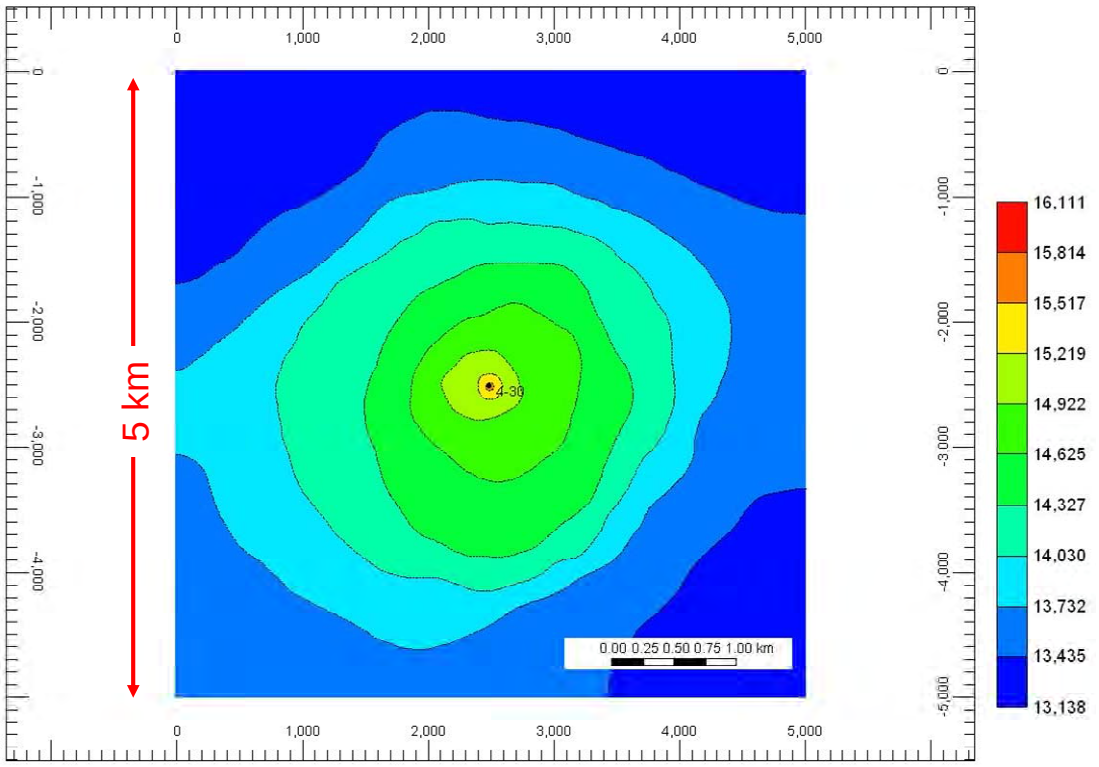


**Figure 6.12**: Detail of BILD grid showing formation pressure after 10 year of injection. Units are in kPa.

## 6.6 MICROSEISMIC MONITORING OF INJECTION EXPERIMENT

A total of ~10,000 metric tons of supercritical $CO_2$ were injected into the BILD formation over a period of 40 days. The passive seismic monitoring started 16 days prior to the start of injection and ended after 47 days of operation (nine days before the end of injection).

Due to the expected small magnitudes (≤-1) of the induced events, seismic monitoring was conducted by two downhole seismometer arrays that consisted of eight, three-component sensors each. The arrays were deployed in two nearby monitoring wells directly above the target horizon at 150 m and 550 m lateral distance to the injection point, respectively (Figures 6.13 and 6.14). The sensor spacing was 15 m. Calibration shots in the injection well were used to determine the orientation of the sensors at each depth in the two monitoring wells. The seismic

field campaign was conducted by ESG Solutions, Kingston/CA. The array in well 2-30 is denominated Array 1 and the one in well C3-30 is referred as Array 2.

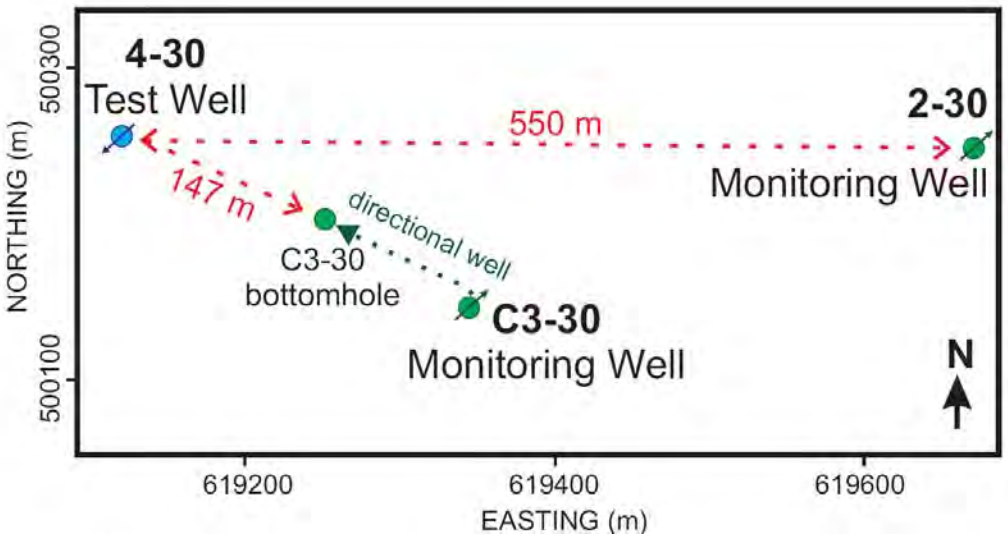


**Figure 6.13**: Map of experiment setup showing injection (4-30) and the two monitoring wells

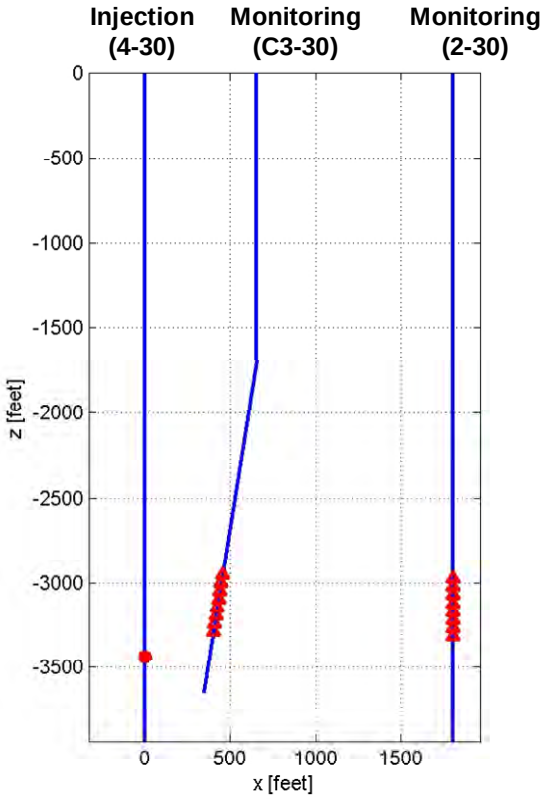


**Figure 6.14**: Depth profile of microseismic monitoring set up setup showing injection and monitoring wells with the downhole arrays (red triangles). Array 1 correspond to 2-30 monitoring well and Array 2 to C3-30 well.

Figure 6.15 shows the Flow Rate, Bottom Hole Pressure (estimated from well head pressure data) and the daily seismicity rate during the injection period.

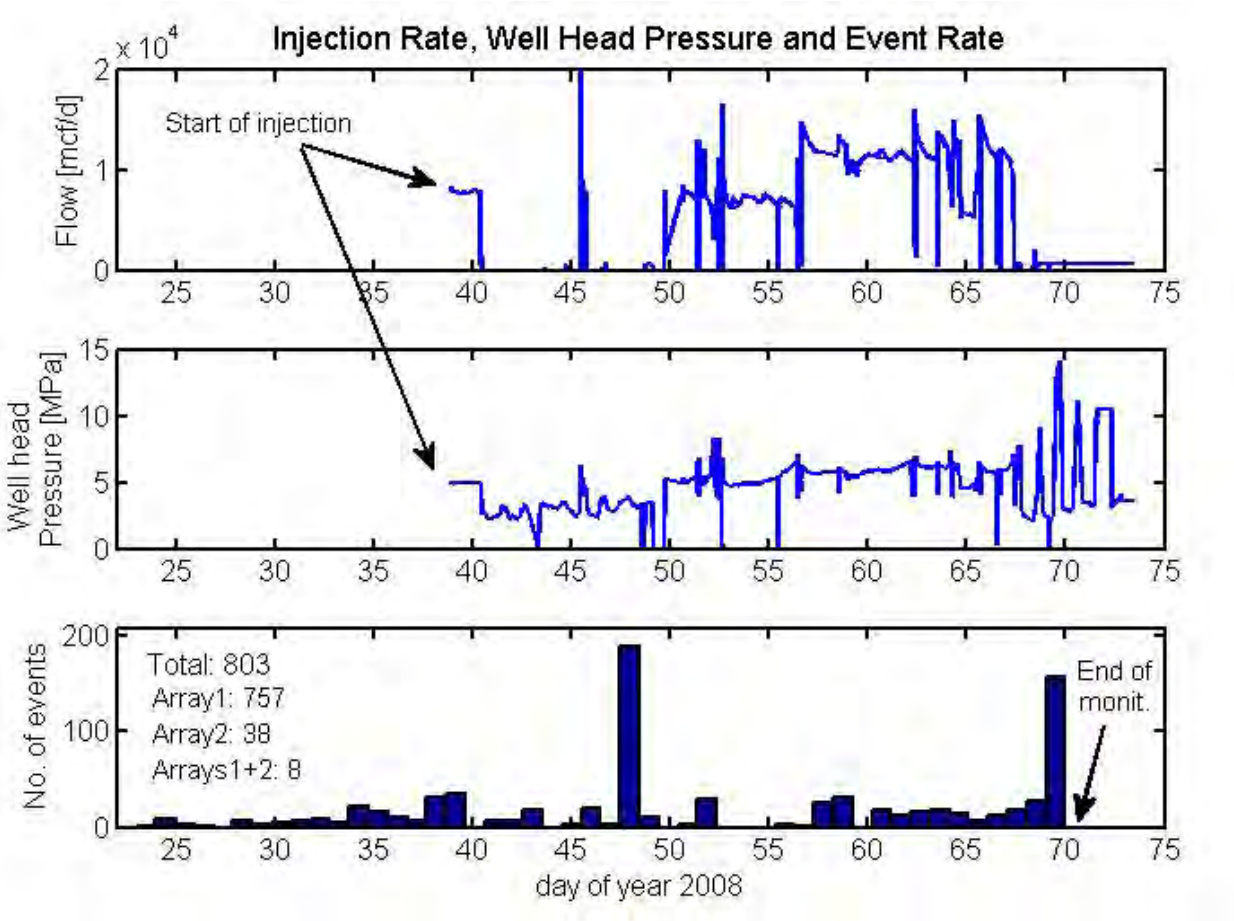


**Figure 6.15**: Injection rate, well head pressure and daily seismicity rate. The total number of events are indicated in the lower plot as well as the no. of evens detected only at Array 1 or Array 2 and the ones detected in both arrays.

### 6.6.1 PRELIMINARY DATA PROCESSING

There were a total 817 detections during the monitoring period. Out of these, 770 events were recorded only in Array 1 (well 2-30), while 39 events were recorded only in Array 2 (well C3-30). 8 events where recorded at both arrays of which 7 were the calibration shots. The remarkable difference in detections at either array cannot be explained by the noise conditions, as there was no general difference observed

between either array. However, individual sensors (sensor 5 on array 1; sensors 9 and 11 on array 2) present a substantial higher noise level than others.

In a first step, all events were inspected to separate seismic events from 'non-seismic' detections such as spikes or other electronic noise. A total of 225 events were classified as seismic events and considered for further evaluation. Of the 225 seismic events, 201 were detected at array 1, 23 events were detected at array 2, and a single event was seen on both sensor arrays. In the next step of processing the seismic recordings phase onsets were determined. It turned out that a high number of events contained an unexpected type of secondary phase onset. Those phases have phase velocities, i.e. apparent velocities along the array, in the range of 1.5-1.6 km/s. Further inspection of these phases revealed that they reflected tube waves propagating along the well with the speed of the fluid in the well. Tube waves are compressional waves generated in a well once an incoming wave encounters a density contrast. Since tube waves suffer little energy loss their amplitude decay remains small over distances as long as ~100 m as is the case here.

A substantial number of the seismic recordings were found to contain strong monochromatic codas of the P waves. These signals might be associated with ringing of the signal cable connecting the sensors. Therefore, to detect additional phases such as shear waves or other secondary phase onsets, a detailed frequency analysis was performed using a Notch filtering. It turned out that the ringing frequency was neither uniform for the entire set of seismic signals nor for all sensors. As a consequence, it was necessary to manually optimize filter parameter for each individual event and sensor. A remarkable observation was that most of the events do not contain S phases suggesting that the signals observed were not emitted from double-couple sources, i.e. shear failure. Furthermore, we observed highly varying signal characteristics among the 225 events. Some events occurred in bursts similar to earthquake swarms as observed in various environments. Some events have precursory signals with constant delay time between first and secondary arrival. This would impose that such signals are generated at the source, and propagate at the

same velocity. Based on the signal frequency and event strength, we classified the events into events with 1) only P waves, 2) P and S phase onsets, 3) a low-frequency onset (~100Hz), 4) a precursory phase, 5) swarm-type behavior. Furthermore, we observed an event-triplet, i.e. three events with highly similar waveforms occurring within a few seconds. This triplet is likely to reflect multiple activation of the same source spot.

The phase velocity of the P waves across the arrays is uniformly in the range of 4.7-5.3 km/s. This would imply that the source cannot be located far from the sensor arrays. Furthermore, arrival times are earliest at one of the inner sensors in most cases, what suggests that the events were generated at the depth of the sensor with earliest arrival time. This observation was clearly unexpected as the sensor arrays initially were deployed to monitor injection-induced seismicity within the BILD formation below the array. Applying a conventional hypocenter determination procedure to the arrival time data, we confirmed that most of the events occurred in direct vicinity of the respective sensor array. A possible interpretation of such a hypocentral distribution would be that $CO_2$ from the deeper injection (described in Section 6.3) is migrating upwards along the monitoring wells. This is in good agreement with the temporal evolution of the events that shows that almost all detected seismic events occurred before the injection into the BILD formation started. Instead, the maximum of the seismicity rate was observed when the deeper injection stopped, which is a common observation derived from other injection experiments.

## 6.7 SUMMARY

An injection-induced microseismicity experiment took place in the Michigan Basin in order to enhance permeability and injectivity of the potential storage reservoir: the Bass Island dolomite (BILD) at ~1050 m depth. The experiment consisted in the

injection of ~10,000 tons of $CO_2$ during a period of 40 days, while microseismic monitoring was in place during 31 days during the injection.

A preliminary geomechanical characterization indicates a Strike Slip present day stress state with a maximum horizontal stress ($S_{Hmax}$) direction of 55° Az. The theoretical estimated value of the least principal stress ($S_{hmin}$) is approximately 17.9 MPa. The injection pressure during the complete experiment was below this value.

Analysis of the microseismic monitoring data highlighted the risk of using automated traditional data processing approaches where tube waves where incorrectly interpreted as S waves. The presence of these tube waves, with strong amplitudes, masked the week S wave signals. A detailed frequency filtering analysis was performed in each event, to extract all the signals.

A total of 803 events were recorded in more than 3 sensors in each of the two monitoring arrays. However, no definite seismic activity could be related to the injection in the BILD. Perhaps, this was due to the small injection pressure or to higher porosity and permeability than anticipated.

A remarkable observation was that most of the events do not contain S phases suggesting that the signals observed were not emitted from double-couple sources, i.e. shear failure.

Applying a conventional hypocenter determination procedure to the arrival time data, it was confirmed that most of the events occurred in direct vicinity of the respective sensor array. A possible interpretation of such a hypocentral distribution would be that $CO_2$ from the deeper injection (described in Section 6.3) is migrating upwards along the monitoring wells. This is in good agreement with the temporal evolution of the events, that shows that almost all detected seismic events occurred before the injection into the BILD formation started. Instead, the maximum of the seismicity rate was observed when the deeper injection stopped, which was a common observation derived from other injection experiments.

# REFERENCES


Albright, J.N. and Pearson, C.F., 1982, Acoustic emissions as a tool for hydraulic fracture location: Experience at the Fenton Hill Hot Dry Site: J. Soc. Pet. Eng., **22**, 523-530l.

Aziz, K. and Settari, A., 1979, Petroleum Reservoir Simulation, Applied Science Publishers, New York.

Bachu, S. and J.C. Shaw, 2004, $CO_2$ Storage in Oil and Gas Reservoirs in Western Canada: Effect of Aquifers, Potential for $CO_2$-Flood Enhanced Oil Recovery and Practical Capacity, In: E.S.Rubin, D.W.Keith and C.F.Gilboy (Eds.), Proceedings of 7th International Conference on Greenhouse Gas Control Technologies. Volume 1: Peer-Reviewed Papers and Plenary Presentations, IEA Greenhouse Gas Programme, Cheltenham, UK.

Barnes, D.A., Wahr, A., Harrison, W.B. III, Grammer, G.M., and Gupta, N., *in press* Geological Carbon Sequestration Potential in Devonian Saline Aquifers of the Michigan Basin, AAPG/EMD/DEG Special Publication on Geological Sequestration of $CO_2$.

Beaubien, S.E., S. Lombardi, G. Ciotoli, A. Annunziatellis, G. Hatziyannis, A. Metaxas and J. Pearce, 2004, Potential hazards of $CO_2$ leakage in storage systems - learning from natural systems, In: E.S.Rubin, D.W.Keith and C.F.Gilboy (Eds.), Proceedings of 7th International Conference on Greenhouse Gas Control Technologies. Volume 1: Peer-Reviewed Papers and Plenary Presentations, IEA Greenhouse Gas Programme, Cheltenham, UK.

Beecy, D.J. and V.A. Kuuskraa, 2001, Status of U.S. Geologic Carbon Sequestration Research and Technology, Environmental Geosciences, V. 8, No. 3, pp. 152-159.

Beinkafner, K., 1986, Use of dipmiter logs to refine structural mapping of Teapot Dome, Wyoming. AAPG Bulletin 70 (8): 1031

Bielinsky, A., A. Ebigbo, A. Kopp, H. Class, R. Helmig, 2005, Numerical Simulation of $CO_2$ Storage in Geological Formations using MUFTE-UG, Workshop on Leakage Modeling, Princeton, http://www.princeton.edu/~cmi/events/Geological%20Storage%20Workshop.htm

Bird, P., 1998, Kinematic history of the Laramide orogeny in latitudes 35-49N, western United States: Tectonics, v. 17, p. 780-801.

Blasing, T.J., 2008, Recent greenhouse gas concentrations, Carbon Dioxide Information Analysis Center, http://cdiac.ornl.gov/pns/current_ghg.html, updated September 2008.

Bleizeffer, D., 2008, Company must curb $CO_2$ venting, Casper Star Tribune Online, http://www.trib.com/articles/2008/06/11/news/wyoming/201ccad6c089b30387257464007f288a.txt

Boness, N., 2005, Physical Properties and Multi-Scale Seismic Anisotropy in the Crust Surrounding the San Andreas Fault Near Parkfield, CA, Doctoral Thesis, Stanford University.

Boness, N. L., and Zoback, M. D., 2004, Stress-induced seismic velocity anisotropy and physical properties in the SAFOD Pilot Hole in Parkfield, CA: Geophys. Res. Lett., 31, L15S17.

Bohnhoff, M., Dresen, G., Ellsworth, W.L., Ito, H., *in press*, Passive Seismic Monitoring of natural and induced earthquakes: Case studies and socio-economic relevance. In: S.Cloetingh and J.Negendank (eds.), ILP volume 'New Frontiers in Integrated Solid Earth Sciences'.

Brook, E.J., 2005, Tiny bubbles tell all, Science Vol 310, pp. 1285 – 1287, 25 November.

Brown, K.M., Bekins, B., Clennell, B., Dewhurst, D. and Westbrook, G.K., 1994, Heterogeneous hydrofracture development and accretionary fault dynamics. Geology (22): 259-262.

Bruant, R.G., M.A. Celia, A.J. Guswa and C.A. Peters, 2002, Safe storage of $CO_2$ in deep saline aquifers, V. 36, n. 11, pp. 240A-245A.

Business and Economic Development Interim Committee, October 6th. http://www.wyopipeline.com/mission/Carbon%20Dioxide%20White%20Paper.pdf

Center for Global Development, 2007, Carbon Dioxide Emissions From Power Plants Rated Worldwide. ScienceDaily. Retrieved September 27, 2008, from http://www.sciencedaily.com /releases/2007/11/071114163448.htm

Chang, C., Zoback, M.D. and Khaksar, A., 2006, Empirical relations between rock strength and physical properties in sedimentary rocks: Journal of Petroleum Science and Engineering **51**, 223-237.

Chiaramonte, L., Zoback, M., Friedmann, J. and Stamp, V., 2008, Seal Integrity and Feasibility of $CO_2$ Sequestration in the Teapot Dome EOR Pilot: Geomechanical Site Characterization. Environmental Geology, Volume 54, Number 8, 1667-1675(9).

Chopra, A.K., Stein, M.H., and Dismuke, C.T., 1990, Prediction of Performance of Miscible-Gas Pilots. JPT, December, pp. 1564-1572.

Cooper, S.P. and Goodwin, L.B., 1998, Fracture characterization and variability within a basement-cored Laramide age anticline, Teapot Dome, Wyoming. AAPG Annual Convention Abstract

Cooper, S.P., Lorenz, J.C. and Goodwin, L.B, 2001, 'Lithologic and Structural Controls on Natural Fracture Characteristics Teapot Dome, Wyoming," Sandia Report, contract No. DE-AC04-94AL85000, U.S. DOE , Albuquerque, NM.

Cooper, S.P., Hart, B., Goodwin, L.B., Lorenz, J.C., and Milliken, M., 2003, Outcrop and Seismic Analysis of Natural Fractures, Faults and Structure at Teapot Dome, Wyoming: Wyoming Geological Association 2003 Field Guidebook.

Crampin, S., 1984, Anisotropy in exploration seismic: First Break, March, 19-21.

Crampin, S., 1985, Evidence for aligned cracks in the Earth's crust: First Break, Vo. 3, No, 3, 12-15.

Crampin, S., 1987, Geological and industrial implications of extensive-dilatancy anisotropy: Nature, 328, 491-496.

Crampin, S., Chesnokov, E. M., and Hipkin, R. G., 1984, Seismic anisotropy - the state of the art II: Geophys. J. R. astr. Soc. , 76, 1-16.

Crampin, S., and Lovell, J. H., 1991, A decade of shear-wave splitting in the Earth's crust: what does it mean? what use can we make of it? and what should we do next?: Geophys. J. Int., 107, 387-407.

Dickinson, W.R. and Snyder, W.S., 1978, Plate tectonics of the Laramide orogeny: Geological Society of America Memoir 151, p. 355-366.

Dake, L.P., 1978, Fundamentals of Reservoir Engineering, Chapter 9, Elsevier Scientific Publishing Co.

Dria, D.E., Pope, G.A,. and Sepehrnoori, K., 1993. Three-Phase Gas/Oil/Brine Relative Permeabilities Measured Under $CO_2$ Flooding Conditions, SPERE, May, pp. 143.

Doughty, C. and K. Preuss, 2004, Modeling Supercritical carbon dioxide injection in heterogeneous porous media. Vadose Zone Journal, V.3, pp. 837-847.

Earth Decision - Gocad 2.1.6 Software

Energy & Minerals Field Institute (Emfi), 2004, ChevronTexaco's Rangely Oil Field Operations, http://inside.mines.edu/Outreach/cont_ed/emfi/emfi2005/ChevronTexaco.pdf

Emmet, W.R., Beaver, K.W. and McCaleb, J.A., 1972, Pennsylvanian Tensleep Reservoir, Little Buffalo Oil field, Big Horn Basin, Wyoming: The Mountain Geologist, V.9, No. 1, p. 21-31.

Encyclopedia Britannica Online, accessed October 2008 http://www.britannica.com/EBchecked/topic/585252/Teapot-Dome-Scandal

Falkowski P, RJ Scholes, E. Boyle, J. Canadell, D. Canfield, J. Elser, N. Gruber, K. Hibbard, P. Högberg, S. Linder, F.T. Mackenzie, B. Moore III, T. Pederson, Y. Rosenthal, S. Seitzinger, V. Smetacek, W. Steffen, 2000, The Global Carbon Cycle: A Test of our Knowledge of Earth as a System, Science 290: 291-296.

Finkbeiner, T., Zoback, M.D., Flemings, P. and Stump, B., 2001, Stress, pore pressure, and dynamically constrained hydrocarbon columns in the South Eugene Island 330 Field, northern Gulf of Mexico. American Association of Petroleum Geologists 85 (6): 1007-1031

Flodin, E.A., 2003, Structural Evolution, Petrophysics, and Large-Scale Permeability of Faults in Sandstone, Valley of Fire, Nevada [Ph.D. Thesis]: Stanford University, 180 pp.

Friedmann, S.J., Nummedal, D., Stamp, V.W., 2004, Science and technology goals of the Teapot Dome field experimental facility. NETL 3rd Annual Carbon Sequestration Conference Proceedings, Alexandria, VA, Exchange Monitor Publications

Friedmann, S.J. and Stamp, V.W., 2006, Teapot Dome: Characterization of a $CO_2$-enhanced oil recovery and storage site in Eastern Wyoming: Environmental Geosciences, v. **13**, no. 3, pp. 181–199

Gaines, J., 2008, Monell Unit $CO_2$ Flood, Patrick Draw Field, Sweetwater County, Wyoming. http://eori.uwyo.edu/downloads/CO2Conf_%20May2008/Jason%20Gaines_Anadarko_EORI_CO2%20Casper%20May%2029%202008.pdf

Gale, J., 2004, Geologic storage of $CO_2$: What do we know, where are the gaps and what more needs to be done?, Energy v. 29, pp. 1329-1338.

GEO-SEQ Project Team, GEO-SEQ Best Practice Manual, Geologic Carbon Dioxide Sequestration: Site Evaluation to Implementation, 2004, Earth Sciences Division, Ernest Orlando Lawrence Berkeley National Laboratory, Berkeley, CA, 40 pp.

Grasso, J.R., 1992, Mechanics of seismic instabilities induced by the recovery of hydrocarbon. Pure and Applied Geophysics 139 (3/4):507-533

Gray, F.D., Head, K.J., Chamberlain, C.K., Olson, G., Sinclair, J. and Besler, C., 1999, Using 3D Seismic to Identify Spatially Variant Fracture Orientation in the Manderson Field, paper SPE 5636 presented at the 1999 SPE Rocky Mountain Regional Meeting, Gillette, WY, May 15-18, 1999 Canadian SEG meeting abstracts, 59-63, 1999 Rocky Mountain Association of Geologists and Denver Geophysical Society 3D Seismic Symposium Expanded Abstracts, CSEG Recorder, 24, 8, AAPG Explorer, September.

Gray, D., Boerner, S., Toodorovic-Marinic, D. and Zheng, Y., 2003, Analyzing fractures from seismic for improved drilling success, World Oil, Vol. 224, No. 10, http://www.worldoil.com/magazine/MAGAZINE_DETAIL.asp?ART_ID=2133&MONTH_YEAR=Oct-2003

Gray, D. and Todorovic-Marinic, D. 2004, Fracture Detection using 3D Azimuthal AVO, CSEG RECORDER, http://www.cseg.ca/publications/recorder/2004/12dec/dec04-fracture-detection.pdf.

Gray, D., 2008, Fracture Detection Using 3D Seismic Azimuthal AVO, CSEG RECORDER, March 2008, pp. 34-43.

Gringarten, 2005. Practice of 3D Modeling; Talk at Stanford University, PE 246 class (https://coursework- .stanford.edu/coursework/servlet/ShowFile?contentid=300119

Gutemberg, B. and Ritcher, C.F., 1941, Seismic of the earth, Geol Soc Am Spec Pap 34:1-133

Haimson, B.C., 1978, Crustal Stress in the Michigan Basin: Journal of Geophysical Research, **83,** 5857-5863.

Hall, S.A, J.M. Kendall, O.I. Barkved, 2002, Fractured reservoir characterization using P-wave AVOA analysis of 3D OBC data, The Leading Edge 21 (8): 777.

Hassler, B., 2006, Carbon Dioxide White Paper Prepared for the Wyoming Joint Minerals,

Hennings, P., Zahm, C., Olson J. And Erslev, E. (2008), Geologic Occurrence and Hydraulic Significance of Fractures in Reservoirs – Field Trip Guidebook, AAPG-SPE-SEG Hedberg Research Conference, Casper, WY.

Hubbert, M.K. and Willis, D.G., 1957, Mechanics of hydraulic fracturing: Pet Trans AIME, **210**, 153-63.

Hycal Energy Research Laboratories Ltd., 2004, DOE-RMOTC, Teapot Dome Miscibility study, final report, December 13, 2004, 29 p.

ICPP Special Report, 2005, Carbon Dioxide Capture and Storage, ISBN 92-9169-119-4, http://www.ipcc.ch/activity/ccsspm.pdf

IEA Greenhouse Gas R&D Programme, 2005, Greenhouse gases, information sheet, http://www.ieagreen.org.uk/1.pdf

IEA Greenhouse Gas R&D Programme, 2001, Putting Carbon back into the ground, ISBN 1 898373 28 0, http://www.ieagreen.org.uk/putcback.pdf

Isaaks, E. H., 1990, The application of Monte Carlo methods to the analysis of spatially correlated data: Ph.D. thesis, Stanford University, Stanford, California, 213 p.

Jahn, F., Cook, M. and Graham, M., 1998, Hydrocarbon exploration and production. Elsevier Amsterdam, 384 pp.

Jaeger, J.C. and N.G.W. Cook, 1969, Fundamentals of rock mechanics, Chapman and Hall, New York, 593 pp.

Jarrell, P.M., Fox, C.E., Stein, M.H. and Webb, S.L., 2002, Practical Aspects of $CO_2$ Flooding. Monograph 22, Society of Petroleum Engineers, Richardson, TX, USA.

Jenner, E., 2001, Azimuthal anisotropy of compressional wave seismic data, Weyburn field, Saskatchewan, Canada, PhD Thesis, Colorado School of Mines.

Jenner, E., 2002, Azimuthal AVO: Methodology and data examples, The Leading Edge 21 (8): 782.

Jenssen, K. and F.M. Orr, 2002, Compositional streamline simulation, SPE Paper, 77379, SPE Annual Technical Conference and Exhibition, San Antonio, TX, Sept. 29-Oct.2.

Jessen K., Kovscek A.R., Orr Jr F.M., 2005, Increasing $CO_2$ storage in oil recovery. Energy Convers Manage 46(2): 293–311.

Journel, A.G., 1994, Geostatistics and reservoir geology, in Computer Applications3: Modeling and Geostatistics, Eds., J.M., Yarus and R.L., Chambers, AAPG, 19-20.

Kocurek G., 1981. Erg reconstruction: the Entrada Sandstone (Jurassic) of northern Utah and Colorado. Palaeogeography, Palaeoclimatology, Palaeoecology 36, 125-153.

Kovscek, A.R. and M.D. Cakici, 2005, Geologic storage of carbon dioxide and enhanced oil recovery. II. Cooptimization of storage and recovery. Energy Conversion and Management 46, 1941–1956

Kovascek, A.R. and Y. Wang, 2005, Geologic storage of carbon dioxide and enhanced oil recovery I: Uncertainty quantification employing a streamline-based proxy for reservoir flow simulation, Energy Conversion and Management, in press, 2005.

Lorenz, J. C., and S. P. Cooper, 2004, Analysis of fracture characteristics and distribution of 48-X-28 well: Rocky Mountain Oilfield Testing Center Report, 31 p.

Lorenz, J.C., 2007, Summary of Published Information on Tensleep Fractures: http://eori.uwyo.edu/downloads/Tensleep_FractureStudy1.doc

Lucier, A., Zoback, M.D., Gupta, N. and Ramakrishnan, T.S., 2006, Geomechanical aspects of $CO_2$ sequestration in a deep saline reservoir in the Ohio River Valley region: Environmental Geosciences, **13** (2), 85–103.

McCutcheon, T., 2003, Time Structure Maps – 3D Seismic Data Interpretation, Teapot Dome Oil Field, Naval Petroleum Reserve No. 3, Natrona County, Wyoming. Rocky Mountain Oilfield Testing Center Report Melzer, S.L., 2007. http://eori.uwyo.edu/downloads/Steve%20Melzer%20Oct%2025%20Presentation.pdf

Milliken, M.D., 2005, Surface Mapping Validates 3D Seismic Faulting Interpretations at Teapot Dome Field, Natrona Co., Wyoming. http://www.searchanddiscovery.com/documents/abstracts/2005rocky/RMmilli.htm

Milliken, M.D. and Koepsell, R., 2003, Imaging Technology offers enhanced interpretation of Teapot Dome reservoirs. Wyoming Geological Association Field Guidebook 2002: 41-62

Miller, E. L., M. M. Miller, C. H. Stevens, J. E. Wright, and R. Madrid, 1992, Late Paleozoic paleogeographic and tectonic evolution of the western U.S. Cordillera, in B. C. Burchfiel, P. W. Lipman, and M. L. Zoback, eds., The Cordilleran orogen: Conterminous U.S.: Denver, Geological Society of America, The Geology of North America, v. G-3, p. 57– 106.

Moos, D. and Zoback, M.D., 1990, Utilization of observations of well bore failure to constrain the orientation and magnitude of crustal stresses: application to continental, deep sea drilling project and ocean drilling program boreholes. Journal of Geophysical Research 95 (B6):9305-9325.

Myers, R.D., 1999, Structure and hydraulics of brittle faults in sandstone [Ph.D. Thesis]: Stanford University, 176 p.

Neves, F. A., A. Al-Marzoug, J. J. Kim, and E. Nebrija, 2003, Fracture characterization of deep tight gas sands using azimuthal velocity and AVO seismic data in Saudi Arabia: The Leading Edge, 22, 469–475.

Nummedal, D., B. Towler, C. Mason, and M. Allen, 2003, Enhanced oil recovery in Wyoming— Prospects and challenges: White paper prepared for Dave Freudenthal, governor of Wyoming, 22 p. http://uwadmnweb.uwyo.edu/AcadAffairs/PolicyStatements/EORfinal.pdf

Oil & Gas Journal, EOR continues to unlock oil resources, 2004, Volume 102, issue 14, April 12, http://www.ogj.com/articles/save_screen.cfm?ARTICLE_ID=202474

Pacala, S. and Socolow,R., 2004, Stabilization Wedges: Solving the Climate Problem for the next 50 Years with Current Technologies, Science, August 13.

Parson, E.A. and D.W. Keith, 1998, Fossil fuels without $CO_2$ emissions, Science v. 282, pp. 1053-1054.

Phillips, W.S., Rutledge, J.T., House, L.S. and Fehler, M.C., 2002, Induced Microearthquake Patterns in Hydrocarbon and Geothermal Reservoirs: Six Case Studies, Pure and applied Geophysics, **159**, 345-369.

Pruess, K., Garcia, J., Kovscek, T., Oldenburg, C., Rutqvist, J., Steefel, C., and Xu, T., 2004, Code intercomparison builds confidence in numerical simulation models for Geologic disposal of $CO_2$. Energy, 29, (9-10), 1431-1444.

Raleigh, C.B., Healy, J.H. and Bredehofft, J.D., 1976, An experiment in earthquake control at Rangeley, Colorado. Science 191:1230-1237

Reinecker, J., Heidbach, O., Tingay, M., Sperner, B. & Müller, B., 2005, The 2005 release of the World Stress Map (available online at www.world-stress-map.org).

Ritcher, C.F., 1935, An instrumental earthquake magnitude scale, Bull Seismol Soc Am 25:1-32.

Rogers, S., 2002, Critical stress-related permeability in fractured rocks. Fracture and in situ stress characterization of hydrocarbon reservoirs. M. Ameen. London, The Geological Society, **209**, 7-16.

Rüger, A., 1996, Reflection Coefficients and Azimuthal AVO Analysis in Anisotropic Media, Doctoral Thesis, Center for Wave Phenomena, Colorado School of Mines.

Rüger, A., 2002, Reflection coefficients and azimuthal AVO analysis in anisotropic media,

Rüger, A. and I. Tsvankin, 1997. Using AVO for fracture detection: Analytic basis and practical solutions, The leading Edge, October, pp. 1429 – 1434. R&D Project Database, http://www.co2captureandstorage.info/co2db.php4

Segall, P. and Fitzgerald, S.D., 1998, A note on induced stress changes in hydrocarbon and geothermal reservoirs. Tectonophysics 289: 117-128

Schlumbergers's Oil Field Glossary, 2008, http://www.glossary.oilfield.slb.com/Display.cfm?Term=tube%20wave

Schwartz, B., T. H. Wilson, and D. H. Smith, 2005, Fracture pattern Dome, Wyoming, Eastern Section AAPG Abstracts with Program, September 18– 20, Morgantown, West Virginia.

Shapiro, S., Rothert, E. Rath, V. and Rindschwentner, J., 2002, Characterization of fluid transport properties of reservoirs using induced microseismicity: Geophysics, **67** (1), 212–220.

Simpson, D.W., 1986, Triggered Earthquakes, Ann Rev. Earth Planet.Sci. 14, 21-42.

Snoke, A. W., 1993, Geologic history of Wyoming within the tectonic framework of the North American Cordillera, in Snoke, A. W., Steidtmann, J. R., and Roberts, S. M., editors, Geology of Wyoming: Geological Survey of Wyoming Memoir No. 5, p. 2-56. (I have a copy Trisha gave me).

Socolow, R., 2005, The stabilization of $CO_2$ emissions in the coming 50 years, talk at the Institut Francais du Petrol, Paris, 15 September, http://www.princeton.edu/~cmi/research/Integration/integrationrpt.shtml

Socolow, R., 2003 Capturing and Storing Fossil-Fuel Carbon, talk at University of California at Berkeley, http://www.princeton.edu/~cmi/research/Integration/integrationrpt.shtml.

Stroud, J., 2008, The Bairoil Complex, http://eori.uwyo.edu/downloads/CO2Conf_%20May2008/John%20Stroud_Merit_EORI_CO2%20Casper%20May%2029%202008.pdf

Tezuka, K., 2006, Hydraulic Injection and Microseismic Monitoring in the Basement Gas Reservoir in Japan: 2006 SPE Forum Series in Asia Pacific - Hydraulic Fracturing Beyond 2010, Macau, China, Society of Petroleum Engineers.

Townend, J., and Zoback, M. D., 2000. "How faulting keeps the crust strong." Geology, 28, 399 - 402.

Twiss, R.J. and Moores, E.M., 1992, Structural Geology, W. H. Freeman, New York. 532 pp.

Wadleigh, E.F., 2005, RMOTC in-house reservoir simulation work products.

White, D.J., G. Furrowes, T. Davis, Z. Hajnal, K. Hirsche, I. Hutcheon, E. Majer, B. Rostron and S. Whittaker, 2004, Greenhouse gas sequestration in abandoned oil reservoirs: The International Energy Agency Weyburn pilot project, GSA Today, V. 14, no. 7, pp. 4–10.

Wiprut, D., and M.D. Zoback, 2000, Fault reactivation and fluid flow along a previously dormant normal fault in the northern North Sea, Geology, v.28, no.7, pp. 595-598.

Wiprut, D.J. and Zoback, M.D., 2002, Fault reactivation, leakage potential, and hydrocarbon column heights in the northern North Sea. In: Koestler AG and Hunsdale R (eds) Hydrocarbon Seal Quantification (NPF Special Publication) 11: 203-219.

Wyoming State Geological Survey, Carbon Dioxide Group: $CO_2$ in Wyoming. http://www.wsgs.uwyo.edu/co2/

Yin, P., 2005, Characterization of Tensleep Sandstone reservoirs: Rocky Mountain Section AAPG Annual Meeting Abstracts and Program, Search and Discovery article 50024:http://www.searchanddiscovery.com/documents/2005/yin2/images/yin2.pdf

Yin, P., Nummedal, D. and Shang, Q., 2005, Reservoir Heterogeneity Caused by Diagenesis in Tensleep Sandstones, Teapot Dome, Wyoming. http://www.searchanddiscovery.net/documents/2005/yin/index.htm

Zheng, Y., Todorovic-Marinic, D. and Larson, G., 2004, Fracture detection (AVAZ): ambiguity and practical solution, 74th Annual Internat. Mtg., Soc. Expl. Geophys., Expanded Abstracts.
http://www.cseg.ca/conventions/abstracts/2004/2004abstracts/091S0209-Zheng_Y_Fracture_Detection.pdf

Zhang, Q., Nummedal, D. and Yin, P., 2005, Stratigraphy, sedimentology and petrophysics of the Tensleep Sandstone at Teapot Dome and in outcrop. http://www.searchanddiscovery.com/documents/abstracts/2005rocky/RMzha.htm

Zhou W., M. Stenhouse, S. Whittaker, D.H.-S. Law, R. Chalaturnyk, W. Jazrawi, 2004, The IEA Weyburn $CO_2$ Monitoring and Storage Project - Modeling of the Long-Term Migration of $CO_2$ from Weyburn, In: E.S.Rubin, D.W.Keith and C.F.Gilboy (Eds.), Proceedings of 7th International Conference on Greenhouse Gas Control Technologies. Volume 1: Peer-Reviewed Papers and Plenary Presentations, IEA Greenhouse Gas Programme, Cheltenham, UK.

Zoback, M.D., 2007, Reservoir Geomechanics: Earth Stress and Rock Mechanics Applied to Exploration, Production and Wellbore Stability, Cambridge Press, Cambridge Press, 449 pp.

Zoback, M.D., Barton, C.A., Brudy, M., Castillo, D.A., Finkbeiner, T., Grollimund, B.R., Moos, D.B., Peska, P., Ward, C.D. and Wiprut, D.J., 2003, Determination of stress orientation and magnitude in deep wells. International Journal of Rock Mechanics and Mining Sciences 40: 1049-1076

Zoback, M.D. and C. Zinke, 2002, Production-Induced Normal Faulting in the Valhall and Ekofisk Oil Fields, Pure App. Geophys V. 159, pp. 403-420.